Large Strain Deformation Behavior of Oriented Triblock Copolymer Cylinders

by

Christian Honeker

B. S., Materials Science
Cornell University, 1991

Submitted to the
Department of Materials Science and Engineering
Program in Polymer Science and Technology
in partial fulfillment of the requirements for the degree of

Doctor of Philosophy in
Materials Science and Engineering

at the

MASSACHUSETTS INSTITUTE OF TECHNOLOGY

June 1997

© Massachusetts Institute of Technology, 1997. All Rights Reserved.

Author ....
Materials Science and Engineering
May 2, 1997

Certified by ....
Edwin L. Thomas
Morris Cohen Professor of Materials Science and Engineering
Thesis Supervisor

Accepted by ....
Linn W. Hobbs
John F. Elliot Professor of Materials Science and Engineering
Chairman, Department Committee on Graduate Students

MASSACHUSETTS INSTITUTE
OF TECHNOLOGY

JUN 1 6 1997 ARCHIVES

Large Strain Deformation Behavior of Oriented Cylinder Triblock Copolymers

by Christian Honeker

Submitted to the Department of Materials Science and Engineering
Program in Polymer Science and Technology
May 2, 1997
in Partial Fulfillment of the Requirements for the Degree of
Doctor of Philosophy in Materials Science and Engineering

Abstract

The morphology of a well-defined single grain of stiff glassy cylinders in a rubbery matrix was observed as a function of deformation to determine the deformation mechanisms and how these depend on the orientation of the applied stress with respect to the microdomain structure. Styrene-diene triblock copolymers were roll-cast to achieve an oriented cylinder morphology with a near single-crystal texture and were deformed to high strains (up to 600%). Static SAXS measurements of cylinder orientation demonstrated highly aligned cylinders (< 15° misorientation) with the closest packed plane parallel to the film surface (< 12° rotational misalignment).

The deformation perpendicular and parallel to the cylinder axis was followed via synchrotron SAXS with simultaneous measurement of load. Deformation was frozen in the samples by high-energy electron irradiation and cryo-microtomed sections were examined by TEM.

Deformation perpendicular to the cylinder axis proceeds in two stages: low strain elastic deformation and high strain deformation, separated by a kinking instability. Initially the composite behaves as a constrained rubber in a state of plane strain. Lateral contraction occurs almost exclusively in the unconstrained direction giving rise to a Poisson ratio of 0.9 for the matrix. At a strain of approximately 130% a shear instability, occurring first in local regions of cylinder misalignment, causes a kinking of the cylinders on opposite sides of the kink in which the cylinders cooperatively turn towards the stretching direction (SD). Kinking relieves the plane strain constraint on the rubber allowing the lower energy process of shear rather than a higher energy bulk dilation process. At high strain the deformation proceeds by a continuous shear with an increase in spacing between cylinders along the SD as the matrix continues to contract laterally. TEM results provide direct evidence of a chevron texture of kinked cylinders when viewed at perpendicular incidence. At parallel incidence faults in the distorted hexagonal lattice are observed. The correlation lengths of the chevrons and faults are estimated to be 5 μm and 0.1 μm respectively. Both real and reciprocal space data are combined to construct a 3-D model of the deformed structure.

Stress relaxation experiments in the perpendicular deformation geometry show that the chevron texture of the kinked cylinder morphology does not change despite a significant drop in stress over time. A mechanism is proposed whereby chains diffuse along the interface to relax their stretched conformations without altering the deformed microdomain structure.

Deformation parallel to the cylinder axis proceeds in four stages: Hookean, neck formation, neck propagation and drawing. SAXS patterns show a discontinuous change from a 1-D profile oriented along the equator to one with two pairs of streaks just above and below the plane of the equator, as the neck passes through the probed region. Dynamic SAXS data during drawing are consistent with segmentation of the glassy cylinders. The gaps between cylinders close upon unloading resulting in minor structural hysteresis. Static SAXS taken in the three principal directions on a large deformation sample demonstrates that the cylinders do not rotate during parallel deformation.

Thesis Advisor: Prof. E. L. Thomas

Title: Morris Cohen Professor of Materials Science and Engineering

Acknowledgments

Almost every aspect of my work and my life here at MIT was pleasurably influenced in some way by the many people with whom I worked and interacted. I wish here to express a few words of thanks.

Professor Edwin (Ned) Thomas acted almost as a coach, always pushing to get more data and better science out of me. He has been there at every stage of this thesis, encouraging critical thinking, providing new insights and perhaps most importantly connecting me with the people, equipment, information and opportunity necessary to perform the best science possible. The chance to travel and meet some of the famous people whose work I benefited from is also much appreciated.

Much of the deformation equipment integral to the thesis was designed and constructed by a number of people. Arthur and Steve Rudolf built the first deformation stage used at Princeton. They also provided design advice and assistance on several small jobs. The second incarnation of the deformation stage benefited greatly from my father, Klaus Honeker who provided a feasible design concept and much direction in its execution. Mr. Bill Nespel machined and assembled the unit, ensuring that it functioned properly. Tom White helped the stage "come alive" and move through his assistance in the design and construction of the control box. Bill Pene constructed the double tilt cradle adding flexible to the SAXS deformation experiments.

The collaboration with Prof. Sol M. Gruner and Dr. Damian A. Hajduk in the biophysics group at Princeton impacted me in several ways. I became a team member in the discovery of a new equilibrium microdomain morphology (the Gyroid). I learned first

hand the practical benefits of combining TEM and SAXS in understanding morphology. I thank Damian for the use of his SAXS beamline ("twitchy") in the early deformation work. These results convinced me that there was something there worth pursuing. Another lesson learned from Damian was the importance of a well-kept notebook. Something which should not be underestimated!

The experience working at the National Synchrotron Light Source at Brookhaven was perhaps the highlight in my graduate student career. I feel quite fortunate that the X-12b beamline is designed to be so user friendly that my first run was an overwhelming success. This is in large part due to the efforts of Dr. Malcolm Capel, the beamline manager. His technical expertise was absolutely essential in generating most of my results. I am slowly realizing how spoiled a user I have become, and might find myself wishing I again had access to X-12b sooner than I think. Tom Langdon also deserves credit as Dr. Capel's able technical assistant who is able to fix (modify) things sometimes at a moment's notice.

Though Ned warned me about taking too much data at Brookhaven, the temptation proved too great to resist. In attempting to analyze this mountain of data, Dr. Robert Wisniewski wrote several useful C programs. In addition, I want to thank him for his constant source of answers for my questions concerning the ins and outs of UNIX and SGIs. He has also been a great friend for many years.

The TEM side of this thesis would have been far less interesting without a source of high energy electrons for cross-linking deformed samples. The initial experiments with Mr. Kenneth Wright at the High Voltage Lab (HVL) at MIT, demonstrated the feasibility of this approach. Additional experiments conducted at Raychem in Menlo Park with the assistance of Dr. Bill Johnson and Mr. James Replogle helped provide the real space data necessary to make sense of those strange SAXS patterns.

TEM micrographs were dissected by taking digital FFTs. Several people helped me here. Phil Thompson introduced me to Khoros which provided me with the first usable FFTs. Rob Lescanec wrote a FFT program to make the process much more convenient. I also thank him for instructive discussions on block copolymer theory and guidance during my early years here. I thank Ken Auerbach for his work in attempting to install an FFT algorithm in the AMT software for the JEOL 200 CX CCD detector.

Working on the Gyroid project brought me into contact with the remarkable Hal Robinson. He connected me to the abstract world of minimal surfaces in a very concrete way, he built them. I still think that his skill is such, that if you can describe an object to him, he can construct a model of it.

Finally, I thank the members of the group (past, present and just visiting) that have contributed to this thesis in their own way (in no particular order): Benita Dair for her invaluable assistance at Brookhaven, advice on english grammar as well as life in general. Bruce Carvalho for encouraging me to continue when I wanted to quit, whether it was taking data at Brookhaven or working on a thesis that kept getting longer instead of getting finished. Yiannis Tselikas for his company on my first trip to Brookhaven in the fall of '94. Apostolos Avgeropoulos for his help in understanding block copolymer chemistry. John Chen for the development of the optical bench and his endlessly diverting video games. Ramon Albalak for the invention of the roll-caster and showing me the myriad uses for a hammer. Stephanie Simmons and Martha Himes for introducing me as a prospective student to what it means to be in Ned's group. Debbie Vezie for teaching me about the dark room and convincing me to put Prof. Argon on my committee. Sam Gido for inspiring me to keep my references organized. MaryJane O'Rourke for her upbeat spirit. Len Radzilowski for attempting to answer my questions, be they about computers, TEM, microtoming, or WWII.

On a more personal note, life at MIT was made more bearable by the pool located not more than 100 yards from the lab. I had fun swimming with Phil C., Phil T., Pete M., Keoki J. and others. Walden now has new meaning for me. I thank Rachel Bredemeier for listening to me (complaining and otherwise). Most important for keeping me sane and in company was Julia Duncan.

Without the patience and support of my parents, none of this would be possible.

TABLE OF CONTENTS

LIST OF FIGURES

LIST OF TABLES

List of Abbreviations

$\parallel\perp$	parallel deformation perpendicular view (or incidence)
$\perp\parallel$	perpendicular deformation parallel view (or incidence)
$\perp\perp$	perpendicular deformation perpendicular view (or incidence)
ABA	symmetric triblock copolymer
BNL	Brookhaven National Laboratory
CCL	console control language
FFT	Fast Fourier Transform
FWHM	full width half maximum
HKL	Miller indices
hkil	Miller-Bravais indices
HVL	High-Voltage Lab (at MIT)
IMDS	intermaterial dividing surface
IR	infrared
L/D	length/diameter ratio
NMR	nuclear magnetic resonance
NSLS	National Synchrotron Light Source
ODT	order-disorder transition
OT	optical transform
PB	polybutadiene
PS	polystyrene
PSD	position sensitive detector
SANS	small angle neutron scattering
SAXS	small angle x-ray scattering
SBS	polystyrene-polybutadiene-polystyrene triblock
SD	stretching direction
SDD	sample-to-detector distance
$(SI)_{18}$	star block copolymer with 18 arms
SIS	polystyrene-polyisoprene-polystyrene triblock
SSL	strong segregation limit
TEM	transmission electron microscopy (microscope)
T_g	glass transition temperature
TPE	thermoplastic elastomer
WAXS	wide angle x-ray scattering

Chapter 1 Introduction

1.1 Opening Remarks

The scientific goal in the present investigation was first introduced to me on a napkin in the student center dining hall. A stress-strain curve was drawn and the question asked: "what is the morphology at various points along the deformation?" Since the composition-morphology relationship is well understood for block copolymers, the impact of this well-defined structure on the large strain deformation properties of these materials seemed the next logical problem to attack. The figure drawn on the napkin was perhaps based on Figure 9 in (Hashimoto et al., 1979), which showed a series of schematic small-angle x-ray scattering (SAXS) patterns mapped to a stress-strain curve for an isotropic styrene-diene TPE with a lamellar morphology. The novelty of the proposed idea was to utilize the highly oriented materials being produced in our lab by the newly invented roll-caster. Samples with a global orientation provide an opportunity to observe the response of an effective single grain to the imposed deformation.

Thus, I embarked on my quest to understand the deformation behavior of glassy oriented cylinders in a rubbery matrix. A review of the extensive literature on block copolymer deformation revealed only a few studies on oriented materials for any morphologies. Initial SAXS experiments on roll-cast oriented cylinders performed in collaboration with Dr. D. A. Hajduk and Prof. S. M. Gruner at Princeton, provided evidence for a dramatic variation in structure with deformation, more complicated than previously thought.

SAXS experiments of increased temporal and spatial resolution conducted at the National Synchrotron Light Source (NSLS) at Brookhaven National Laboratory (BNL) yielded an almost movie-like series of patterns complete with moving peaks which could change shape, disappear and later reappear at new locations. What was needed, however, was a real space model which could account for the observed diffraction patterns. The problem of "freezing" in the deformation in a highly elastomeric material for study via TEM was addressed by high-energy electron irradiation. Through cross-linking, significant amounts of deformation were captured in tensile samples similar. TEM on these samples provided direct information on the deformed structure in several projection directions.With a real space 3-D model at hand, an attempt was made to elucidate the mechanism of the deformation on the basis of the *in-situ* SAXS data.

This thesis focuses on the deformation behavior at large strain for highly oriented styrene-diene TPEs with a morphology of glassy PS cylinders in a diene matrix. Three topics are investigated: deformation perpendicular to the cylinder axis, deformation parallel to the cylinder axis and stress relaxation perpendicular to the cylinder axis. Deforming cylinders in either of the two principal directions (perpendicular to or parallel to the cylinder axis) leads to mechanical instabilities reflected in a stress softening in the stress-strain curves. These mechanical instabilities are shown to be due to structural transitions at a critical strain in the respective directions.

In perpendicular deformation, the Poisson effect places the cylinders in a state of biaxial compression. The cylinders resist the compression in the constrained direction (along the cylinder axis), while the unconstrained direction responds immediately to the applied stress. Regions of local cylinder misalignment serve as nucleation sites for the tilting of cylinders towards the stretching direction. Since the cylinders are connected by bridging molecules, the rotation becomes a cooperative kinking of the cylinders, which quickly spreads throughout the volume of the sample to relieve the compressive stress. The SAXS signature for the kinking structure is a characteristic X-pattern, which corresponds to the chevron texture as seen in TEM. The kinking transition coincides with the stress-softening in the stress-strain curve on first loading. Further deformation involves shearing of the cylinders with respect to one another as they turn towards the stretching direction.

In parallel deformation, the mechanical instability is a sharp yield point at small strain (< 5%) coinciding with the formation of a localized neck. The neck grows and propagates along the gauge region, transforming unnecked material (at low strain) into necked material (at higher strain) in a transition zone (region of strain gradient). SAXS patterns taken of the necked region are consistent with previous TEM results showing cylinder segments aligned in the stretching direction with breaks between segments. Further deformation of the necked region results in drawing, whereby the mean distance between rods increases with deformation. These gaps close when unloaded, leaving the PS cylinders broken but aligned in the stretching direction.

SAXS studies of stress relaxation in perpendicular deformation shows that the chevron angle and intercylinder spacing do not change despite a significant drop in stress. Measurement of the thickness change via x-ray transmission measurements suggests that relaxation occurs primarily via motion of the matrix chains in the unconstrained (neutral) direction. The sample held at constant deformation gets thicker while remaining at constant width. The rate of stress relaxation depends strongly on molecular architecture. An 18-armed star block copolymer stress relaxes slower than a 2-armed star (linear triblock) due to a high bridging fraction for a multi-armed block copolymer (see Chapter 6).

1.2 Thesis Organization

Chapter 2 is a review of block copolymer orientation methods and previous deformation studies conducted on oriented samples with a cylinder morphology. A rational approach to understanding structure-mechanical property relationships for TPEs is presented. Chapter 3 provides some background on diffraction from a hexagonally packed cylinder morphology. Chapter 4 presents the experimental methods used to probe the deformed morphology in reciprocal space (via synchrotron SAXS) and in real space (via TEM on samples cross-linked with high energy electron radiation). Chapter 5 is a experimental study on the details of the evolution of morphology with deformation when the stretching direction is applied perpendicular to the cylinder axis. Chapter 6 compares the stress relaxation behavior in the perpendicular deformation geometry of a linear triblock to that of a star block copolymer. Chapter 7 extends the understanding of the high strain deformation mechanism when force is applied along the cylinder axis. Chapter 8 outlines directions for future investigations of all three deformation experiments, and suggests areas for experimental improvement. An appendix briefly reviews diffraction with emphasis on several distortion effects.

1.3 Bibliography

Hashimoto, T., M. Fujimura, K. Saijo, H. Kawai, J. Diamant and M. Shen (1979). Strain-induced plastic-to-rubber transition of a SBS block copolymer and its blend with PS. Multiphase Polymers. S. L. Cooper and G. M. Estes, ACS Advances in Chemistry Series: 257-275.

Chapter 2 Role of Morphology on Mechanical Properties*

2.1 Introduction

This literature review will examine the role of morphological orientation in the investigation of the mechanical properties of multiphase polymer systems with special emphasis on the cylinder morphology in ABA triblock copolymers. Thermoplastic elastomers (TPEs) represent a class of multiphase polymers, which have a typical domain structure on a 10 nm length scale and a typical grain structure on a 1000 nm length scale. There are four main TPE materials of commercial importance, each consisting of a hard block (crystalline or glassy) coupled to a rubbery soft block: polystyrene/elastomer, polyurethane/elastomer, polyester/elastomer and polyamide/elastomer. The first is a simple triblock, while the latter three are made up of segmented multiblocks of the indicated constituents. In addition, TPEs can be made by the fine scale blending of a hard thermoplastic homopolymer with an elastomer (Holden, 1987; Wolfe, 1987).

The common feature of a TPE is the presence of a soft domain, that gives rise to the elastomeric nature of the material, in intimate contact with a hard domain, that increases the modulus and enhances the mechanical integrity of the composite material. A key attribute of most TPEs is the ability to tailor toughness and large strain elasticity by varying the ratio of hard and soft fractions. Upon the addition of heat and/or solvent, a TPE system becomes reversibly homogeneous and processible.

Thermoplastic elastomers (TPEs) are a large and rapidly growing segment of the non-tire rubber market. Practical advantages, including lower fabrication costs,

---

*. This chapter represents a section of a review article published as: Honeker, C. C. and Thomas, E. L. *Chemistry of Materials* **1996**, *8*, #8, 1702.

recyclability, and higher manufacturing speed, have stimulated the replacement of conventional thermosetting rubber articles for low-temperature applications without aggressive solvents. The various classes of TPEs provide a spectrum of tailorable properties applicable to markets such as: automotive, household appliances, tools, electrical, and medical. Presently TPEs represent an estimated 12% of the non-tire market share, yet this percentage is expected to double by the first decade of the next century (Rader, 1996).

The best understood TPEs are the styrenics, primarily because of the excellent molecular and hence morphological control of the structure. However, despite numerous previous studies on this system, a quantitative structure-property relationship remains elusive.

2.1.1 Structure of a Model TPE

In this study, the focus is on perhaps the most ideal class of TPEs, the polystyrene/ polydiene/polystyrene ABA triblock copolymers.

In block copolymers, three levels of structure can be distinguished:

- the local chemical microstructure of the blocks
- the size and shape of the microdomains
- the superstructure of the grains

Figure 2-1 illustrates this hierarchical structure for a triblock comprised of a majority of polybutadiene (PB) and a minority of polystyrene (PS). Scale bars are included to provide an indicator of the respective length scales. Typically, hundreds to thousands of such units make up each respective block Both blocks are noncrystalline and it is only the incompatibility of the two monomers that drives the self assembly into A-rich and B-rich microdomains. The size and shape of the microdomains are dictated primarily by the

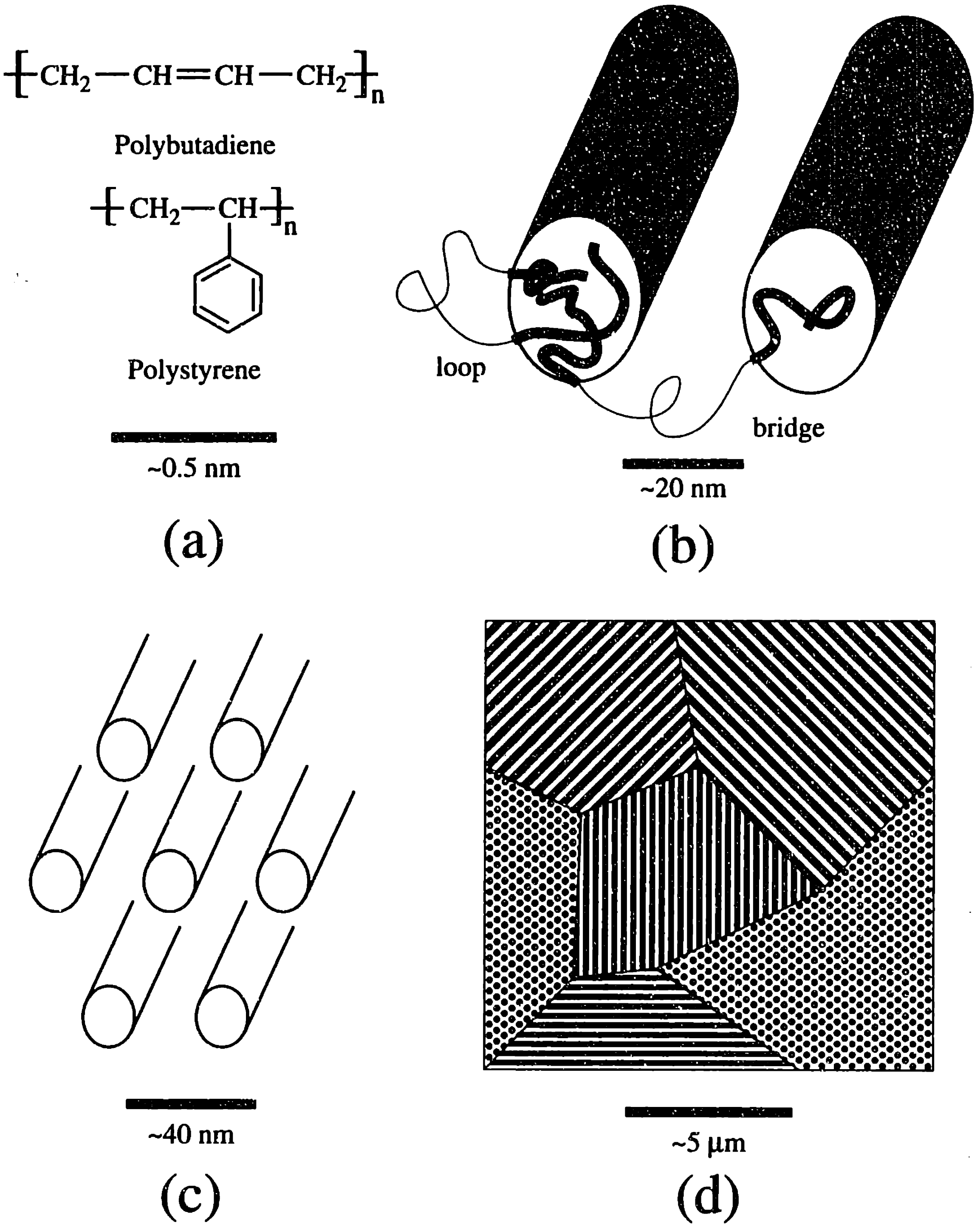

Figure 2-1: Structure of an ABA triblock copolymer viewed on several length scales.
(a, b) Synthetic variables determine structure at the smallest length scales.
(c, d) The microdomain geometry, grain size, and orientation are some examples of important morphological variables.

relative volume fractions of the two blocks. In this example, the minority glassy PS block forms cylindrical microdomains embedded in the majority rubbery PB matrix. These cylindrical microdomains, which are comprised of a PS interior and are surrounded by a polybutadiene corona, in turn, assemble themselves onto a 2-D hexagonal lattice. Two types of conformations are shown for the rubbery midblock: loops and effective bridges (including catenated loops), which are key for stress transfer between the glassy domains. If, in preparing a bulk sample, the self-assembly process occurs quiescently, i.e., without the application of hydrodynamic flow or electromagnetic fields, then small regions of parallel cylinders randomly nucleate and grow until impingement. These impinged regions form a grain structure much like a polycrystalline material and the grains typically contain hundreds of cylinders. Just as in other crystalline materials, minimization of high energy grain boundaries drives grain growth when the system is annealed above the glass transition temperature (T_g) of the higher T_g block.

Grain sizes of block copolymers are usually in the 1-10 micron range (Balsara et al., 1996) so that a macroscopic sample of copolymer (> 1mm) will generally exhibit isotropic properties. If an applied bias field is present during the self assembly process, then instead of random nucleation of the microdomains, a single crystal-like orientation can develop. Another way to develop a highly aligned structure is to texture an initially random polygrain structure by application of a bias field to the already microphase separated state. A number of processes that achieve aligned structures to varying degrees are described in Section 2.3.

2.2 Structure - Property Relationships

An ideal investigation of the structure-mechanical property relation in block copolymers involves several aspects:

- Control of synthetic and morphological variables.
- Application of molecular and morphological characterization tools to assess initial morphology and to follow the evolution of the morphology as a function of temperature and mechanical variables.

The main features of the styrene-diene composition-morphology diagram in the strong segregation limit (SSL - with χN large, where the Flory-Huggins interaction parameter χ represents the relative incompatibility between dissimilar monomers and N is the numbers of statistical segment lengths (proportional to the molecular weight of the polymer) were first outlined in (Molau, 1970). It is possible to predict what the equilibrium microdomain structure should be *based on composition alone*. This has several advantages in block copolymer deformation studies. Polymer chemists are thus able to reproducibly synthesize a molecule with the desired microdomain structure. Secondly, models useful for interpretation of deformation results can be constructed based on the appropriate microdomain geometry. Unfortunately, many deformation studies (Smith et al., 1969; Robinson et al., 1970; Pedemonte et al., 1976; Akovali et al., 1977; Chen et al., 1977; Diamant et al., 1982; Ramsteiner et al., 1984), and even recent ones (Seguela et al., 1988; Yamaoka et al., 1993), have not paid sufficient attention to whether or not a sample has achieved the equilibrium microdomain structure or to whether the sample is globally aligned. Solvent casting, especially for highly volatile, preferential solvents, is known to induce non-equilibrium metastable microdomain structures, and many early studies (Smith and Dickie, 1969; Robinson and White, 1970; Akovali et al., 1977; Diamant et al., 1982) are of limited value since they measure the mechanical properties of metastable samples. However, with the appropriate annealing regimen, it is possible in most cases, to drive the system to microdomain equilibrium even in samples cast from preferential solvents. To get a global equilibrium morphology, i.e., a sample consisting of a single large grain composed of well-ordered microdomains, special processing is needed. In any case, a check of the initial morphology should be performed so that a proper setting for further interpretation is provided, even in studies of mechanical properties not emphasizing the role of morphology.

2.2.1 The Importance of Large Scale Morphology

Often, after the synthesis of a new polymer, preliminary experiments are performed to determine the material properties. In attempts to understand the link between the molecular structure of a material (e.g., the chemical nature of the constituents in the new polymer) and its physical characteristics, measurements generally include some type of deformation experiment to extract mechanical information, since it will often be the mechanical properties of the new material that determine its commercial usage. Presently, polymer chemists are still far from being able to design polymers with the appropriate mechanical properties, although the field of polymer science and engineering has come a long way towards this goal. Mechanical properties, e.g., modulus, toughness and strength, however, depend on much more than the chemistry, molecular microstructure and local conformation of the polymer chain. Structures on larger length scales such as grains, grain boundaries and line defects can mask or even dominate the response of the material to a mechanical stimulus. These larger scale structural aspects, and in turn the macroscopic properties, are significantly influenced by the processing history of the sample. In order to better understand the impact on macroscopic mechanical properties of introducing or replacing a particular side group or incorporating a novel monomeric species, it is necessary to link the molecular response to the macroscopic stimulus in a more direct way. This can be done by controlling the morphology (i.e., through orientation), so that the potentially obscuring effects of the aforementioned supra-molecular defect structures are reduced. The techniques used to manipulate morphology rely on the ability to couple an externally applied field to some molecular and/or supramolecular feature in the polymer. A brief discussion of these orientation techniques is provided in the following section.

2.3 Orientation Methods

There are many ways to couple an external field to a polymer system for the purpose of inducing microdomain orientation. Most mechanical means rely on a hydrodynamic flow field to influence the domain structure, either through stress transfer to the stiffer microdomain component, or through a perturbation of the overall chain conformation prior to microdomain formation. Electrical and magnetic fields can provide a molecular stimulus through the dielectric and diamagnetic anisotropy of the monomeric units as well as a morphological stimulus through a composition-dependent variation of the dielectric constant (Amundson et al., 1991; Amundson et al., 1992). It is the latter driving force that induces microdomain orientation in most cases. In contrast to the strong effect of flow fields, the driving force for electric or magnetic field-induced orientation is weak.

A particular orientation method in most studies of block copolymers is selected for studying the orientation method itself or as a convenient means to prepare oriented samples for further study. The fluid dynamics of the various hydrodynamic flow field techniques can be complex and have been reviewed (Larson, 1992). Here, emphasis will be placed on the various methods as a tool for preparing samples for subsequent deformation study. One restriction in considering these techniques for orienting morphologies is that the resultant samples should have a uniform orientation throughout a volume large enough for tensile testing.

2.3.1 Extrusion

Extrusion is a common commercial processing method for thermoplastic elastomers (Walker, 1979; Bhowmick et al., 1988). Several attempts of relating the orientation due to the processing to the structure have been made (Pedemonte et al., 1974; LeBlanc, 1977; Riep, 1983). The most successful investigation was carried out by Keller and co-workers, who were the first to apply extrusion to orient a block copolymer. They demonstrated a dramatic success in inducing global orientation in extruded plugs of a poly(styrene-butadiene-styrene) (SBS) TPE (Keller et al., 1970; Folkes et al., 1973). Molten (but still microphase-separated) material was squeezed through an orifice into a heated glass capillary, before being cooled to room temperature. Flow through the glass capillary was found to impart additional shear, enhancing the quality of orientation. However, due to the variation in shear profile, the degree of orientation varied from the surface of the plug (maximum shear) to the core (minimum shear). Nevertheless, full advantage of the macroscopic nature of the orientation was made in experiments probing mechanical properties, birefringence, and swelling behavior. Details of some of these pioneering deformation studies will be discussed in Section 2.5.1.

2.3.2 Reciprocating Shear

A significant advancement in the techniques used to orient block copolymers was made by Skoulios and Hadziioannou with the introduction of a reciprocating shear apparatus (Manthis et al., 1977; Skoulios, 1977; Hadziioannou et al., 1979; Hadziioannou et al., 1979). The equipment consisted of two parallel plates with an adjustable gap. The block copolymer was sheared by the oscillatory motion of the bottom plate with respect to a stationary top plate. Both blocks were heated with shearing conducted under vacuum for several hours. The reciprocating shear technique has been recently revived (Almdal et al., 1992; Koppi et al., 1994; Mortensen et al., 1995) and is becoming a common technique for orientation (Muller et al., 1993; Okamoto et al., 1994). One advantage to this technique is the simplicity of the flow field (simple shear). This led to the development of a theory (Cates et al., 1989; Fredrickson, 1994) that is able to predict the experimentally observed “flipping” transition of lamellae diblocks (Koppi et al., 1993), whereby the lamellar normals rotate from the shear gradient (parallel configuration) to the vorticity (perpendicular configuration) direction as the order disorder transition (ODT) is approached or shear rate increased.

2.3.3 Press Molding

A common method used to orient block copolymers, but whose orientation mechanism is much less understood is press molding. Typically, the copolymer is heated and compressed to a desired thickness. The resulting biaxial flow field produces a film within which the morphology is radially oriented. Press molding has been typically applied to block copolymers with cylindrical morphology (Pedemonte et al., 1975; Pedemonte et al., 1976; Tarasov et al., 1978; Pakula et al., 1985). Only a few press-molding studies have been carried out on block copolymers with lamellar morphology (Yamaoka and Kimura, 1993; Yamaoka, 1996).

2.3.4 Roll-Casting

A new orientation technique called "roll-casting" has recently been developed in our laboratory (Albalak et al., 1993; Albalak, 1994; Albalak et al., 1994). Roll-casting involves the slow evaporation of solvent from a homogeneous solution with the simultaneous application of a periodic flow field to produce films with an oriented morphology. The most important difference between roll-casting and the aforementioned orientation techniques is that the flow field is applied to a solution as opposed to an unoriented, microphase separated solid above the glass transition of the hard block. As it might be anticipated for a microphase-separated system, the initial grain size and degree of domain alignment influence the final degree of global order in an orienting process (Scott et al., 1992). By beginning with a homogeneous material and allowing the morphology to develop (i.e., induce microphase separation) in the presence of the flow field, the final morphology can have superior orientation with fewer defects. In order to access the homogeneous state, a solvent for high molecular weight polymers is necessary since heating of the material will lead to thermal decomposition before reaching the disordering temperature.

In comparison to the various orientation methods discussed above, the roll-casting method offers some distinct advantages:

- Problems associated with thermal degradation are minimized by roll-casting at room temperature (though heating is also possible)
- Resulting films are large (e.g. 20 cm x 6 cm x 2 mm)
- A large number of variables can be changed to influence the process
- The process occurs relatively quickly (e.g. within 45 min) and is simple

Thus, inducing block copolymer orientation from an initially homogeneous solution represents an improvement over orienting an inhomogeneous solid heated above its glass transition in two respects: 1) orienting a developing structure results in fewer morphological defects than an established structure that has to be reoriented and 2) thermal degradation is minimized.

2.3.5 Other Orientation Methods

There are a number of other orientation methods available, but none have been used to prepare samples for mechanical deformation studies so far.

2.3.5.1 Flow in a Rheometer

The application of an axi-symmetric flow field to induce orientation in block copolymers using either parallel plate (Morrison et al., 1987; Morrison et al., 1989; Morrison et al., 1990; Larson et al., 1993; Winey et al., 1993; Winey et al., 1993; Zhang et al., 1995; Zhang et al., 1995) or cone-and-plate rheometry (Scott et al., 1992) has been successful. Both cylinders (Morrison et al., 1987; Morrison and Winter, 1989; Morrison et al., 1990) and lamellae (Larson et al., 1993; Winey et al., 1993; Winey et al., 1993; Zhang and Wiesner, 1995; Zhang et al., 1995) orient in the flow direction. Excellent control of shear strain, shear rate and temperature and ease of measurement of shear stress during orientation are afforded. The flow field for the cone-and-plate geometry is well-characterized as simple shear, but the sample size is too small for tensile testing purposes.

2.3.5.2 Couette Flow

This technique pioneered by Terrisse (Terrisse, 1973), has been used to orient block copolymer triblocks (Morrison et al., 1993; Jackson et al., 1995; Jackson et al., 1995) and diblocks (Balsara et al., 1994; Balsara et al., 1994). The device operates using the same principle as a Couette viscometer with two concentric cylinders, one rotating with respect to the other. Recent studies using this technique have focused on the effects of shear on triblocks (Morrison et al., 1993; Jackson et al., 1995; Jackson et al., 1995) and diblocks (Balsara and Hammouda, 1994; Balsara et al., 1994) ODT.

2.3.5.3 Electric Field

A fundamentally different method of orientation of block copolymers was first recognized by Le Meur (Le Meur et al., 1971) in observing light diffracting from highly solvent swollen lamellae subjected to electric fields (15 kV/cm). This technique operates on the principle that domains of differing dielectric constants respond differently to an electric field. The result is that a globally oriented structure represents a minimum in the electrostatic contribution to the free energy of the system. (Amundson et al., 1991; Amundson et al., 1992; Amundson et al., 1993; Amundson et al., 1994) also determined that weakly segregated lamellae orient themselves parallel to the field. The driving force for morphological alignment in an electric field, however, is significantly smaller and the kinetics considerably slower (up to hundreds of minutes) than that of a hydrodynamic flow (Amundson et al., 1993).

2.3.5.4 Channel Die

This technique relies on a similar principle as press molding, but under conditions of plane strain. It involves the compressing of the "molten" material into a deep channel die. The material flows along one direction while being constrained in the other two. Semicrystalline block copolymers have been oriented using this technique (Cohen et al., 1994; Kofinas et al., 1994; Kofinas et al., 1995), but deformation studies have only been carried out on Nylon 6 (Galeski et al., 1991), polyethylene (Song et al., 1990; Galeski et al., 1992) and poly(ethylene terephthalate) (PET) (Bellare et al., 1993). Variable shear gradients due to the changing geometry during compression and the relatively short residence time under flow can lead to orientation gradients. Recently, however, several commercially available styrene-diene triblock copolymers were oriented via the channel die technique (Lee et al., 1996).

2.4 Styrenic Block Copolymers

Control of molecular and morphological characteristics in many early structure-property studies on block copolymers has been deficient. The Kraton® family of polymers (Shell Oil Co.) has been the subject of numerous investigations, but only in some cases has it been acknowledged that the nominal triblock material contains up to 20 wt% of diblock (Fetters et al., 1972). It is well-known that because of the absence of bridging midblock conformations, diblocks do not provide the mechanical strength that triblocks do (Morton, 1971), and thus significantly detract from the mechanical properties, especially at higher strains. Additionally, the influence of polydispersity in molecular weight is often neglected. Despite early claims to the contrary (Holden et al., 1969; Morton, 1971; Holden, 1986), studies have shown an enhanced load bearing capacity at large strains for larger molecular weight samples (at constant composition) (Chen and Cohen, 1977; Hashimoto et al., 1979). It may very well be that this molecular weight effect has been masked by the numerous other uncontrolled variables in early deformation studies. The microstructure of the rubber block has a significant impact on its glass transition temperature, (e.g. T_g of 1,4-polybutadiene and 1,2-polybutadiene are -106°C and -28°C, respectively (Tate et al., 1986)). This will also have an impact on the mechanical properties. A detailed analysis of the rubber block microstructure, that strongly depends on the polymerization solvent and temperature, should also be reported.

In addition to the synthetic structural variables, the morphological variables should also be controlled. These variables include those necessary for complete morphological characterization: domain type, domain and grain size, defect density, degree of orientation, etc. (see Figure 2-1). Care should be taken in sample preparation. If an isotropic sample is desired, no bias that could possibly lead to texturing should be allowed. Indeed, recent morphological studies have indicated that it is particularly difficult to prepare block copolymer samples with complete morphological isotropy due to substrate-induced orientation (Hasegawa et al., 1987), particularly at lower molecular weights where the morphology can be perturbed simply by handling (Hajduk et al., 1995). If an anisotropic sample is desired, a preparation route must be to used that induces a globally textured sample. Morphological probes of local regions would therefore be representative of the sample as a whole. In either the fully isotropic or the highly anisotropic case, a reproducible procedure of sample preparation should be used, as a large number of samples is generally necessary for accurate mechanical property measurements. This is of special importance in anisotropic samples since a number of different loading geometries are of interest (e.g., see Figure 2-4).

Finally, in an ideal deformation study, one would monitor, as a function of deformation, those structural parameters which most influence the macroscopic response in the course of the mechanical deformation. A number of structure probes have been used in block copolymer deformation studies (see Table 2-1). These tools do indeed provide information on the morphology (transmission electron microscopy (TEM), small-angle x-ray scattering (SAXS), small-angle neutron scattering (SANS), light scattering, birefringence) and the molecule (infrared (IR) dichroism, birefringence, nuclear magnetic resonance (NMR), SANS) during measurement of mechanical properties (small strain: thermal expansion, modulus-temperature and modulus-frequency curves; large strain: stress-strain curves, yield point, ultimate stress/strain, stress relaxation, creep, toughness, swelling behavior, etc.). Unfortunately, it is fairly rare that several probes are combined in a particular deformation study. Many of the best studies which are highlighted in this review do employ several characterization techniques. The most popular techniques include SAXS, birefringence, and TEM. The techniques can also be grouped according to whether they can be performed during the deformation process (SAXS, birefringence, light scattering) or whether some arresting procedure is necessary in order to freeze the morphology at a particular deformation before examination (TEM, NMR).

Table 2-1: Structural Characterization Techniques used in Deformation Studies

Technique	Deformation Study on Oriented Samples	Deformation Study on Unoriented Samples
SAXS	(Manthis et al., 1977; Odell et al., 1977; Tarasov et al., 1978; Hadziioannou et al., 1979; Hadziioannou et al., 1979; Pakula et al., 1985; Albalak, 1994; Honeker and Thomas)	(Inoue et al., 1971; Seguela et al., 1981; Richards et al., 1987; Polizzi et al., 1989; Polizzi et al., 1990)
SANS		(Richards and Mullin, 1987; Richards et al., 1995)
light scattering		(Inoue et al., 1971)
birefringence	(Folkes et al., 1971; Folkes et al., 1976)	(Henderson et al., 1968; Fischer et al., 1969; Wilkes et al., 1969; Canevarolo et al., 1986)
TEM	(Pedemonte et al., 1974; Folkes et al., 1976; Pedemonte et al., 1976; Odell and Keller, 1977; Honeker and Thomas)	(Hendus et al., 1966; Beecher et al., 1969; Fujimura et al., 1978; Hashimoto et al., 1979; Kotaka et al., 1980; Yamaoka and Kimura, 1993),
IR dichroism		(Zhao, 1992; Sakamoto et al., 1993)
NMR		(Gronski et al., 1985)

With the preparation of styrene-dienes of different morphologies came the, now obvious, realization that the microdomain geometry influences the mechanical response. The stress-strain curves for a series of unoriented DEXCO® SIS triblocks with varying amounts of the glassy PS phase are shown in Figure 2-2. The 18 wt% PS sample contains spherical regions of PS in a rubbery matrix, the 30 wt% PS sample exhibits a cylindrical PS microdomain geometry, while the 45 wt% PS sample has a lamellar morphology. As can be seen from the data, the reinforcement by the PS of the rubbery matrix is dependent upon the weight fraction of PS. The initial modulus increases by factors of approximately

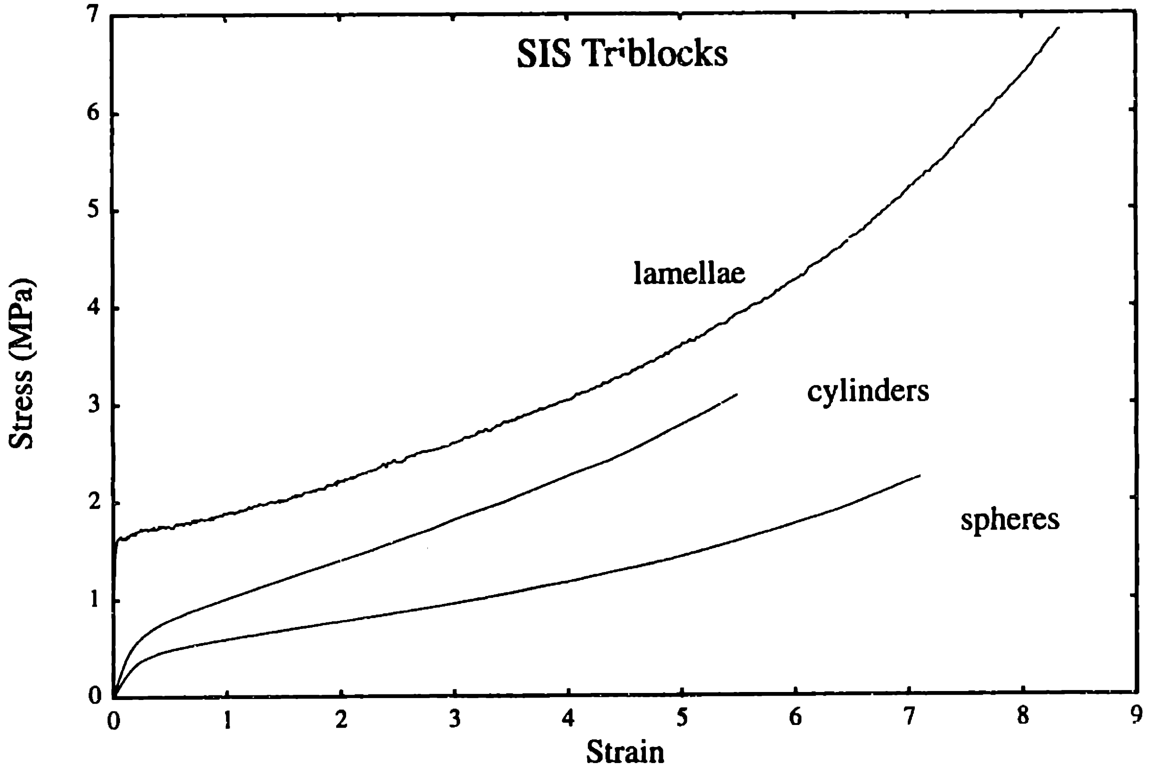

Figure 2-2: Stress-strain curves for polystyrene-polyisoprene-polystyrene (SIS) triblock copolymers cast without bias field. An increase in load bearing capacity with increasing PS volume fraction is observed. Spheres: PS weight fraction 0.18, block molecular weights 10-89-10. Cylinders: PS weight fraction 0.30, block molecular weights 14-66-14. Lamellae: PS weight fraction 0.45, block molecular weights 22-29-22.

2 and 20 for the cylinder and lamellar morphologies over that for spheres. Of the three possible classical morphologies, respectively with rubber as a majority (or near majority) phase, the understanding of the impact of the glassy cylinder morphology on the mechanical response is most advanced. The cylinder morphology is the most prevalent morphology (in the range 20-30 wt% PS) in commercially available styrene-diene based TPE materials. Hence, it is not surprising that more studies have been performed on samples containing oriented cylinders than on samples with spherical and lamellar microdomains.

A variety of deformation-related structural questions in styrene/diene systems have been investigated with varying degrees of success. For example, one striking aspect observed in cyclic stress-strain traces of samples with glassy phase continuity in the stretching direction during the initial drawing is that of "stress softening". The initial deformation proceeds with high modulus and yielding and is often accompanied by necking. After relaxation, the second loading cycle exhibits a much more rubbery character with a significantly lower initial modulus and no yield point or necking phenomena (Figure 2-3). Early studies speculated about a break-up of the PS "network" on the first draw (Beecher et al., 1969). The high modulus and yield point could be restored by annealing the sample at various temperatures before the second loading (Beecher et al., 1969; Kelterborn

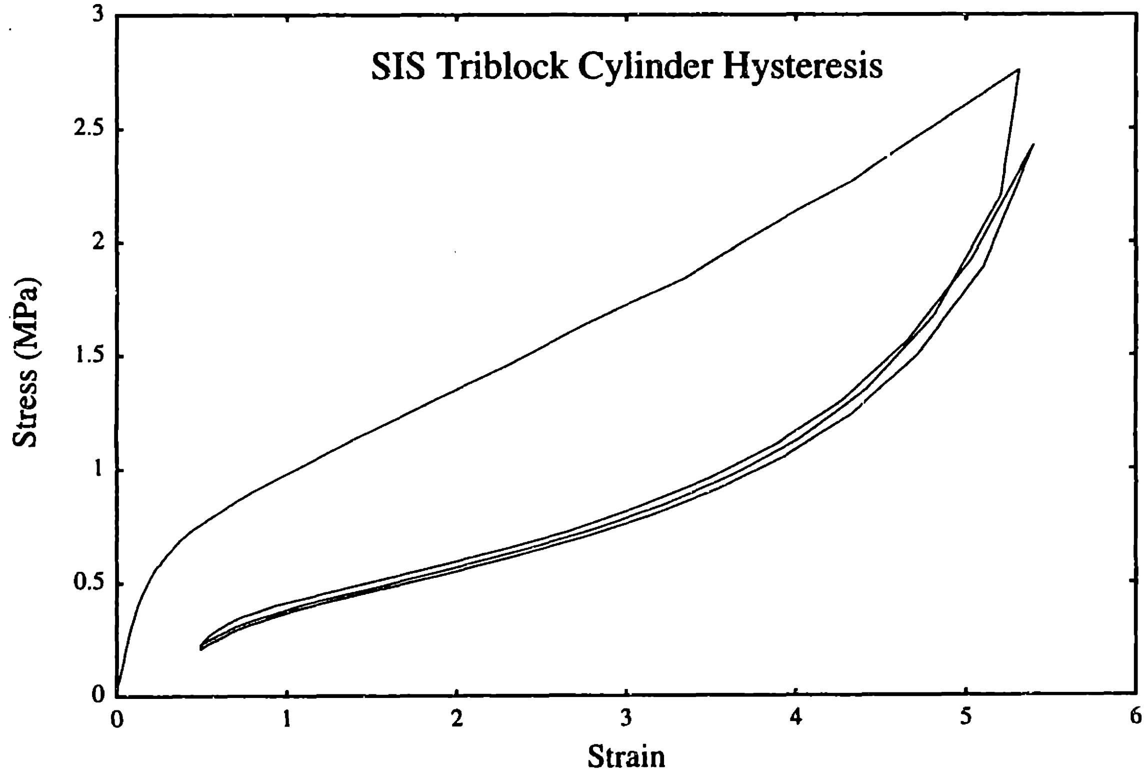

Figure 2-3: Two loading/unloading cycles of an SIS block copolymer with a cylindrical morphology (0.30 weight fraction PS). Note the drop in load-bearing capacity and lack of hysteresis in the second cycle. This deformation-induced change in mechanical property is known as "stress-softening".

et al., 1982; Canevarolo et al., 1986). However, it was not until highly oriented material became available, that direct information of the cylinder break-up via TEM imaging provided a basis for the construction of detailed shear-lag models to compare with experimental stress-strain curves (Odell and Keller, 1977).

Other deformation issues, that have not nearly received enough attention to provide satisfactory explanations, include some of the following: How do the respective A and B block chain dimensions respond to deformation in each of the microdomain morphologies? How does an increase in the molecular weight result in an increase in toughness at high strains? What is the interplay of molecular orientation and microdomain orientation at large strains? How does the morphology change at high strains? What is the bridging fraction (the ratio of effective midblock bridges to loops) in the various microdomain structures? How does this impact the mechanical properties and how might this key molecular parameter be controlled? How well do composite models predict the moderate to large strain mechanical properties? Some of these questions have been examined, while some have not yet been broached. Next, some of the most significant deformation studies of the cylinder morphology, with a particular emphasis on oriented systems, will be reviewed.

2.5 Deformation Experiments on Cylindrical Morphology

2.5.1 Small Strain Deformation

As mentioned previously, Keller and co-workers pioneered the area of structure-property relationships in oriented block copolymers. They modeled the small strain deformation behavior of a SBS sample with a total molecular weight of 85,000 and 25 wt% PS as a composite of stiff fibers in a rubbery matrix. The elastic anisotropy of the oriented cylindrical morphology was completely characterized (Arridge et al., 1972). All five independent elastic constants were determined for this hexagonal crystal and the results compared to predictions of several fiber reinforced composite theories (Arridge and Folkes, 1972). The ratio of the moduli perpendicular and parallel to the cylinder axis was determined to be about 100.

A detailed study on the mechanical response of this system up to moderate (<120%) strains was performed by Odell and Keller using a combination of SAXS, TEM, and birefringence techniques (Odell and Keller, 1977). Deformation in two principal directions was investigated (Figure 2-4). It was found that the deformation in the direction perpendicular to the cylinders proceeded in an affine manner up to 20% strain* while that in the direction parallel to the cylinders (see Figure 2-4) was affine only up to about 3%, at which point the material yielded. A closer examination of the yielded material in the parallel deformation experiment determined that the deformation in the necked region

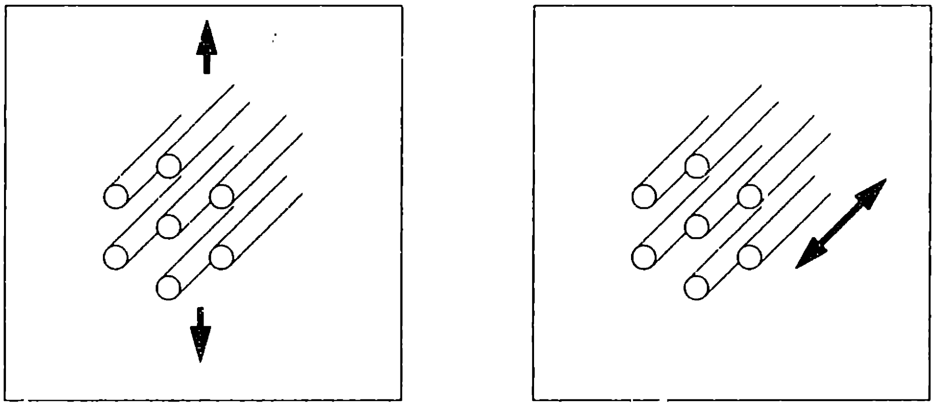

Figure 2-4: Two principal deformation directions in a cylindrical microdomain morphology, perpendicular to the cylinder axis and parallel to the cylinder axis.

---

* A later study (Hadziioannou et al., 1979) determined the limit of affine deformation in the perpendicular direction to be approximately 45% for a triblock of block molecular weights 7-35-7 (K).

reached 80% before the neck propagated across the sample. From direct measurement of photographs of the necked region, the Poisson's ratio was found to be 0.48, essentially that of an incompressible rubber. Birefringence measurements on the necked region supported the argument that the butadiene carried most of the load after yielding.

Finally, and most significantly, direct evidence for the break-up of the PS cylinders was presented by Keller and Odell in TEM micrographs* of a sample deformed by an unspecified amount in the direction parallel to the cylinders and then unloaded. Sample preparation involved deforming the material until neck formation and subsequently storing the material in a strained condition until the stress had relaxed. Thereafter, the sample was hardened with OsO_4 and microtomed thin enough (~ 50 nm) so that "overlapping" cylinders in the 2-D projection did not complicate measurement of rod lengths. The TEM micrographs showed a yielded section with the PS phase appearing as short rodlets approximately 70 - 110 nm in length but still macroscopically aligned. Although microscopic evidence of the structure of the deformed material had already been presented (Pedemonte et al., 1974), Odell and Keller's micrographs, together with their related experiments presented a much clearer picture than did the earlier studies of the mechanical response of oriented cylinders to deformations up to about 80%. For deformation behavior beyond the yield point, composite theories were again applied to the system. Yielding was modeled as a progressive breaking of cylinders into shorter segments that can bear a higher load, borrowing a concept from composite theory known as "shear lag". Another model with fewer assumptions, the "random break" model, provided values for the lengths of the

---

*· (Pedemonte et al., 1974) earlier presented TEM micrographs of an oriented sample in parallel deformation. Orientation was induced by extrusion and the deformation was captured by quenching in liquid nitrogen.

broken rods that are in agreement with rod lengths measured in TEM images on material deformed to 80% strain. Further discussion of these results is found in Chapter 7 on Parallel Deformation.

2.5.2 Large Strain Deformation

The first large strain SAXS study of a press-molded block copolymer with a cylindrical morphology was conducted by (Tarasov et al., 1978). The SAXS patterns were recorded on photographic film and interpreted in terms of the break-up of the cylinders into long rodlets (which remain aligned) for parallel deformation and a break-up of the cylinders into a chevron-type structure for deformations perpendicular to the cylinder axis. The SAXS experiments are of particular interest, not only because they were the first large deformation studies, but also because the incident beam was directed at several different angles with respect to the deformation direction, giving different planar sections of the reciprocal space scattered intensity distribution. These patterns gave additional evidence for the interpretation that the texture of domains at large perpendicular deformation consisted of a zig-zag chevron pattern (corresponding to a 4-point pattern in reciprocal space) of bent cylinders that were predominantly oriented at a particular angle with respect to the deformation direction (Figure 2-5). This angle was determined to increase with deformation, reaching a value of 55^{o} at a strain of 700%. Unfortunately the 3-D information carefully obtained by the authors in reciprocal space was not reconstructed self-consistently into a 3-D real space model.

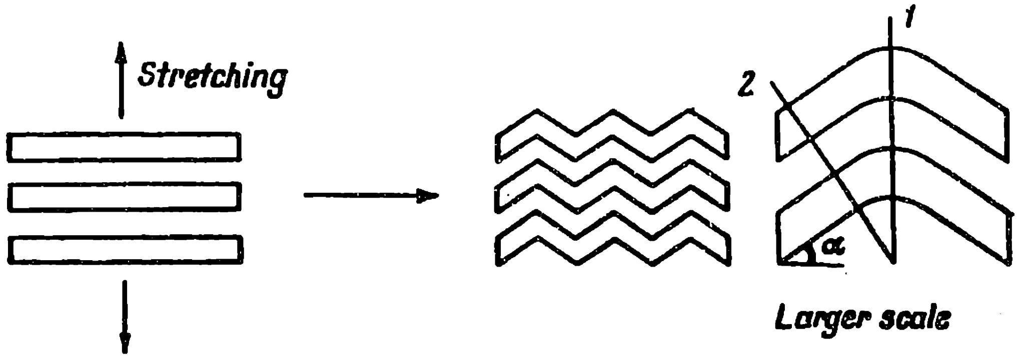

Figure 2-5: Schematic illustration of the changes of the hexagonal cylinder lattice in a monocrystal (longitudinal section is illustrated) when stretching is applied in a direction normal to the cylinder axis. Figure taken from (Tarasov et al., 1978)

A more recent deformation study of oriented cylinders by SAXS considered the nature of the four-point pattern in more detail (Pakula et al., 1985). Four-point patterns, as often observed in the SAXS of polymers and liquid crystals, come in a great variety. Nevertheless, they generally consist of one or more intensity maxima in each of the four quadrants (see Figure 2-6). The main conclusion of (Pakula et al., 1985) based on x-ray investigations of samples oriented via press-molding, was that deforming oriented cylinders in *any* orientation with respect to the stretching direction results in the same final morphological state at high deformation: a chevron structure of bent cylinders. This “universal high deformation state” was also found for a sample which was initially comprised of a random orientation of grains. Again, at large deformations (> 100% strain), the same four-point pattern was observed. This indicated that the deformation behavior at large strains is controlled by the molecular orientation of the rubber blocks, while at low strains the deformation is controlled more by the initial morphological state. A serious limitation of this study was that the two-dimensional SAXS patterns were reconstructed using a one-dimensional detector scanned across the diffraction plane.

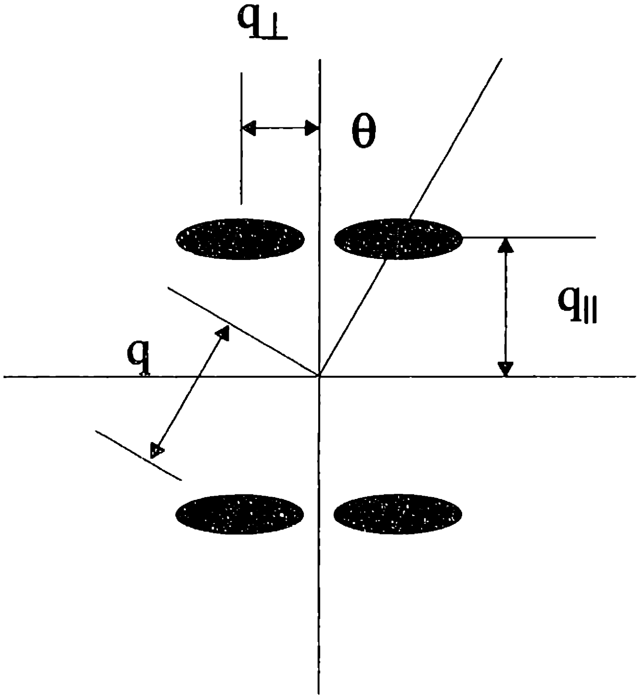

Figure 2-6: Schematic of a four-point pattern often observed in the SAXS of polymers. The radial vector **q** to the first lobe can be decomposed into a component parallel and perpendicular to the SD (assumed vertical). The lobes themselves can be variously oriented.

These studies show that when a block copolymer consisting of a minority glassy component in a rubbery matrix component is deformed, there is a competition between chain orientation and domain orientation along the stretching direction. The strain is accommodated primarily in the soft rubbery matrix with the rubbery chains orienting along the stretch axis. The glassy domains tend to rotate their long axis towards the stretch axis. However, since the cylindrical domains in block copolymers have rather extraordinary aspect ratios (approximately 1000:1 for a polygrain structure and essentially infinite for the single crystal samples), the reorientation process must be highly cooperative, involving whole grains or, as we have seen for the single crystal samples, a breakup of the structure into a chevron morphology with a characteristic length scale on the order of microns. As is the case for polycrystalline deformation, compatibility (Malvern, 1969) of the overall grain structure requires a complex deformation response, that varies from grain to grain.

2.6 Future Outlook

The elastic moduli and small strain response of ABA block copolymers organized into large near-single crystal samples composed of glassy cylinders have been successfully measured and fit using composite theories. This approach adequately accounts for the role of the morphological response to the deformation in the small strain behavior of these thermoplastic elastomers.

Each of the three morphologies found in styrene/diene TPEs responds differently to deformation (Honeker et al., 1996). The spherical morphology deformation process parallels the deformation observed in an ideal network most closely (Prasman, 1997). Globally oriented samples with a cylindrical morphology behave anisotropically at both large and small strains. Though small strain behavior is well understood, the well-ordered structure observed at large strain has not yet been fully explained. There have been too few large strain deformation studies on oriented lamellae for conclusions to be drawn. The higher PS content results in localized deformation (necking) and also reduces the time-dependent (viscoelastic) nature of the deformation.

Large strain deformation carries both the morphology and the chain dimensions far from their equilibrium ground states. Molecular structural variables become more important once the glassy domain structure is broken. The exact nature of the relationship between domain structure and chain extension at large strains remains elusive. It is clear that a morphologically well-defined starting point will aid in the interpretation of the structure at large strains, as the dynamic evolution of the morphology with deformation can be followed from this state to the unknown state using scattering experiments. Once the morphological structure at large deformations is made clear, the impact of synthetic variables, such as molecular weight (Chen and Cohen, 1977; Bard et al., 1987) effective bridging fraction (Watanabe, 1995; Brinkmann et al., 1996), chain architecture (Bi et al., 1974; Bi et al., 1976), and chemical identity (Li et al., 1995) on determining this structure and hence the large strain mechanical properties can be better evaluated.

Chain topology (midblock bridge vs. loop conformations; diblock vs. triblock) is expected to become important at large strains and at high temperatures (Zhulina et al., 1992; Matsen et al., 1994; Matsen, 1995; Turner, 1995; Watanabe, 1995) where the glassy domains no longer constrain the deformation. There have been few experiments (Richards and Welsh, 1995) and some theory (Amundson et al., 1993; Hamley, 1994; Wang, 1994; Turner, 1995) on the response of the rubbery chain to deformation for each type of morphology. Experimental measurement requires morphological control as well as chain labeling to increase the signal in neutron scattering experiments to follow the chain response. Spectroscopic methods (IR dichroism, NMR) give information on more local segmental motions, but these need to be combined with morphological measurements to enhance interpretation.

The determination of the macroscopic mechanical properties is only one area where the texturing or orientation of the morphology has aided in revealing molecular phenomena in TPEs. The measurement of the anisotropy of chain dimensions within the microdomain space of lamellar diblocks necessitates a highly oriented morphology (Hadziioannou et al., 1982; Hasegawa et al., 1985; Hasegawa et al., 1987; Matsushita et al., 1988; Matsushita et al., 1990; Matsushita et al., 1990; Koizumi et al., 1995; Matsushita et al., 1995). The difference in the self-diffusion of diblocks parallel and perpendicular to the microdomain interface again requires macroscopically oriented samples (Dalvi et al., 1993). Finally, as is common in determining the crystal structure of small and large molecules, effort is being made to prepare near-single-crystal material for the identification of new morphologies with scattering techniques (Mortensen et al., 1995).

Future work will involve increased use of processing techniques in combination with an increased awareness of global equilibrium to produce well-characterized samples. Deformation studies, particularly in the large strain region, will provide information towards answering some of the aforementioned questions. A basic understanding of structure-mechanical property relations of the relatively simple styrene-diene system will provide a context for deformation investigations of other TPEs. Increasing synthetic complexity can dramatically impact higher order morphological features (e.g., change the morphology diagram, influence chain conformation and domain structure). A procedure utilizing a combination of controlled chemistry, controlled morphology, and multiple characterization techniques will offer the best approach to unravel the molecular and nanoscale influences on the small- and large-strain behavior of TPEs.

2.7 Bibliography

Akovali, G., J. Diamant and M. Shen (1977). "Polyblends of poly(styrene-b-butadiene-b-styrene) and polystyrene. I. Mechanical properties." Journal of Macromolecular Science: Physics **B13**(1): 117-131.

Albalak, R. J. (1994). "The anisotropic thermal expansion of 'single-crystal' triblock copolymer films." Polymer **35**(19): 4115-4119.

Albalak, R. J. and E. L. Thomas (1993). "Microphase-Separation of Block Copolymer Solutions in a Flow Field." Journal of Polymer Science Part B: Polymer Physics **31**: 37-46.

Albalak, R. J. and E. L. Thomas (1994). "Roll-casting of block copolymers and of block copolymer-homopolymer blends." Journal of Polymer Science Part B: Polymer Physics **32**: 341-350.

Almdal, K., K. A. Koppi, F. S. Bates and K. Mortenson (1992). "Multiple ordered phases in a block copolymer melt." Macromolecules **25**: 1743-1751.

Amundson, K. and E. Helfand (1993). "Quasi-static mechanical properties of lamellar block copolymer microstructure." Macromolecules **26**: 1324-1332.

Amundson, K., E. Helfand, D. D. Davis, X. Quan and S. S. Patel (1991). "Effect of an electric field on block copolymer microstructure." Macromolecules **24**: 6546-6548.

Amundson, K., E. Helfand, D. D. Davis, X. Quan, S. S. Patel and S. D. Smith (1992). "Effect of an electric field on block copolymer microstructure." Macromolecules **25**: 1200.

Amundson, K., E. Helfand, X. Quan, S. D. Hudson and S. D. Smith (1994). "Alignment of lamellar block copolymer microstructure in an electric field. 2. Mechanisms of alignment." Macromolecules **27**: 6559-6570.

Amundson, K., E. Helfand, X. Quan and S. D. Smith (1993). "Alignment of lamellar block copolymer microstructures in an electric field. 1. Alignment kinetics." Macromolecules **26**: 2698-2703.

Arridge, R. G. C. and M. J. Folkes (1972). "The mechanical properties of a 'single crystal' of SBS copolymer - a novel composite material." Journal of Physics Part D: Applied Physics **5**: 344-358.

Balsara, N. P., H. J. Dai, H. Watanabe, T. Sato and K. Osaki (1996). "Influence of defect density on the rheology of ordered block copolymers." Macromolecules **29**: 3507-3510.

Balsara, N. P. and B. Hammouda (1994). "Shear effects on solvated block copolymer lamellae: Polystyrene-polyisoprene in dioctyl phthalate." Physical Review Letters **72**(3): 360-363.

Balsara, N. P., B. Hammouda, P. K. Kesani, S. V. Jonnalagadda and G. C. Straty (1994). "In-situ small-angle neutron scattering from a block copolymer solution under shear." Macromolecules **27**: 2566-2573.

Bard, J. K. and C. I. Chung (1987). Chapter 12: Research on thermoplastic elastomers. Thermoplastic Elastomers: A Comprehensive Review. N. R. Legge, G. Holden and H. E. Schroeder. Munich, Hanser: 303-323.

Beecher, J. F., L. Marker, R. D. Bradford and S. L. Aggarwal (1969). "Morphology and mechanical behavior of block polymers." Journal of Polymer Science Part C **26**: 117-134.

Bellare, A., R. E. Cohen and A. S. Argon (1993). "Development of texture in poly(ethylene terephthalate) by plane-strain compression." Polymer **34**: 1393-1403.

Bhowmick, A. K. and H. L. Stephens, Eds. (1988). Handbook of Elastomers: New Developments & Technology. New York, Marcel Dekker.

Bi, L.-K. and L. J. Fetters (1976). "Synthesis and properties of block copolymers. 3. Polystyrene-polydiene star block copolymers." Macromolecules **9**: 732-742.

Bi, L.-K., L. J. Fetters and M. Morton (1974). "The synthesis, mechanical behavior and morphology of star triblock copolymers." Polymer Preprints ACS Polymer Chemistry Division **15**(2): 157-163.

Brinkmann, S. and R. Stadler (1996). Personal communication.

Canevarolo, S. V., A. W. Birley and D. A. Hemsley (1986). "Effect of processing conditions on SBS thermoplastic rubber." British Polymer Journal **18**(1): 60-64.

Cates, M. E. and S. T. Milner (1989). "Role of shear in the isotropic-to-lamellar transition." Physical Review Letters **62**(16): 1856-1859.

Chen, Y.-D. M. and R. E. Cohen (1977). "The influence of molecular weight on the large deformation behavior of SBS triblock copolymer elastomers." Journal of Applied Polymer Science **21**: 629-643.

Cohen, R. E., A. Bellare and M. A. Drzewinski (1994). "Spatial organization of polymer chains in a crystallizable diblock copolymer of polyethylene and polystyrene." Macromolecules **27**: 2321-2323.

Dalvi, M. C. and T. P. Lodge (1993). "Parallel and perpendicular chain diffusion in a lamellar block copolymer." Macromolecules **26**: 859-861.

Diamant, J., D. Soong and M. C. Williams (1982). "The mechanical properties of styrene-butadiene-styrene (SBS) triblock copolymer blends with polystyrene (PS) and styrene-butadiene copolymer (SBR)." Polymer Engineering and Science **22**(11): 673-683.

Fetters, L. J., B. H. Meyer and D. McIntyre (1972). "The effect of diblock and homopolymer impurities on the morphology of triblock polymers." Journal of Applied Polymer Science **16**: 2079-2089.

Fischer, E. and J. F. Henderson (1969). "The stress-strain-birefringence properties of styrene-butadiene block copolymers." Journal of Polymer Science Part C **26**: 149-160.

Folkes, M. J. and A. Keller (1971). "The birefringence and mechanical properties of a "single crystal" from a three-block copolymer." Polymer **12**: 222-236.

Folkes, M. J., A. Keller and J. A. Odell (1976). "Optical and swelling properties of macroscopic "single crystals" of an SBS copolymer. II. Samples possessing a cylindrical morphology." Journal of Polymer Science Part B: Polymer Physics **14**: 847-859.

Folkes, M. J., A. Keller and F. P. Scalisi (1973). “An extrusion technique of "single-crystals" of block copolymers.” Colloid and Polymer Science **251**(1): 1-4.

Fredrickson, G. H. (1994). “Steady shear alignment of block copolymers near the isotropic-lamellar transition.” Journal of Rheology **38**(4): 1045-1067.

Fujimura, M., T. Hashimoto and H. Kawai (1978). “Structural change accompanied by plastic-to-rubber transition of SBS block copolymers.” Rubber Chemistry and Technology **51**: 215-224.

Galeski, A., A. S. Argon and R. E. Cohen (1991). “Morphology of bulk nylon 6 subjected to plane strain compression.” Macromolecules **24**: 3953-3961.

Galeski, A., Z. Bartczak, A. S. Argon and R. E. Cohen (1992). “Morphological alterations during texture-producing plastic plane strain compression of high-density polyethylene.” Macromolecules **25**: 5705-5718.

Gronski, W., D. Emeis, A. Brüderlin, M. M. Jacobi, R. Stadler and C. D. Eisenbach (1985). “Deuterium magnetic resonance studies on strained selectively deuterated elastomers.” British Polymer Journal **17**(2): 103-110.

Hadziioannou, G., A. Mathis and A. Skoulios (1979). “'Monocristaux' de copolymeres trisequences SIS presentant la structure cylindrique: III. Etude de la deformation par cisaillement.” Colloid and Polymer Science **257**: 344-350.

Hadziioannou, G., A. Mathis and A. Skoulios (1979). “'Monocristaux' de copolymeres trisequences styrene/isoprene/styrene presentant la structure cylindrique: I. Etude de l'orientation par diffraction des rayons X aux petits angles.” Colloid and Polymer Science **257**: 15-22.

Hadziioannou, G., A. Mathis and A. Skoulios (1979). “'Monocristoux' de copolymeres trisequences styrene/isoprene/styrene presentant la structure cylindrique: II. Etude de la deformation par elongation.” Colloid and Polymer Science **257**: 337-343.

Hadziioannou, G., A. Mathis and A. Skoulios (1979). “Obtention de 'monocristaux' de copolymeres trisequences SIS par cisaillement plan.” Colloid and Polymer Science **257**: 136-139.

Hadziioannou, G., C. Picot, A. Skoulios, M.-L. Ionescu, A. Mathis, R. Duplessix, Y. Gallot and J.-P. Lingelser (1982). “Low-angle neutron scattering study of the lateral extension of chains in lamellar styrene/isoprene block copolymers.” Macromolecules **15**: 263-267.

Hajduk, D. A., P. E. Harper, S. M. Gruner, C. C. Honeker, E. L. Thomas and L. J. Fetters (1995). “A reevaluation of bicontinuous cubic phases in starblock copolymers.” Macromolecules **28**: 2570-2573.

Hamley, I. W. (1994). “Strain-induced instabilities in hexagonal columnar phases.” Physical Review E **50**(4): 2872-2880.

Hasegawa, H., T. Hashimoto, H. Kawai, T. P. Lodge, E. J. Amis, C. J. Glinka and C. C. Han (1985). "SANS and SAXS studies on molecular conformation of a block polymer in microdomain space." Macromolecules **18**: 67-78.

Hasegawa, H., H. Tanaka, T. Hashimoto and C. C. Han (1987). Macromolecules **20**: 2120.

Hasegawa, H., H. Tanaka, T. Hashimoto and C. C. Han (1987). "SANS and SAXS studies on molecular conformation of a block polymer in microdomain space. 2. contrast matching technique." Macromolecules **20**: 2120-2127.

Hashimoto, T., M. Fujimura, K. Saijo, H. Kawai, J. Diamant and M. Shen (1979). Strain-induced plastic-to-rubber transition of a SBS block copolymer and its blend with PS. Multiphase Polymers. S. L. Cooper and G. M. Estes, ACS Advances in Chemistry Series: 257-275.

Henderson, J. F., K. H. Grundy and E. Fischer (1968). "Stress-birefringence properties of S-I block copolymers." Journal of Polymer Science Part C **16**: 3121-3131.

Hendus, H., K.-H. Illers and E. Ropte (1966). "Strukturuntersuchungen an SBS Blockcopolymeren." Colloid and Polymer Science **216-217**: 110-119.

Holden, G. (1986). Elastomers, Thermoplastic. Encyclopedia of Polymer Science and Engineering. H. F. Mark, M. Bikales, C. G. Overberger, G. Menges and J. I. Kroshwitz. New York, John Wiley & Sons. **5:** 416-430.

Holden, G. (1987). Chapter 13: Applications of thermoplastic elastomers. Thermoplastic Elastomers. N. R. Legge, G. Holden and H. E. Schroeder. Munich, Hanser: 481-506.

Holden, G., E. T. Bishop and N. R. Legge (1969). "Thermoplastic elastomers." Journal of Polymer Science Part C **26**: 37-57.

Honeker, C. C. and E. L. Thomas (1996). "Impact of morphological orientation in determining mechanical properties in block copolymers systems." Chemistry of Materials **8**(8): 1702-1714.

Honeker, C. C. and E. L. Thomas (1997). In preparation.

Inoue, T., M. Moritani, T. Hashimoto and H. Kawai (1971). "Deformation mechanism of elastomeric block copolymers having spherical domains of hard segments under uniaxial tensile stress." Macromolecules **4**: 500-507.

Jackson, C. L., K. A. Barnes, F. A. Morrison, J. W. Mays, A. I. Nakatani and C. C. Han (1995). "A shear-induced martensitic-like transformation in a block copolymer melt." Macromolecules **28**: 713-722.

Jackson, C. L., F. A. Morrison, A. I. Nakatani, J. W. Mays, M. Muthukumar, K. A. Barnes and C. C. Han (1995). Chapter 16: Shear-induced changes in the order-disorder transition temperature and the morphology of a triblock copolymer. Flow-Induced Structure in Polymers. A. I. Nakatani and M. D. Dadmun. Washington D. C., ACS. **597:** 233-245.

Keller, A., E. Pedemonte and F. M. Willmouth (1970). "Macro-lattice from segregated amorphous phases of a three block copolymer." Nature **225**: 538-539.

Kelterborn, J. C. and D. S. Soong (1982). "Time-dependent morphologies and viscoelastic properties of block copolymers." Polymer Engineering and Science **22**(11): 654-672.

Kofinas, P. and R. E. Cohen (1994). "Morphology of highly textured poly(ethylene)/ poly(ethylene-propylene) (E/EP) semicrystalline diblock copolymers." Macromolecules **27**: 3002-3008.

Kofinas, P. and R. E. Cohen (1995). "Melt processing of semicrystalline E/EP/E triblock copolymers near the order-disorder transition." Macromolecules **28**: 336-343.

Koizumi, S. and T. Hashimoto (1995). "SANS study of segmental distribution of block copolymer chains confined in a microdomain space." Physica B **213 & 214**: 703-706.

Koppi, K. A., M. Tirrell and F. S. Bates (1993). "Shear-induced isotropic-to-lamellar transition." Physical Review Letters **70**(10): 1449-1452.

Koppi, K. A., M. Tirrell and F. S. Bates (1994). "Epitaxial growth and shearing of the body centered cubic phase in diblock copolymer melts." Journal of Rheology **38**(4): 999-1027.

Kotaka, T., M. Tetsuhiro and K. Arai (1980). "Morphology-mechanical property relationship of a SBS block copolymer and its blends with homopolymers." Journal of Macromolecular Science Physics **B17**(2): 303-336.

Larson, R. G. (1992). "Flow-induced mixing, demixing, and phase transitions in polymeric fluids." Rheologica Acta **31**: 497-520.

Larson, R. G., K. I. Winey, S. S. Patel, H. Watanabe and R. Bruinsma (1993). "The rheology of layered liquids: lamellar block copolymers and smectic liquid crystals." Rheologica Acta **32**: 245-253.

Le Meur, J., J. Terrisse and S. e. G. C. (1971). "Proprietes optiques de copolymeres organises et orientes." Journal de Physique Colloque C5 **32**: 301-304.

LeBlanc, J. L. (1977). "Stress-strain behavior, hardness, and thermometrically properties of butadiene-styrene block copolymers as a function of processing technique." Journal of Applied Polymer Science **21**: 2419-2437.

Lee, H. H., R. A. Register, D. A. Hajduk and S. M. Gruner (1996). "Orientation of triblock copolymers in planar extension." Polymer Engineering and Science **36**(10): 1414-1424.

Li, D. and R. Faust (1995). "Polyisobutylene-based thermoplastic elastomers. III. Synthesis, characterization, and properties of Poly(α-methylstyrene-b-isobutylene-b-α-methylstyrene) triblock copolymers." Macromolecules **28**: 4893-4898.

Malvern, L. E. (1969). Introduction to the Mechanics of a Continuous Medium. Englewood Cliffs, Prentice-Hall.

Manthis, A., G. Hadziioannou and A. Skoulios (1977). "Unit cell deformation under elongation stress of oriented SIS three-block copolymers." Polymer Engineering and Science **17**(8): 570-572.

Matsen, M. W. (1995). "Bridging and looping in multiblock copolymers." Journal of Chemical Physics **102**(9): 3884-3887.

Matsen, M. W. and M. Schick (1994). "Lamellar phase of a symmetric triblock copolymer." Macromolecules **27**: 187-192.

Matsushita, Y., K. Mori, Y. Mogi, R. Saguchi, I. Moda and M. Hagasawa (1990). "Chain conformation of a block polymer in a microphase-separated structure." Macromolecules **23**: 4317-4321.

Matsushita, Y., K. Mori, R. Saguchi, I. Noda, M. Nagasawa, T. Chang, C. J. Glinka and C. C. Han (1990). "Chain conformation and locations of parts of a block polymer in a lamellar structure." Macromolecules **23**: 4387-4391.

Matsushita, Y., Y. Nakao, R. Saguchi, K. Mori, H. Choshi, Y. Muroga, I. Noda, M. Nagasawa, T. Chang, C. J. Glinka, et al. (1988). "Phase contrast matching in lamellar structures composed of mixtures of labeled and unlabeled block copolymer for small-angle neutron scattering." Macromolecules **21**: 1802-1806.

Matsushita, Y., M. Nomura, I. Noda and M. Imai (1995). "Lamellar microphase-separated structure of ABA triblock copolymers." Physica B **213 & 214**: 697-699.

Molau, G. E. (1970). Colloidal and morphological behavior of block and graft copolymers. Block Polymers. S. L. Aggarwal. New York, Plenum Press: 79-106.

Morrison, F., G. L. Bourvellec and H. H. Winter (1987). "Flow-induced structure and rheology of a triblock copolymer." Journal of Applied Polymer Science **33**: 1585-1600.

Morrison, F. A., J. W. Mays, M. Muthukumar, A. I. Nakatani and C. C. Han (1993). "Shear-induced morphological structures in triblock copolymers." Macromolecules **26**: 5271-5273.

Morrison, F. A. and H. H. Winter (1989). "Effect of unidirectional shear on the structure of triblock copolymers. 1. SBS." Macromolecules **22**: 3533-3539.

Morrison, F. A., H. H. Winter, W. Gronski and J. D. Barnes (1990). "Effect of unidirectional shear on the structure of triblock copolymers. 2. SIS." Macromolecules **23**: 4200-4205.

Mortensen, K., K. Almdal, F. S. Bates, K. Koppi, M. Tirrell and B. Norden (1995). "Shear devices for in situ structural studies of block-copolymer melts and solutions." Physica B **213 & 214**: 682-684.

Morton, M. (1971). Styrene-Diene Block Copolymers. Encyclopedia of Polymer Science and Technology. M. Bikales. New York, Wiley-Intersciene. **15:** 508-530.

Muller, R., J. J. Pesce and C. Picot (1993). "Chain conformation in sheared polymer melts as revealed by SANS." Macromolecules **26**: 4356-4362.

Odell, J. A. and A. Keller (1977). "Deformation behavior of an SBS copolymer." Polymer Engineering and Science **17**(1): 544-559.

Okamoto, S., K. Saijo and T. Hashimoto (1994). "Real-time SAXS observations of lamella forming block copolymers under large oscillatory shear deformation." Macromolecules **27**: 5547-5555.

Pakula, T., K. Saijo, H. Kawai and T. Hashimoto (1985). "Deformation behavior of SBS triblock copolymer with cylindrical morphology." Macromolecules **18**: 1294-1302.

Pedemonte, E., G. Dondero, G. Alfonso and F. de Candia (1975). "Three-block copolymers: morphologies and stress-strain properties of samples prepared under various experimental conditions." Polymer **16**: 531-538.

Pedemonte, E., G. Dondero, F. de Candia and G. Romano (1976). "Correlation between physical-mechanical properties and morphological features of cruciform styrene-butadiene block copolymers." Polymer **17**: 72-76.

Pedemonte, E., A. Turturro and G. Dondero (1974). "Correlation between morphology and stress-strain properties of three block copolymers I. Stress-softening effect." British Polymer Journal **6**: 277-282.

Polizzi, S., P. Boesecke, N. Stribeck, H. G. Zachmann and R. Bordeiau (1990). "Small angle x-ray scattering investigations of SBS block copolymers during stretching." Polymer **31**: 638-645.

Polizzi, S., N. Stribeck, H. G. Zachmann and B. R. (1989). "Morphological changes in SBS block copolymers caused by oil extension as determined by absolute small angle x-ray scattering." Colloid and Polymer Science **267**(4): 281-291.

Prasman, E. (1997). Morphology and mechanical behavior of oriented blends of styrene - isoprene - styrene triblock copolymer and mineral oil. Masters thesis, Massachusetts Institute of Technology.

Rader, C. P. (1996). Thermoplastic Elastomers: TPEs shine with growth rates three to five times that of rubber or plastics. New York, McGraw-Hill Co.

Ramsteiner, F. and W. Heckmann (1984). "Deformation behaviour of styrene-butadiene block copolymers." Polymer Communications **25**(June): 178-179.

Richards, R. W. and J. T. Mullin (1987). SANS and time resolved SAXS studies of triblock copolymers in extension. Scattering, Deformation, and Fracture in Polymers. G. D. Wignall, B. Crist, T. P. Russell and E. L. Thomas. Pittsburgh, Materials Research Society. **79**: 299-308.

Richards, R. W. and G. Welsh (1995). "Deformation of matrix macromolecules in a uniaxially extended styrene-isoprene-styrene linear triblock copolymer." European Polymer Journal **31**(12): 1197-1206.

Riep, P. W. (1983). thesis, Brunel University Uxbridge MiddleSex England.

Robinson, R. A. and E. F. T. White (1970). Mechanical properties of styrene-isoprene block copolymers. Block Polymers. S. L. Aggarwal. New York, Plenum Press: 123-136.

Sakamoto, J., S. Sakurai, K. Doi and S. Nomura (1993). "Molecular orientation of SBS triblock copolymer with cylindrical microdomains of polystyrene." Polymer **34**(23): 4837-4840.

Scott, D. B., A. J. Waddon, Y.-G. Lin, F. E. Karasz and H. H. Winter (1992). "Shear-Induced Orientation Transitions in Triblock Copolymer Styrene-Butadiene-Styrene with Cylindrical Domain Morphology." Macromolecules **25**: 4175-4181.

Seguela, R. and J. Prud'homme (1981). "Deformation mechanism of thermoplastic 2-phase elastomers of lamellar morphology having a high volume fraction of rubbery microphase." Macromolecules **14**: 197-202.

Seguela, R. and J. Prud'homme (1988). "Affinity of grain deformation on mesomorphic block polymers submitted to simple elongation." Macromolecules **21**: 635-643.

Skoulios, A. (1977). "Properties of oriented block copolymers." Journal of Polymer Science Polymer Symposia **58**: 369-380.

Smith, T. L. and R. A. Dickie (1969). "Viscoelastic and ultimate tensile properties of SBS block copolymers." Journal of Polymer Science Part C **26**: 163-187.

Song, H. H., A. S. Argon and R. E. Cohen (1990). "Morphology of highly textured high-density polyethylene." Macromolecules **23**: 870-876.

Tarasov, S. G., D. Y. Tsvankin and Y. K. Godovsky (1978). "The structural changes during the deformation of oriented and isotropic B-S block copolymers." Polymer Science USSR **20**: 1728-1739.

Tate, D. B. and T. W. Bethea (1986). Butadiene Polymers. Encyclopedia of Polymer Sciene and Technology. H. F. Mark, M. Bikales, C. G. Overberger and G. Menges. New York, John Wiley & Sons. **2**: 538-590.

Terrisse (1973). Ph.D. Thesis. thesis, Universite Louis Pasteur de Strasbourg.

Turner, M. S. (1995). "The bending modulus of triblock copolymer lamellae: Stress relaxation via the bridge-to-loop process." Macromolecules **28**: 6878-6882.

Walker, B., Ed. (1979). Handbook of Thermoplastic Elastomers. New York, Van Nostrand Reinhold.

Wang, Z.-G. (1994). "Response and instabilities of the lamellar phase of diblock copolymers under uniaxial stress." Journal of Chemical Physics **100**(3): 2298-2309.

Watanabe, H. (1995). "Slow dielectric relaxation of a styrene-isoprene-styrene triblock copolymer with dipole inversion in the middle block: A challenge to a loop/bridge problem." Macromolecules **28**: 5006-5011.

Wilkes, G. L. and R. S. Stein (1969). "Effect of morphology on the mechanical and rheooptical properties of a SBS block copolymer." Journal of Polymer Science Part A-2 **7**: 1525-1537.

Winey, K. I., S. S. Patel, R. G. Larson and H. Watanabe (1993). "Interdependence of shear deformations and block copolymer morphology." Macromolecules **26**: 2542-2549.

Winey, K. I., S. S. Patel, R. G. Larson and H. Watanabe (1993). "Morphology of a lamellar copolymer aligned perpendicular to the sample plane: Transmission electron microscopy and SAXS." Macromolecules **26**: 4373-4375.

Wolfe, J. R. J. (1987). Elastomer-thermoplastic blends as thermoplastic elastomers. Thermoplastic Elastomers. N. R. Legge, G. Holden and H. E. Schroeder. Munich, Hanser Publishers: 117-131.

Yamaoka, I. (1996). "Effects of morphology on mechanical properties of styrene-butadiene-styrene triblock copolymer/methyl methacrylate-styrene copolymer blends." Polymer **37**(4): 5343-5356.

Yamaoka, I. and M. Kimura (1993). "Effects of morphology on mechanical properties of a SBS triblock copolymer." Polymer **34**(21): 4399-4409.

Zhang, Y. and U. Wiesner (1995). "Symmetric diblock copolymers under large amplitude oscillatory shear flow: entanglement effect." Journal of Chemical Physics **103**: 4784.

Zhang, Y., U. Wiesner and H. W. Spiess (1995). "Frequency dependence of orientation in dynamically sheared diblock copolymers." Macromolecules **28**: 778.

Zhao, Y. (1992). "Structural changes upon annealing in a deformed SBS triblock copolymer as revealed by infrared dichroism." Macromolecules **25**: 4705-4711.

Zhulina, E. B. and A. Halperin (1992). "Lamellar mesogels and mesophases: A self-consistent field theory." Macromolecules **25**: 5730-5741.

Chapter 3 SAXS from Cylindrical Block Copolymers

3.1 Introduction

For the present study a structural probe is needed for a material which has large periodicities, an anisotropic morphology, and a time dependent mechanical response. Small-angle x-ray scattering (SAXS) probes the morphology on length scales typical of a block copolymer domain (10-100 nm) over a sampling volume on the order of 1 mm^3. However, SAXS studies of anisotropic materials require the use of 2-D detectors, which preclude the use of slit collimation provided by the Kratky cameras typically used in many laboratories. Furthermore, it is important to note that these thermoplastic materials exhibit *viscoelastic behavior* (the stress (strain) supported at fixed strain (stress) decreases (increases) over time), a fact ignored in many previous studies. Any static scattering experiments attempting to elucidate the morphology at a particular amount of deformation will be integrating over a set of continuously changing morphological states as the material relaxes.

Synchrotron SAXS is well-suited to attack this problem. The need for high spatial and temporal resolution is easily satisfied. The domain spacing of our materials fall typically in the range of 25-40 nm, but at large deformations the spacing can increase up to 100 nm or more. A deformation stage that I custom-built to fit in the X-12B beamline at the National Synchrotron Light Source (NSLS) at Brookhaven enables in-situ deformation experiments with simultaneous measurement of load to be carried out during SAXS data acquisition. With the need for in-situ deformation experiments at NSLS established, a closer examination of the type of structural information provided by SAXS is in order. A more general background on X-ray diffraction from perfect and imperfect crystals is provided in Appendix A.

The dimensions of interest in small-angle scattering (SAXS) are much larger than the sub-nanometer scale typical in wide angle (atomic) diffraction and range from 10's to 100's of nm. Here, it is not the interference between the electron clouds of neighboring atoms which needs to be considered, but rather interference from the variations in electron density between supermolecular structures which are important. As a consequence, perfect crystals and homogeneous materials in general do not scatter x-rays at low angles. SAXS from polymers is predominantly due to two kinds of inhomogeneities on the length scale discussed here: a) alternations between crystalline and amorphous regions (or more generally, regions of different phases) and b) microvoids. It is mainly for this reason that the theories developed to treat small-angle scattering have focused on the diffuse scatter from weak correlations over regions with varying electron density. Samples exhibiting sharp Bragg reflections stemming from periodicities of 10's of nm, in contrast, are less common.

The intensity of SAXS is proportional to the square of the electron density difference between phases. Therefore, it is clear that phases with only a small difference in electron density (which generally scales with bulk density: $\rho_{PS} = 1.04\ \mathrm{gm/cm^3}$ and $\rho_{PI} = 0.91\ \mathrm{gm/cm^3}$, (Gobran, 1990)) will only scatter weakly. The PS/PI system, however, has sufficient electron density contrast to scatter x-rays strongly. The scattered intensity is observed to be much greater than the background intensity.

This chapter provides background on some of the elements of diffraction theory specific to the cylinder morphology that are used throughout the thesis. Specifically, the observed diffraction pattern is described in terms of a form factor modulating the intensity of the hexagonal lattice in reciprocal space. The expected reflection ratios for a structure with p6mm symmetry are derived in Section 3.3.

3.2 Form Factor and Lattice Factor

The basic structural unit in a crystal of a block copolymer with a cylindrical morphology is a cylinder of radius R and infinite length (see Figure 3-1). The "lattice" is a 2-D net with p6mm symmetry (see Figure 3-2). The convolution of the cylinder with the hexagonal net results in a 3-D crystal with two-dimensional symmetry (plane group p6mm). The Fourier Transform of a cylinder is a Bessel function of the form (Bear et al., 1950):

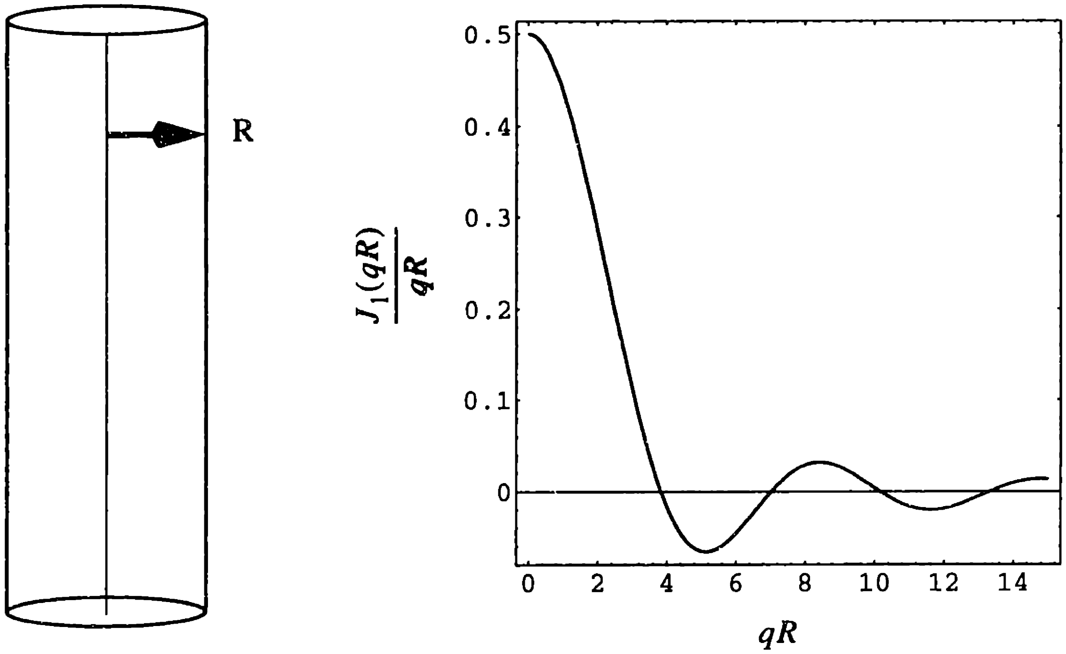

Figure 3-1: Left: A PS cylinder of infinite height and radius R, when Fourier transformed, yields a scattered amplitude of the form shown at right.

$$F_{unit}(q) \sim \frac{J_1(qR)}{qR} \tag{3.1}$$

The Fourier Transform of the hexagonal real space lattice is a hexagonal reciprocal space lattice which has been rotated by 60° (see Figure 3-2). Using the convolution theorem (equation (A.16) in Appendix A) the scattered amplitude of the crystal is the product of the Bessel function with the reciprocal space lattice. The diffracted intensity (the observable quantity) is the square of the scattered amplitude. Thus, we see that the cylinder form factor

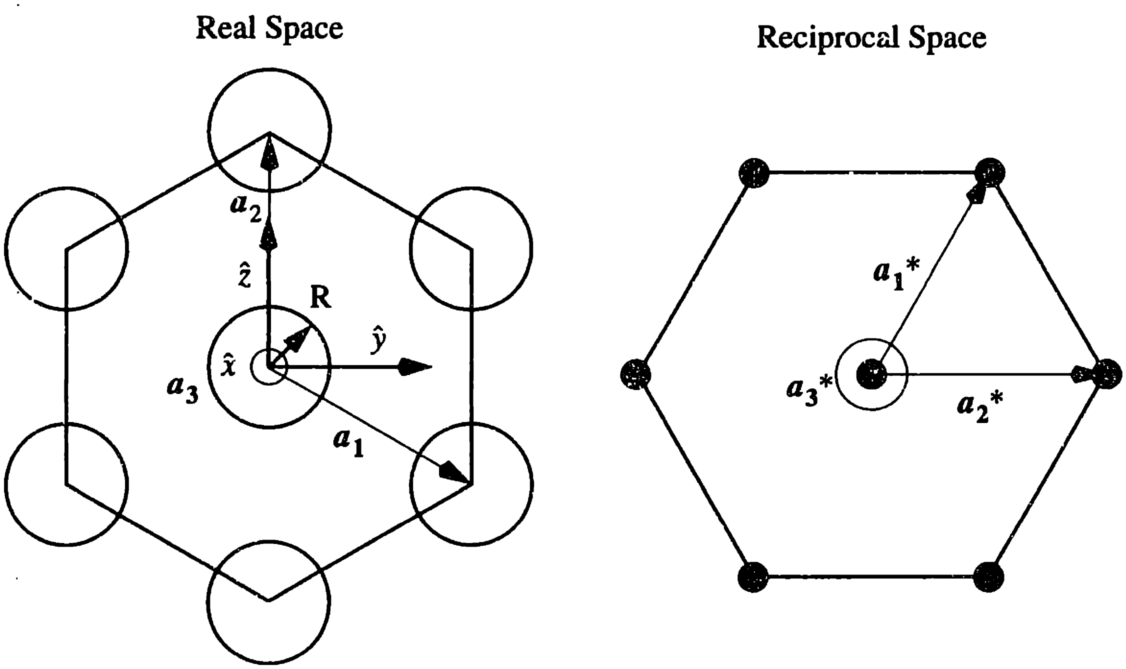

Figure 3-2: The relationship between real and reciprocal space hexagonal nets is a rotation by 30°. The symmetry of both nets is p6mm. The real space and reciprocal space basis vectors using the Miller (HKL) notation are shown superimposed on a Cartesian coordinate system.

is sampled at the positions of the reciprocal space lattice. The positions of the peaks yield information about the lattice while the intensities of the peaks contain information about the contents of the unit cell, which, in this case, consists of one cylinder. If the lattice is randomized, this effect can be plotted in 1-D (see Figure 3-3). Depending on the position of the successive zeros of the form factor (see Table 3-1) (which in turn depends on the

Table 3-1: Positions of Zeros of the First Order Bessel Function $J_1(qR)$

Zero Number	Position (qR)
1	3.8317
2	7.0156
3	10.1735
4	13.3237

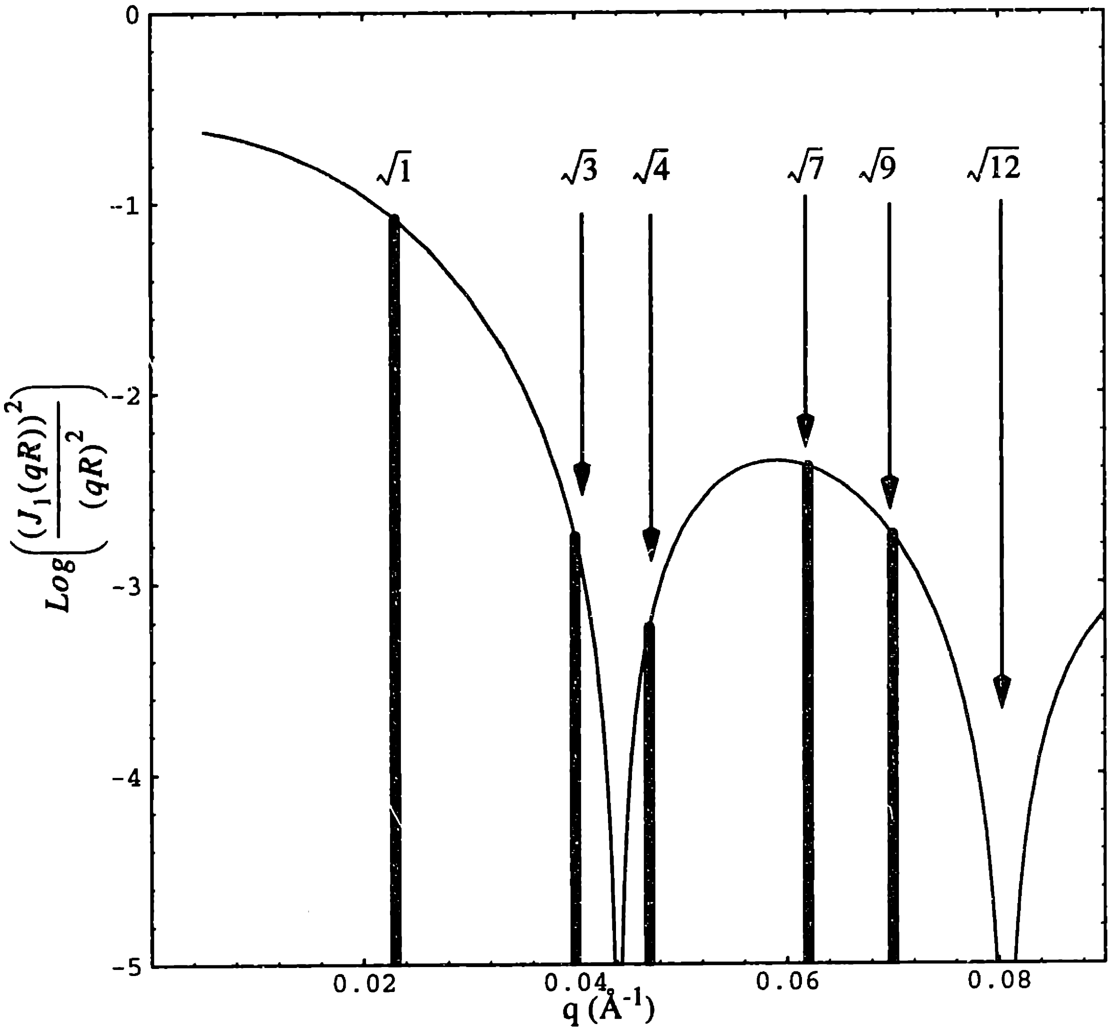

Figure 3-3: Multiplication of the square of the form factor (solid thin line) with the lattice factor (solid thick lines) results in the 1-D scattering function shown above for an unoriented sample. The curve is constructed for a cylinder with a radius $R = 87$Å. The reflection ratios label the peak positions with increasing q. Note that the $\sqrt{12}$ peak is suppressed by the second zero of the form factor.

overall composition through the radius R - see equation (3.5)), certain peaks may be suppressed. For block copolymers of volume fractions 0.2 - 0.3 (i.e. the cylinder morphology), the $\sqrt{3}$ and $\sqrt{4}$ peaks are strongly modulated. Variations in the radius R of the cylinder will act to broaden the zeros of the form factor and somewhat mitigate the dramatic drop in intensity at each zero.

The radius R of a cylinder depends on both the volume fraction f and the intercylinder spacing a. This can be shown with the help of Figure 3-4. The volume fraction f can assumed to be equal to the area fraction, which reduces the calculation to a determination of the white (PS) area within the parallelogram relative to the total area of parallelogram.

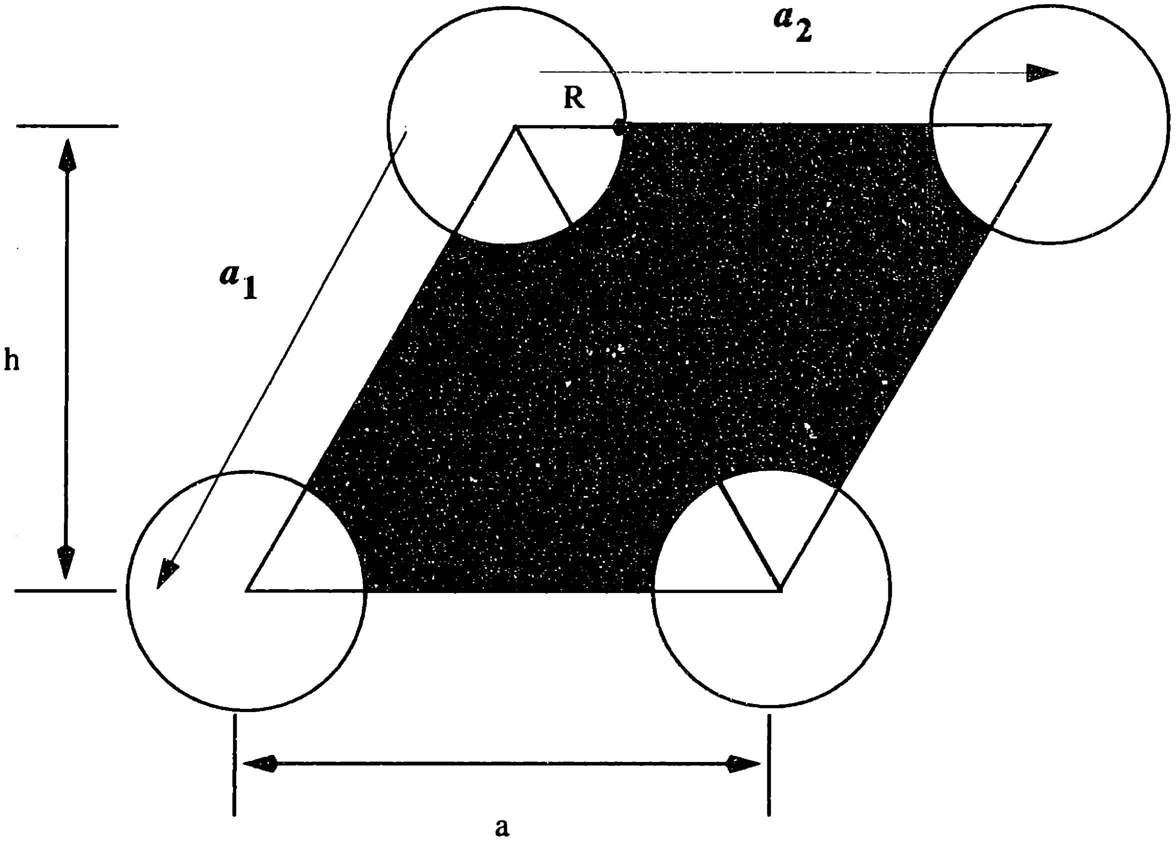

Figure 3-4: The 2-D unit cell of the cylinder structure used to determine the relation between intercylinder distance a, radius R and volume fraction f. The PS cylinders are represented in white while the rubber matrix is black. The area of the parallelogram is a*h while the area of the PS cylinder within the parallelogram is πR^2 as the cell is primitive.

$$\text{white area} = \pi R^2 \tag{3.2}$$

$$\text{total area} = \frac{\sqrt{3}}{2}a^2 \tag{3.3}$$

Therefore the volume fraction f is

$$f = \frac{2\pi}{\sqrt{3}}\left(\frac{R^2}{a^2}\right), \tag{3.4}$$

which leads to

$$R = a\sqrt{\left(\frac{\sqrt{3}}{2\pi}f\right)}. \tag{3.5}$$

3.3 Allowed Reflection Ratios for the Cylinder Morphology

To emphasize the symmetrical relationship between the indices of planes in the same family, the Miller-Bravais (hkil) notation is used throughout the thesis. However, calculations are best done using the Miller (HKL) notation, (Jackson, 1991) (p. 64), which is employed in the following derivation of the allowed reflections ratios for the cylinder morphology.

Using the Cartesian coordinate system in Figure 3-2, we write the lattice vectors $\mathbf{a}_1$, $\mathbf{a}_2$ and $\mathbf{a}_3$ in terms of the unit vectors $\hat{x}$, $\hat{y}$, $\hat{z}$ as:

$$\boldsymbol{a}_1 = \frac{\sqrt{3}}{2}a\hat{y} - \frac{1}{2}a\hat{z} \tag{3.6}$$

$$\boldsymbol{a}_2 = a\hat{z} \tag{3.7}$$

$$\boldsymbol{a}_3 = c\hat{x} \tag{3.8}$$

Where $\hat{x}$ and $\mathbf{a}_3$ point along the cylinder axis and a is the intercylinder spacing. We now calculate various cross products:

$$\boldsymbol{a}_1 \times \boldsymbol{a}_2 = \begin{vmatrix} \hat{x} & \hat{y} & \hat{z} \\ 0 & \frac{\sqrt{3}}{2}a & -\frac{1}{2}a \\ 0 & 0 & a \end{vmatrix} = \frac{\sqrt{3}}{2}a^2\hat{x} \tag{3.9}$$

$$\boldsymbol{a}_2 \times \boldsymbol{a}_3 = \begin{vmatrix} \hat{x} & \hat{y} & \hat{z} \\ 0 & 0 & a \\ c & 0 & 0 \end{vmatrix} = ac\hat{y} \tag{3.10}$$

$$\boldsymbol{a}_3 \times \boldsymbol{a}_1 = \begin{vmatrix} \hat{x} & \hat{y} & \hat{z} \\ c & 0 & 0 \\ 0 & \frac{\sqrt{3}}{2}a & -\frac{1}{2}a \end{vmatrix} = \frac{1}{2}ac\hat{y} + \frac{\sqrt{3}}{2}ac\hat{z} \tag{3.11}$$

The volume V is found from the relation

$$V = \boldsymbol{a}_1 \bullet (\boldsymbol{a}_2 \times \boldsymbol{a}_3) = \frac{\sqrt{3}}{2} a^2 c. \qquad (3.12)$$

Using the definition of the reciprocal lattice vectors $\boldsymbol{a}_1^*, \boldsymbol{a}_2^*, \boldsymbol{a}_3^*$:

$$\boldsymbol{a}_1^* = \frac{2\pi}{V}(\boldsymbol{a}_1 \times \boldsymbol{a}_2) = \frac{2\pi}{a}\left(\frac{2\sqrt{3}}{3}\hat{y}\right) \qquad (3.13)$$

$$\boldsymbol{a}_2^* = \frac{2\pi}{V}(\boldsymbol{a}_3 \times \boldsymbol{a}_1) = \frac{2\pi}{a}\left(\frac{\sqrt{3}}{3}\hat{y} + \hat{z}\right) \qquad (3.14)$$

$$\boldsymbol{a}_3^* = \frac{2\pi}{V}(\boldsymbol{a}_1 \times \boldsymbol{a}_2) = \frac{2\pi}{c}\hat{x}. \qquad (3.15)$$

Now any reciprocal lattice vector can be expressed as a linear combination of the reciprocal lattice basis vectors above:

$$\boldsymbol{q}_{HKL} = H\boldsymbol{a}_1^* + K\boldsymbol{a}_2^* + L\boldsymbol{a}_3^*. \qquad (3.16)$$

The magnitude of $\boldsymbol{q}_{HKL}$ represents the distance to the reciprocal lattice point at coordinates H, K, L. Taking c to be infinite, the L component vanishes and we are left with a 2-D hexagonal net with the distances between points:

$$|\boldsymbol{q}_{HK}| = \frac{4\pi}{(\sqrt{3})a}\sqrt{(H^2 + HK + K^2)}. \qquad (3.17)$$

Normalizing with respect to the smallest distance $|\boldsymbol{q}_{10}|$, we find that the reflection ratios are described by:

$$\frac{|\boldsymbol{q}_{HK}|}{|\boldsymbol{q}_{10}|} = m = \sqrt{(H^2 + HK + K^2)} \qquad (3.18)$$

where m is called the modulus.

The Miller-Bravais (hkil) notation arises out of a need to represent the symmetry of a hexagonal system in the notation for planes and directions (Buerger, 1956) (pp. 104-106). The repetition of the 2 basis vectors ($\mathbf{a}_1$ and $\mathbf{a}_2$) by the 2π/3 rotation of a 3- or 6-fold axis creates a third vector ($\mathbf{a}_3$) which lies in the same plane as $\mathbf{a}_1$ and $\mathbf{a}_2$. If this third axis is represented in the indices, the equivalent planes will display a three fold relationship and the indices will be permutable. Since any point in a plane is defined by two coordinates, the inclusion of a third basis vector is redundant. It is for this reason that calculations (particularly cross-products) are performed using the Miller (HKL) notation.

To convert from Miller (HKL) to Miller-Bravais (hkil) notations when considering directions or planes, the following equations are used (Jackson, 1991) (p. 69):

$$h = \frac{1}{3}(2H - K) \tag{3.19}$$

$$k = \frac{1}{3}(2K - H) \tag{3.20}$$

$$i = -\frac{1}{3}(H + K). \tag{3.21}$$

To convert from Miller-Bravais (hkil) notation to Miller (HKL) notation when directions are being considered, the following equations are used:

$$H = 2h + k \tag{3.22}$$

$$K = 2k + h. \tag{3.23}$$

When planes are considered, the i index is simply dropped. Note that the last index remains the same in both notations, as it is not involved in the above considerations. In other words, $L = l$ for all cases.

The modulus m can be written using either notation:

$$m = \sqrt{(h^2 + hk + k^2)}. \tag{3.24}$$

Table 3-2 lists the first 12 reflection ratios expected for a sample with a cylinder morphology.

Table 3-2: Allowed Reflection Ratios

{hkil}	m
$\{10\bar{1}0\}$	$\sqrt{1}$
$\{11\bar{2}0\}$	$\sqrt{3}$
$\{20\bar{2}0\}$	$\sqrt{4}$
$\{21\bar{3}0\}$	$\sqrt{7}$
$\{30\bar{3}0\}$	$\sqrt{9}$
$\{22\bar{4}0\}$	$\sqrt{12}$
$\{31\bar{4}0\}$	$\sqrt{13}$
$\{40\bar{4}0\}$	$\sqrt{16}$
$\{32\bar{5}0\}$	$\sqrt{19}$
$\{41\bar{5}0\}$	$\sqrt{21}$
$\{33\bar{6}0\}$	$\sqrt{27}$
$\{42\bar{6}0\}$	$\sqrt{28}$

As mentioned above, the advantage of the Miller-Bravais (hkil) notation is that the family of planes {hkil} or directions <hkil> can be obtained through a permutation of the indices. For the Miller (HKL) notation this is not so. As an example, consider the [100] direction using the Miller (HKL) notation. This direction corresponds to the $\frac{1}{3}[2\bar{1}\bar{1}0]$ direction using the Miller-Bravais (hkil) notation (Figure 3-5). Table 3-3 lists the family members for $\langle 100 \rangle$ and $\langle 2\bar{1}\bar{1}0 \rangle$. The [110] direction is part of the <100> family.

Table 3-3: Comparison of $\langle 100 \rangle$ and $\langle 2\bar{1}\bar{1}0 \rangle$ Family Members.

$\langle 100 \rangle$ (Miller HKL notation)	$\langle 2\bar{1}\bar{1}0 \rangle$ (Miller-Bravais hkil notation)[a]
[100]	$[2\bar{1}\bar{1}0]$

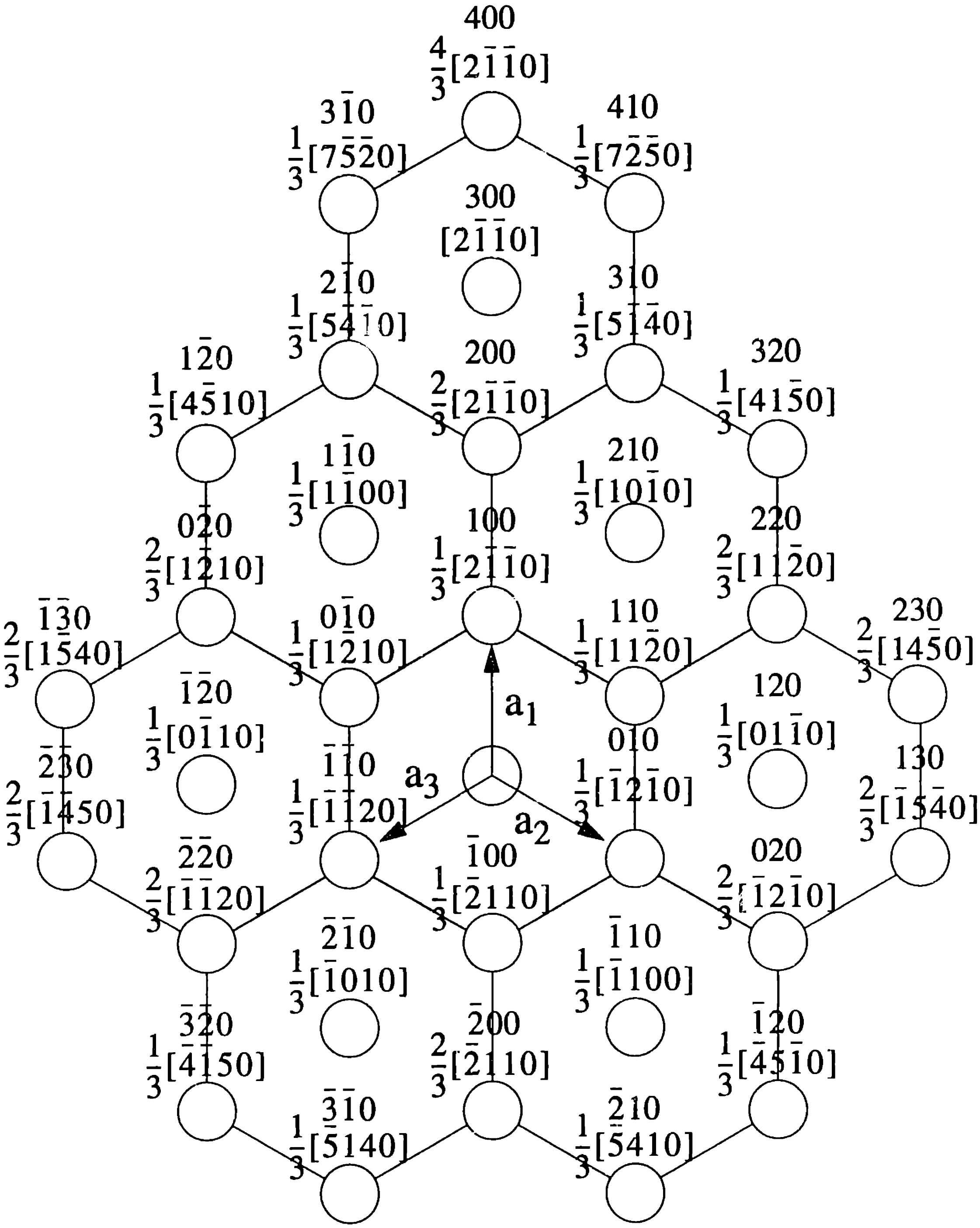

Figure 3-5: Real space 2-D hexagonal net showing directions indexed according to the Miller (HKL) notation (unbracketed) and the Miller-Bravais (hkil) notation (bracketed). The prefactor to the Miller-Bravais notation is usually factored out, but is necessary for calculations.

Table 3-3: Comparison of $\langle 100\rangle$ and $\langle 2\bar{1}\bar{1}0\rangle$ Family Members.

$\langle 100\rangle$ (Miller HKL notation)	$\langle 2\bar{1}\bar{1}0\rangle$ (Miller-Bravais hkil notation)[a]
$[110]$	$[11\bar{2}0]$
$[010]$	$[\bar{1}2\bar{1}0]$
$[\bar{1}00]$	$[\bar{2}110]$
$[\bar{1}\bar{1}0]$	$[\bar{1}\bar{1}20]$
$[100]$	$[1\bar{2}10]$

[a] The prefactor of 1/3 has been factored out, but is necessary for calculations.

3.4 Bibliography

Bear, R. S. and O. E. A. Bolduan (1950). "Diffraction by cylindrical bodies with periodic axial structure." Acta Crystallographica **3**: 236-241.

Buerger, M. J. (1956). Elementary Crystallography: An Introduction to the Fundamental Geometrical Features of Crystals. New York, John Wiley and Sons Inc.

Gobran, D. A. (1990). Phase separation and morphology of diblock and segmented block copolymers. Ph. D. thesis, University of Massachusetts.

Jackson, A. G. (1991). Handbook of Crystallography: For Electron Microscopists and Others. New York, Springer-Verlag.

Chapter 4 Experimental Methods

4.1 Introduction

This chapter describes the experimental methods used to probe the morphology as a function of deformation. Two of the three materials studied are commercially available, while one was previously synthesized by Dr. L. J. Fetters. Sample preparation via roll-casting is outlined, followed by a description of the methods used to collect data at the National Synchrotron Light Source (NSLS), where the majority of the experiments reported in the thesis were carried out. Finally, the experiments used to capture significant amounts of deformation in samples for TEM via high-energy electron irradiation are detailed.

4.2 Materials

The two commercial linear triblock copolymers with the trade names Vector 4211-D and Vector 8508-D were provided by Dexco (Baton Rouge, LA). 4211 is a poly(styrene-isoprene-styrene) (SIS) linear triblock with nominal block molecular weights of 15k-72k-15k (15-71-15 x 10^3 gm/mol) and a composition of 30 wt% PS, while 8508 is an SBS linear triblock copolymer with nominal block molecular weights of 10k-46k-10k with a composition of 32 wt% PS. The block molecular weights are calculated on the basis of the overall molecular weight and the composition.

SI (11k-34k)$_{18}$ has a "star"-like architecture with 18 linear "arms" emanating from a common center, and is hence called a star block copolymer. Dr. L. J. Fetters synthesized the star block copolymer as part of a series to investigate the solid state morphology as a function of composition at constant arm number. Each arm is a poly(styrene-isoprene) (SI) diblock of block molecular weights 11k-34k yielding a weight fraction of 0.27 (volume fraction of 0.24). The diblocks are arranged such that the star has a polyisoprene core with a polystyrene corona (see Figure 4-1). This material has been previously studied by Herman (Herman, 1986; Herman et al., 1987) and is known (via TEM) to form a cylinder

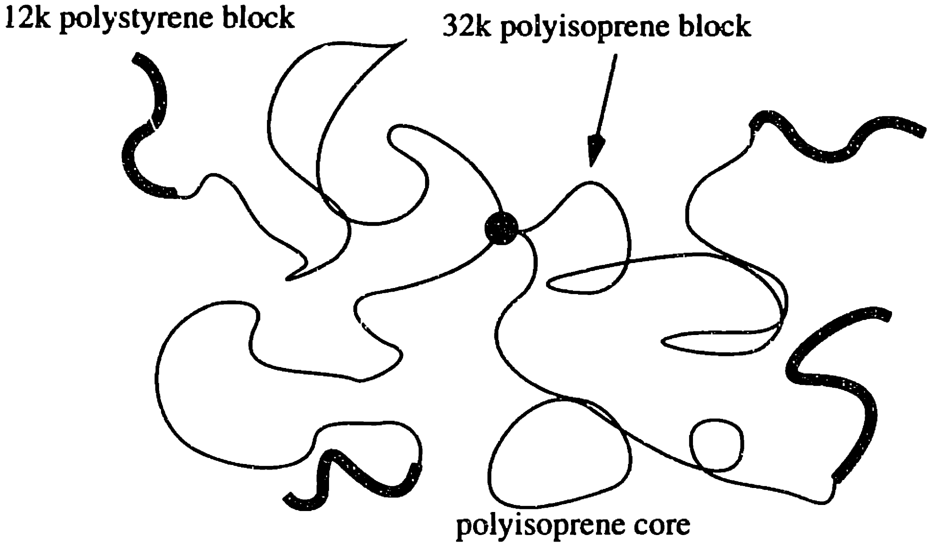

Figure 4-1: Schematic of the star block copolymer SI $(11k\text{-}34k)_{18}$. Only 4 "arms" are shown for clarity. The number code represents the block molecular weights of each diblock copolymer arm (x 10^{-3} gm/mol) with the subscript indicating the number of arms. The span molecular weight is defined as the molecular weight of a central block separating two outer PS blocks and serves as a basis for comparing star to linear triblocks. In this case the span molecular weight is 68 x 10^3 gm/mol.

morphology. The description of the synthesis and characterization of the star block copolymer can be found elsewhere (Herman, 1986). Despite being synthesized more than 10 years ago, the star block copolymer still has a narrow molecular weight distribution (see Figure 4-2) meaning that the material has not degraded significantly (i.e. no branching). Table 4-1 lists the molecular characteristics of all three polymers.

Table 4-1: Molecular Characteristics

Architecture	Block Molecular Weights[a]	wt% PS	vol%[b] PS	Overall M_w (x 10^3 gm/mol)[c]	PDI $\frac{M_w}{M_n}$
linear SIS	15k-72k-15k	29[c]	26	101	1.06
linear SBS	10k-46k-10k	30[c]	27	66	1.05
star $(SI)_{18}$	$(11k\text{-}34k)_{18}$	24[c]	21	800	1.04

a. Determined from the composition (wt% PS) and the overall molecular weight.
b. Determined from composition and the densities: $\rho_{PS} = 1.04$, $\rho_{PI} = 0.90$, $\rho_{PB} = 0.89$ gm/cm^3.
c. Determined by Dr. L. J. Fetters.

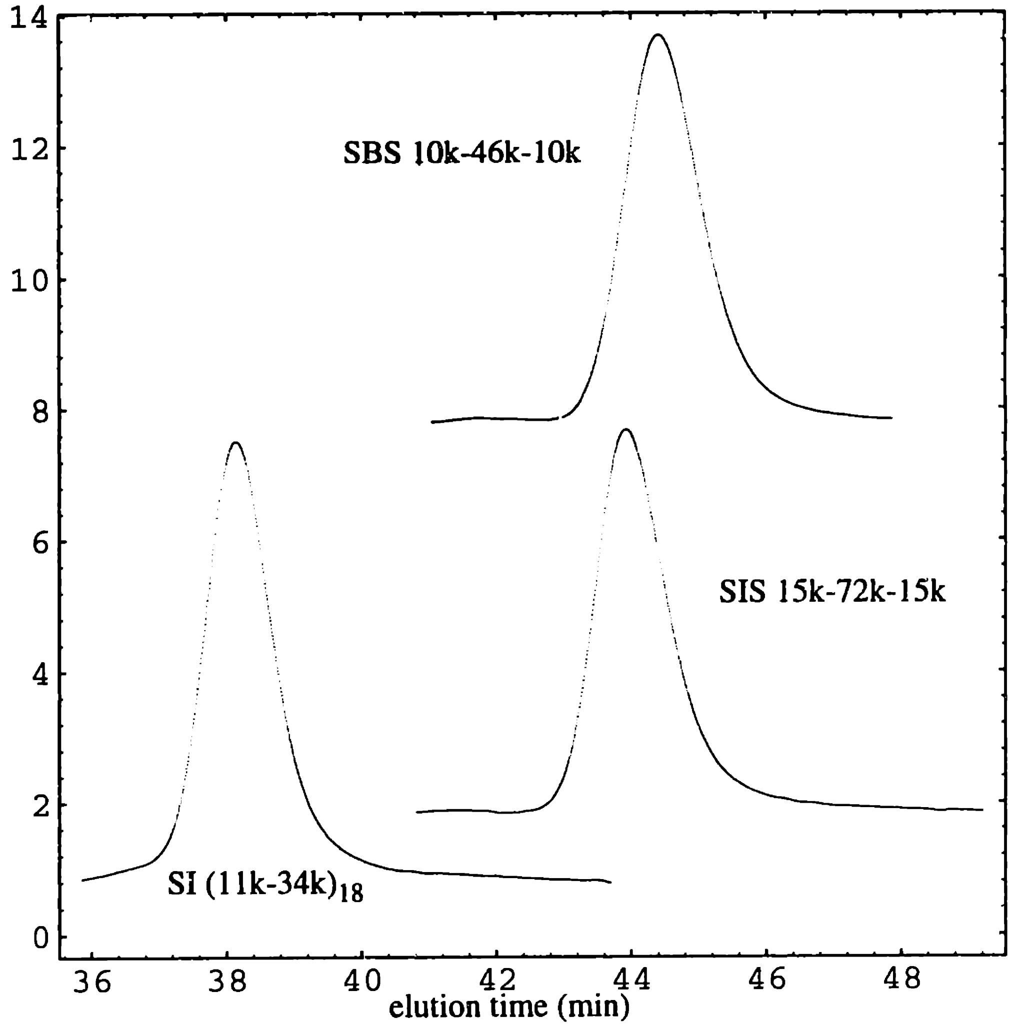

Figure 4-2: Plot of refractive index intensity (arbitrary scale) vs. elution time for the three samples used in this study. The data has been digitized from the raw GPC traces provided by Dr. L. J. Fetters and offset for clarity. There is no significant fraction of high or low molecular weight species contaminating the samples.

4.3 Sample Preparation

Oriented films are produced by a technique developed by Dr. Ramon Albalak in our lab (Albalak, 1994; Albalak et al., 1994). The essential features of the roll-caster are shown in Figure 4-3. Two parallel rollers, one of stainless steel and the other of Teflon®, counter-rotate at a constant frequency. The rollers are separated from each other by a micrometer-controlled distance (gap) and are driven by independent motors at constant speed. A

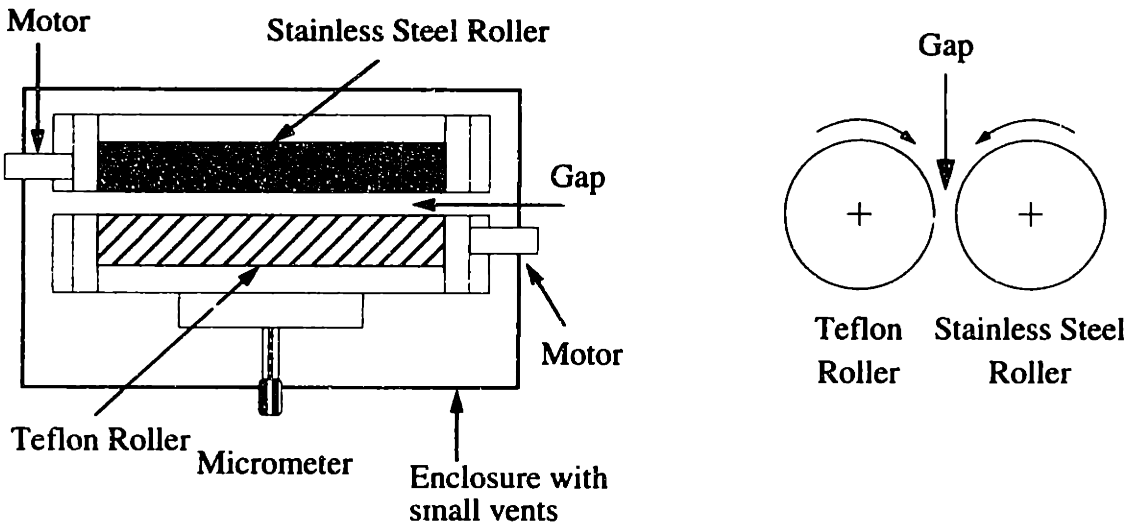

Figure 4-3: Left: Schematic plan view of the Roll-Caster. Two parallel rollers counterrotate at a fixed separation controlled by a micrometer. Right: Cross-sectional view.

concentrated, homogeneous polymer solution is poured into the gap region and initially coats both the Teflon® and stainless steel rollers uniformly. The film in the gap undergoes both extensional and shear flow (Albalak and Thomas, 1994). As the solvent evaporates, the material becomes more viscous and a film preferentially forms on the stainless steel cylinder. During the roll-casting procedure the film passes the gap region hundreds of times, though it is thought that the critical morphology-orienting period occurs during the concentration at which microphase separation takes place.

The procedure used to produce oriented films is as follows:

1 the gap and roller speed is set

2 the solution is introduced into the gap region

3 the apparatus is partially enclosed by a box to slow solvent evaporation

4 if a thicker film is required, the gap is increased sequentially with subsequent addition of solution

5 the finished oriented film is allowed to dry on the steel roll and is

removed.

Typical gap sizes range from 0.05 mm to 0.4 mm. With gaps larger than 0.4 mm, more than one charge of solution is needed to obtain films of uniform thickness. Films with thicknesses of up to 2.0 mm have been roll-cast by increasing the gap and adding material in steps of 0.3 - 0.5 mm. The roller speeds are typically set at 9 rpm (shear rate of 0.14 s^{-1}), though a range from 5 (or less) to 35 rpm (0.083 - 0.58 s^{-1}) is possible. The solution concentration chosen is 1wt/2vol (polymer/solvent) (ca. 33%) as a compromise between the speed of dissolution and solution viscosity. Higher concentration solutions take longer to prepare and are closer to the order-disorder concentration. Lower concentrations require smaller gaps settings to prevent flow of solution from the gap region. The ideal solvent is both non-preferential, residing equally in both phases throughout the roll-casting procedure and slow to evaporate. Toluene is generally considered a non-preferential solvent, but cumene has been found to be slightly less preferential (Annighoefer et al., 1983). In addition, cumene is a heavier molecule with a lower vapor pressure than toluene. The evaporation rate of cumene is slower, leading to an extended period of time during which orientation occurs in the partially microphase-separated semi-fluid/semi-solid. However, cumene-roll-cast films take longer to dry.

A freshly roll-cast film still contains 5-10% solvent and is allowed to dry on the rollers for several hours (overnight if possible) to enhance mechanical integrity. Dry films suffer less damage during removal (by hand) from the stainless steel roller. Isopropanol or ethanol is a non-solvent for both blocks and is used to assist in the film removal by weakening the polymer/metal interface. Once the film is removed, it is held between Teflon® sheets to relax in such a way as to render the film flat, as it has an inherent predisposition to curl. The Teflon® sheets are separated by spacers so that dimensional changes are not constrained. The roll-caster imparts a significant amount of chain stretching along the flow direction which leads to a distortion of the microstructure

(Albalak, 1994). During film drying and annealing, the physical dimensions of the film change. It is important to freely allow these dimensional changes to occur so that no additional stresses are induced. The Teflon® sandwich is placed in an oven for the drying and annealing process. The film is dried under vacuum for 1-2 days before the temperature is ramped to the annealing temperature of 120 °C for 5-7 days.

Tensile specimens are stamped out using steel-ruled dies (Quality Die Co., Haverhill Ma (508) 374-8027) of four sizes (see Table 4-2). The die is attached to the top of an Arbor press, while the sample is attached to a plywood substrate with the desired morphological orientation parallel to one edge of the square substrate. A metal plate is attached to one side of the substrate to guide the orientation of the die to the edge of the substrate, which, in turn is correctly oriented with respect to the desired morphological direction. The die is pressed into the substrate, cutting through the film in one stroke. Subsequent samples are taken at locations in the film spaced by at least one die-width.

Table 4-2: Steel Rule Die Sizes

Die #	Width (mm)	Length (mm)
1	1	25
2	2	32
3	3	32
4	4.76	38

4.4 Deformation Stages

4.4.1 Instron

An Instron 4501 equipped with a 5kN load cell and an extensometer is used to perform tensile tests mimicking those conducted at NSLS. A PC-compatible computer running the Instron Series IX software interfaces with the 4500 Instron controller. Various deformation protocols, including deformation cycling and stress relaxation experiments, can be programed into the computer. Typical testing parameters for a stretch-to-failure test are: 40 mm/min stretching rate, 20 mm gage, extensometer edges separated by 15 mm with a sampling rate of 5 pt/sec. A second sampling rate after a user-specified time is generally set to 1 pt/sec.

One problem encountered in stretching these TPEs is that of sample slippage. As the sample is deformed to large strain, the thickness decreases significantly while the stress increases dramatically (see, for example, Figure 5-34). Hence there is a tendency for the samples, especially those of larger cross-sectional area, to slip. The stress at a given strain increases as a function of the cross-sectional area, while the gripping area (at constant gage length) increases with the width. The samples least likely to slip are therefore, very wide and thin. However, the knife edges of the extensometer, though not particularly sharp, do introduce a stress concentration, which acts as a potential point of failure. These stress concentrations become more severe for thin samples.

The grip faces on the pneumatic grips provided by Instron, though serrated, were found to perform poorly with these materials. Special grip faces with a saw-tooth pattern were custom machined out of heat-treated stainless steel. Sample slippage ceased to be a problem with these grips. However, the failure point almost always was found to occur in one of two places: at the grips, or less likely, at the extensometer knife edges. Information about the ultimate properties of the material was compromised to gain a more accurate reading of strain at large deformations, as unloading the sample from high strain is necessary to determine hysteresis.

4.4.2 Mini-Deformation Stage

A tensile stage was custom-designed with assistance from Mr. K. Honeker and built by Mr. B. Nespel (Nuclear Engineering Machine Shop at MIT) to fit into the sample chamber at the NSLS X-12B beamline. A schematic of the experimental set-up at Brookhaven is shown in Figure 4-4. The tensile stage is placed on a double-tilt cradle, custom-built by Mr. B. Pene (Western Tool and Engineering Co., Burlingame Ca), which is mounted in the sample chamber. The load cell is activated by a display which, in turn, sends a signal to a strip chart recorder located outside of the hutch. The door to the hutch is interlocked and must remain closed when the photon shutter is open and x-rays enter the hutch area. A video camera, directed towards the display, reports the load on the sample to a closed-circuit monitor at the computer console at the end of the beamline. The user is thereby aware of the stress state of the sample.

Load is recorded via a strip chart recorder and later digitized (Section 4.5.2.2). Strain is determined via the number of steps that the stepper motor makes at a constant step rate. It is assumed that each motor step drives the gears to stretch the sample and that no steps are "missed".

A schematic of the tensile stage is shown in Figure 4-5. The main elements which will be discussed are: stepper motor, load cell, and grips.

A stepper motor (Airpax 4SHG-12A56S; Phillips Co., Cheshire CT) turns the two threaded drive rods at the same speed. Each drive rod is made up of a right handed thread and a left-handed thread which are press-fitted together. The handedness of the threading reverses at the midplane between the grip faces to provide symmetric stretching. The stretching rate can vary from 7.92 mm/min to 30 mm/min, though a modification by Dr. Carl Zimba to the control box has recently extended the slowest speed down to 2.5 mm/min. The maximum travel of the stage is approximately 90 mm.

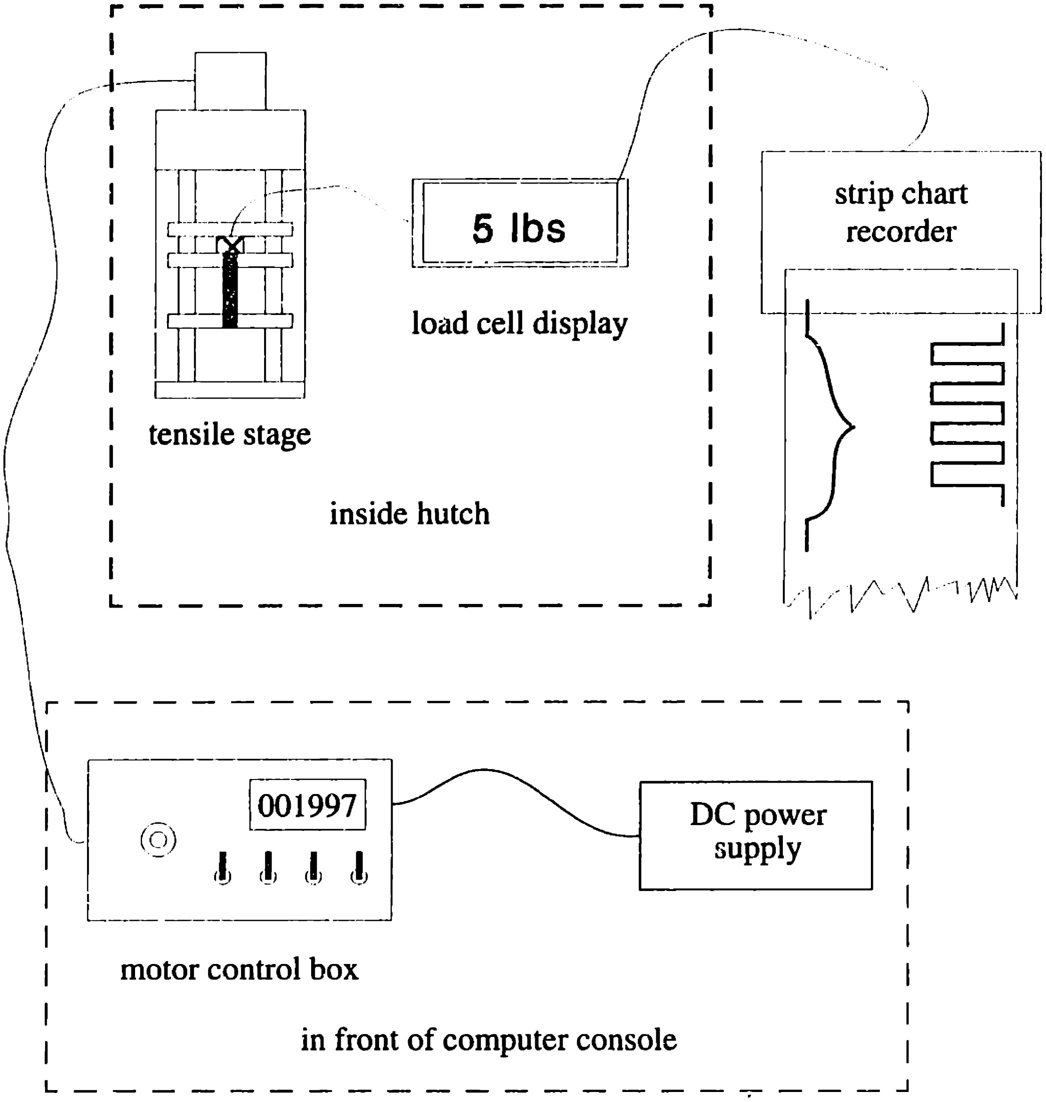

Figure 4-4: Essential elements of the mini-deformation stage designed for insertion into the X-12B beamline at the NSLS at Brookhaven. The tensile stage is mounted on a double tilt stage (not shown) so that the center of the sample (shaded) is located at the beam position. The load cell display provides a voltage (excitation) to the load cell as well as a signal to a strip chart recorder which is located outside the hutch. The power, speed and direction of the stepper motor is provided by the motor control box via a long cable. The control box includes an index counter displaying the number of motor steps which is related to the displacement of the sample.

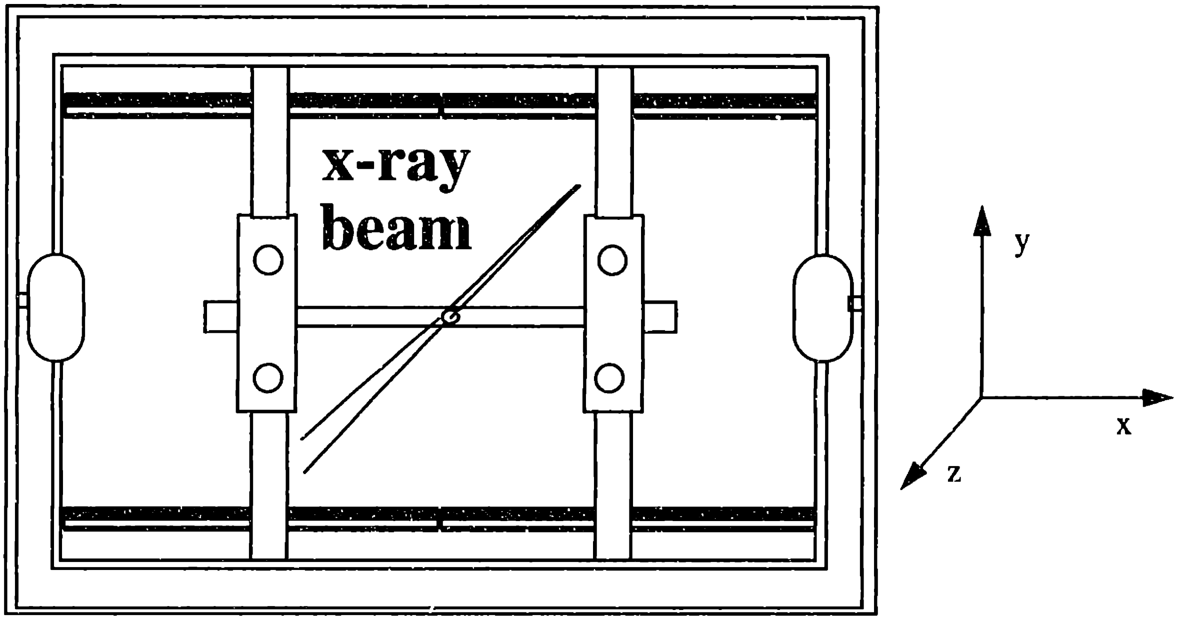

Figure 4-5: Schematic of the tensile stage. Provision is made so that the sample is stretched symmetrically about its mid-plane (see text). A double tilt stage (not shown) enables the sample to be tilted about the SD (x axis) and about the normal to the SD (y axis). The coordinate axes represent the laboratory reference frame and are consistent with those used by Dr. M. Capel, the X-12B beamline manager. The x, y, and z axes correspond to the horizontal, vertical and beam directions respectively. Figure kindly provided by Benita Dair.

The load cell (model #31; Sensotec, Columbus OH) has a 50-lbs capacity and is activated by a display (model GM; Sensotec, Columbus OH). The display acts as signal conditioner, amplifier and power supply and provides shunt calibration in order that the load cell can be calibrated electronically based on a primary calibration performed at the factory.

The griping system consists of 2 pairs of plates whose faces have a saw tooth pattern. The top plate is screwed into the bottom plate to clamp one end of the tensile specimen. The sample/grip assembly is then mounted on the two pairs of dowel pins located on the top and bottom cross-members of the tensile stage. To further minimize sample slippage at high deformation, three Belleville washers are placed between each screw head and the top plate. These washers have a concave and convex side and act as springs so that as the sample becomes very thin, gripping pressure is maintained.

4.5 Deformation Experiments at the NSLS at Brookhaven

4.5.1 X-12B beamline 2-D SAXS facility.

The capabilities of the X-12B beamline are detailed in (Capel, 1993) and (Capel et al., 1995). Up to date information can be found on the homepage of the beamline manager, Dr. Malcolm Capel, at http://crim12b.nsls.bnl.gov/x12b_info.html#manuals. Only information directly relevant for acquisition and analysis of the SAXS data are outlined here. The beamline optics provide a doubly-focused monochromatic beam over a wavelength range $1.6 < \lambda < 0.92$ Å. The wavelength chosen for all NSLS experiments is 1.549 Å, which corresponds to the 8 keV +/- 10 eV Holmium L_{III} absorption line in the XAFS spectrum. The sample-to-detector distance (SDD) has varied over the 5 runs conducted for these deformation experiments from a low of 148 cm to a high of 254 cm. Table 4-3 lists the calibration information used to convert pixels on the detector to q (Å^{-1}).

Table 4-3: Brookhaven Calibration Information

parameter	BNL #1 Oct 1994	BNL #2 Aug 1995	BNL #3 Nov 1995	BNL #4 short Aug 1996	BNL #4 long Aug 1996	BNL #5 Sept 1996
center coords.	263, 242	261, 256	275, 256	270, 256	261, 252	271, 257
secondary calibration	128 pixels = 93.0 Å.	209 pixels = 93.0 Å	157 pixels = 93.9 A	126 pixels = 92.2 A	209 pixels = 93.0 A	213 pixels = 93.0 A
primary calibration			291 pixels = 50.7 Å	229 pixels = 50.7 Å		
SDD (cm)	148.2	243.1	188.6	148.5	245.9	254.3
Q (Å^{-1})/ pixel	0.5288×10^{-3}	0.3287×10^{-3}	0.4259×10^{-3}	0.5412×10^{-3}	0.3260×10^{-3}	0.3168×10^{-3}
λ (Å)	1.549	1.549	1.549	1.549	1.549	1.549

The primary calibrant is a cholesteryl myristate polycrystal with a d-spacing of 50.7Å

(Craven et al., 1976). The secondary calibrant is a dried and stained duck tendon. The d-spacing in tendon collagen is known to change over time (and with humidity) (Bolduan et al., 1950). Two runs (BNL #3 and BNL #4) of the duck separated by 8 months showed only a 1.8% change in spacing. The average of the two measurements was used as the spacing of the secondary standard to calibrate the remaining runs. The coordinates of the center of the image are determined by finding the center of the diffraction ring from any polycrystal scatterer.

The 2-D position-sensitive gas-proportional detector (PSD) used at the X-12B beamline is described in detail elsewhere (Capel et al., 1995). The salient features are described in Table 4-4. The nonuniformity of detector response is corrected by a compensation matrix generated from a uniform illumination to smooth the modulations in intensity caused by the discrete positions of the anode wires. The uniform illumination is from gas scatter in a partially evacuated downstream flight path. Further details of the calculations performed in a compensation as well as other details of the various detectors used at the X-12B beamline are described on the web page at http://crim12b.nsls.bnl.gov/x12b_det.html.

Table 4-4: 2-D PSD Detector Characteristics

Parameter	Value
size	10 cm x 10 cm
# of pixels	508 x 496
dynamic range	32-bit
max count rate (cps)	6×10^5

The user launches and monitors deformation experiments from the computer console of the X-12B beamline. The executive PS runs a DOS-based control system (named CONSOLE) written by Dr. M. Capel which has a graphical user interface (gui). Within CONSOLE is a script programming environment written in CLL (console control language) which contains editors to generate control scripts. The default CLL script is the X-12B mezzanine interface shown in Figure 4-6. From this "main menu" the user can:

1 launch an experimental sequence script (*.exs)
2 edit macro definitions (*.mac)
3 adjust or tune the monochromator (mono adjust)
4 move the sample stage (scan motors)

The experimental sequence script (*.exs) defines the "order of events" during a run; controlling movement of motors, the taking of a background, tuning of the monochromator, opening of the shutter, executing the time slice sequence script (*.tsm) (which defines the number and duration of active and pause slices) and transferring the data to disk from memory. Once the *.exs, *.tsm, and *.mac files have been selected, the user enters the user-specified variables appropriate for the experiment in the macro definitions file (*.mac), interprets the scripts (a step which checks for errors in script programming or variable definitions) and executes the script.

4.5.2 Data Collection

4.5.2.1 2-D SAXS data

Two modes of deformation experiments were carried out at X-12B: constant strain-rate deformation and stress relaxation. The stretching rate was generally set at the slowest speed, which resulted in strain-rates ranging from 0.5 - 1 min^{-1} depending on the initial gage length.

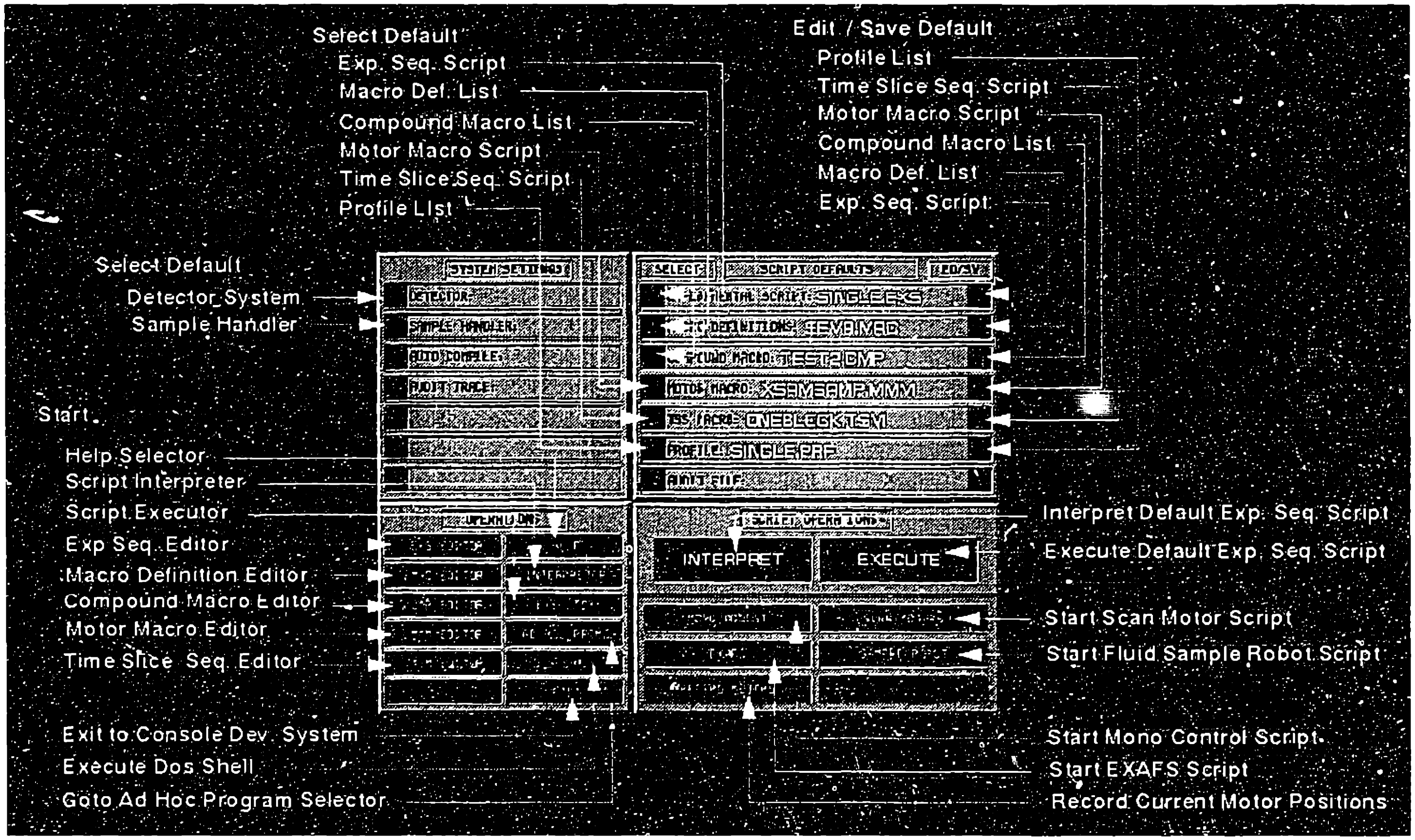

Figure 4-6: Screen capture of a sample experimental set-up in the CCL mezzanine interface taken from the X-12B web site. The script files (upper right) appropriate to the experiment are selected and edited. The user then interprets and executes the scripts (large buttons on right). The beam flux is maximized by tuning the monochromator (mono adjust). Finally, the position of the sample is determined by moving the sample stage while monitoring beam flux (scan motors). The remaining operations are used by Dr. M. Capel to program and modify scripts and for other tasks.

A typical data acquisition sequence for a constant strain-rate experiment is shown in Table 4-5. The first block takes a long exposure (120 s active dwell) pattern of the unstretched sample. Stretching commences at the start of the first active dwell of the second block. Note that the time slice sequence begins with a pause dwell before the corresponding active dwell. The second block is made up of series of relatively short (10 s) exposures each of which is separated by a 10 s pause. The third block samples the scattering at the largest deformations at one minute intervals. The stretching is reversed during the third block. The final portion of unloading is again sampled at high frequency (10 s on/10 s off). The sample is generally fully unloaded before the end of the SAXS data acquisition sequence.

Table 4-5: Typical Constant Strain-rate Deformation SAXS Sampling Frequency

block #	# of slices	pause dwell (s)	active dwell (s)
1	1	10	120
2	15	10	10
3	8	30	30
4	15	10	10

A typical data acquisition sequence for a stress relaxation experiment is shown in Table 4-5. In this case the sampling frequency is highest at the very start of the experiment.

Table 4-6: Typical Stress Relaxation SAXS Sampling Frequency

block #	# of slices	pause dwell (s)	active dwell (s)
1	1	10	120
2	30	10	10
3	20	60	60
4	60	120	180

As for the constant-strain rate experiments, stretching begins at the first active dwell of the second block. The sample generally reaches the holding strain during the first block so that the initial stress relaxation is also sampled at high frequency. 50 patterns are taken during the first hour of stress relaxation. Thereafter a long exposure is taken every 5 minutes for as long as practical. Stress relaxation experiments are begun in the evening and allowed to continue through the night until the next morning.

These parameters (as well as background acquisition information, sample position and monitor (ionization chamber) performance acquisition information) would be entered in the macro definition file $MIT4.MAC. These definitions along with MITM.EXS and FOURBLOCK.TSM would constitute the appropriate scripts for a dynamic deformation experiment with a variable SAXS pattern acquisition frequency. Note, however, that the scripts described here were set-up by Dr. M. Capel and are thus subject to change depending on the rest of the CONSOLE environment as well as user input.

4.5.2.2 Load Data

Load data was collected via a strip-chart recorder (Fischer RecordAll Series 5000). Full scale was set at 5 lbs for most samples (50 lbs for samples of larger cross-section). The chart speed was chosen appropriate for the duration of the experiment: for constant-strain rate experiments, the chart speed was set at 1 or 2 in/min, while for stress relaxation of long duration (> 1 hour), the chart speed was set to 0.2 in/min. The strip chart speed was determined to be within 3% of the indicated speed. The load cell was calibrated via the manufacturer's recommended procedure. The load-time curves were scanned and digitized using UN-SCAN-IT 2.0. Thereafter, the load-time data was converted to engineering stress-strain using the following relations:

$$\sigma = \frac{\text{load}}{A_o} \tag{4.1}$$

$$e = \frac{\begin{array}{c}\underline{\text{time}}\\ \dot{l}\end{array}}{l_o} = \frac{\Delta l}{l_o} \tag{4.2}$$

where A_o is the initial area, $\dot{l}$ the stretching rate and l_o the initial gauge length.

The SAXS data acquisition periods were synchronized with the load-time data via a signal sent from the control system to the strip chart. The result is a square-wave function where the one side represents active data acquisition and the other represents pause (see Figure 4-4).

4.6 SAXS Data Reduction

2-D SAXS data was reduced in three ways: peak position, various 1-D integrations and sample transmission. NEED TO ADD DISCUSSION ABOUT SAXS DATA TREATMENT - SEE NED'S COMMENTS.

4.6.1 Peak position

Peak positions were determined by hand. A viewer program (frnew) written by Dr. Capel displays the 2-D data files and enables the user to select the minimum and maximum intensity thresholds as well as the coordinates of any pixel picked by the mouse. A common problem in the display of 2-D SAXS data is in the large dynamic range of the intensities (> 10^4) compared with the dynamic range of conventional output (256 levels for screen or monochrome printer). Thresholding enables a subset of the full dynamic range to be represented in the available output range. The minimum threshold is increased to eliminate all but the "tip" of the peak of interest and the maximum threshold is reduced so that the most intense pixels are just saturated. The peak position is then chosen as the position of the darkest (black) pixel with the zoom-in window at maximum magnification (8x). The error in the procedure is estimated at +/- 1 pixel.

The alignment of the detector is approximately 45° with respect to the vertical (see Figure 4-7). All 2-D SAXS patterns are reoriented so that the vertical direction is along y.

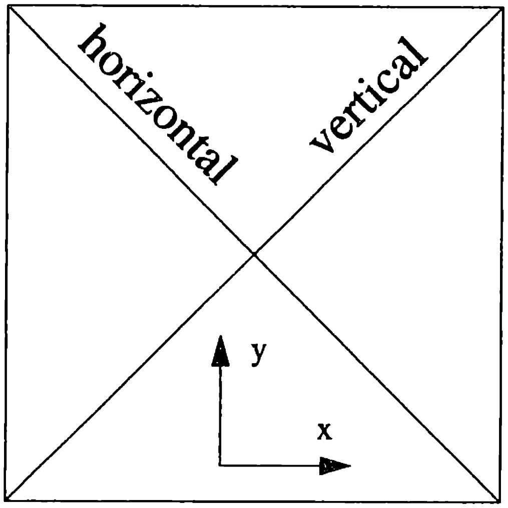

Figure 4-7: Orientation of the detector with respect to the laboratory reference frame.

4.6.2 1-D Integrations

A second program written by Dr. Capel (fi_gui) supplies a suite of integration routines a subset of which are summarized in Table 4-7. These integration modes are used in the reduction of the 2-D SAXS data in this thesis to 1-D SAXS profiles. A schematic description of the integration modes is presented in Figure 4-8. The description "fixed

Table 4-7: Integrations Used in 2-D SAXS Data Reduction

Integration Mode	Method
circular, fixed radial	Intensity is integrated over 360° of azimuth into 1 pixel wide bins which range from the origin to a user-specified max. radius. The result is an azimuthal integration over the entire azimuth.
sectorial, fixed radial	Same as circular except that the integration is broken into sectors. In addition to the max. radius, the user defines the min. radius, the number of sectors as well as their angular width.
norm arbitrary radial, fixed radial	Intensity is integrated along the norms of a user-defined vector. The user defines the start and end coordinates of the vector as well as the norm width.
theta dependence of sector	Intensity is integrated along a radius interval for user-defined angular range(s). The user specifies the min. and max. radii as well as the number of sectors and their angular range.

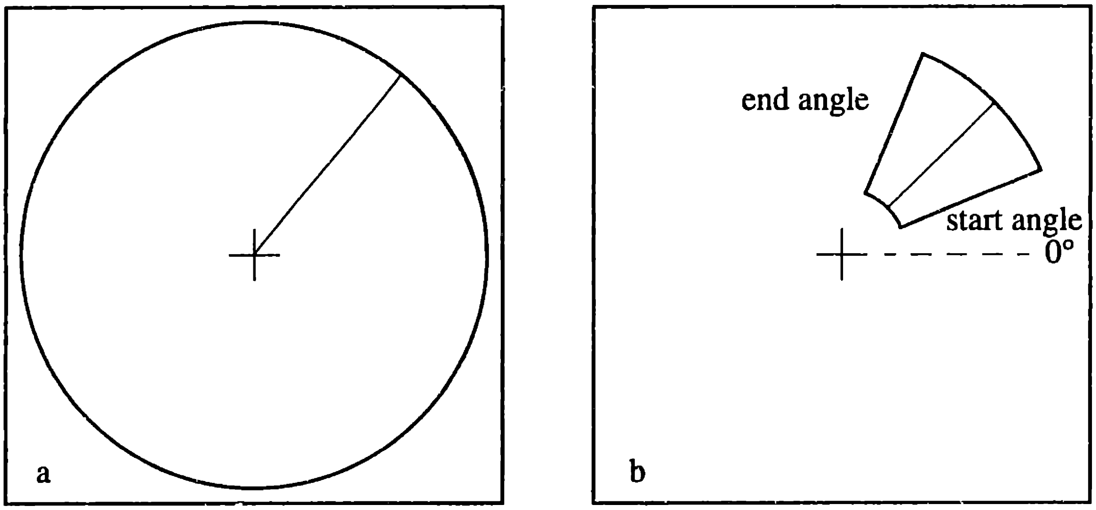

circular, fixed radial

sectorial, fixed radial

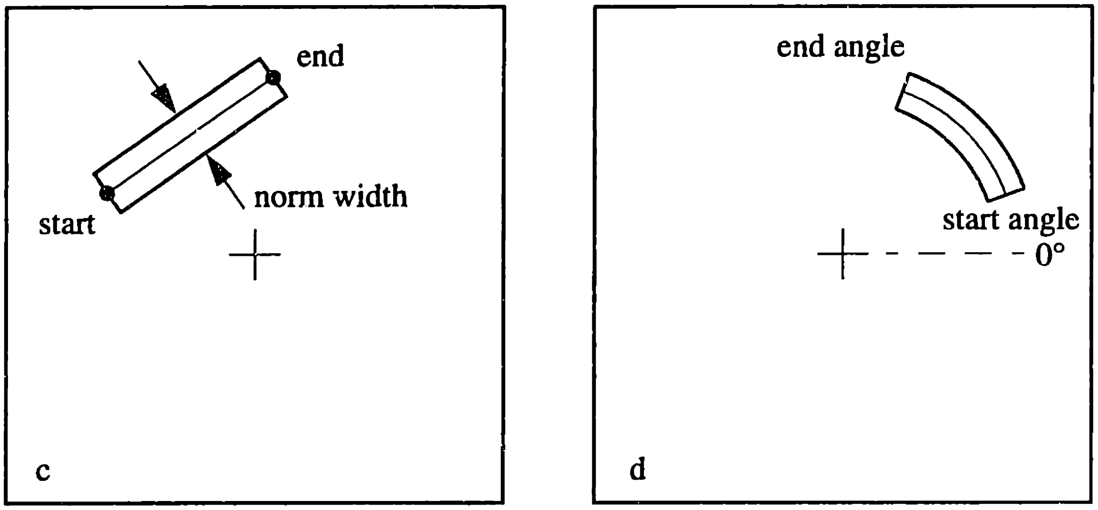

norm arbitrary radial, fixed radial

theta dependence of sector

Figure 4-8: Schematic depicting the four integration modes used to reduce the 2-D SAXS data to 1-D profiles. The heavy lines mark the boundary of the integration region, while the light line represents the orientation of the q axis. For example, in (d), the integration is in a direction normal to the line resulting in a 1-D scan along the azimuth. Only one sector is shown in each case, although in (b) and (d) multiple sectors are possible.

radial" refers to the fact that each step along the pixel-axis of the 1-D profile is one pixel in width. For example, a circular, fixed radial integration to a max. radius of 250 pixels would result in an I vs. q plot with each q increment equal to one pixel. Only the theta dependence of sector integration mode operates differently. Here each step is equivalent to 1°.

Since the number of pixels in the x and y directions are unequal there is a 1% (508/496) uniform compression in the y (vertical) axis (see Table 4-4). This distortion is taken into account in all binning operations in fi_gui.

4.6.3 Sample Transmission

The X-12B beamline includes two ionization chambers which act as flux monitors at the entrance and exit of the sample area. The number of counts recorded by the monitors is proportional to the flux and is recorded in the header of each data file taken. The ratio of the counts recorded by the downstream monitor to that recorded by the upstream monitor represents the fraction of the x-ray beam which is transmitted through the sample space (ignoring absorption by air). The sample transmission (T) can in turn be related to the sample thickness (t) via Beer's law (Alexander, 1985) p. 68.

$$T(t) = \frac{I(t)}{I_o} = e^{-\mu t} \qquad (4.3)$$

where μ is the linear absorption coefficient and $I(t)$ and I_o the intensity at a given thickness and the unattenuated intensity respectively.

Assuming that the sample transmission is related to sample thickness in the form shown in equation (4.3), one can estimate the engineering strain (e) of the sample in the beam direction as follows. The strain in the beam direction (ZZ using laboratory coordinates - see Figure 4-7) is defined as

$$e_{ZZ}(t) = \frac{t - t_o}{t_o} \qquad (4.4)$$

where t_o is the initial thickness of the sample, and in terms of equation (4.1) and equation (4.3)

$$e_{ZZ}(t) = \frac{\ln T(t)}{\ln T(t_o)} - 1 \qquad (4.5)$$

As the thickness of the sample generally decreases during deformation, $e_{ZZ}(t)$ is negative which means that $\ln T(t) < \ln T(t_o)$ and $T(t) > T(t_0)$ as $T(t) < 1$. The transmission increases during deformation as the sample becomes thinner.

Engineering strain (e) is used throughout the thesis, in part because the extension ratio is often used to express the extent of deformation in rubber. True strain (ε) in the force direction is used when calculating the Poisson ratio. ε is defined in terms of a displacement increment

$$d\varepsilon = \frac{dl}{l}. \tag{4.6}$$

Thus, the true strain at a given gauge length has a logarithmic form

$$\varepsilon(l) = \int_{0}^{\varepsilon} d\varepsilon = \int_{l_o}^{l} \frac{dl}{l} = \ln\left(\frac{l}{l_o}\right). \tag{4.7}$$

Using equation (4.2) and equation (4.7) the relationship between true strain (ε) and engineering strain (e) is simply

$$\varepsilon = \ln(e+1). \tag{4.8}$$

Thus, the thickness strain can also be written in terms of the true strain (using equation (4.5))

$$\varepsilon_{ZZ}(t) = \ln\left(\frac{\ln T(t)}{\ln T(t_o)}\right). \tag{4.9}$$

4.7 High-Energy Electron Irradiation

Several definitions pertaining to radiation cross-linking are useful. Dose is the amount of energy given to a material in grays. Gray is the unit of absorbed dose (1 gray (Gy) = 1 J/kg = 100 rad). The G value is the magnitude of a particular reaction occurring per 100 eV of energy absorbed. G(S) = the number of polymer chain scissions per 100 eV absorbed. G(X) = the number of polymer crosslink sites per 100 eV absorbed.

Table 4-8 lists G(S), G(X) and G(S)/G(X) ratios for polystyrene, natural rubber, polybutadiene and a poly(styrene/butadiene) copolymer. The relative scission-to-crosslinked ratio G(S)/G(X) gives an indication of how often chain scission occurs per crosslink formed. A ratio greater than one leads to the degradation of the polymer. The table indicates that a styrene-diene copolymer experiences more crosslinking than chain scission.

Table 4-8: Approximate Cross-link and Scission Yields for Irradiated Polymers[a,b]

polymer	G(X)	G(S)	G(S)/G(X)
polystyrene	0.045	<0.018	0.4
natural rubber	1.1	0.22	0.16
polybutadiene	3.8	-	0.1-0.2
poly(styrene-butadiene) copolymer[c]	2.8	0.39	0.2-0.5

a. From (McGinniss, 1986)

b. Irradiation at room temperature under vacuum or inert atmosphere (nitrogen).

c. 23.4% PS

There is only one study on the influence of irradiation on the properties of styrene-diene block copolymers that I am aware of. Here, commercial styrene-diene block copolymers not unlike the ones in this thesis, have been irradiated in vacuum to improve the tensile strength and the elongation at break (Huai et al., 1994). The results indicate that the ultimate properties decrease slightly with dose (up to 20 kGy) before increasing at medium dose (50-200 kGy) and finally decreasing significantly at the highest dose (400 kGy). No clear explanation for the observed variation of ultimate properties with dose was given.

4.7.1 High-Voltage Lab (HVL) at MIT

The HVL experiments were conducted using a Van de Graaf generator at an energy of 2.6 MeV with the assistance of Mr. Kenneth Wright. Samples were held in a stretching jig at fixed deformation and passed underneath the scan horn by a conveyer belt. Each pass delivered approximately 25 kGy (2.5 Mrad) dose to the sample. Dosages of up to 800 kGy (80 Mrad) were delivered in this way.

4.7.2 Raychem

The experiments at Raychem were conducted under more controlled circumstances. Measurements of load history and dosage were made on samples stretched to various deformations. The investigators included Mr. Bill Johnson (Chief Engineer of Radiation Services) and Mr. M. James Replogle (of the Process Technology Laboratory). Beamline #1 with a nominal accelerating voltage of 800 keV (approximately 2 keV are lost per cm air) uses a resonant core transformer as its source. Beam currents of 1.2 mAmp and 5.0 mAmp were used. The electron beam is rastered over an area of approximately 30 cm (at 300 Hz) by 7.5 cm (at 2200 Hz) at the mouth of the scan horn. The electron flux has a Gaussian distribution, but is relatively uniform over the above area. The stretching stage was located approximately 2 feet below the scan horn. Since the deformed samples have cross-sections of no more than 8 cm by 0.5 cm, it is assumed that the entire sample received a uniform dose of radiation. Dosage was determined using LDPE films (approximately 0.5 mm thick) by placing them next to the sample during each run and later measuring the trans-vinylene unsaturation concentration via FT-IR (Lyons et al., 1993; Johnson et al., 1995). Liquid crystal temperature strips were taped on the stretching frame to determine the maximum temperature (T_{range} = 100 - 250 °F in increments of 5 °F) reached during the irradiation experiment. Due, in part, to a blower located on the scan horn, the frame never reached 100 °F (37.8 °C).

Table 4-9 lists the samples irradiated and reported in the thesis.

Table 4-9: Irradiated Samples Reported in Thesis

Location	Deformation Direction	Holding Strain (%)	Captured Strain (%)	Dose (kGy)
HVL	Perpendicular	400	180	800
HVL	Parallel	200	40	400
Raychem	Perpendicular	600	120	400
Raychem	Parallel	600	115	338

4.8 TEM

Samples for TEM were prepared by microtoming, staining and carbon coating. The microtoming was performed using a Reichert-Jung Ultracut FC 4E at temperatures -90°C (knife) and -110°C (sample). The nominal settings included: 70 nm section thickness, 1.5 mm/s knife speed. Sections were transferred to 600 mesh copper grids using a concentrated sucrose solution. Staining was performed under OsO_4 vapors for 1-2 hours. The stained sections were finally carbon coated (Ladd Research Industries).

TEM was carried out on a JEOL 200CX (with a tungsten or with a LaB_6 electron source). Standard conditions were the following: 200 keV, condenser aperture #2 (300 μm) spot size (C1) #3, objective aperture #4 (40 μm), magnification 7k-37k. A rotate/tilt holder was used to vary the incident beam direction with respect to the section. The tilt axis was determined by depositing PS latex spheres (0.087 and 0.173 μm in diameter obtained from SPI) on the section via nebulizing (Devilbliss nebulizer model 40; Somerset PA). By following the motion of the spheres as a function of tilt, the tilt axis at that particular magnification can be determined quite accurately.

Micrographs were taken using Kodak Electron Image Film SO-163 and subsequently developed in Kodak D-19 at full strength for 5 minutes. The developed negatives were then rinsed in flowing water (2 minutes) and fixed with Kodak Rapid Fixer for 5 minutes. Enlarged prints of selected negatives were made using Agfa Brovira-Speed BH310RC glossy grade hard (paper #s 2, 3, 4) (obtained from Crimson Tech. Cambridge Ma. (617) 868-5150) at projector magnifications of 2-5x. These prints were subsequently digitized at 150 - 600 dpi (UMAX UC 630 scanner).

Optical transforms (OTs) were performed on an optical diffractometer (Chen, 1994). Circular regions of up to 3.1 cm in diameter on the negative are optically transformed. The diffraction pattern is subsequently magnified (up to approximately 10x) by the projector lenses onto flat film (Polaroid 55 positive/negative 4 x 5 instant sheet film). The OT negative is then developed as per the manufacturer's instructions.

Digital Fourier transforms (FFTs) were carried out using NIH Image version 1.28b6 (ftp site at zippy.nimh.nih.gov). Images were 512 x 512 pixels. By thresholding the image in frequency space, placing windows about desired peaks and subsequently performing an inverse Fourier transform, it is possible to "Fourier filter" the image (Pradere et al., 1990) (and references therein). Good references on optical/digital transforms and image processing include (Misell, 1978), (Gonzalez et al., 1977), (Beeston et al., 1973), and (Jähne, 1993).

4.9 Bibliography

Albalak, R. J. (1994). "The anisotropic thermal expansion of 'single-crystal' triblock copolymer films." Polymer 35(19): 4115-4119.

Albalak, R. J. and E. L. Thomas (1994). "Roll-casting of block copolymers and of block copolymer-homopolymer blends." Journal of Polymer Science Part B: Polymer Physics 32: 341-350.

Alexander (1985). X-ray Diffraction Methods in Polymer Science. Malabar, Robert Krieger.

Annighoefer, F. and W. Gronski (1983). "Block copolymers with highly oriented lamellar morphology." Makromolekulare Chemie Rapid Communications 4: 123-127.

Beeston, B. E. P., R. W. Horne and R. Markham (1973). Electron Diffraction and Optical Diffraction Techniques. Amsterdam, North-Holland.

Bolduan, O. E. A. and R. S. Bear (1950). "Unidirectional nature of the large periodic structure of collagen fibrils." Journal of Polymer Science 5(2): 159-168.

Capel, M. (1993). "X12B - a facility for time-resolved x-ray diffraction for biology and macromolecular systems at the NSLS." Synchrotron Radiation News 6(2): 22-27.

Capel, M. C., G. C. Smith and B. Yu (1995). "One- and two-dimensional x-ray detector systems at NSLS beam line X12B, for time-resolved and static x-ray-diffraction studies." Review of Scientific Instruments 66(2): 2295-2299.

Chen, J. (1994). A short description of the optical diffractometer and the birefringence apparatus, MIT.

Craven, B. M. and G. T. DeTitta (1976). "Cholesteryl myristate: Structures of the crystalline solid and mesophases." Journal of the Chemical Society Perkin Transactions II(7): 814-822.

Gonzalez, R. C. and P. Wintz (1977). Digital Image Processing. Reading, Addison-Wesley.

Herman, D. S. (1986). A compositional study of the morphology of 18-armed poly(styrene-isoprene) star-block copolymers. Masters thesis, University of Massachusetts.

Herman, D. S., D. J. Kinning, E. L. Thomas and L. J. Fetters (1987). "A compositional study of the morphology of 18-armed poly(styrene-isoprene) star block copolymers." Macromolecules 20: 2940-2942.

Huai, Y., J. You, L. Xiangshan, Z. Zhudi and C. Xinfang (1994). "Variation with radiation dose of tensile strength and elongation at break of styrene-butadiene-styrene triblock copolymer." Polymer 35(15): 3345-3347.

Jähne, B. (1993). Digital Image Processing. Berlin, Springer-Verlag.

Johnson, W. C. and B. J. Lyons (1995). "Radiolytic formation and decay of trans-vinylene unsaturation in polyethyene: Fourier transform infra-red measurements." Radiation Physical Chemistry 46(4-6): 829-832.

Lyons, B. J. and W. C. Johnson (1993). Chapter 5: Radiolytic formation and decay of trans-vinylene unsaturation in polyethylene. Irradiation of Polymeric Materials. E. Reichmanis. Washington, ACS. 527: 62-73.

McGinniss, V. D. (1986). Cross-linking with radiation. Encyclopedia of Polymer Science. H. F. Mark, M. Bikales, C. G. Overberger, G. Menges and J. I. Kroshwitz. New York, John Wiley & Sons. 4: 418-449.

Misell, D. L. (1978). Image Analysis, Enhancement and Interpretation. Amsterdam, North-Holland Publishing Company.

Pradere, P. and E. L. Thomas (1990). "Image processing of partially periodic lattice images of polymers: The study of crystal defects." Ultramicroscopy 32: 149-168.

Chapter 5 Perpendicular Deformation

5.1 Introduction

The mechanical anisotropy of a macroscopically oriented cylinder morphology is best observed by comparing the stiffness of the composite in directions both perpendicular and parallel to the cylinder axis. This structural anisotropy has mechanical consequences even in a single deformation experiment. Stretching the composite transverse to the orientation direction establishes a global anisotropic stress distribution in the rubber matrix even at small strains. The stiff glassy cylinders prevent the flexible rubber matrix from flow in the axial direction. The matrix is therefore subjected to a state of plane strain by the uniaxial deformation. Since the bulk modulus of rubber is much larger than the shear modulus, the rubber resists dilation in preference to shear. The compressive stress on the cylinders rapidly increases to a point at which they kink via shear instability. This morphological transformation relieves the plane strain constraint. Further deformation occurs via shearing of the matrix both parallel and perpendicular to the cylinder axis as the cylinders turn toward the stretching direction (SD).

This description of a deformation perpendicular to the cylinders is based on a combination of SAXS and TEM data. The initial quality of orientation strongly influences the onset of kinking and is discussed first. SAXS and TEM experiments with the incident beam both parallel and perpendicular to the cylinder axis establish an oriented and textured initial morphology with some misorientation about the cylinder normals as well as rotationally misoriented grains. The deformation process is then followed via synchrotron SAXS at perpendicular incidence. The kinking transition is detected by a splitting of the 1-D SAXS pattern into an X. TEM on a permanently deformed sample provides an explanation of this X-pattern in terms of a chevron texture. The chevrons are found to have a correlation length of approximately 5 μm and extend indefinitely in the SD. SAXS with the incident beam parallel to the cylinder axis furnishes data on matrix contraction normal to the cylinder axis from which a Poisson ratio can be determined. Corresponding TEM projections show a distorted lattice of cylinders with planar faults separating regions of coherent packing. The fault separation distance (correlation length) is measured to be approximately 0.1 μm. These two orthogonal viewpoints in both real and reciprocal space are combined into a 3-D model of the deformed structure. The mechanics of the deformation process is then discussed in terms of the two stages of deformation, the low strain regime separated from the high strain regime by the kinking transition.

5.1.1 SAXS

5.1.1.1 Perpendicular Incidence

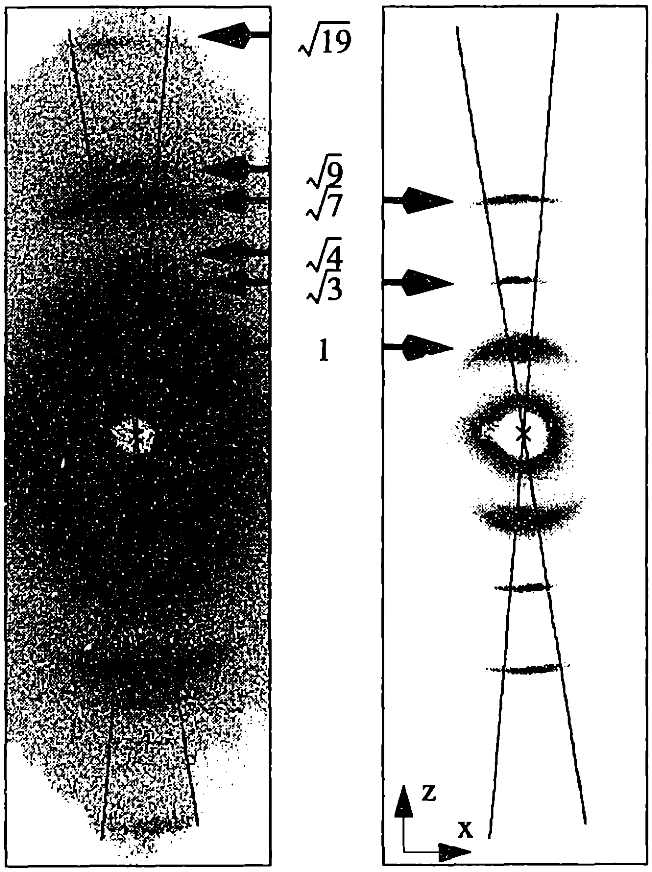

Figure 5-1: 2-D SAXS patterns of an unstretched sample viewed normal to the cylinder axis. Two different intensity thresholds have been chosen. The crossed lines through the origin indicate the range of azimuthal integration used for Figure 5-13.

The initial degree of order in a roll-cast sample is important in order to understand the deformation behavior. Figure 5-1 shows a pair of 2-D SAXS patterns viewed normal to the cylinder axis*. In the left figure the intensities of the weak peaks are emphasized at the expense of saturating the strongest peaks, while in the right figure the strongest peaks are more clearly represented. A series of intensity maxima along the meridian indicates that the cylinders are primarily aligned in the horizontal direction. The degree of alignment of the cylinders is reflected in the intensity distribution as a function of the azimuthal angle μ

(Figure 5-2). If the cylinder alignment were perfectly horizontal (and infinite in extent), the diffraction pattern would show a series of delta functions with no azimuthal width. As can be seen in Figure 5-2, the cylinders do have a finite distribution of their normals about the vertical direction. The azimuthal full width at half maximum intensity (FWHM) ($\Delta\mu$) of the $\sqrt{3}$ peak for this particular sample is approximately 15.3 degrees, though the peaks are slightly asymmetric.

Consideration of the observed peaks provides some information about the quality of orientation normal to the cylinders (lateral registry in the y-z plane). Since all allowed reflections for a sample with $p\frac{6}{m}mm$ symmetry are observed, one can conclude that the 2-D packing of the cylinders is not that of a perfect single crystal. If it were, then the detector plane would intercept only a subset of the total number of allowed peaks. Figure 5-3 demonstrates this more clearly. A perfect single crystal sample would diffract in the manner shown (black dots) at left when the x-ray beam is oriented down the cylinder axis. When the incident x-ray beam is along directions normal to lines AA', BB', or CC', only the subset of the allowed reflections which intersect the Ewald sphere (approximated by the lines AA', BB', or CC') would be observed as indicated in Table 5-1. A fiber-symmetric sample with perfectly parallel cylinders would exhibit a set of diffraction rings when the x-ray beam is incident down the fiber axis. For a uniaxial orientation any x-ray incident normal to the cylinders would result in the Ewald sphere intersecting the rings and intensity would be recorded at all allowed $|q_{hkil}|$ values. As will be seen in next section, roll-cast samples have a degree of lateral registry somewhere between the two extremes of a single crystal and a uniaxial texture.

---

[*] All 2-D SAXS patterns have intensity represented on a log scale by 256 gray levels.

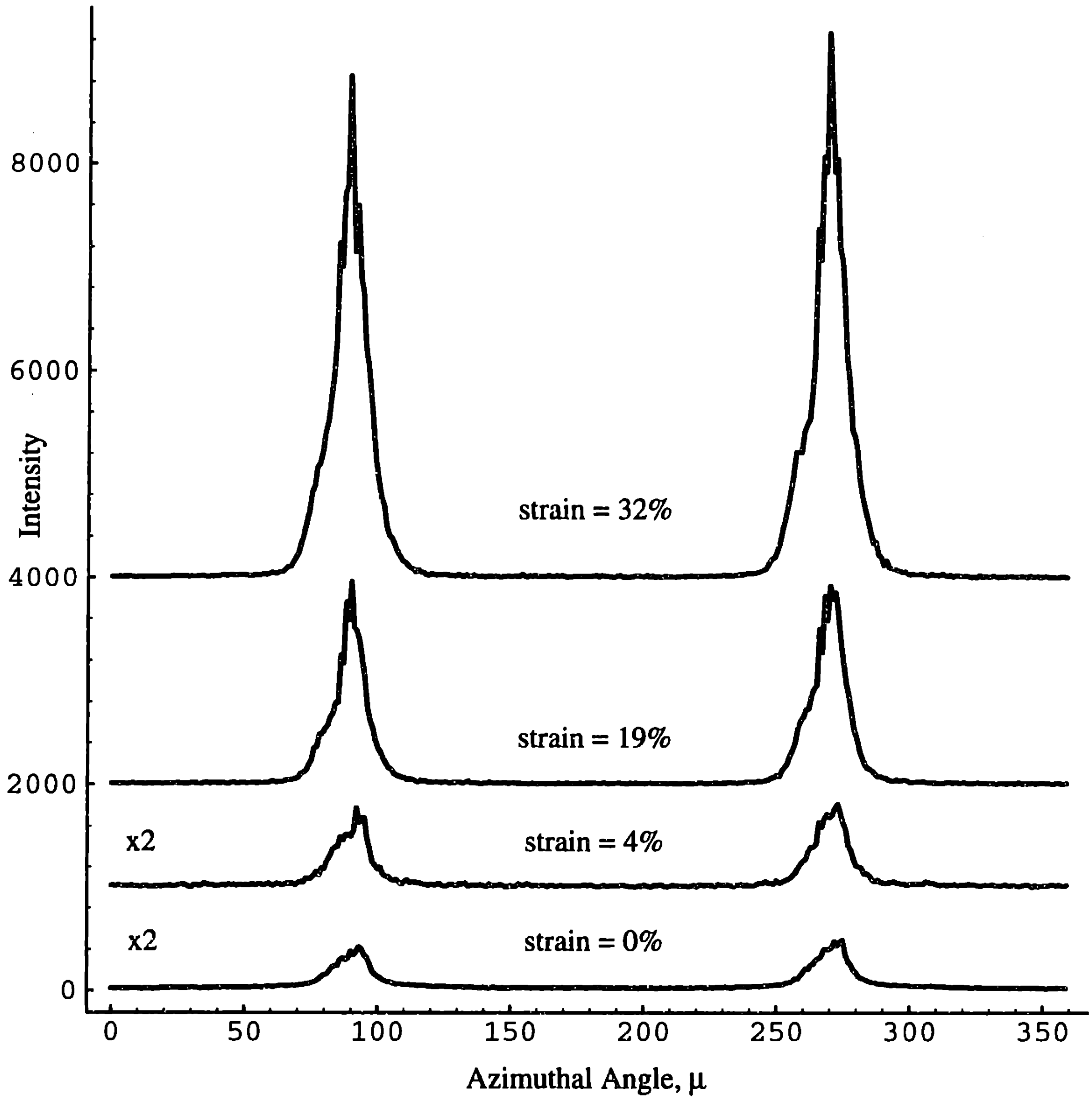

Figure 5-2: Intensity vs. azimuthal angle of the $\sqrt{3}$ peak for the first four patterns in a perpendicular stretch perpendicular view experiment. The average strains during data acquisition are indicated. The average widths of the peaks (FWHM) are 15.3, 14.9, 13.6, and 12.5 degrees. The intensities have been normalized in terms of exposure time and the plots have been offset for clarity. Note the dramatic growth in the $\sqrt{3}$ peak intensity as the deformation proceeds.

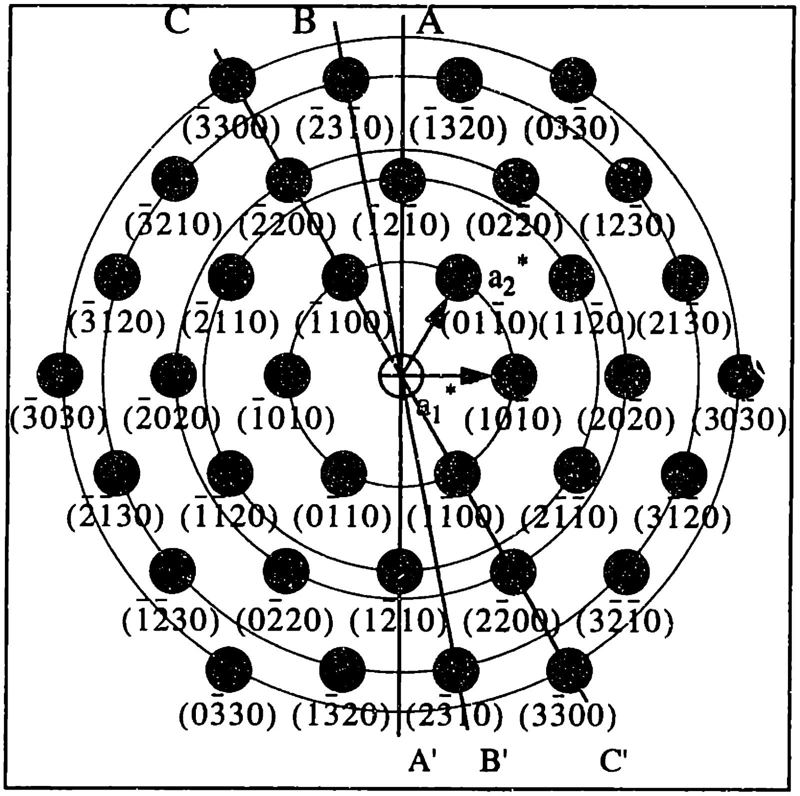

Table 5-1: Observed Reflection Ratios (⊥ View)

Line	Perfect Crystal
AA'	$\sqrt{3}$, $\sqrt{12}$
BB'	$\sqrt{7}$
CC'	1, $\sqrt{4}$, $\sqrt{9}$

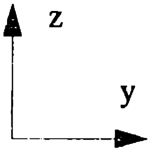

Figure 5-3: Left: The (hkil) section of reciprocal space of a sample with symmetry $p\frac{6}{m}mm$. The black dots refer to the diffracted peak positions of a perfect crystal, while the rings refer to the intensity distribution of a uniaxial (fiber-symmetric) sample. Right: Table listing the expected reflections for indicated trace of the Ewald sphere (lines AA', BB', CC') passing through the origin of the diagram at left. Note that it is possible for a sample with a cylinder morphology to exhibit a reflection for every allowed $|q_{hkil}|$ when x-rays are incident normal to the cylinders, even if the azimuthal misorientation is not complete (see Section 5.1.1.2).

The initial morphological state of roll-cast samples with a cylindrical morphology deduced from an x-ray pattern incident normal to the cylinder axis is one in which the cylinders are highly oriented along the flow direction. There is some degree of lateral misregistry (mosaicity of grains) sufficient to spread intensity from all nearby {hkil} peaks into the Ewald sphere. This will be discussed in the subsequent section.

5.1.1.2 Parallel Incidence

If the incident x-ray beam is in the axial direction of the roll-cast cylinders, direct information about the lateral degree of orientation is revealed (Figure 5-4). As is apparent, there are grains of cylinders with a degree of rotational misorientation about the x-axis.

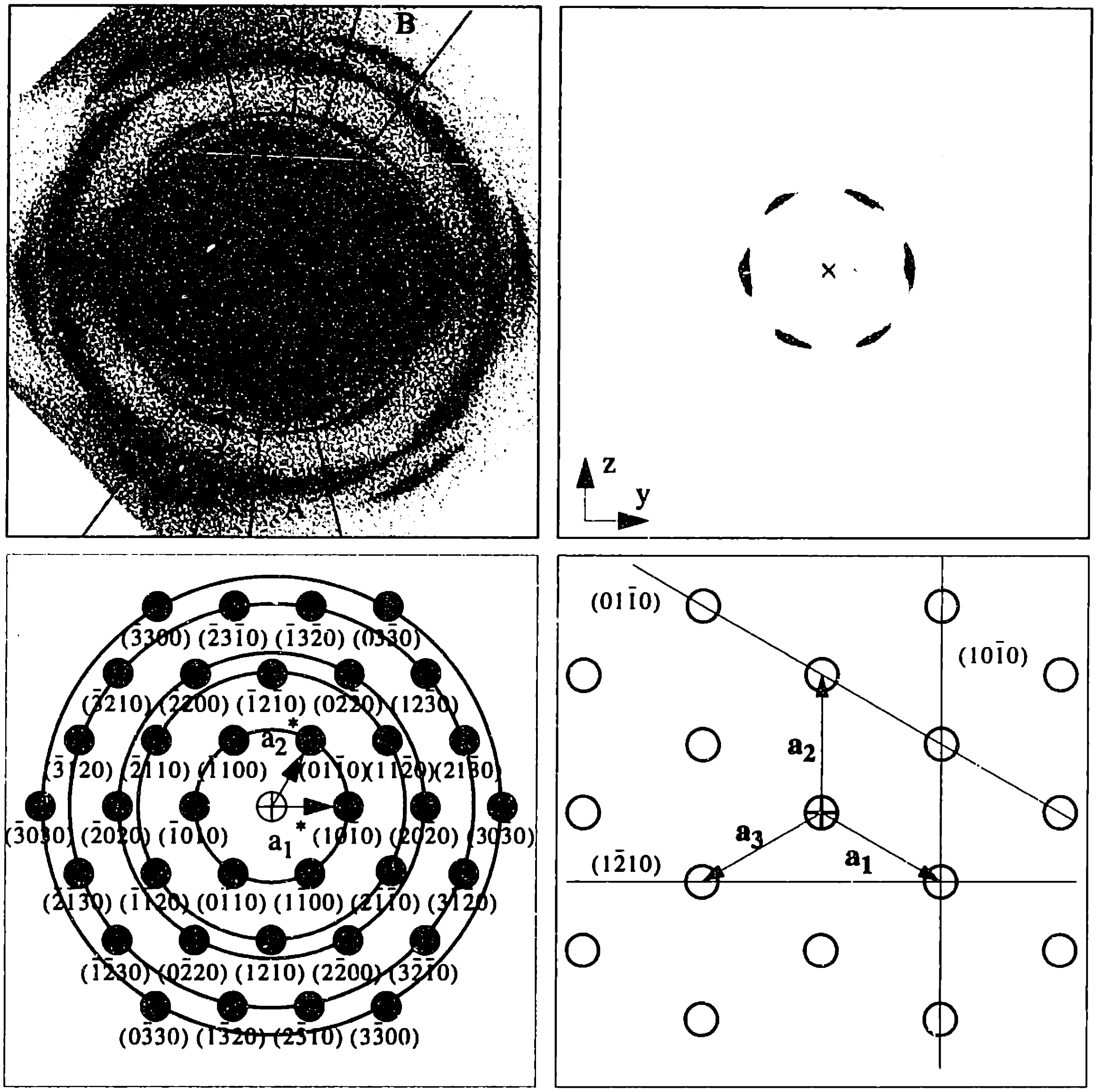

Figure 5-4: Top: Axial view of a roll-cast sample of SIS 15k-72k-15k at two different threshold values. The lines bounding regions A and B represent the limits of the azimuthal integrations for Figure 5-5. The circle of radius q = 0.044 Å^{-1} represents the location of the zero of the form factor. Bottom left: Indexed pattern for the axial view. With increasing radii the rings represent spacing ratios of: $1, \sqrt{3}, \sqrt{4}, \sqrt{7}, \sqrt{9}$. Bottom right: Hexagonally packed cylinders oriented correctly with respect to the observed SAXS patterns. The film edge is parallel to the $\{10\bar{1}0\}$ planes and the SD is vertical.

Most grains are, however, predominately aligned in such a way that the closest-packed planes are parallel to the film edge. As discussed in the previous section, a perfectly oriented sample viewed normal to the cylinder axis would yield a subset of all allowed reflection ratios. Taking a vertical cut through the origin of the pattern in Figure 5-4 explains the observation of all allowed reflection ratios in the scattering curve taken at normal incidence (Figure 5-13 bottom). Depending on the orientation of the hexagonal lattice with respect to the SD (here: vertical), peaks of differing intensities would be observed in a perpendicular view (see Figure 5-5). Since the hexagonal lattice is oriented such that the $(\bar{1}2\bar{1}0)$ plane is vertical, the $\sqrt{3}$ and $\sqrt{7}$ peaks are relatively strong compared to the $\sqrt{1}$ and $\sqrt{4}$ peaks (curve (b) of Figure 5-5). If the lattice were rotated by 30°, the $\sqrt{1}$, $\sqrt{4}$, $\sqrt{9}$ peaks would dominate (curve (c) of Figure 5-5). The bottom curve of Figure 5-13, however, is more consistent with curve (a) than with curves (b) or (c) of Figure 5-5. This is due to a difference in the sampling volume of the x-ray beam with respect to the morphology. The cross-section of the x-ray beam is on the order of 1 x 1 mm^2 at the sample. With a nominal sample thickness of 1 mm, the x-ray beam averages over many more axially misoriented grains when incident normal to the cylinder axis than when incident along the cylinder axis. Since the cylinders generally have a better parallel than lateral correlation, a pattern integrating over a smaller lateral distance (curve (b)) will show a higher degree of lateral orientation. In other words, a perpendicular incidence pattern is not equivalent to a cut through a parallel view pattern unless the number of cylinders traversed is the same.

The degree of lateral misorientation can be further quantified by integrating across a fixed radial width at constant radius as a function of azimuthal angle for the axial view in Figure 5-4. In this way information about the azimuthal peak width for a particular set of diffraction peaks (at constant radius) is obtained. Figure 5-6 shows this information for five such integrations with the zero of the azimuthal angle along the y axis (see Figure 5-4). The smaller the peak width in azimuthal angle, the less is the rotational misorientation within the probed volume. Variations in peak width as a function of radius provide information about type II lattice distortions. Those peaks at the same azimuthal angle represent higher orders of the lowest spatial frequency. In fact, any intensity repeated every 60° (within each

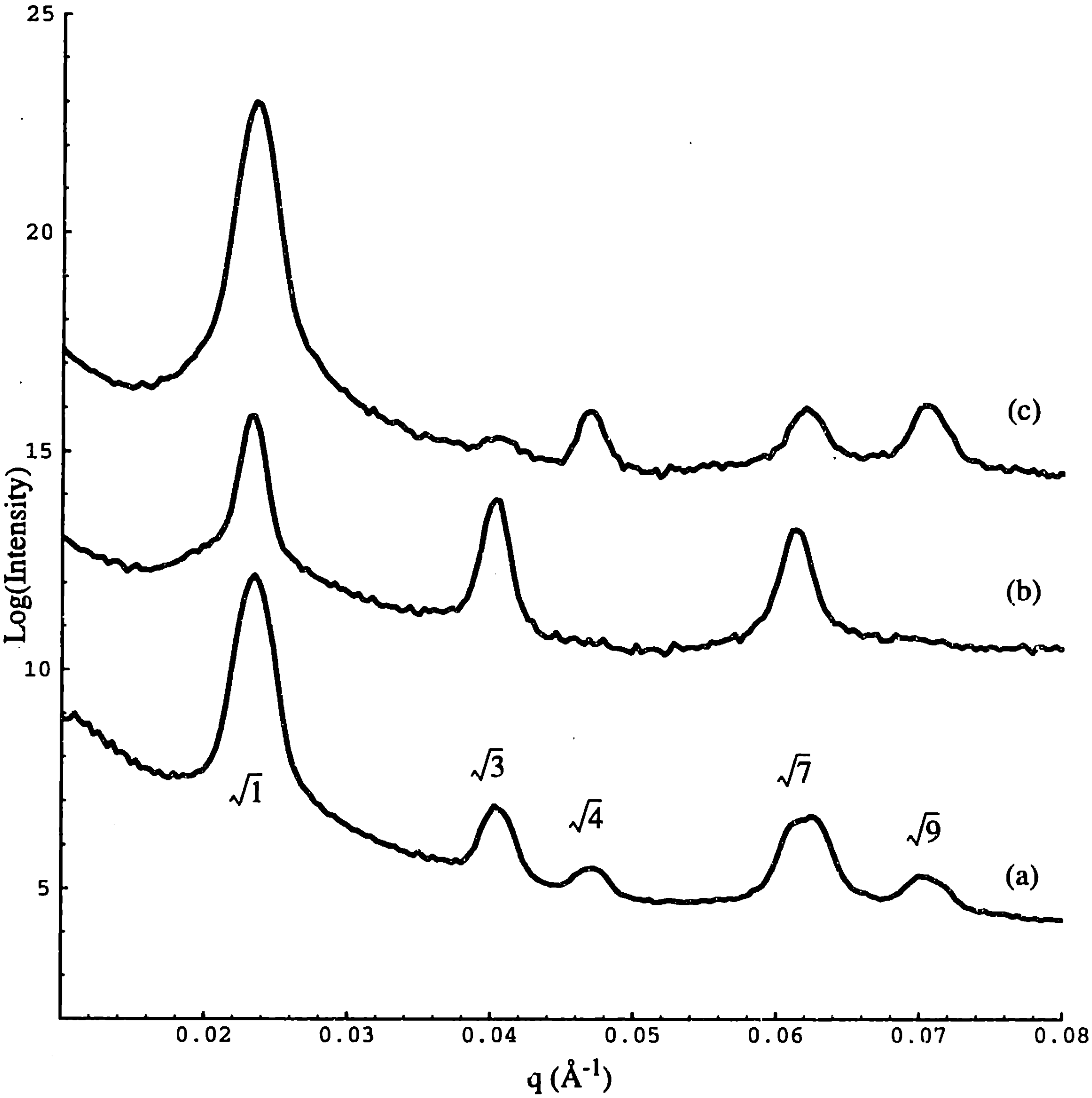

Figure 5-5: Azimuthal integrations of the pattern in Figure 5-4 showing how different "slices" of reciprocal space may give various scattering curves of the same structure. Curve (a) is a full azimuthal integration and exhibits all expected reflection ratios. Curves (b) and (c) are azimuthal integrations of regions A and B of Figure 5-4 respectively. Note that intensities of the observed peaks vary dramatically depending on the orientation and the degree of orientation of the 2-D SAXS pattern in Figure 5-4.

ring) originates from the same lattice. For example, a perfect lattice would produce infinitely narrow peaks for the $\sqrt{1}$, $\sqrt{4}$ and $\sqrt{9}$ diffraction rings and no intensity for the $\sqrt{3}$ and $\sqrt{7}$ diffraction rings at azimuthal angles of 60n (n =0, 1, 2, 3, 4, 5). The $\sqrt{3}$ intensity for this hypothetical lattice is shifted by 30° (i.e., at 60n + 30), while the $\sqrt{7}$

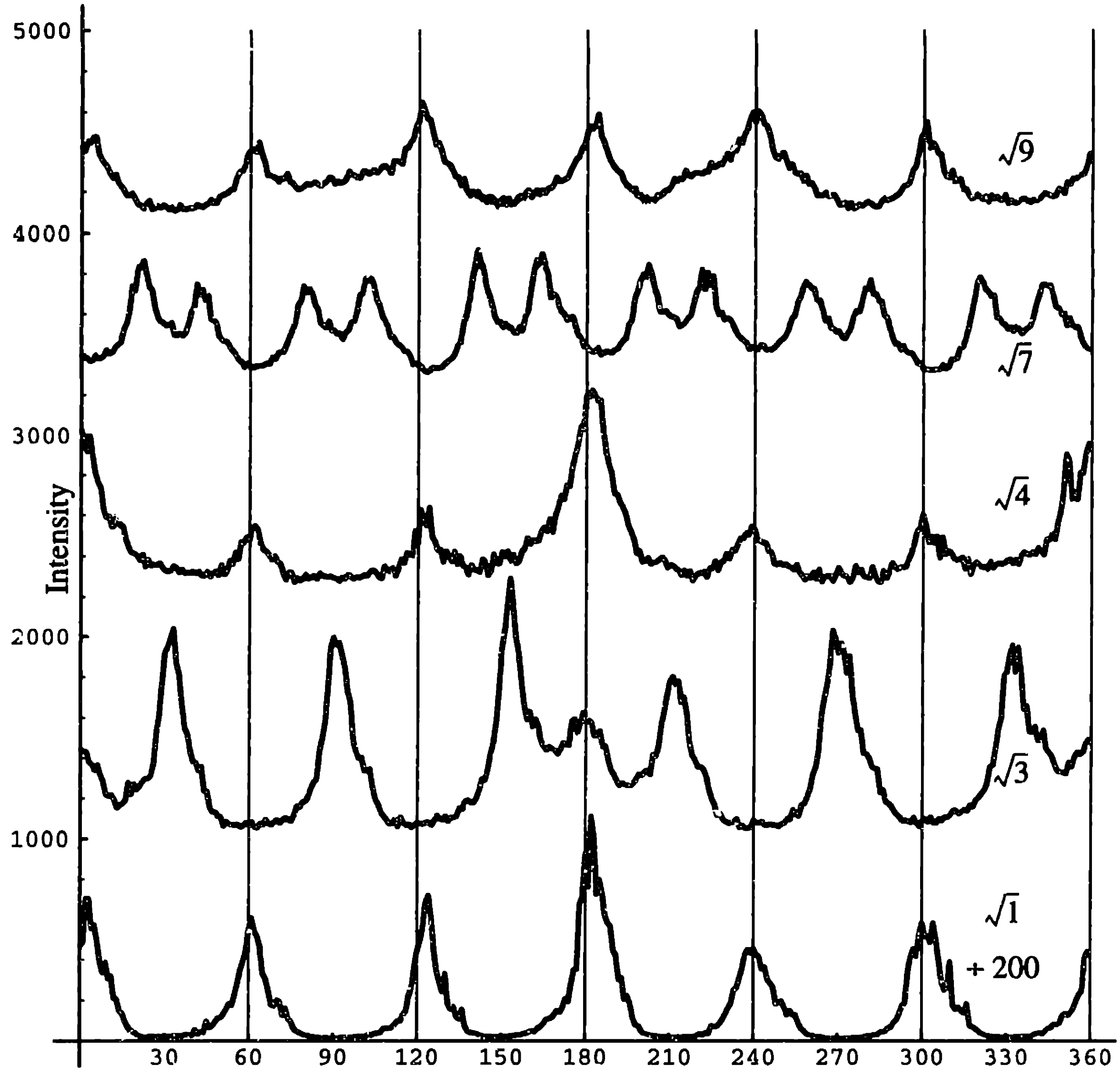

Azimuthal Angle, μ

Figure 5-6: Intensity vs. azimuthal angle for five radial integrations of finite radial width in the axial view of Figure 5-4. The five radii correspond to the five diffraction rings observed. The average width (FWHM) of the peaks within each ring are: 12.5 ± 1.8, 11.2 ± 2.8, 10.3 ± 1.4, 9.7 ± 1.4, 11.6 ± 1.2 degrees for the 1, $\sqrt{3}$, $\sqrt{4}$, $\sqrt{7}$, $\sqrt{9}$ reflection ratios respectively. Note that the equatorial flare introduces spurious intensity at 0 and 180° for the first three rings. The intensity of the $\sqrt{1}$ curve has been divided by 200 while the remaining curves have been offset for clarity. Vertical lines have been included at intervals of 60° as guides to the eye.

intensity splits into twelve peaks located at 60n ± 15. Introduction of a lattice that is rotationally misoriented by an amount ε produces scattered intensity at the above angles plus a shift in azimuthal angle of ε. Since the intensity of the $\sqrt{1}$ peak never falls to zero at any azimuthal angle, it is reasonable to assume that there are grains of cylinders oriented at all angles about the cylinder axis. The dominant orientation is that represented by the peaks in Figure 5-6.

5.1.2 TEM

5.1.2.1 Perpendicular View

A TEM view normal to the cylinder axis is shown in Figure 5-7. Although the cylinder trajectory is primarily parallel, numerous defects are observed. The defects can be characterized as individual defects (e.g., a cylinder terminating as a point defect) and grain

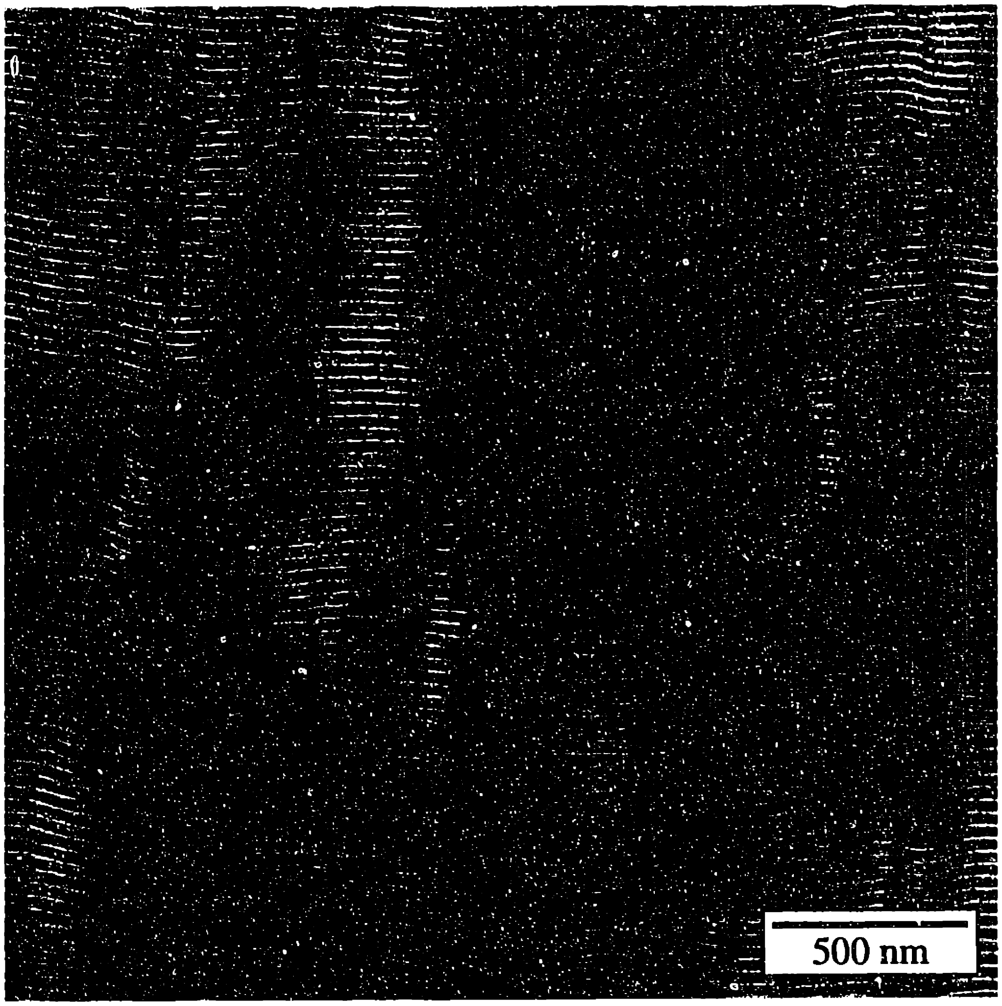

Figure 5-7: TEM of roll-cast SIS 15k-72k-15k at normal incidence. The rubber is stained dark with OsO_4. The PS cylinders are oriented along the flow field (horizontal), but exhibit a variety of defects.

boundary defects (e.g., misalignment whereby bundles of cylinders shift in direction relative to the overall orientation). There are also discontinuities of the PS phase (white) in stripes normal to the cylinder orientation. There are many possible explanations for these breaks. These include lattice rotation, lattice shift, and microtome film buckling, etc. Rotational misorientation about the axial direction would reduce contrast as the incident beam integrates through regions containing both phases (Figure 5-8). As is common in fibrous composite materials, PS cylinder-breaks due to "handling" (including buckling of the microtomed section) may also explain the PS phase discontinuity in the projected TEM image.

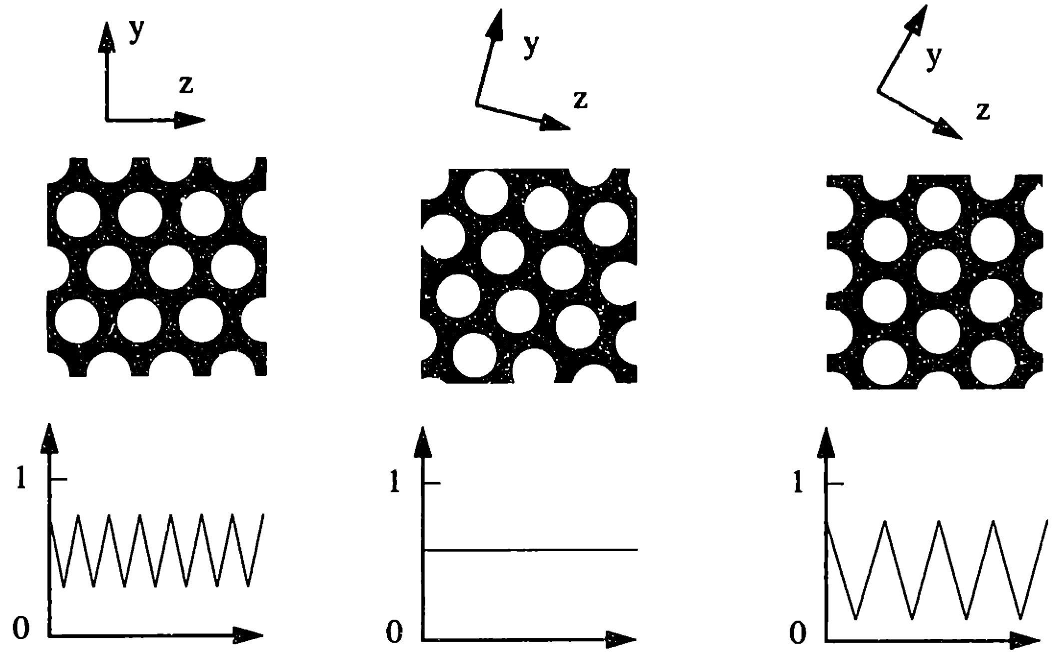

Figure 5-8: Top: Schematic cross-sections of equal thickness with different lattice orientations. The incident e-beam is vertical and perpendicular to the cylinder axis.
Top left: predominant orientation of roll-cast films.
Top center: lattice rotated by 15° cw.
Top right: lattice rotated by 30° cw.
Bottom: Schematic contrast in terms electron beam transmission as a function of sample position. Note that a slight rotation of the lattice influences both the spacing and contrast at perpendicular incidence.

To develop a better understanding of the influence of the misorientation (defects) present in Figure 5-7, digital Fourier filtering was performed (Figure 5-9). The FFT of Figure 5-7 indicates the degree of misorientation in the TEM image. The degree of alignment of the cylinders as observed in the image seems to be representative of the volume that the x-ray beam probes (compare Figure 5-9b to Figure 5-1). The peak spacing ratios indicate a layered structure in the 2-D projected image. There are two sets of peaks originating from the real space image, a strong set of peaks on top of a weak set of peaks. These two sets come from regions that are rotationally misoriented relative to each other. The strong peaks at higher spatial frequencies represent the predominant lattice orientation (Figure 5-8 left) while the weaker peaks at lower spatial frequencies belong to a lattice misoriented by approximately 30° (Figure 5-8 right). Those regions of little or no contrast in Figure 5-9 (e) and (f) give rise to the weak peaks in (b) and come from regions containing the rotationally misoriented lattice.

Figure 5-9: on page 129: Series of digital FFT pairs. (b) is the FFT of the original image (a). Passing the strongest peaks of the FFT in (b) yields (d). Performing an inverse FFT results in the Fourier filtered image in (c). Though the predominant spacings contributing to the original image are enhanced, defect regions are still apparent. Passing the second strongest peaks at higher spatial frequencies (f) adds further detail to the Fourier filtered image (e). The regions of little or no contrast in the Fourier filtered images include regions of rotational misorientation which give rise to the weak peaks at low spatial frequencies in (b).

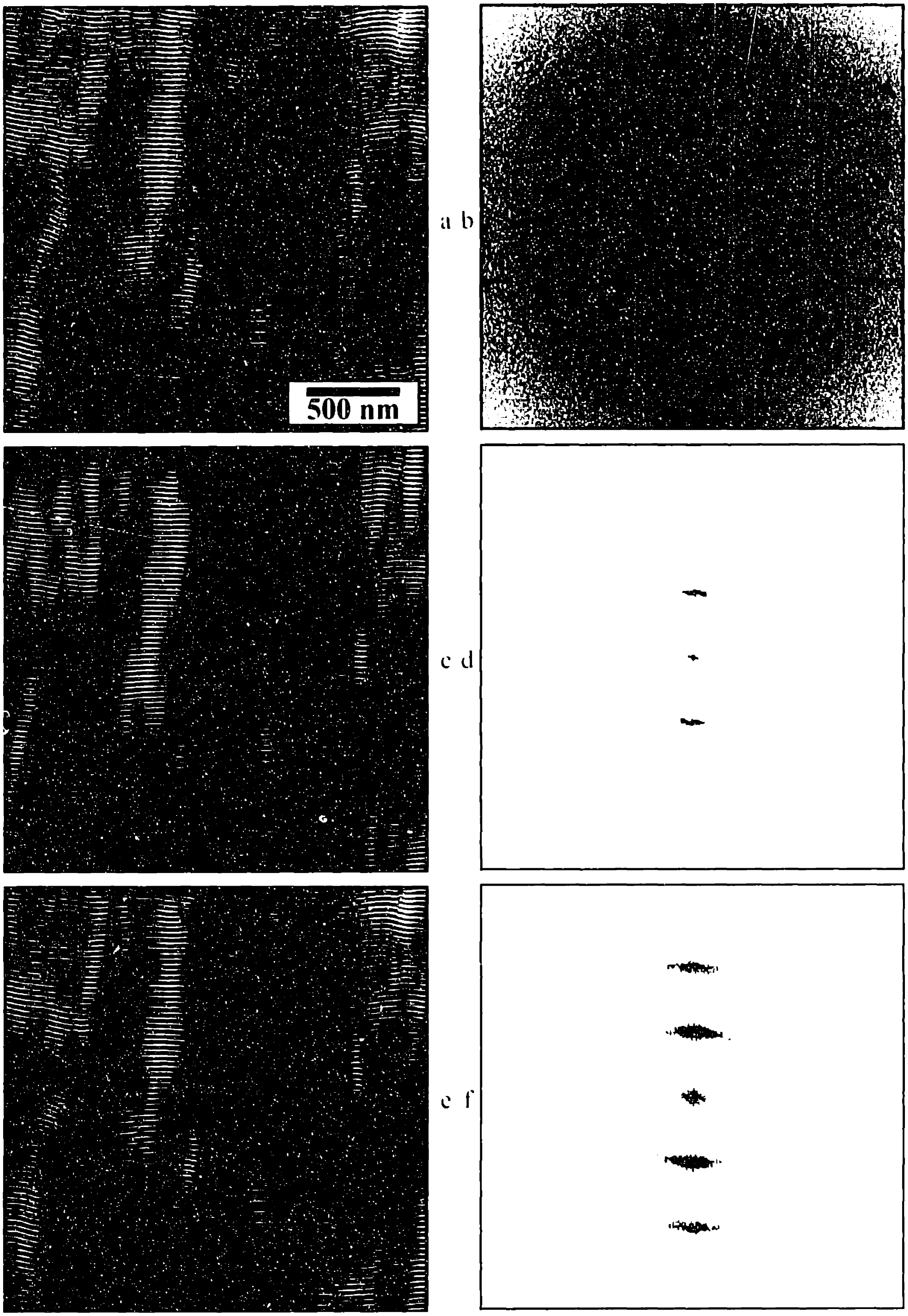

Figure 5-9 caption on page 128.

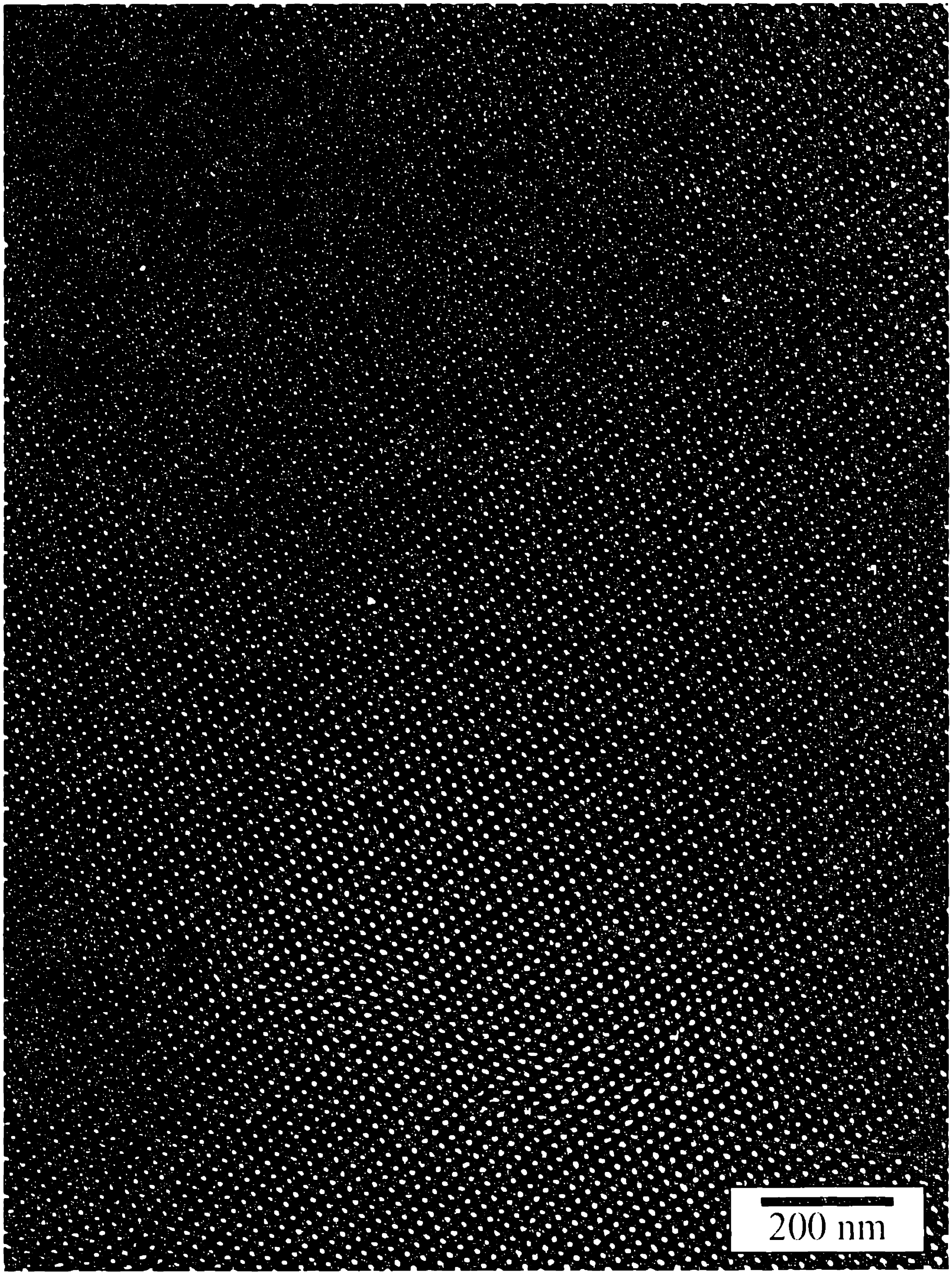

Figure 5-10 Caption on page 137.

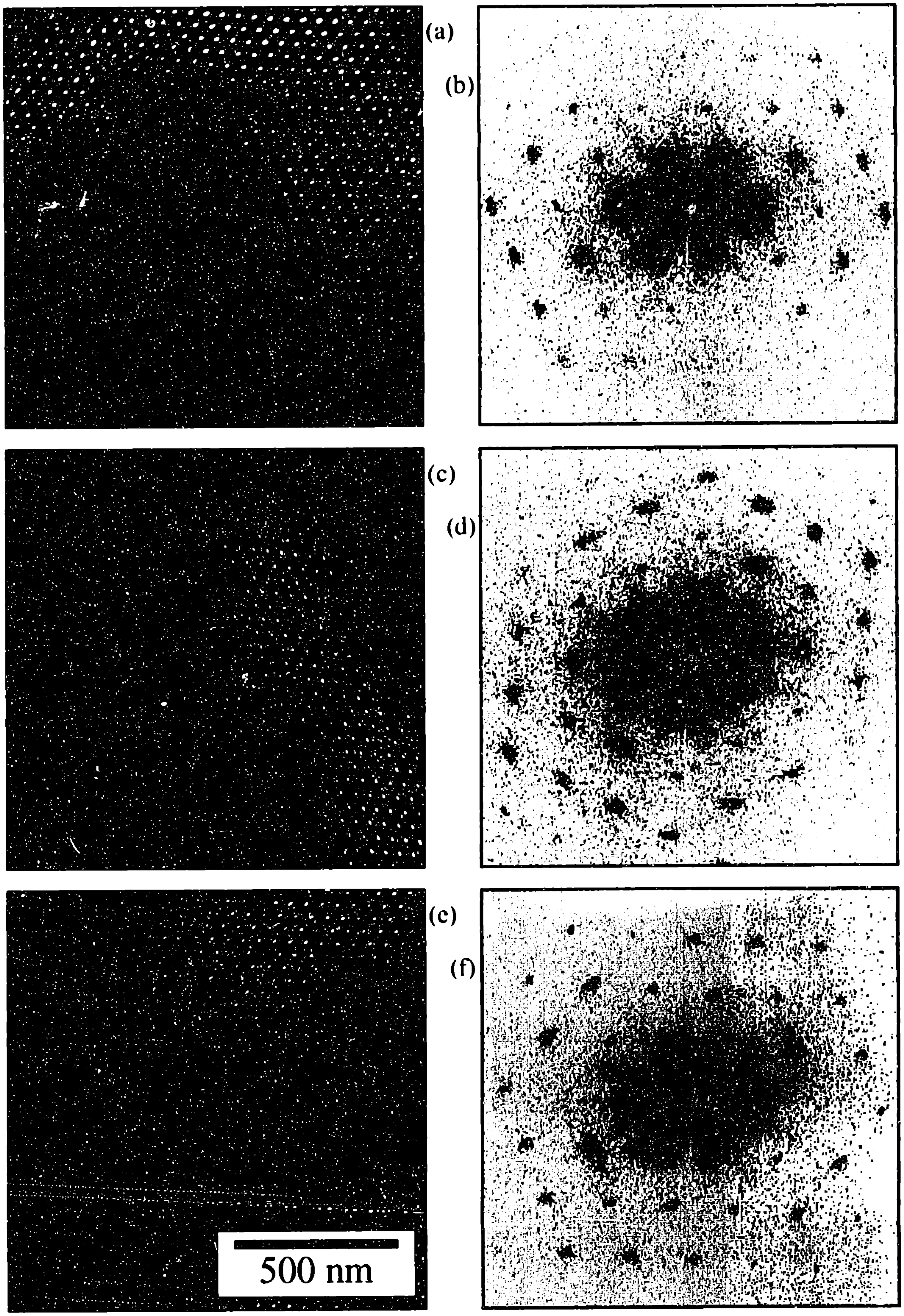

Figure 5-11

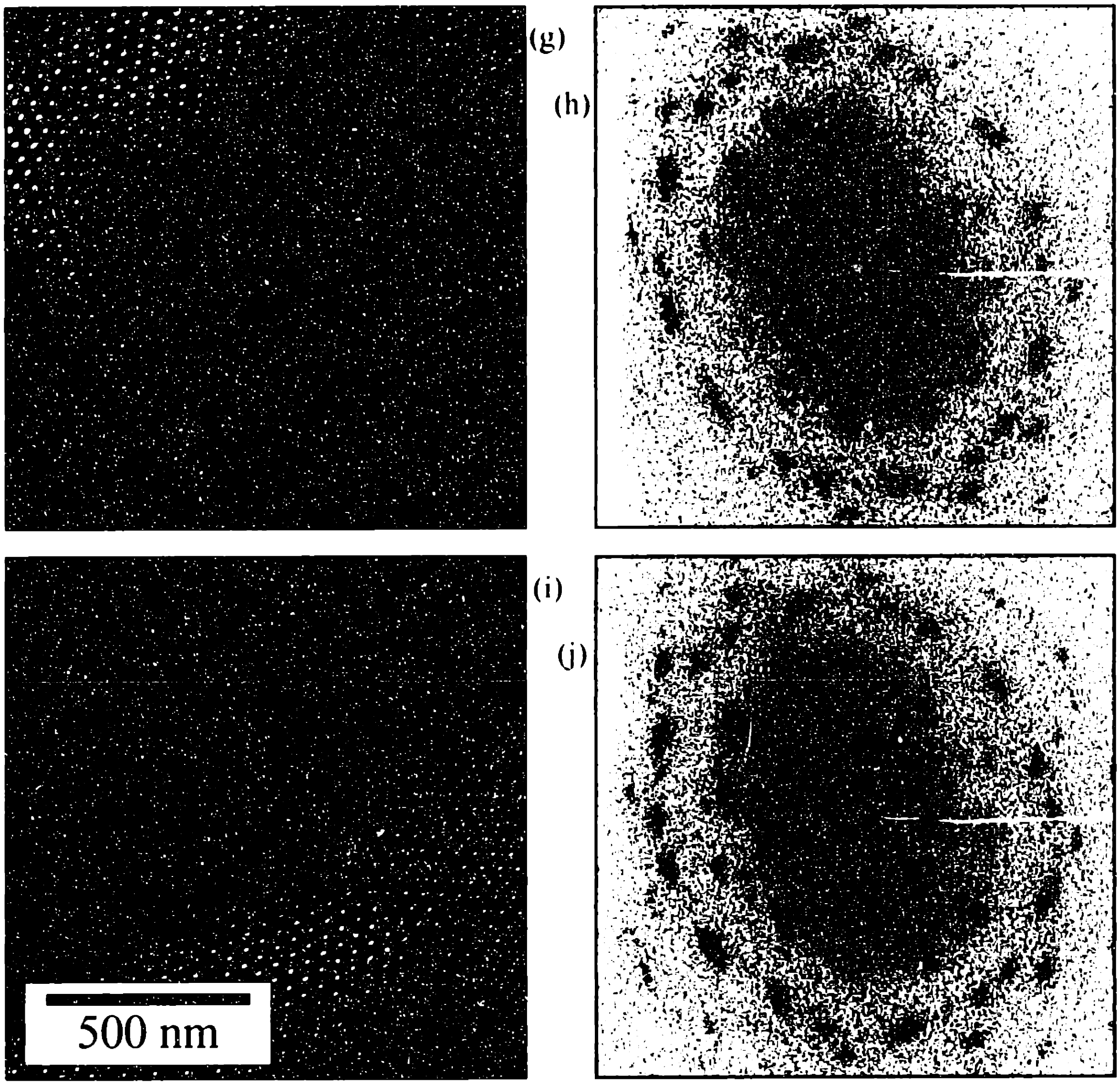

Figure 5-11

5.1.2.2 Parallel View

TEM micrographs taken with the incident beam down the cylinder axis give direct information about the lateral degree of order in the hexagonal lattice. As a local technique, however, TEM is not suited to provide information about the *global* degree of order in the sample. Figure 5-10 implies a nearly perfectly ordered lattice, but it represents only 2 x 1.4 μm of the sample area, which, at a thickness of 0.1 μm represents a volume of approximately 0.3 μm^3. In contrast, a typical SAXS experiment probes a volume of 1 mm^3, which is a factor of 3 x 10^9 larger.

TEM excels at providing information about the different types of defects which together manifest themselves in the SAXS patterns taken of roll-cast films (see Figures 5-1 and 5-4). An example of the rotational misalignment of grains of cylinders about their axes is shown in Figure 5-11. Three adjacent grains have two different orientations. Grain (c) is misoriented with respect to grains (a) and (e) by an angle of approximately 24°. The OTs (b) and (f) indicate that grains (a) and (e) have the same relative orientation. Grain (c) is thus the misoriented grain. Low angle grain boundaries are one type of defect which can be found in roll-cast films. The boundaries between grain B and grains A and C are a good example (see Figure 5-11 g and i). OTs taken at the boundary ((h) and (j)) show how a combination of misoriented grains can spread the intensity of a highly ordered hexagonal diffraction pattern into that observed experimentally (compare Figure 5-11 (h) and (j) with Figure 5-4).

Figure 5-10: on page 131: TEM micrograph with the electron beam incident parallel to the cylinder axis. The field of view is part of a far larger grain showing a high degree of lateral registry. Viewing the figure at low angles reveals dislocation defects.
Figure 5-11: (page 133 and page 135): TEM micrographs at parallel incidence and their corresponding OTs. The grains ((a), (c), and (e)) are directly adjacent to one another. It is likely that grains (a) and (e) are the same as they both have the same orientation. The OTs ((h) and (j)) taken directly at the interface between grains ((g) and (i)) indicate how rotational misorientation contributes to the SAXS pattern in Figure 5-4. The angle between the grains is approximately 25°.

5.2 Perpendicular Stretch Perpendicular Incidence

5.2.1 SAXS

5.2.1.1 Progression of Deformation

Figure 5-12 shows a stress-strain plot of a roll-cast 4211 sample with a cross-sectional area of 3.3 x 1.6 mm^2. The horizontal dashed lines at the top and bottom indicate

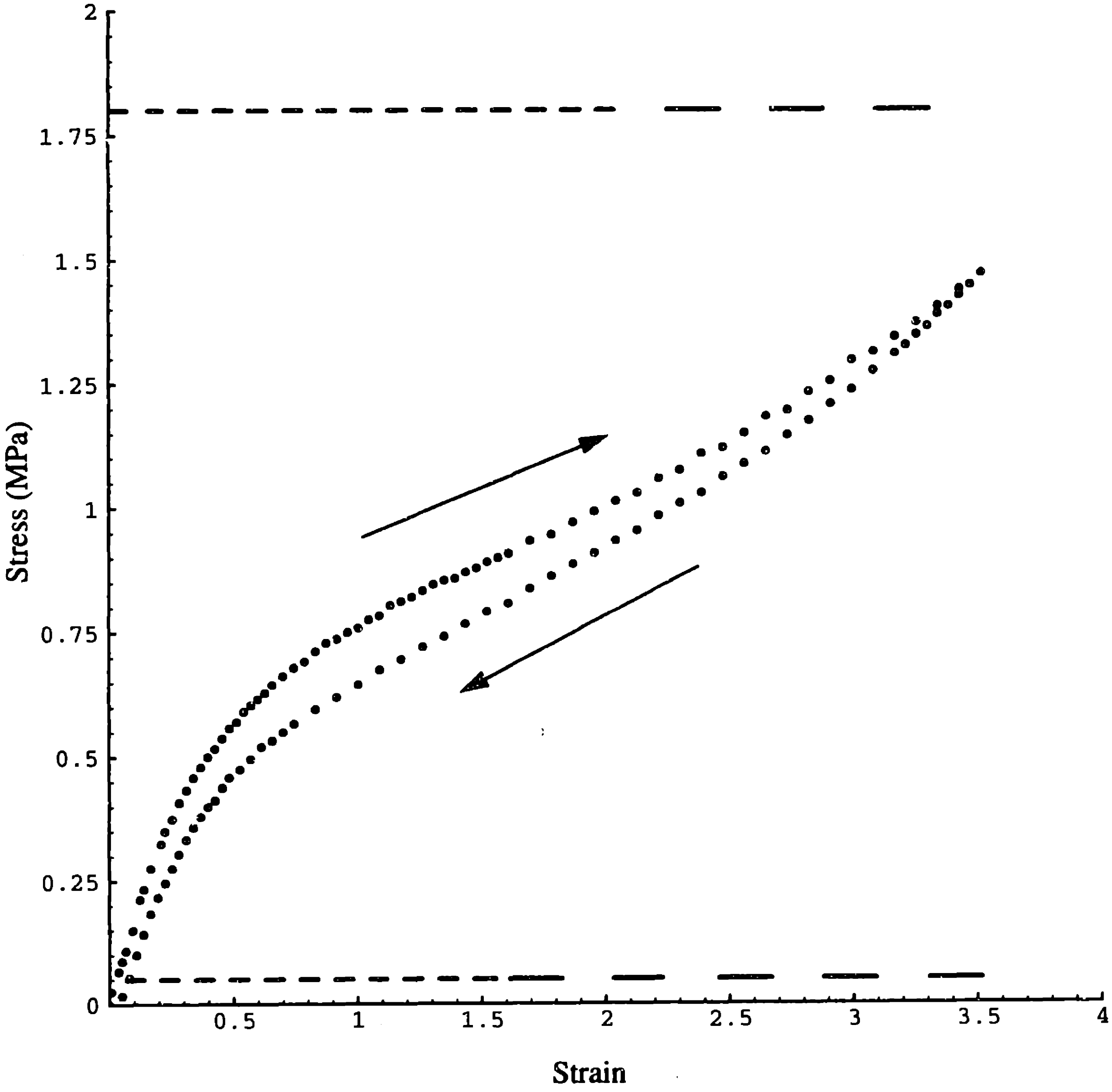

Figure 5-12: Stress-strain plot of a perpendicular stretch perpendicular x-ray incidence (⊥⊥) experiment. The horizontal dashed lines at the top and bottom indicate data acquisition periods for the loading and unloading cycles, respectively. Larger exposure times are required for highly deformed specimens which become thin due to the Poisson effect. The short and long dashes correspond to 10 and 30 s exposures, respectively.

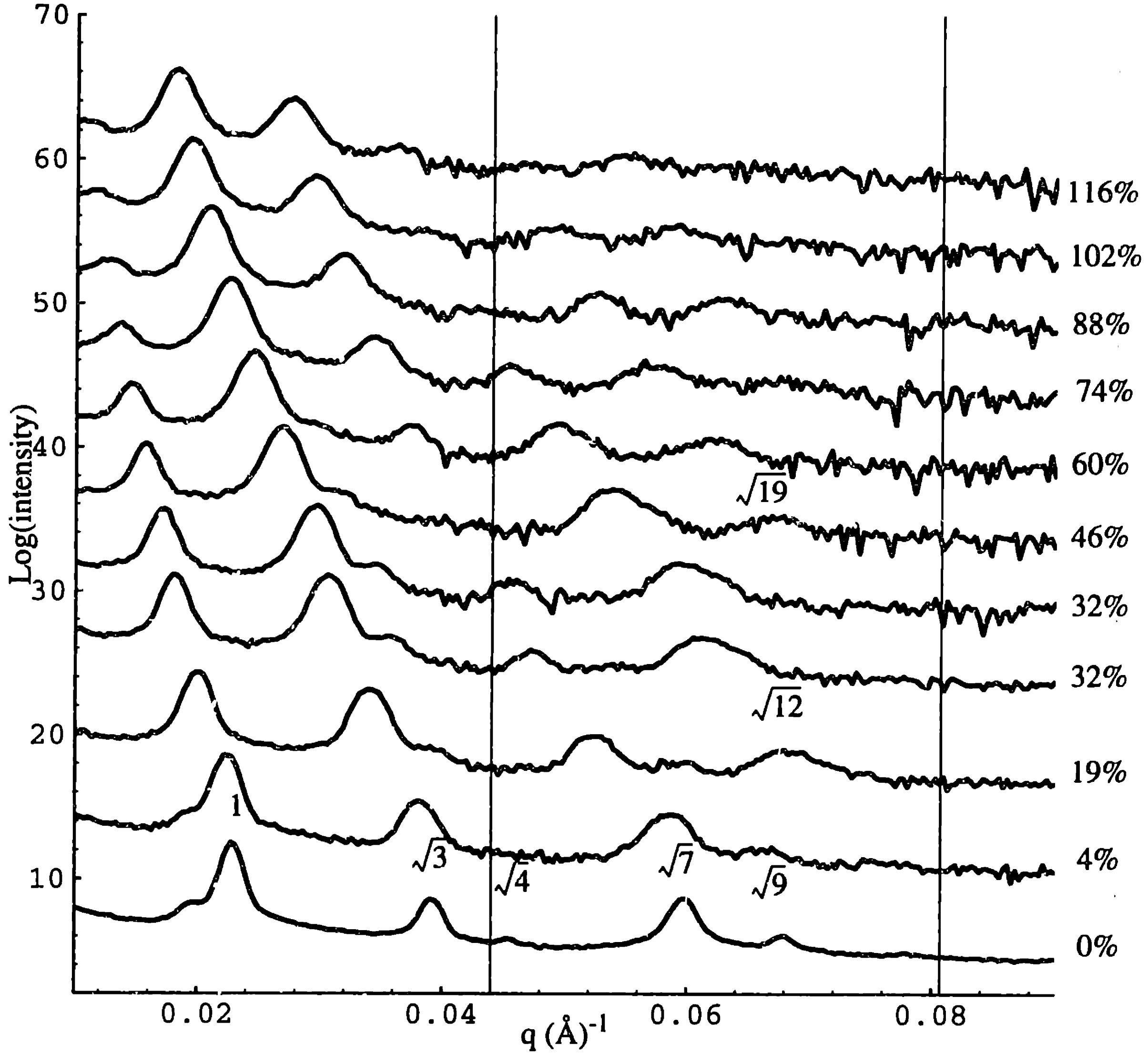

Figure 5-13: Plot of log(intensity) vs. q, integrated over approximately 20° of azimuthal angle and centered about the SD for the first four recorded SAXS patterns in a perpendicular deformation run. Subsequent integrations were performed along the SD in a rectangle 40 pixels wide (see Figures 5-16 and 5-17). The data for strain = 32% are plotted twice to compare the two different integration techniques. The first and second form factor zeros for a cylinder of radius = 87 Å are indicated by the thin vertical lines. The average strains during data acquisition are indicated and the plots have been offset for clarity. The ratios of the peak positions at higher q to the peak position of the first peak are those expected for a sample with a cylindrical morphology for all strain values (see Figure 5-14).

the SAXS sampling frequency on loading and unloading, respectively. The morphology is undergoing a continuous change during the constant strain-rate deformation, so that each recorded SAXS pattern represents an integration over a finite time (equivalent strain increment). This means that each recorded SAXS pattern is made up of an evolving diffraction pattern. All SAXS measurements as a function of deformation will therefore be taken with respect to the average strain during the course of a SAXS pattern acquisition.

Figure 5-13 shows plots of the log(intensity) vs. scattering vector (q). The first four plots from the bottom are determined from azimuthal integrations of 20° width about the meridian (Figures 5-1 and 5-15). The remaining plots result from rectangular integration regions as seen in Figures 5-16 and 5-17. The two plots at a strain of 32% are for comparison purposes of the integration techniques. The rectangular integrations tend to shift the peaks slightly towards the origin as compared to the azimuthal integration technique. The relative peak ratios remain the same nonetheless.

As the sample is stretched normal to the cylinder axis in a perpendicular deformation perpendicular view ($\perp\perp$) experiment, the peaks move towards the origin and the relative intensities change (Figure 5-13). This variation in peak intensity with deformation is due to the movement of peaks away (or towards) the Ewald sphere and movement of peaks into (or out of) the zeros of the form factor. As an example of the latter case, consider the first zero of the cylinder form factor, which falls between the $\sqrt{3}$ and the $\sqrt{7}$ peak in the unstretched sample ($q = 0.044$ Å^{-1}) (Figure 5-13 bottom). This zero nearly cancels the $\sqrt{4}$ peak intensity. As the sample is deformed, the $\sqrt{7}$ peak moves towards the origin and the position of the first form factor zero. At a strain of 46%, the $\sqrt{7}$ peak has disappeared but it reappears at a strain of 60%. The $\sqrt{12}$ peak similarly moves away from the second zero of the form factor and gains intensity (strain = 32%). Thus, it is seen that the peaks are moving through the zeros of the form factor towards the origin. As will be discussed in Section 5.1.1.2, the decrease in intensity of the $\sqrt{1}$ peak is due to movement of the centroids of a pair of $\{1\bar{1}00\}$ peaks away from the Ewald sphere.

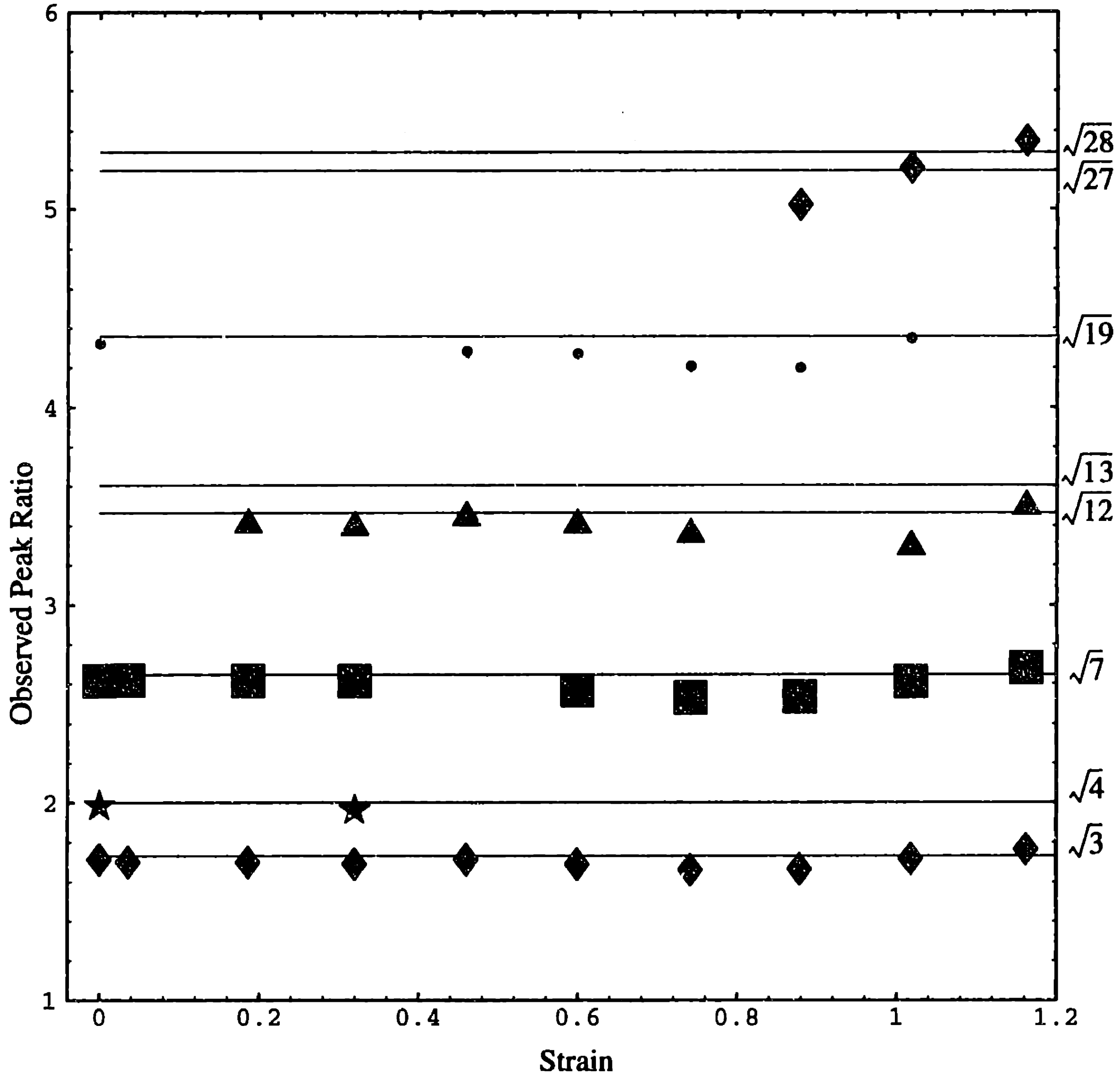

Figure 5-14: Plot of the observed peak ratio vs. deformation for a perpendicular stretch perpendicular view experiment. Gaps are left where peaks could not be clearly identified. These data are taken from the plot of Figure 5-13 and show that the peak ratios remain constant up to a strain of 120%.

If the relative peak intensities are taken as a guide to the position of the zeros of the cylinder form factor, it is possible to estimate the variation of the position of this zero as a function of deformation. A close inspection of Figure 5-13 indicates that the zeros remain fairly constant in position. The position of the second zero cannot be determined with much accuracy due to the weakness of the peaks at high q. The first zero remains approximately at $q = 0.044$ Å^{-1}. As peaks move towards the origin, they disappear as they pass through this zero. The PS cylinder cross-section, which controls the position of the zero, is not affected by the deformation up to this point.

A plot of observed reflection ratios $\frac{q_n(\varepsilon)}{q_1(\varepsilon)}$ as a function of deformation in the SD is shown in Figure 5-14 and it demonstrates that the base reflection ratios observed for the unstretched sample do not change up to a deformation of 120% strain. This indicates that the periodicity in the SD remains coherent during the deformation and only changes in dimension. As all allowed reflection ratios are observed, this coherence as a function of deformation extends to all lattice orientations and indicates an affine deformation, regardless of rotational misorientation about the axial direction up to a deformation of approximately 120%.

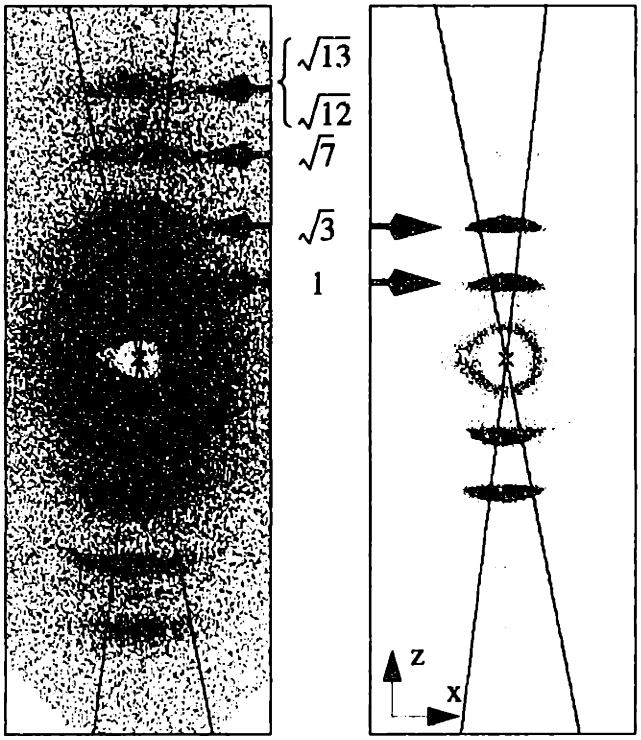

Figure 5-15: 2-D SAXS pattern for a ⊥⊥ deformation experiment at 19% deformation. The dashed lines indicate the angular range over which the azimuthal integration for Figure 5-13 was taken.

Figure 5-15 is a snapshot of the deformation process in the perpendicular view at an average strain of 19% and should be compared against Figure 5-1. As indicated by Figure 5-13 the peaks have moved towards the origin and the relative intensities have changed in response to the deformation. The higher order peaks have faded, while the $\sqrt{3}$ peak has grown to nearly the intensity of the $\sqrt{1}$ peak. At 60% deformation the $\sqrt{3}$ peak becomes the predominating feature (Figure 5-16). At 100% it is clear that the broadening of the peaks does not follow an arc of constant q centered at the origin, but rather follows a flatter profile (Figure 5-18). At a strain of 144% the two centroids of intensity of the $\sqrt{3}$ peak have split asymmetrically into two pairs of peaks connected by a "saddle" of lower intensity (Figure 5-17). The intensity of the $\sqrt{1}$ peak has faded quite dramatically, while the $\sqrt{7}$ peak has gained in intensity. With increasing deformation each pair of peaks moves

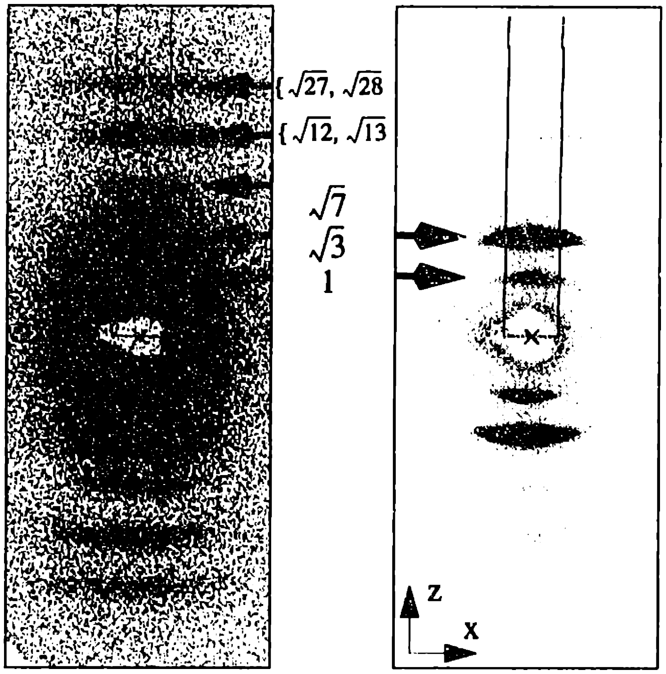

Figure 5-16: 2-D SAXS pattern for a $\perp\perp$ deformation experiment at 60% deformation. The dashed lines indicate the rectangular region of integration for Figure 5-13.

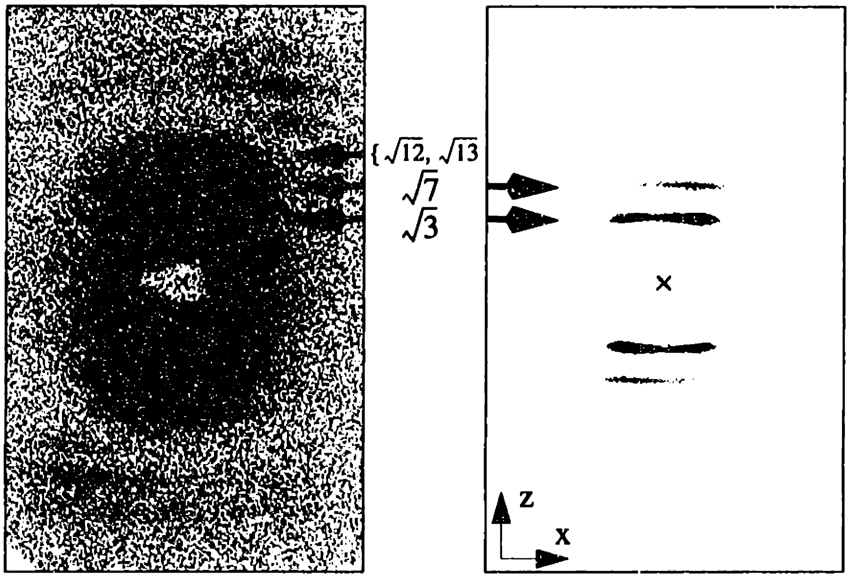

Figure 5-17: 2-D SAXS pattern for a $\perp\perp$ deformation experiment at 144% deformation. Note the formation of an asymmetric split in the intensity of the $\sqrt{3}$ peak.

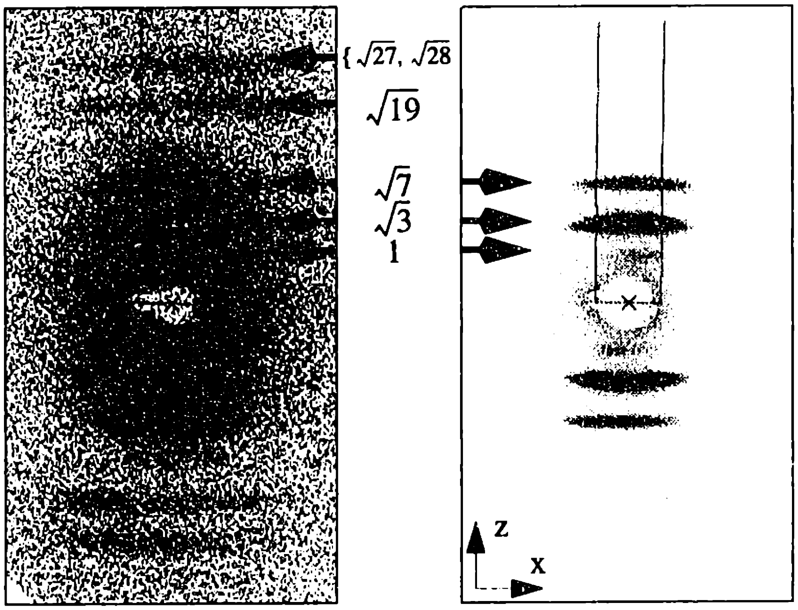

Figure 5-18: 2-D SAXS pattern for a ⊥⊥ deformation experiment at 102% deformation.

away from each other. This is shown for 236% and 320% in Figures 5-19 and 5-20, respectively. The $\sqrt{7}$ set of peaks continue to gain in intensity compared to the $\sqrt{3}$ set of peaks.

Upon formation of the X-pattern, it is possible to observe the zero of the form factor as an absence of intensity between the strong inner layer lines and a diffuse set of peaks at the tips of the arms of the X (see Figures 5-19 and 5-20). The zero of the form factor is always found perpendicular to the cylinder axis (see section 3.2). At large deformations (> 120%), the normals to the cylinder axes are predominantly oriented along the arms of the X. There is, however, a small fraction of the cylinder population giving rise to scattered intensity in the SD. The zero of the form factor is thus distributed along a circular arc extending from one arm of the X to the other across the SD. Since there are no cylinder normals in the x- and z-directions, the absence of intensity at high q in these directions cannot be attributed to the form factor zero.

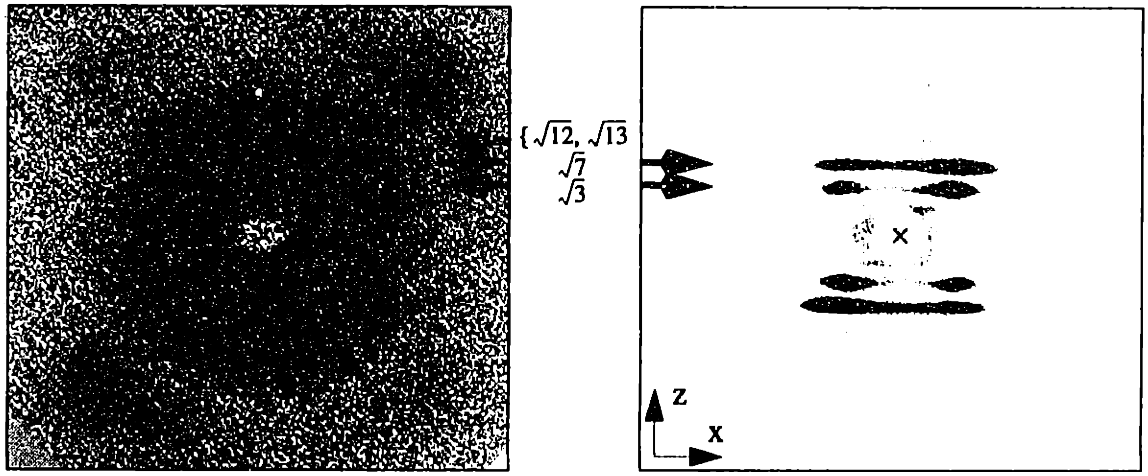

Figure 5-19: 2-D SAXS pattern for a ⊥⊥ deformation experiment at 236% deformation. Note the first zero of the form factor (depicted by the circle) between the inner dark peaks and the diffuse weak intensity at the corners.

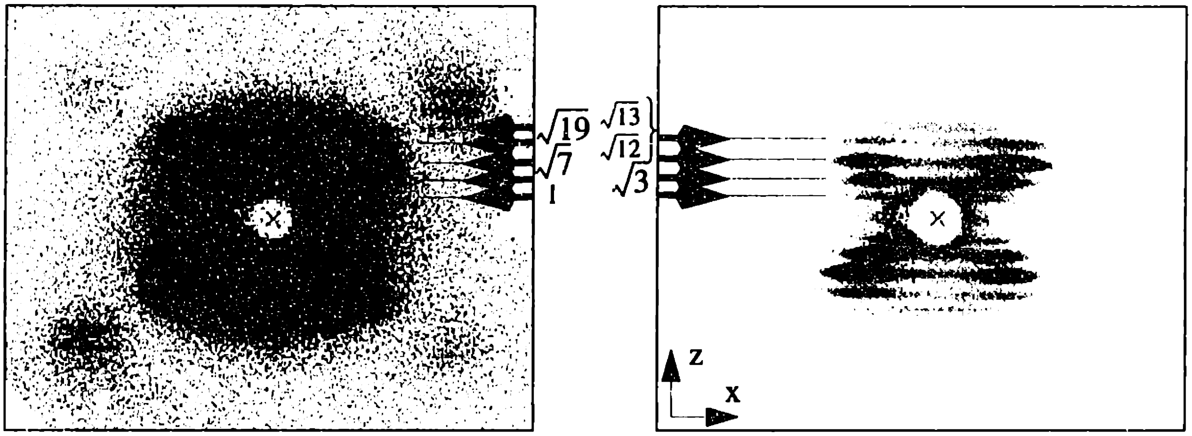

Figure 5-20: 2-D SAXS pattern for a ⊥⊥ deformation experiment at 320% deformation. Note that the arms of the X do not intersect the origin.

Upon unloading, the qualitative development of these patterns reverses itself. However, the split between pairs of peaks is still resolved at much lower deformations than during the first loading cycle. The exact point at which the broad streaks localize into pairs of distinct peaks upon loading is difficult to establish, but is in the vicinity of 130% strain. Figure 5-21 provides a closer look at this transition by plotting the intensity of the $\sqrt{3}$ peak as a function of q_x.

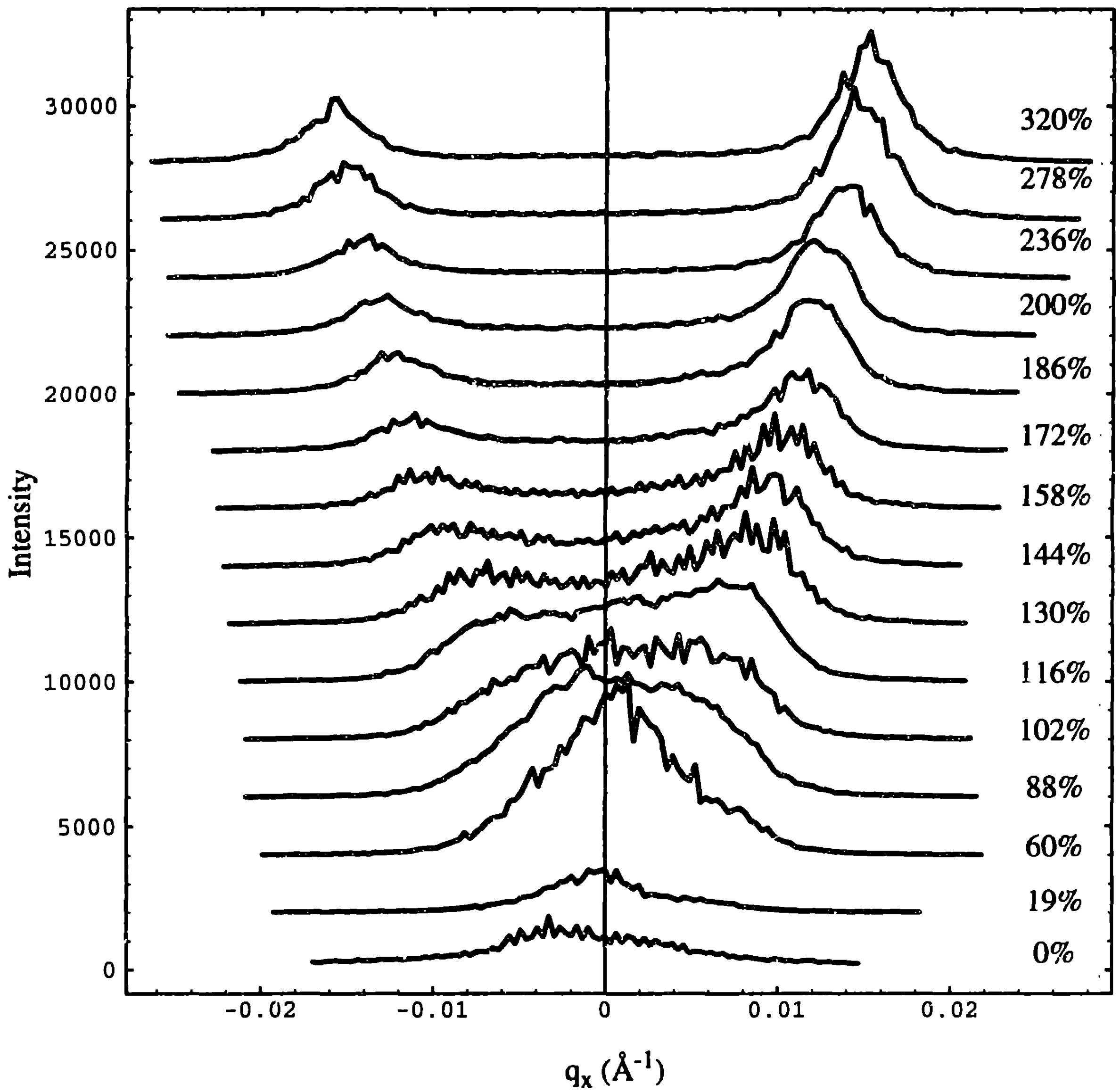

Figure 5-21: Intensity vs. q for the $\sqrt{3}$ peak obtained by placing a rectangle around the peak and integrating in the SD. The split is resolved at a strain of 130%, but begins to form earlier.

5.2.1.2 Trace of Deformation

The 2-D SAXS patterns describing the progression of deformation in the perpendicular incidence geometry can be quantified by considering the peak positions as a function of the deformation. Though the position of the centroid of a peak may not always be the same as the position of the peak maximum, in the following it is the position of the peak maximum that is reported (see section 4.6.1). Figure 5-22 shows the trace of the

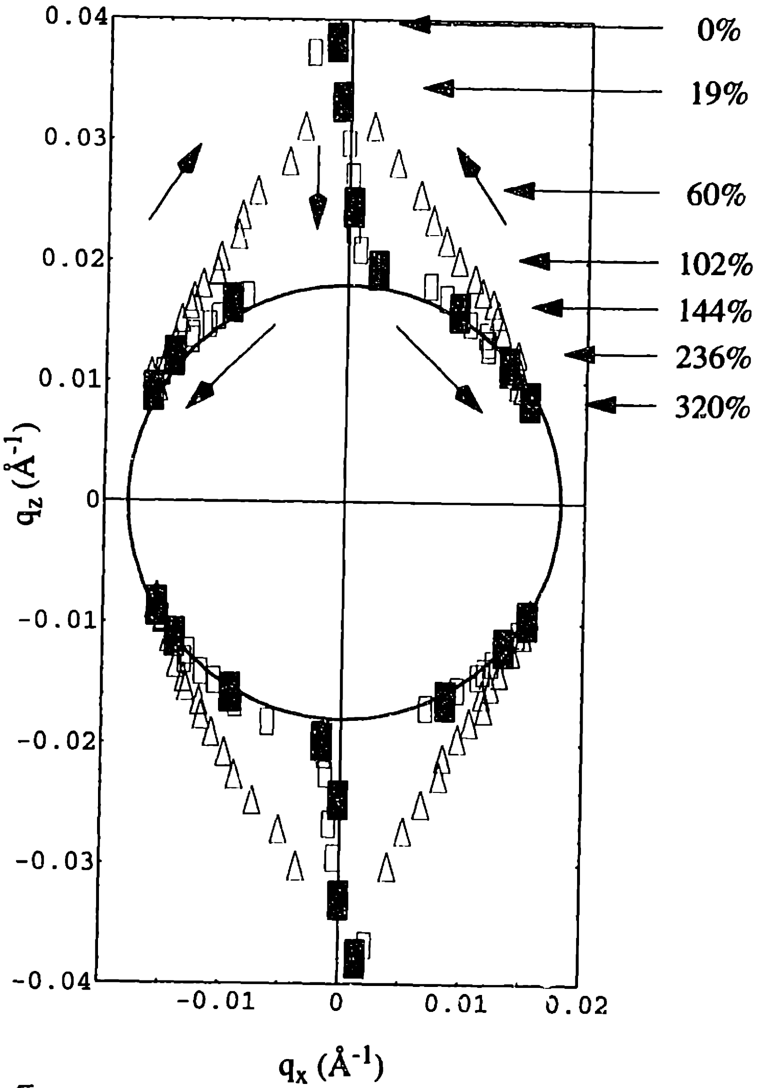

Figure 5-22: Trace of $\sqrt{3}$ peak position during a loading/unloading cycle in a perpendicular stretch perpendicular x-ray beam incidence experiment. The arrows indicate the direction of peak movement during the deformation. A circle of radius 0.018 Å^{-1} has been placed about the origin. The filled points represent data from the patterns shown in

position of the $\sqrt{3}$ peak for the deformation run described previously. The direction of the deformation is indicated by arrows. The $\sqrt{3}$ peaks move towards the origin during the loading cycle and as shown in Figure 5-17, split apart to form an x-pattern. Upon unloading, the peaks follow a different, more direct path back towards the initial point of the deformation. The figure shows a slight asymmetry about the stretching direction which is also reflected in the 2-D SAXS patterns (Figures 5-18 and 5-19). It has been found to be difficult to align the morphology with the stretching direction to give a perfectly symmetric x-pattern during a perpendicular stretch.

5.2.1.3 X-angle vs. Deformation

After the peaks split into an x-pattern, the arms of the "X" rotate away from each other with increasing deformation. Figure 5-23 tracks the angle between the arms of the "X" as a function of deformation. The X is first resolved at approximately 130% strain at an angle of 50° and continues to increase as far as the sample is stretched. At the highest deformations, the rate of increase levels off and becomes asymptotic. Upon unloading the X is observed down to an angle of 10° and a strain of 25%. The hysteresis of the X-arm

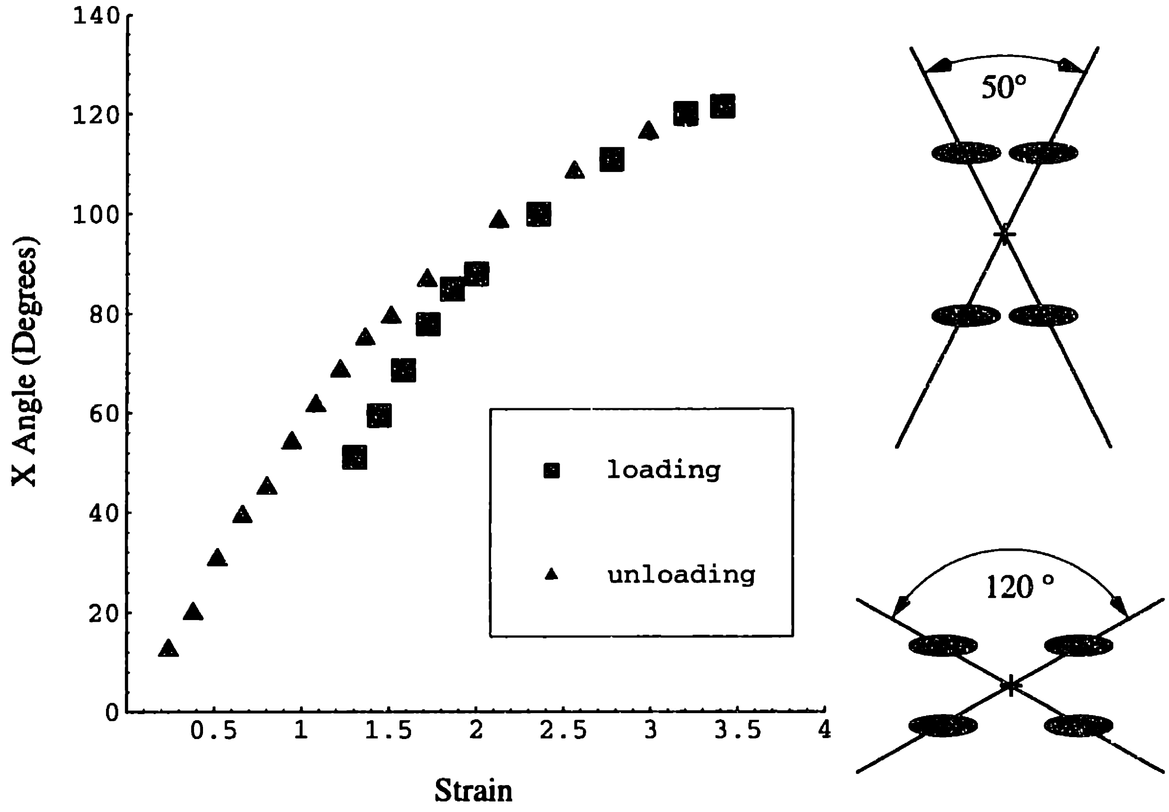

Figure 5-23: Left: Plot of the angle between the $\sqrt{3}$ peaks in an "X" pattern as a function of deformation. Right: Schematic diagrams of the extremes of the positions of the $\sqrt{3}$ peak.

motion during a loading/unloading cycle becomes most pronounced at the lowest deformations during unloading. The unloading portion of the X-angle curve is linear and extends back to the origin in contrast to the loading portion which begins only after a strain of approximately 130%.

5.2.1.4 $D_{(\bar{1}2\bar{1}0)}$-spacing vs. Deformation

A plot of the d-spacing of the $\sqrt{3}$ peak as a function of deformation (see Figure 5-24) clearly indicates that there are two distinct regions to the deformation process in the perpendicular direction. Initially the $\sqrt{3}$ peak moves in towards the origin in a linear fashion. Measured in terms of strain ($\frac{\Delta l}{l_o}$), the slope of the line is 0.94. An affine deformation would result in an equality between micro-strain (measured via SAXS) and macro-strain (sample displacement). The initial deformation is therefore nearly affine. After formation of the X pattern, there is a small increase in $\sqrt{3}$ peak spacing of approximately 0.03 as measured by a linear fit. This increase in intercylinder-spacing after the X-pattern formation is qualitatively observed in Figure 5-22 as a deviation of the position of the peak maxima from the trace of a circle centered around the origin. A deformation at constant intercylinder-spacing would be seen as a movement of the peak maxima at a constant distance from the origin (in this case represented by the circle in Figure 5-22). The cross-over from the initial linear increase in peak spacing with strain behavior to the (nearly) constant spacing deformation behavior occurs at the intersection of the two fits at 115% strain. This may give a better indication of the critical strain at which the X pattern forms. Hysteresis is again observed upon unloading. However the unloading curve rejoins the linear loading curve during the final 75% unloading strain.

5.2.1.5 Strain in Transmission

The sample transmission is a measure of the thickness of the sample (Section 4.6.3) and can be reduced in terms of true strain (Equation (4.9)). Figure 5-25 plots the thickness strain (along the y-direction) vs. the macroscopic strain (along the z-direction) using the

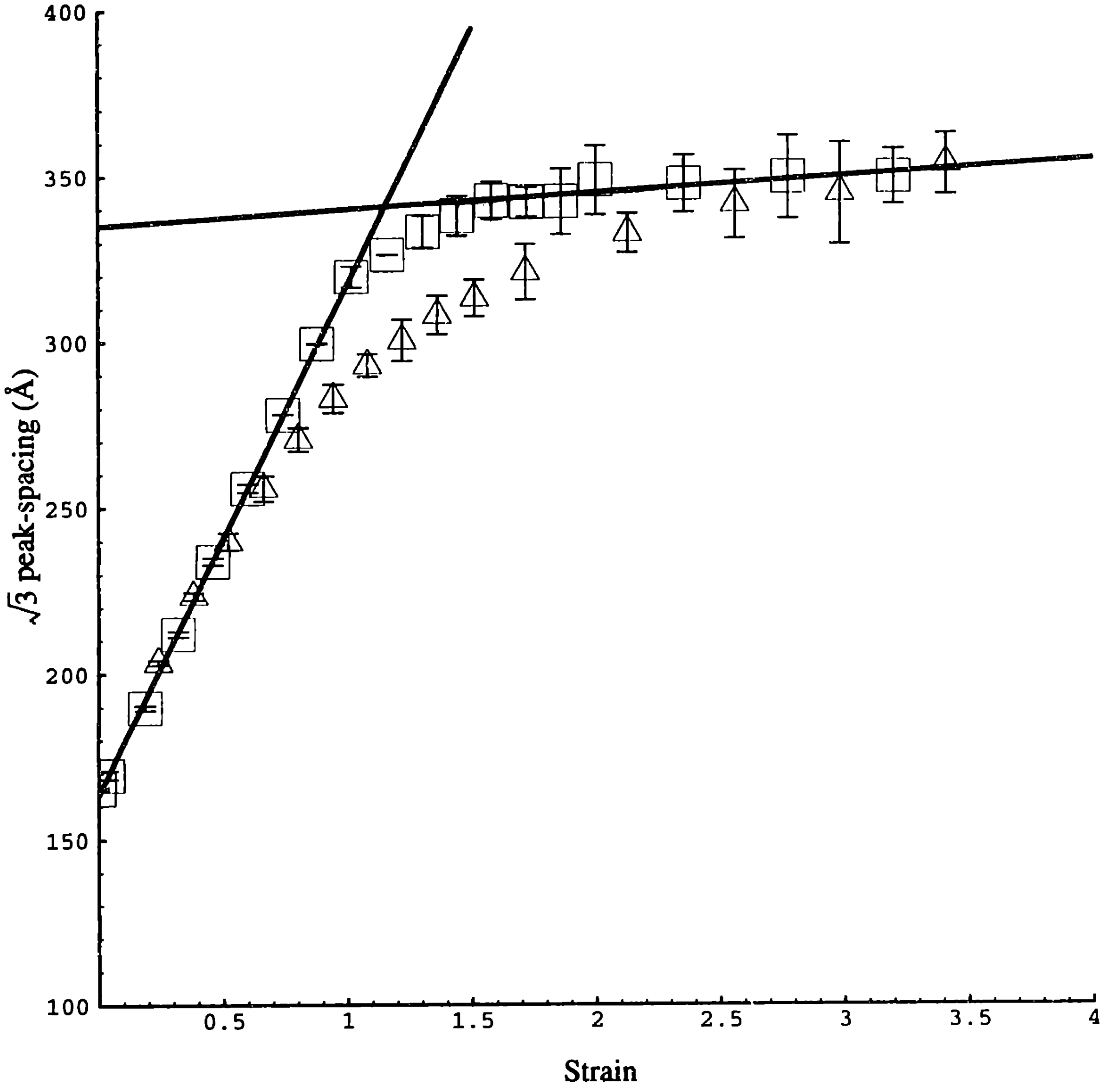

Figure 5-24: Plot of d-spacing vs. deformation for the $\sqrt{3}$ peak. There are two regimes of deformation. The initial linear region indicates a nearly affine deformation, while at higher deformations (> 1.5) the spacing increases very slowly with deformation. The solid lines indicate best fits over the respective regions. The intersection of the lines occurs at a strain of 1.15. The error bars in the linear regime represent the high/low values of two measurements whereas after the formation of the X-pattern, the error bars represent the standard deviation of four measurements.

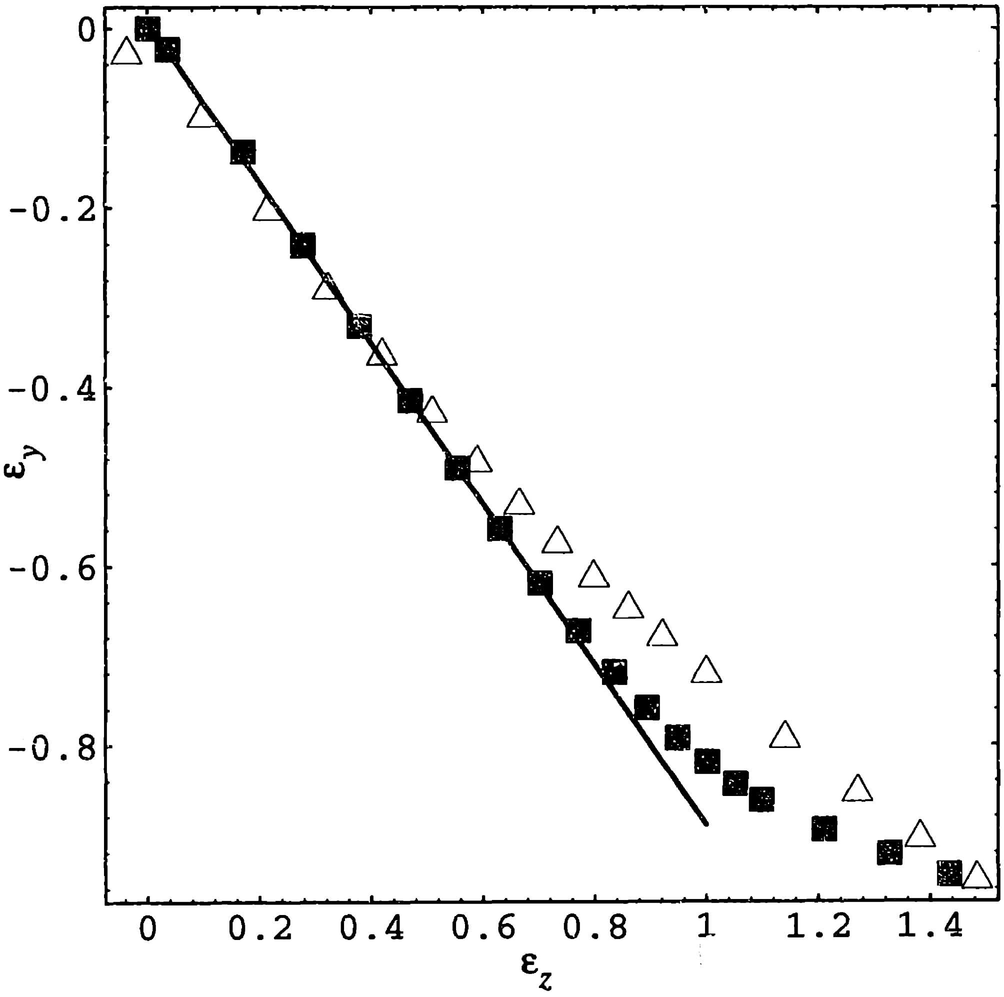

Figure 5-25: Plot of true strain along y vs. true macrostrain as determined via transmission measurements. The filled squares and hollow triangles represent loading and unloading respectively. The solid line is the best fit: $\varepsilon_y = -0.90*\varepsilon_z + 0.0072$ with $R^2 = 0.9996$.

transmission data included in each SAXS pattern. A linear fit to the loading portion of the curve yields a slope of -0.9. The slope gives a measure of the contraction in the y-direction per unit extension in the z-direction and can thus be thought of as a Poisson ratio in the y-z plane ν_{yz}. A second measure of the Poisson ratio is made in Section 5.3.1.2 and further discussion of ν_{yz} will be postponed until then.

5.2.2 TEM

5.2.2.1 120% Deformation

High energy electron beam irradiation induced crosslinking was used in an attempt to permanently capture a significant amount of deformation in a sample for TEM investigation. The irradiation experiment consists of stretching a sample to the desired strain and then irradiating the sample at fixed strain. In this instance, the sample was stretched to 620% strain, irradiated with 800 keV electrons for approximately 15 minutes before breaking (Figure 5-26). The residual deformation was measured to be approximately 120%, while the total dose was approximately 410 kGy. Note that the residual strain of a sample stretched to similar deformations and unloaded (see Figure 5-34) is less than 40%, so that the irradiation serves to capture about 20% of the total deformation as compared to 6.5% of the total deformation without radiation.

Experiments conducted at Raychem provide stress-time histories during the course of the irradiation. Figure 5-26 demonstrates that there is an immediate and significant increase in the stress relaxation rate upon irradiation. The sample immediately turns white and fluoresces during irradiation. The radiation-induced chemical processes in these samples are thought to be quite complex and are beyond the objective of this study. The main molecular changes are, however, chain scission and cross-linking (see Section 4.7). A TEM image of this sample viewed transverse to the cylinder axis is shown in Figure 5-27. The image shows that the PS cylinders have been bent into a chevron-like texture. The sharp boundary separating the parallel cylinders and aligned in the SD is a tilt-wall. On either side of the wall, the PS cylinders remain parallel at a fixed angle with respect to the deformation direction. It is this chevron texture which gives rise to the X-patterns observed in the SAXS experiments (e.g. Figure 5-19).

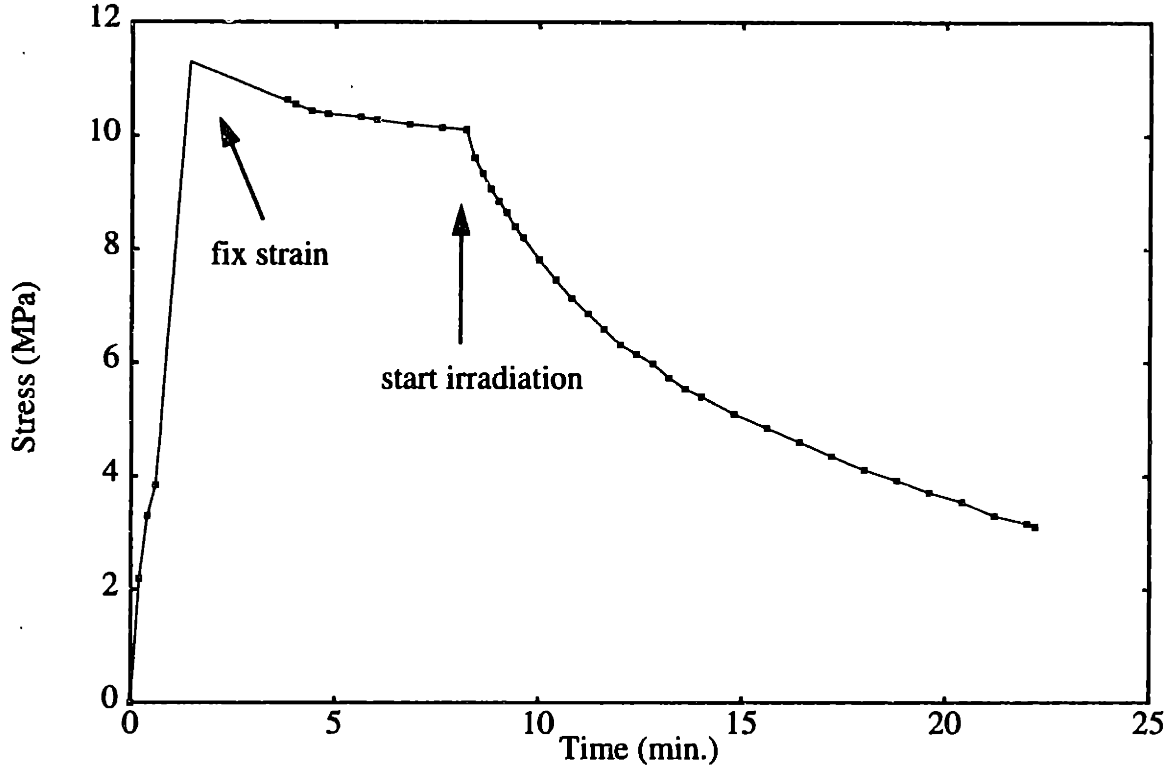

Figure 5-26: Stress-time history for the perpendicular stretch and irradiation experiment at Raychem. The sample was stretched to 620% strain and after approximately 6 min of stress relaxation, an 800 keV electron beam at a current of 1.2 mA was applied. Irradiation continued until break for a total dose of 410 kGy. The residual strain was measured to be approximately 120%. The early gap in data points is due to difficulties with charging of the load cell.

SAXS on this same sample helps to connect the real space TEM projection with the reciprocal space SAXS patterns taken during the dynamic experiments. Figure 5-28 compares the SAXS pattern and the optical transform (OT) corresponding to the image in Figure 5-27. The smaller X-angle of the SAXS pattern indicates that the region in Figure 5-27 incidentally has a particularly large chevron angle. The X-angle (68°) corresponds to a deformation of approximately 120% in the unloading curve of Figure 5-23, agreeing well with the macroscopically measured 120% deformation. A series of the TEM images and OTs support the notion that there is a finite distribution of chevron angles.

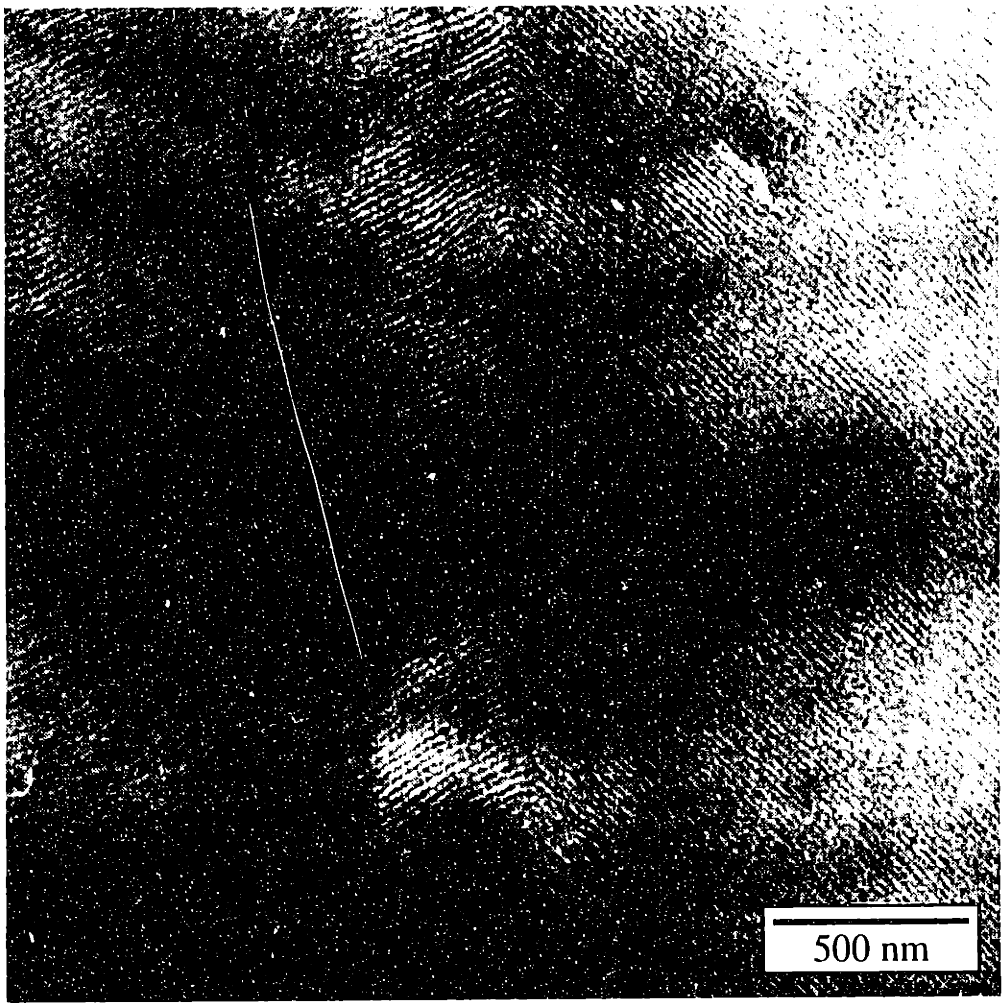

Figure 5-27: TEM image at normal incidence of a roll-cast SIS 15k-72k-15k sample stretched to 620%, irradiated and unloaded to 120% (see Figure 5-26). The initially straight PS cylinders have bent into a chevron-like texture by the deformation. The approximate chevron angle is 112° (see Figure 5-28).

To examine the X of the OT in further detail, digital Fourier transforms of the micrograph in Figure 5-27 are carried out in Figure 5-29. A series of Fourier transform pairs supports the conclusion that the second peak (strongest) dictates the spacing between cylinders while the weaker first peak provides a modulation at larger spacing which acts to enhance the moire nature of the tilted cylinder pattern. Within each grain of cylinders, on either side of the tilt boundary, which are oriented at the same angle with respect to the SD, there exist subgrains of cylinders, which have a slightly different orientation than the rest of the cylinders within the grain. An example is shown just to the right of the tilt boundary

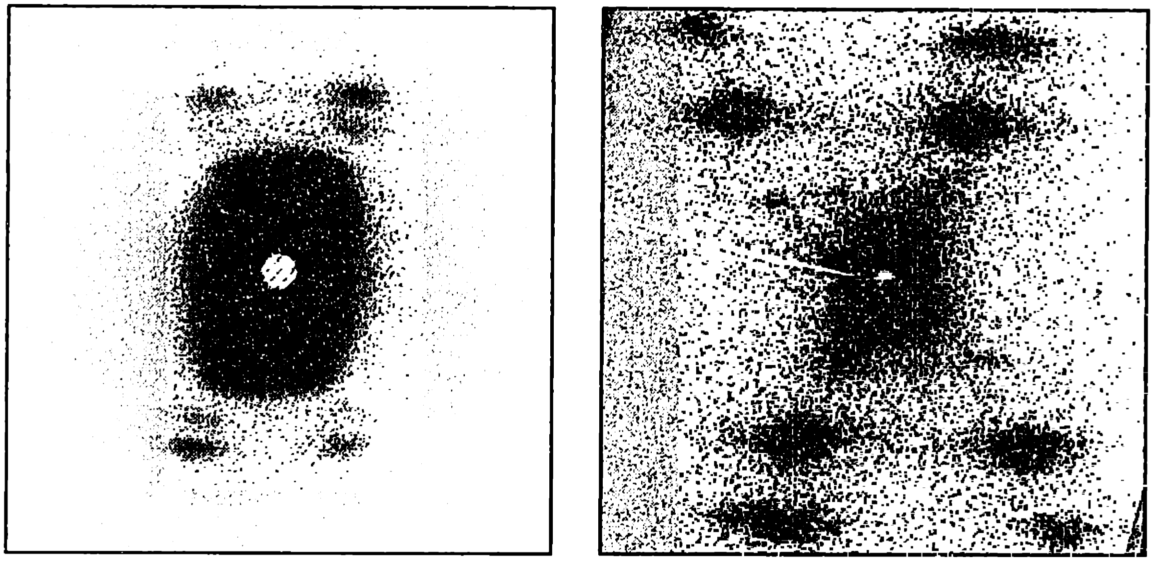

Figure 5-28: Left: SAXS pattern at normal incidence (y-direction) of the sample stretched to 624%, irradiated and unloaded to 120%. The X-angle (based on strongest ($\sqrt{3}$) peak) is 68 degrees. Right: Optical transform of the TEM negative from Figure 5-27. The X-angle is measured to be 52°. The zero of the form factor lies just outside the first three peaks in each arm.

in Figure 5-29 (e.g. c). The shape transform of these subgrains has a broadening effect on the peaks in the optical transform and the SAXS patterns at perpendicular incidence. The peaks in the X-patterns becomes more streaked in the x-direction as the width of the subgrains decreases. This broadening effect due to the shape transform of grains with finite width is even more pronounced at parallel incidence where the fault spacing is much smaller than the chevron spacing.

Despite the severe treatment during deformation that the irradiated sample suffers, there are a number of similarities between the SAXS pattern and OT of the irradiated sample and the X-patterns observed during the dynamic stretching experiments. In both cases, the strongest peak in each arm is the second one, which in the dynamic experiments is known to correspond to the $\sqrt{3}$ peak. The first peak is visible in the SAXS pattern of Figure 5-28 and very faint in the OT, but in both cases the second peak dominates. A second similarity is the observation that the peaks making up the two paris of arms in the X are not colinear. Most likely this phenomena is a consequence of the intensity lobe making up the first ($\sqrt{1}$) reflective intersecting the Ewald sphere when the incident beam is perpendicular to the cylinder axis. Whatever the explanation for the non-colinearity of the arms of the X, it is observed in both the static reciprocal data (SAXS and OT) and the dynamic data. Establishing the similarity between the X pattern in the SAXS of the irradiated sample and those observed in the dynamic experiments enables a model of the deformed structure to be built on the basis of the TEM projections (see Section 5.5)

Figure 5-29: on page 159: Series of digital FFT pairs taken from Figure 5-27. (b) is the FFT of the original image (a). Passing the strongest four peaks of the X (d) results in two sets of fringes to make up a chevron pattern (c). Notice the contrast modulations within a layer arising from the beating of the layers from the opposing set of fringes (e.g., upper left). The strongest pair of peaks on the left arm of the X (f) arises from the fringes on the left of the image (e). Combining the first peaks with the second (strongest) peaks from the left arm of the X (h), adds a second set of fringes at lower spatial frequency. This second set of fringes is oriented at a different angle compared to those arising from the strong second peaks which creates waviness and a moire pattern in some regions (e.g., upper left region in (g)).

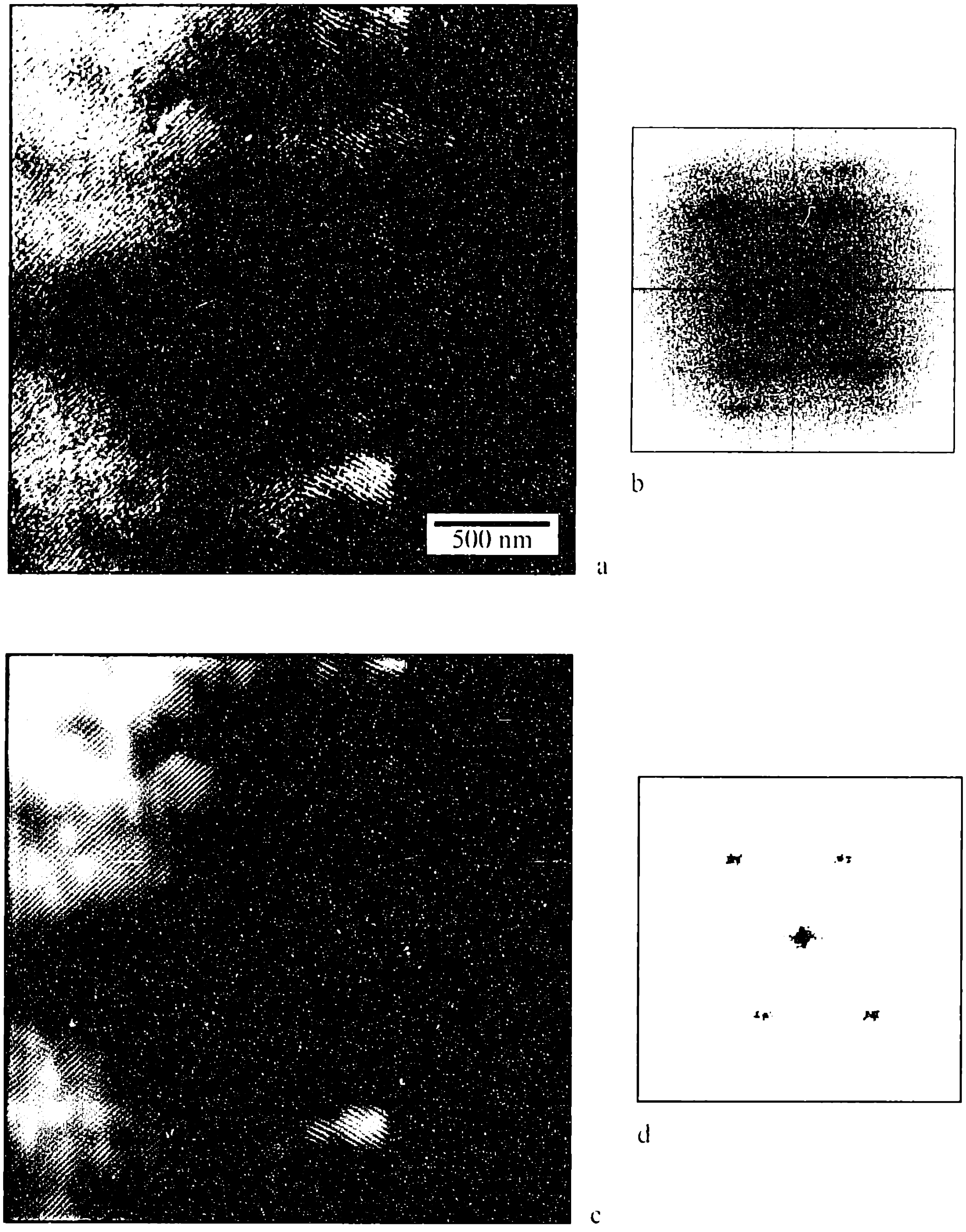

Figure 5-29 caption on page 158.

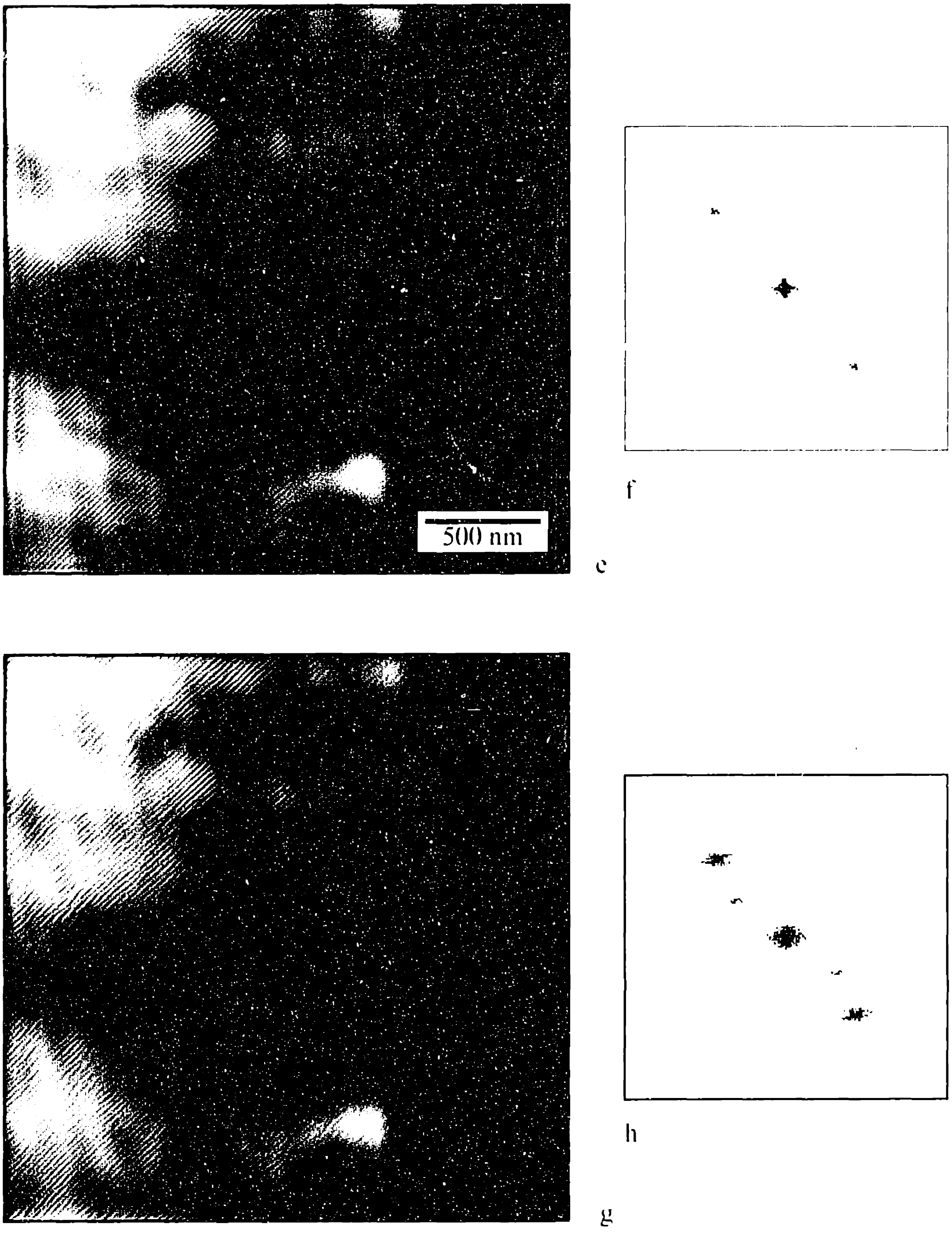

Figure 5-29 caption on page 158.

5.2.2.2 180% Deformation

Irradiation experiments conducted at the High Voltage Laboratory (HVL) captured larger amounts of deformation than those conducted at Raychem. However, the stress-time history is not available. A sample stretched to 410% strain and irradiated with 80 MRad was unloaded and found to retain 180% strain. TEM at normal incidence in Figure 5-30 shows a larger chevron angle compared to Figure 5-27. This particular sample was stretched slightly asymmetrically, i. e., the force direction was not entirely normal to the

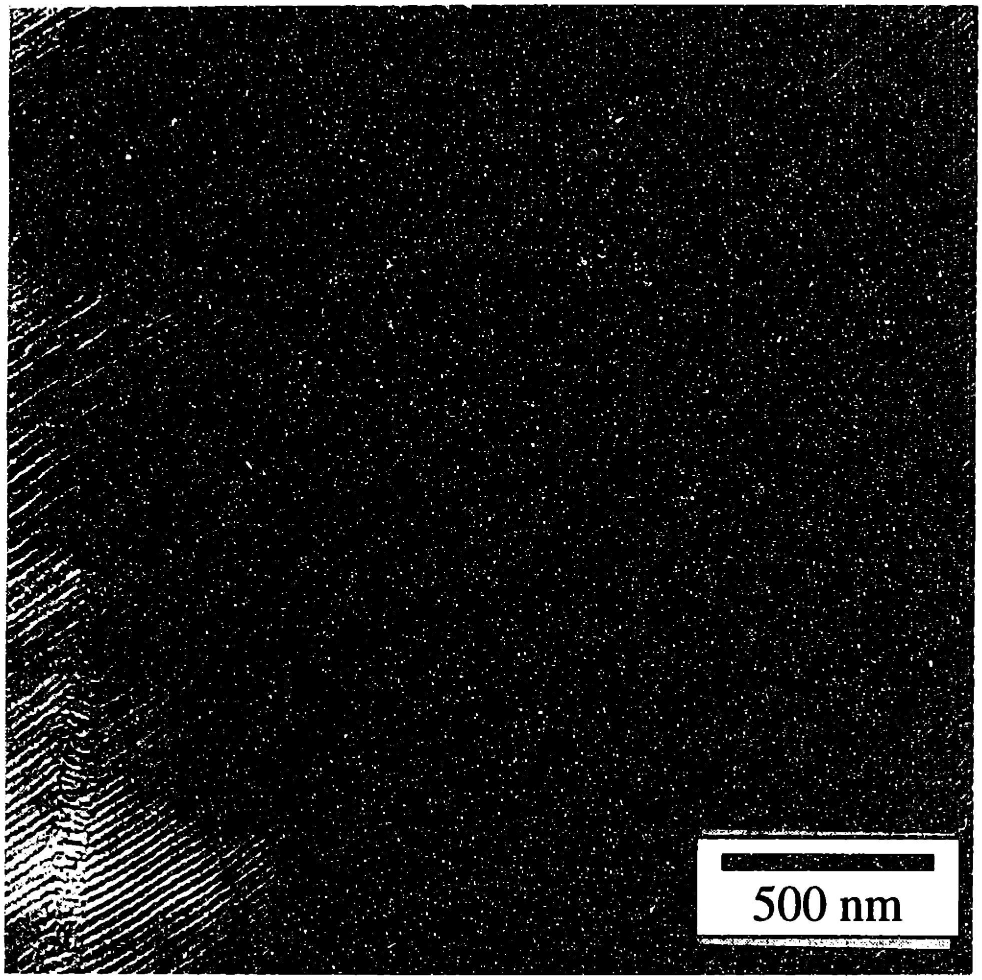

Figure 5-30: TEM image at normal incidence of a roll-cast SIS 15k-72k-15k sample stretched to 410%, irradiated and unloaded to 180%. Examples of chevron boundaries oriented both up and down are visible. The width of the central band is approximately 1 μm. The variation in contrast strength across the image is most likely due to rotational misalignment within the section. The approximate chevron angle is 95° (see Figure 5-31).

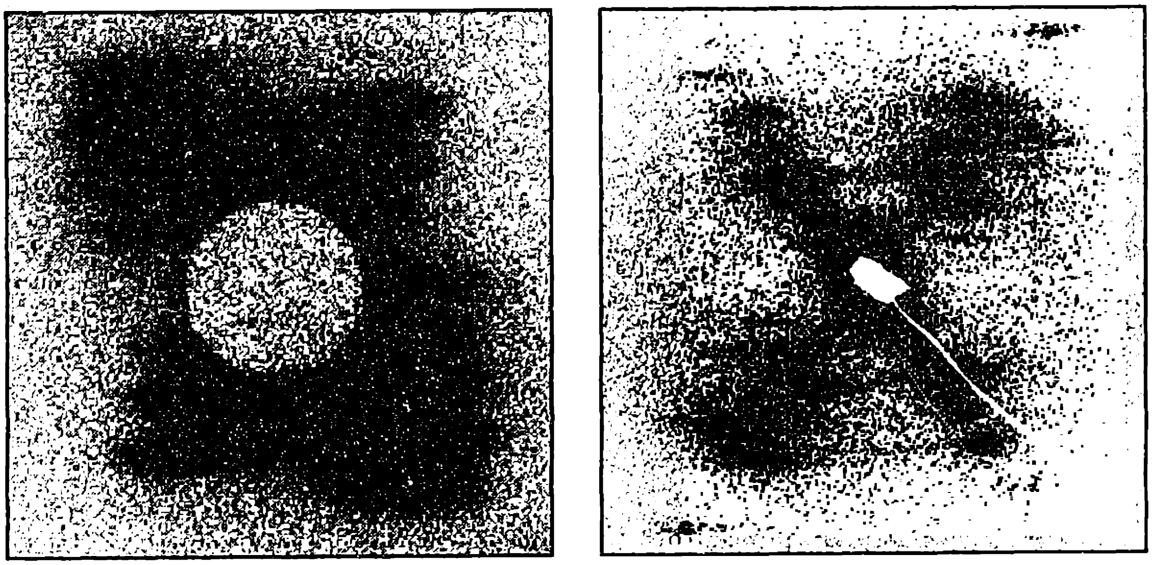

Figure 5-31: Left: SAXS pattern at normal incidence (y-direction) of the sample stretched to 410%, irradiated and unloaded to 180%. The X-angle (based on strongest ($\sqrt{3}$) peak) is 86 degrees. Right: Optical transform of TEM negative from Figure 5-27. The X-angle is measured to be 85°.

cylinder axis. Figure 5-31 shows the corresponding SAXS pattern and OT of the same TEM area. Comparison with OT in Figure 5-28 right indicates that the X-angle is larger in the HVL sample than in the Raychem sample. Additionally, the X-angle measured via SAXS (86 degrees) corresponds to a permanent deformation of approximately 170% using the unloading curve in Figure 5-23, which agrees well with the macroscopically measured permanent deformation.

At lower magnifications in the TEM, it is possible to visualize the larger structure of these chevrons over many square microns. For both the RayChem and the HVL samples, montages of several closely spaced negatives were taken and enlarged yielding a contiguous field of view of approximately 22 x 20 μm^2 and 29 x 20 μm^2, respectively. The chevron boundaries remain straight and aligned with the stretching direction. The tilted cylinder regions themselves are not uniform but contain small shear bands (the aforementioned subgrains) which occasionally interrupt the cylinder trajectory. In the case of the asymmetrically stretched HVL sample, thin bands of approximately 1 µm width were spaced approximately 10 μm apart (see Figure 5-30). There was, however, not enough information available to determine a reliable distance between tilt boundaries. Despite the aperiodicity in tilt boundary spacing, an average correlation width is estimated at 5 μm.

Assuming that the PS cylinders do not fracture, it is possible to estimate the maximum tensile strain experienced by the PS as a function of bending. Figure 5-32 shows an enlarged region of the chevron boundary which suggests that most PS cylinders continuous across the boundary. In bending a PS rod, the material at the outside of the bend is in tension while that beneath the neutral axis is in compression. Assuming that the

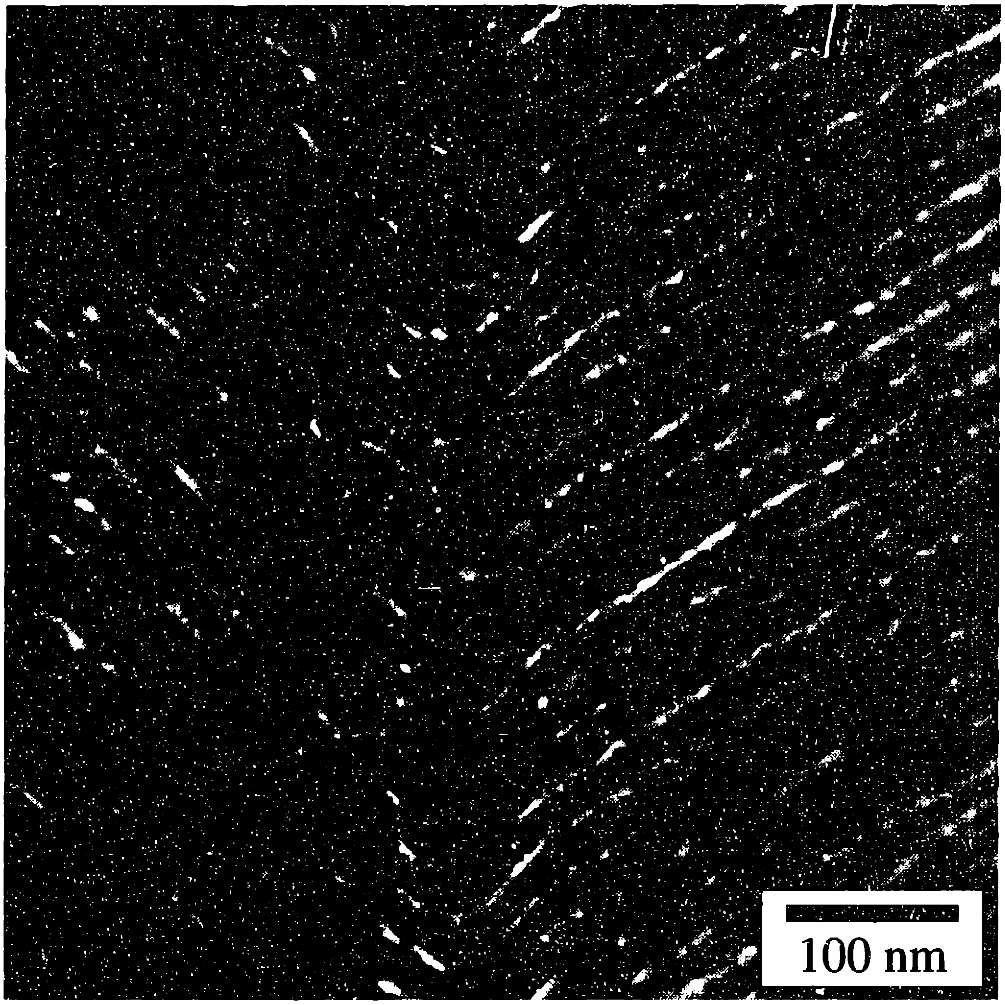

Figure 5-32: Close-up region of a chevron boundary (from Figure 5-30) for the HVL sample. The PS (white) phase may be continuous across the boundary.

outermost bending at the tip follows the contour of a sphere, the maximum strain would be found in a plane which bisects the bent rod (see Figure 5-33). The maximum tensile strain at the largest bend, based on the maximum X-angle of Figure 5-23, can be thus estimated as 20%. In other experiments the maximum X-angle was found to by 140° which results in

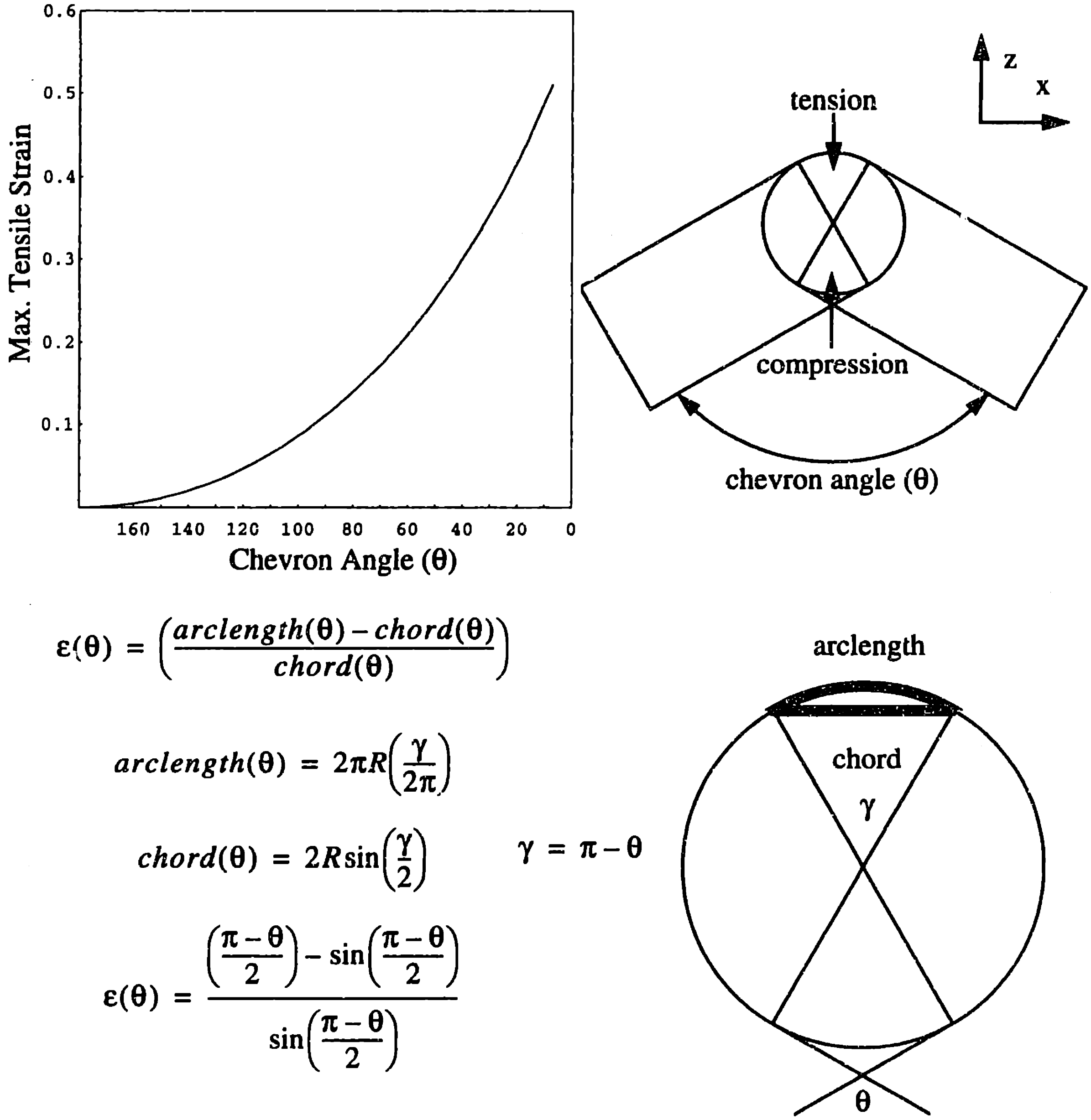

$$\varepsilon(\theta) = \left(\frac{arclength(\theta) - chord(\theta)}{chord(\theta)}\right)$$

$$arclength(\theta) = 2\pi R\left(\frac{\gamma}{2\pi}\right)$$

$$chord(\theta) = 2R\sin\left(\frac{\gamma}{2}\right) \qquad \gamma = \pi - \theta$$

$$\varepsilon(\theta) = \frac{\left(\frac{\pi-\theta}{2}\right) - \sin\left(\frac{\pi-\theta}{2}\right)}{\sin\left(\frac{\pi-\theta}{2}\right)}$$

Figure 5-33: Estimate of maximum tensile strain in the PS cylinders at a chevron boundary. Assuming that the stretched material takes on a spherical shape, the maximum tensile strain is based on the ratio of the arclength to the chordlength of the circle bisecting the bent rod. The smallest observed chevron angle is approximately 40° which yields a maximum tensile strain of 30% in the PS.

a maximum tensile strain of 30% at the outmost region of the chevron bend. This amount of strain is much more than the elongation at break of bulk PS (2.5%) (Van Krevelen, 1990) (p. 417). The PS at the tilt boundary does not fracture, but acts as a hinge undergoing plastic deformation as the chevron angle decreases. The resistance to flow during unloading is somewhat less than during loading due to the Baushinger effect which may help account for the hysteresis in the X-angle curve during unloading (Figure 5-23). This small amount of deformation might explain the fact that structurally, the sample recovers almost to its initial state.

5.3 Perpendicular Stretch Parallel Incidence

5.3.1 SAXS

5.3.1.1 Progress of Deformation

Figure 5-34 shows a strain-strain plot of a roll-cast 4211 sample with a cross-section of 1.2 x 1.92 mm^2 for a perpendicular stretch parallel x-ray incidence (⊥||) experiment. The reduced cross-section of this particular sample generates a higher stress at a given strain than for the ⊥⊥ experiment shown in Figure 5-12. The sample has also been stretched to a higher deformation due to the choice of a smaller initial gage length. The same sampling frequency as that used for the experiment in Figure 5-12 is employed which means that there is a larger strain increment during a given exposure time in these ⊥|| experiments.

Figure 5-36 shows plots of the log of intensity vs. q_z from rectangular integrations along the SD for 19 selected 2-D SAXS patterns. As the cylinders are deformed normal to their axes, the hexagonal pattern shown in Figure 5-4 changes continuously. Those peaks along the SD move toward the origin, while the peaks normal to SD move away from it. The remaining peaks move according to the magnitude of their components along and normal to the SD, respectively. The shape of the "rings" of diffraction seen in Figure 5-4 is immediately distorted into ellipses (see Figures 5-35 and 5-37). The hexagonal symmetry

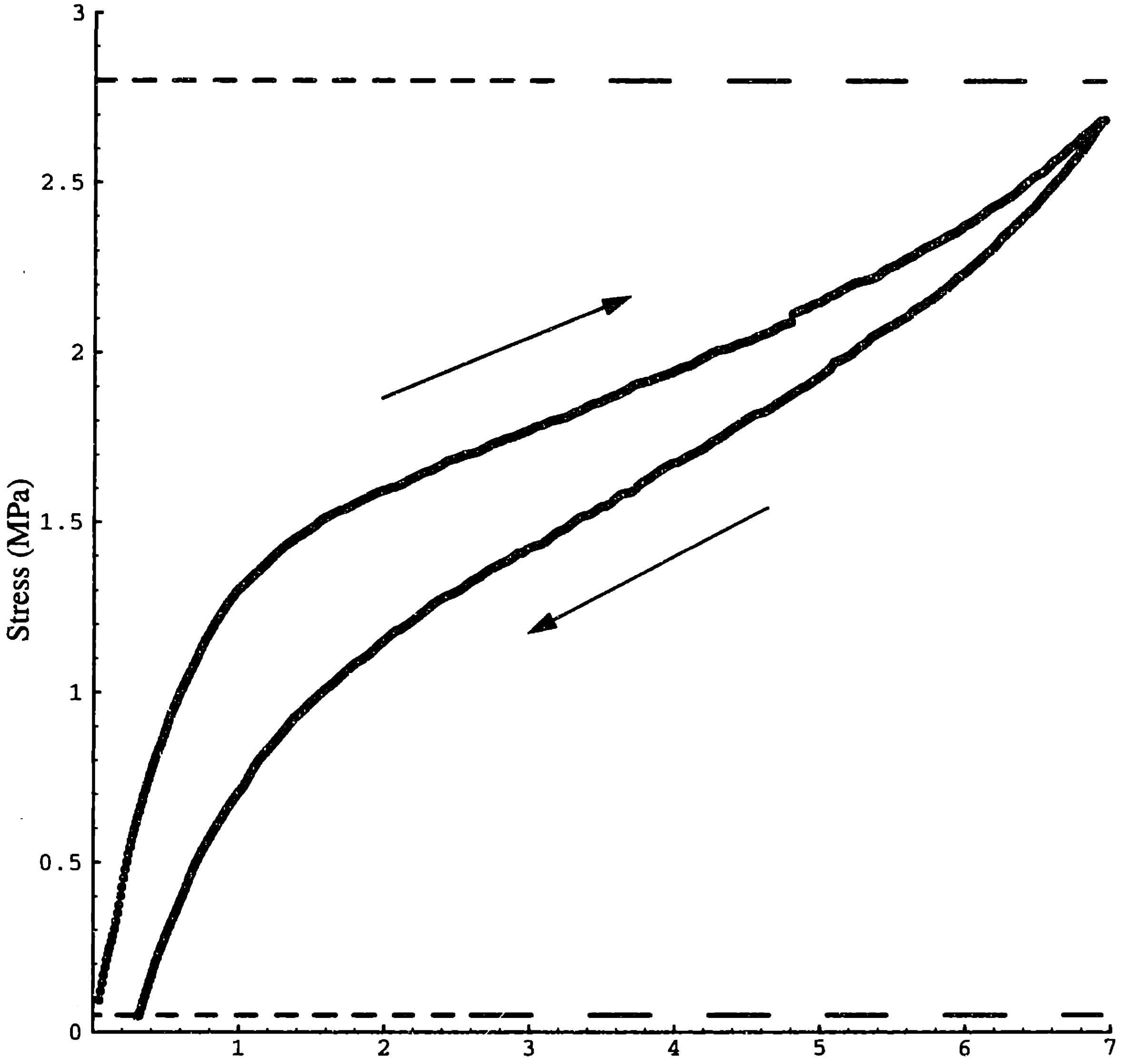

Figure 5-34: Stress-strain plot of the perpendicular stretch parallel x-ray incidence experiment discussed in this section. The dashed lines at the top and bottom indicate data acquisition periods for the loading and unloading cycles, respectively.

of the cylinder packing is immediately broken by the deformation. The symmetry of the remaining patterns about the origin during the course of the deformation is that of the point group 2mm.

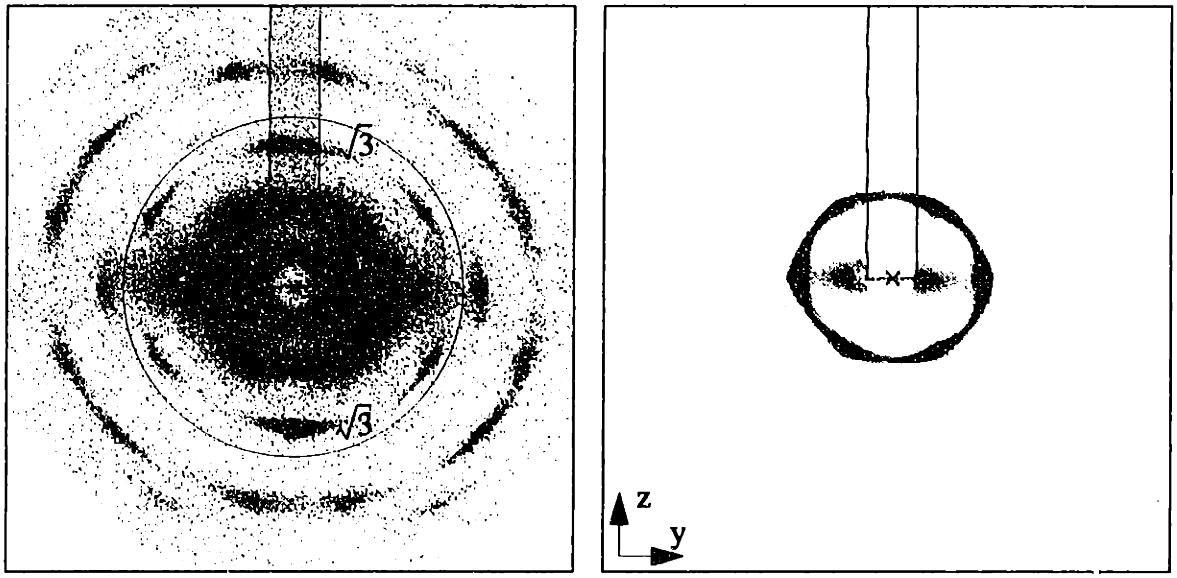

Figure 5-35: 2-D SAXS pattern for a ⊥|| deformation experiment at 6.7% deformation. In the following figures, the rectangle indicates the range over which the integration for Figure 5-36 was performed and the circle of radius q = 0.044 Å^{-1} represents the location of the zero of the form factor. Note that at a strain of 6.7%, the pattern is no longer hexagonal and that the two $\sqrt{3}$ peaks in the SD have grown in intensity compared to the other four $\sqrt{3}$ peaks.

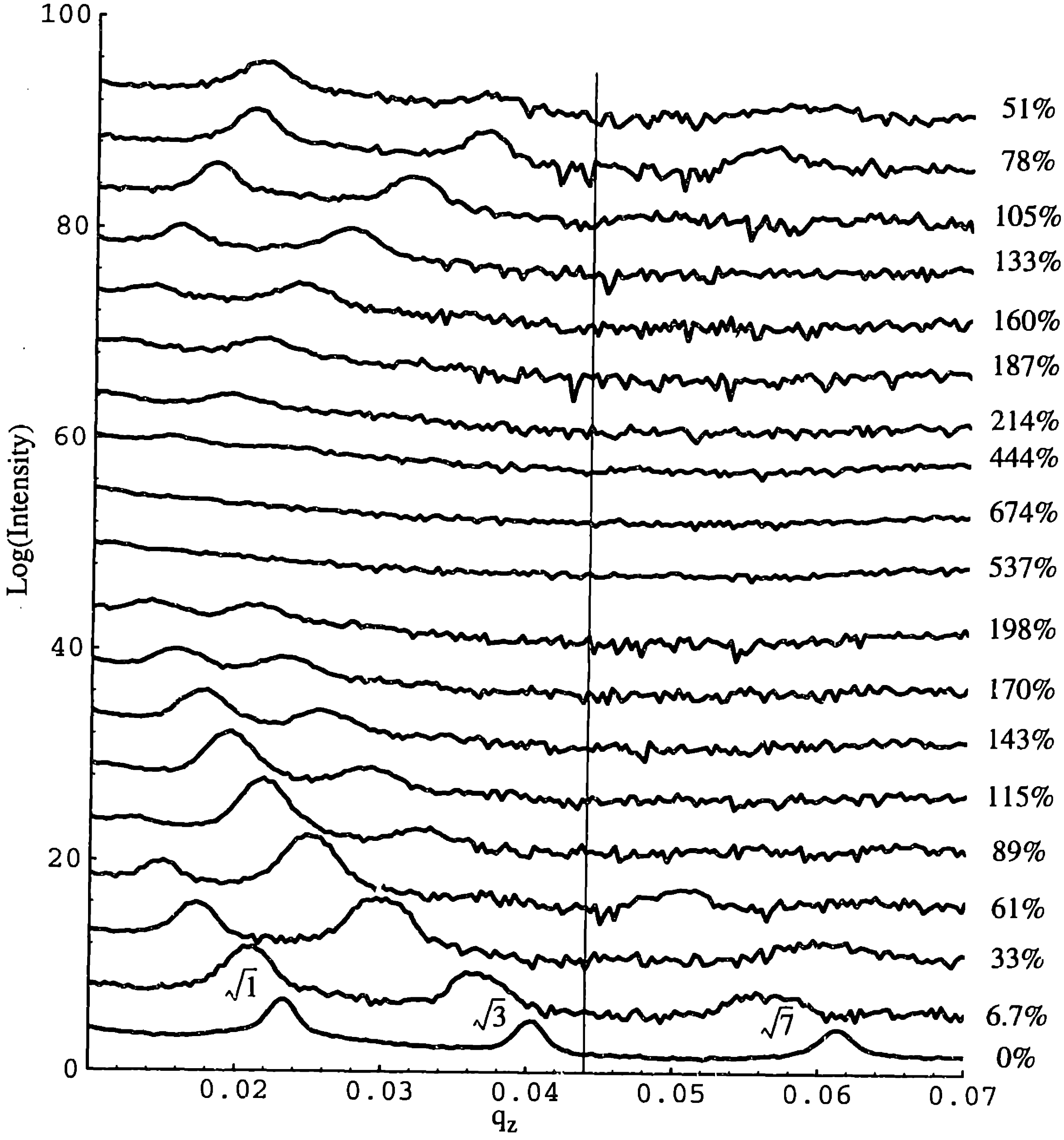

Figure 5-36: Log intensity vs. q_z from a rectangle 40 pixels wide (see Figures 5-37 to 5-40) showing peak motion in the SD. The thin vertical line indicates the zero in the form factor. The applied strain is given to the right of the corresponding curve.

As in the perpendicular x-ray incidence experiment, the intensities of the observed peaks are modulated by the form factor. In Figures 5-35 and 5-37 the $\sqrt{3}$ peaks along the SD, the $(\bar{1}2\bar{1}0)$ and $(1\bar{2}10)$ peaks according to the indexing of Figure 5-4, gain in intensity as they move away from the zero of the form factor (indicated by the circle). Upon further increase in deformation, the two $\sqrt{1}$ peaks normal to the SD, $(\bar{1}010)$ and $(10\bar{1}0)$,

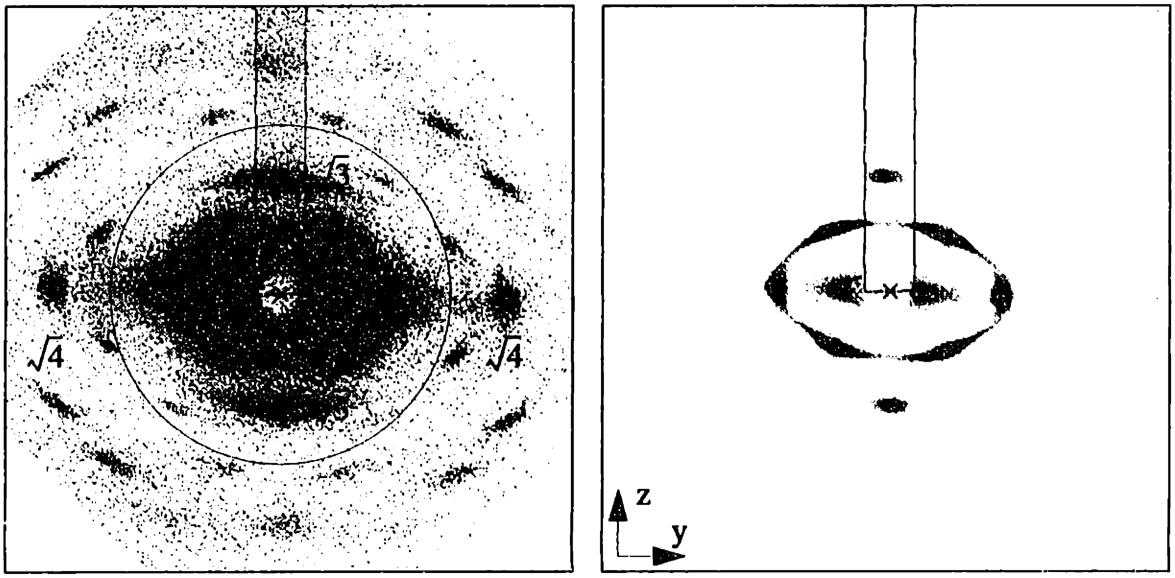

Figure 5-37: 2-D SAXS pattern for a ⊥∥ deformation experiment at 33% deformation. The circle of radius q = 0.044 Å^{-1} represents the location of the zero of the form factor. Note the further increase in intensity of the $\sqrt{3}$ peaks in the SD. The $\sqrt{4}$ peaks normal to the SD have now become stronger than the surrounding $\sqrt{3}$ peaks. The point group symmetry of the pattern is now 2mm, due to the deformation.

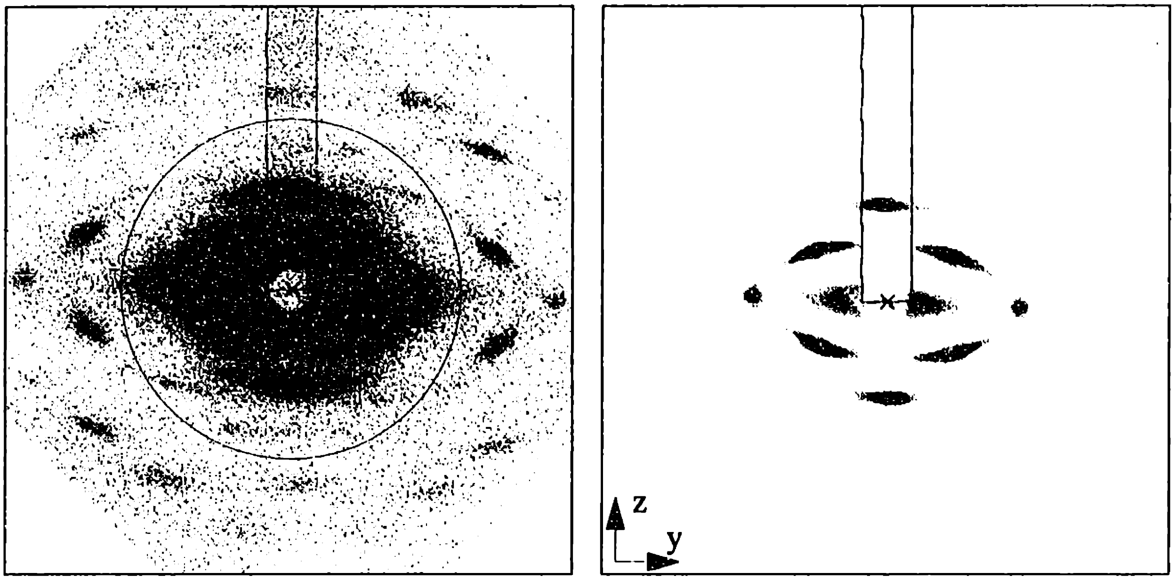

Figure 5-38: 2-D SAXS pattern for a ⊥∥ deformation experiment at 61% deformation. The $\sqrt{3}$ peaks in the SD are now as strong as the $\sqrt{1}$ normal to the SD. The remaining $\sqrt{3}$ peaks normal to the SD have now grown in relative intensity.

move away from the origin and lose intensity. In Figure 5-39, at 143% strain, these two

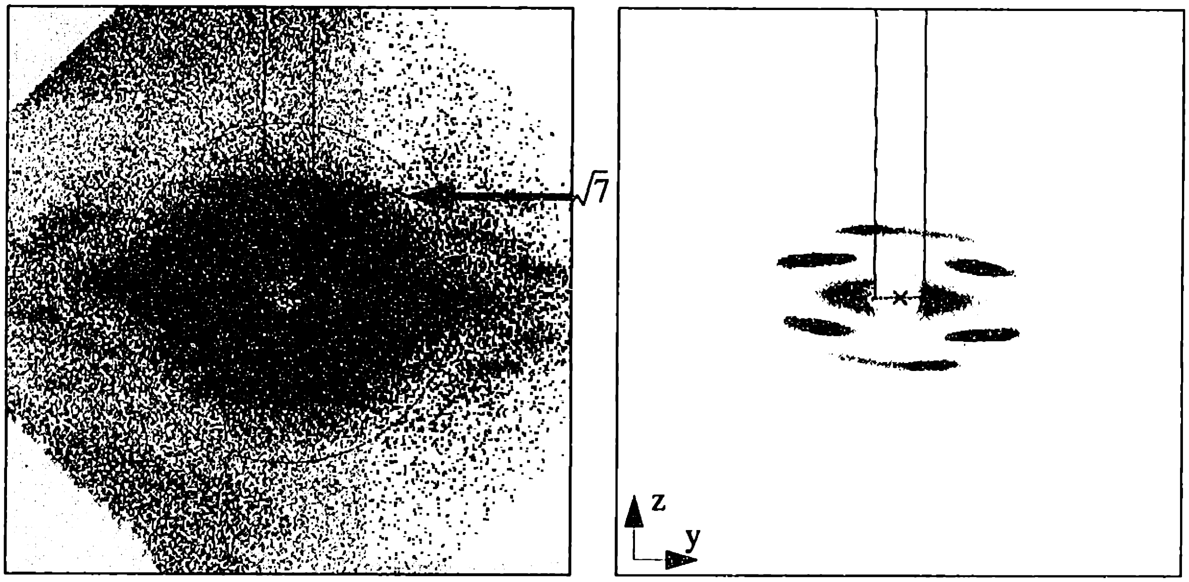

Figure 5-39: 2-D SAXS pattern for a $\perp\parallel$ deformation experiment at 143% deformation. The $\sqrt{3}$ peaks in the SD have become quite broad in the equatorial direction. In addition, intensity belonging to the $\sqrt{7}$ peaks is visible in the SD. The four $\sqrt{1}$ lobes closest to the origin remain the most intense features of the SAXS pattern at the highest deformations.

peaks are very weak, but they later regain relative strength, as they move beyond the zero of the form factor (Figure 5-40). The peaks at higher values of q are more difficult to observe. Those along the stretching direction become obscured by the first zero of the form factor as they move towards the origin, while those near the equator (normal to SD) move away from the origin and become obscured by the second zero of the form factor. Those peaks neither along nor normal to the SD are collapsed towards the q_y axis at large q_y (see Figures 5-38 and 5-39). The elliptical shape of the diffraction "rings" at low deformations (< 100%) may still be discerned at higher deformations if one connects the peaks belonging to the same family (e.g. the $\sqrt{1}$ peaks in Figure 5-40). These ellipses have, however, very large ratios of the major/minor axes.

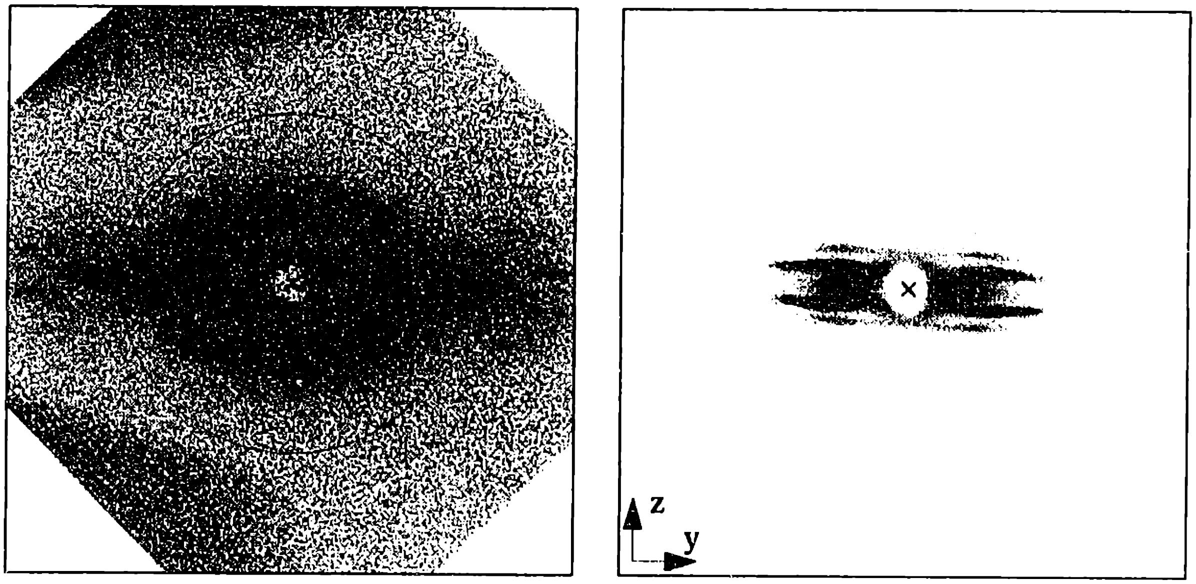

Figure 5-40: 2-D SAXS pattern for a $\perp\parallel$ deformation experiment at 374% deformation. The $\sqrt{3}$ and $\sqrt{12}$ peaks in the SD seem to have split into four streaks just above and below the strong $\sqrt{1}$ lobes. The $\sqrt{1}$ peaks normal to the SD have reappeared and can be discerned at relatively large q.

5.3.1.2 Peak Motion

The movement of the $\sqrt{3}$ peak $(\bar{1}2\bar{1}0)$ in the SD provides information about the intercylinder spacing in the SD as a function of deformation. As in the perpendicular incidence case, rectangular regions of integration yield 1-D plots of intensity vs. q_z (Figure 5-36) from which the spacing of the $\sqrt{3}$ peak as a function of deformation can be extracted (Figure 5-41). The increase in spacing is linear over a large deformation range. Data at even larger strains are unavailable due to the loss in intensity of the $\sqrt{3}$ peak along the SD (Figure 5-35). Until formation of the X-pattern (Figure 5-21), the $\sqrt{3}$ peak remains on the Ewald sphere. Thereafter, the peak splits in two and the centroids of these peaks are no longer on the y-z plane (Figure 5-17). This means that the intensity detected on the y-z plane is the component of the $\sqrt{3}$ peak in the SD (compare Figure 5-17 with 5-39 and see 5-63). At the larger deformations (> 200% strain), the $\sqrt{3}$ peak localizes into two distinct peaks in the y-z plane (Figure 5-40) on either side of the z-axis, which causes a further reduction in intensity in the profiles at high strain in Figure 5-36.

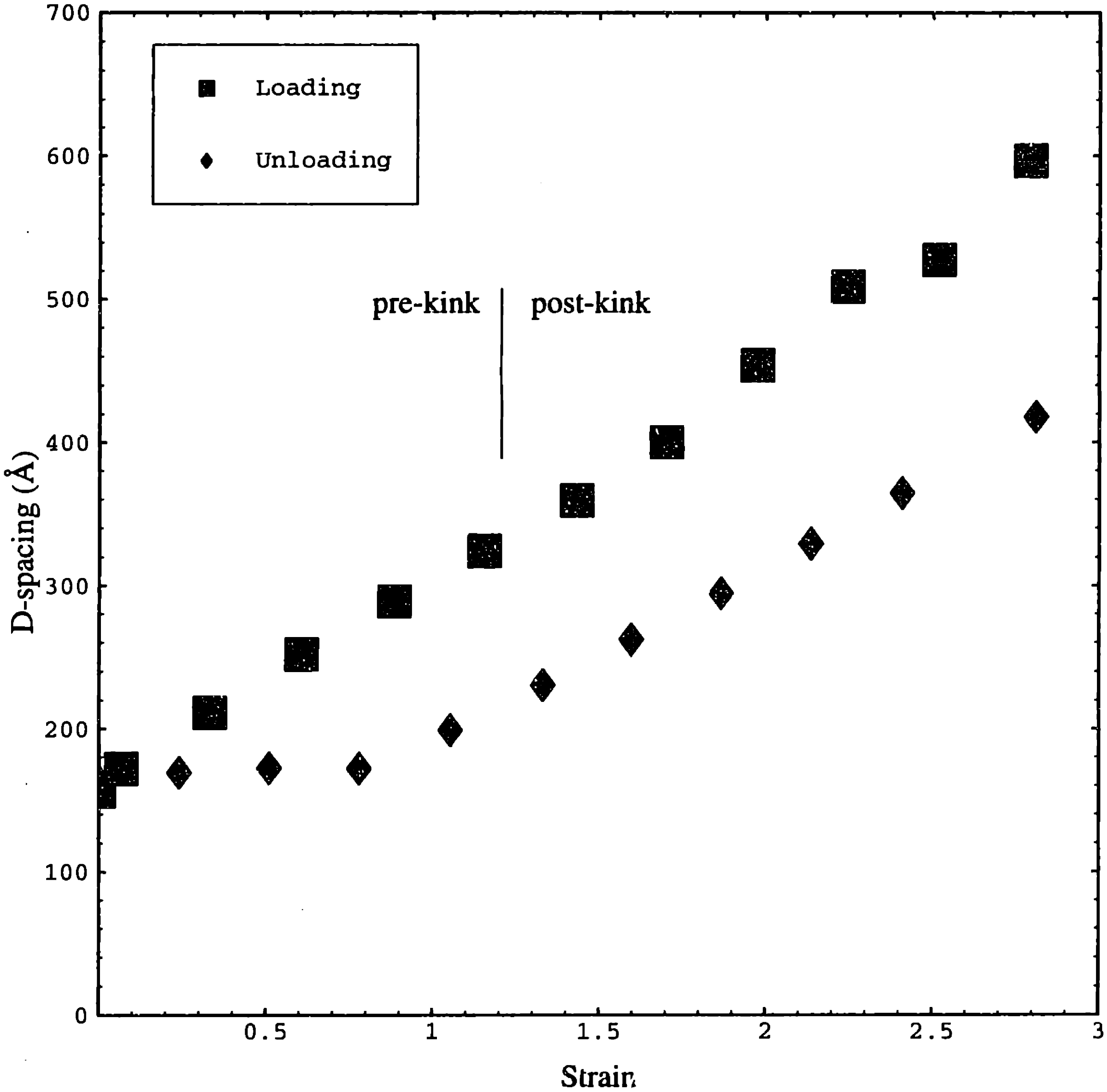

Figure 5-41: "D"-spacing as a function of deformation for the $\sqrt{3}$ peak in the stretching direction. Data beyond 300% are unavailable due to loss of $\sqrt{3}$ peak intensity in the SD. Note the hysteresis upon unloading.

A comparison in terms of microstrain vs. macrostrain in the SD gives a measure of "affineness", the degree to which the lattice deforms in direct response to the macroscopic deformation. The $\sqrt{3}$ spacing data is reduced to microstrain and plotted against macrostrain in Figure 5-42. The fit indicates an "affineness" of 97% up to a strain of 300%. This measure of the affineness of the cylinder deformation is only valid up to a strain of

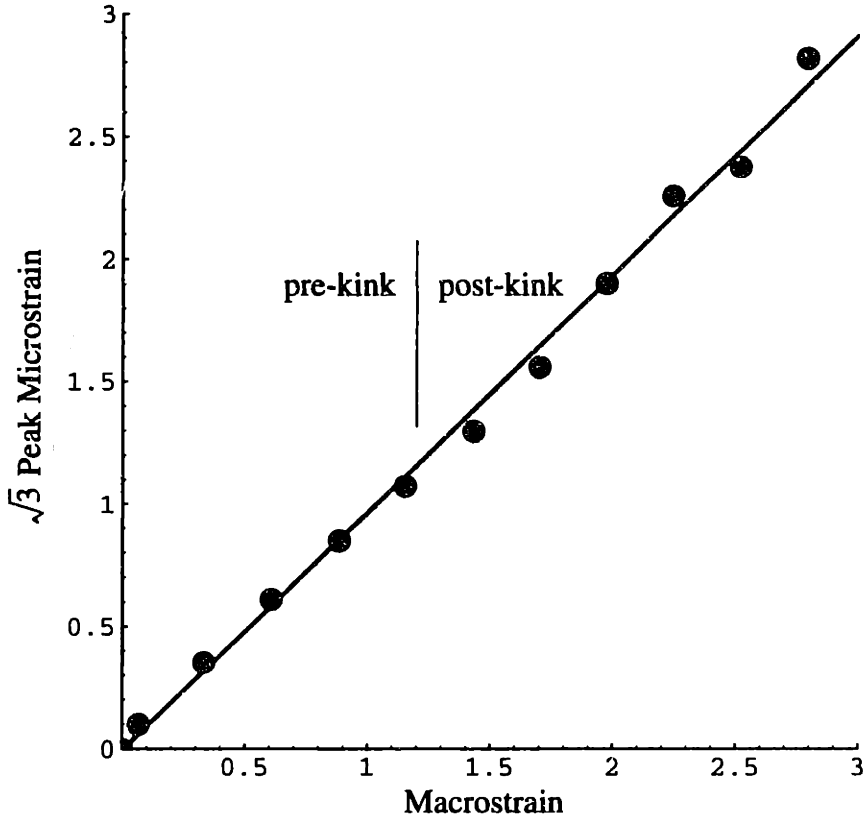

Figure 5-42: $\sqrt{3}$ peak microstrain vs. macroscopic strain in loading for the perpendicular stretch parallel incidence experiment under discussion. The solid line is the best fit: microstrain = 0.971*macrostrain - 0.0058 with R^2 =0.996.

130%, however. The formation of the X-pattern at this strain means that the centroid of the $\sqrt{3}$ peak is no longer in the y-z plane. The $\sqrt{3}$ peak intensity observed at parallel incidence is due to the streaking that intercepts the y-z plane (Figure 5-63). The $\sqrt{3}$ peak spacing measured at parallel incidence (Figure 5-41) therefore represents a component of the actual $\sqrt{3}$ peak spacing which is measured at perpendicular incidence (Figure 5-24). This is the reason that the morphological transition observed at perpendicular incidence is not seen when examining the $\sqrt{3}$ peak spacing dependence on deformation at parallel incidence.

The movement of the $\sqrt{1}$ $(10\bar{1}0)$ peak normal to the SD provides information about the Poisson effect, or the contraction of the lattice in the lateral (y) direction due to stretching in the z-direction. Similar integrations yield intensity vs. q_y plots which indicate that the $\sqrt{1}$ peak moves away from the origin and passes through the zero of the form factor (Figure 5-43). At a strain of 115%, the $\sqrt{1}$ peak has moved into the zero of the form factor

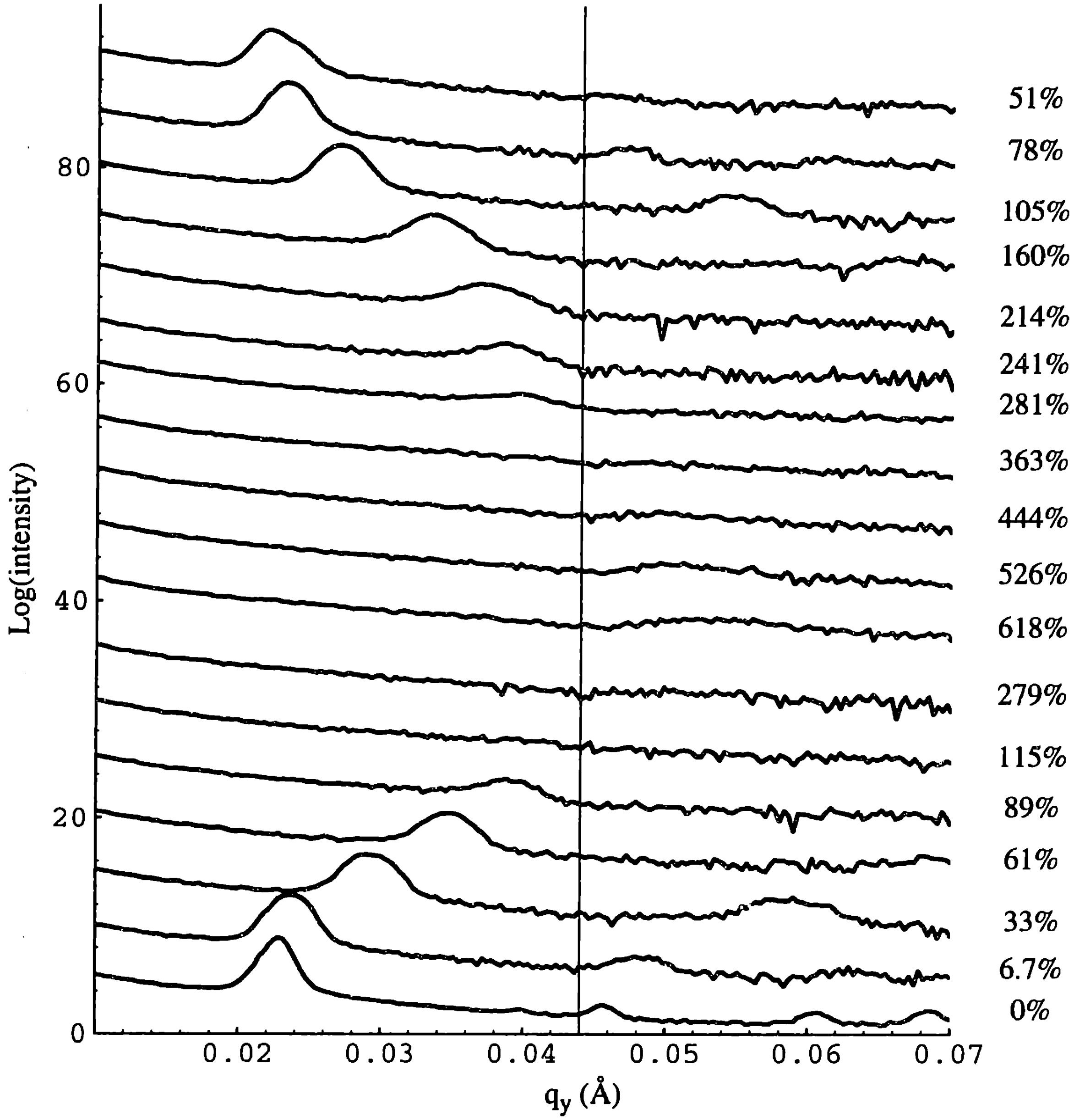

Figure 5-43: Selected log intensity vs. q_y plots showing peak movement normal to the SD as a function of deformation. The thin line indicates the zero of the form factor. The strain direction is reversed at 690% deformation.

and the peak can barely be distinguished from the equatorial streak at a strain of 143%

(Figure 5-39). At a strain of 374% the peak can clearly be resolved outside the zero of the form factor (Figure 5-40). Compared to earlier in the deformation process, the peak has broadened and lost intensity.

The spacing of the $\sqrt{1}$ peak as a function of deformation shows two distinct regions (Figure 5-44). Initially, there is an approximately linear decrease in spacing, but at larger deformations (> 200%), the spacing remains fairly constant. The cross-over between the two regimes is obscured by the zero of the form factor, which is indicated by the dashed line. Linear extrapolations of both regions yield a cross-over value of 92%. This cross-over occurs at a slightly smaller strain than the cross-over for the $\sqrt{3}$ peak in the perpendicular incidence which is at 115% strain (Figure 5-24). This suggests that the transition from affine to non-affine behavior in the perpendicular stretch affects both intercylinder spacings normal to the cylinder axis in a similar way. The difference in the cross-over strains (92% vs. 115%) is in part due to the difference in the cross-sections of the samples (parallel view experiment vs. perpendicular view experiment) (Figure 5-59).

With microstrain information from two orthogonal directions, it is possible to cross-plot the data in order to estimate the Poisson's ratio in the yz plane, υ_{yz}, which is defined as the negative ratio of the lateral contraction to the extension in the SD:

$$\nu_{yz} = \frac{-\varepsilon_y}{\varepsilon_z}. \tag{5.1}$$

For a body with orthotropic symmetry, there are six Poisson's ratios (Ward, 1975) (see also (Kim, 1996) and (Jones, 1975) (Chapter 2)). A plot of ε_y vs. ε_z yields a slope of $-\nu_{yz}$. The slope in Figure 5-45 yields a Poisson ratio of 0.91. As the data in the y direction are sparse, only a few points are available. This result agrees favorably with the previously reported υ_{yz} of 0.9 in Section 5.2.1.5.

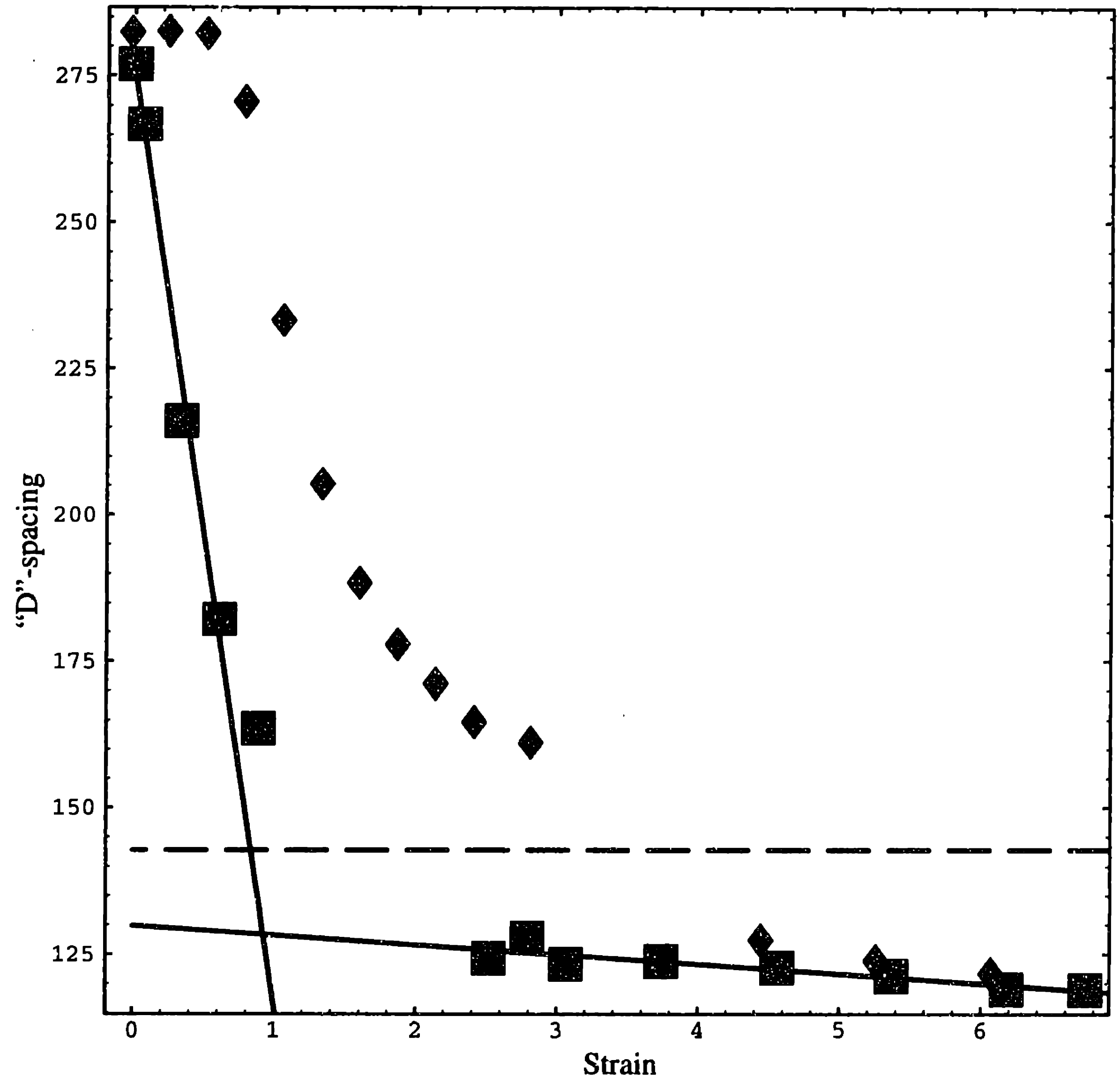

Figure 5-44: Plot of "d"-spacing vs. deformation for the $(10\bar{1}0)$ ($\sqrt{1}$) peak in the y direction. The boxes represent loading while the diamonds represent unloading. These data indicate a two-stage process in the lateral (y) dimension of the distorted hexagonal lattice. The cross-over between the two linear regimes occurs at a strain of approximately 0.9. The dashed line represents the zero of the form factor.

Furthermore, an analysis of data from Hadziioannou et al. gives similar results (Hadziioannou et al., 1979). Figure 5-46 plots true strain normal to the SD vs. true strain in the SD measured in both real and reciprocal space. The Poisson ratios (υ_y) for the real and

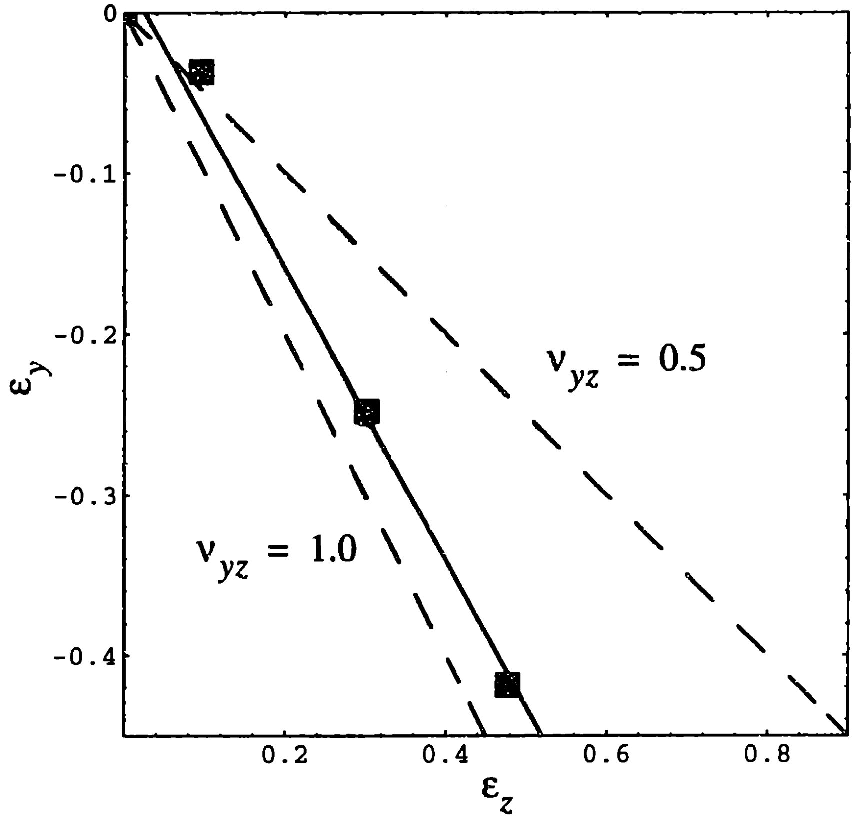

Figure 5-45: Plot of ε_y (microstrain in y direction) vs. ε_z (microstrain in SD). The solid line indicates a fit to: $\varepsilon_y = -0.91 * \varepsilon_z + 0.023$ with $R^2 = 0.988$. The dashed lines represents a Poisson ratio of 0.5 and 1.0 respectively.

reciprocal data are 0.86 and 0.91, respectively. The available data suggests that the Poisson ratio in the y-z plane for this composite is closer to 1.0 than the usual value of 0.5 for rubbery materials. This significance of this result will become apparent in Section 5.6.1.

5.3.2 TEM

5.3.2.1 120% Deformation

The sample discussed in Section 5.2.2.1 was also examined via TEM projections down the original cylinder axis, [0001] parallel incidence. Figure 5-47 shows the distorted hexagonal lattice resulting from a deformation history in which the sample was initially stretched to 624%, irradiated and subsequently unloaded to a final (and permanent) deformation of 120%. The SAXS pattern and the OT of the negative corresponding to the irradiated sample are shown in Figure 5-48 and indicate that the extent of deformation is in

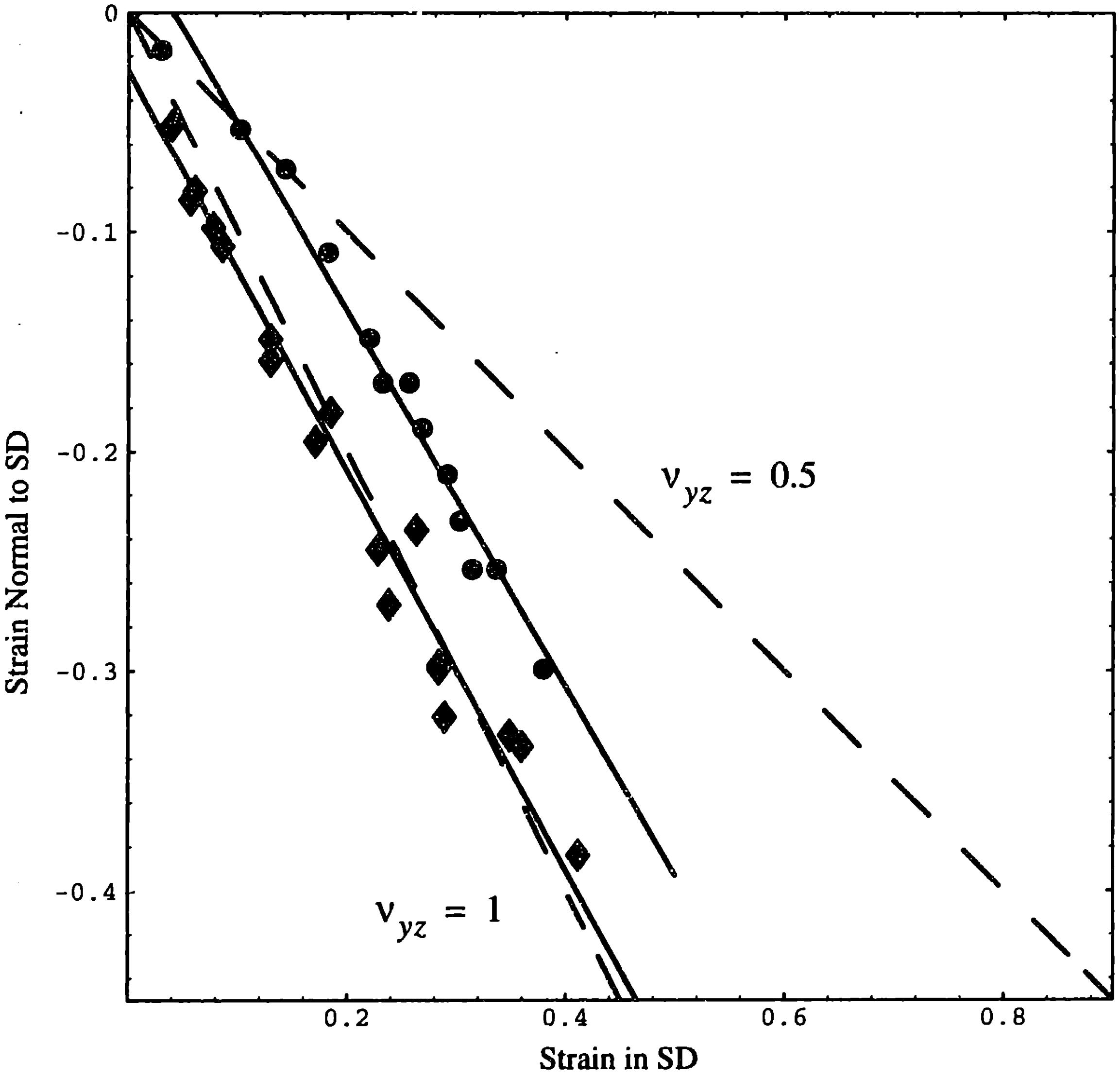

Figure 5-46: Plot of strain normal to the SD vs. strain in the SD for a perpendicular stretch experiment of an oriented SIS 7.5-35-7.5 sample. Data is taken from (Hadziioannou et al., 1979). Note that the hexagonal lattice of Hadziioannou et al. is rotated by 60° with respect to the SD in comparison to roll-cast samples. Both direct space measurements of the sample dimensions (diamonds) and reciprocal space measurements of the lattice (circles) have nearly the same slope in this plot. The real space fit yields the equation: $y = -0.86*x + 0.035$ with $R^2 = 0.976$. The reciprocal space data fit yields the equation: $y = -0.91*x - 0.027$ with $R^2 = 0.976$. The dashed lines indicate a Poisson ratio of 0.5 and 1, respectively. The fits agree well with the fit in Figure 5-45.

between that represented by the SAXS patterns of the Figure 5-38 (65% strain) and Figure 5-39 (143% strain), consistent with the macroscopically measured 120% strain. The initially hexagonal lattice has been distorted, but the distortion is not uniform. Parts of the

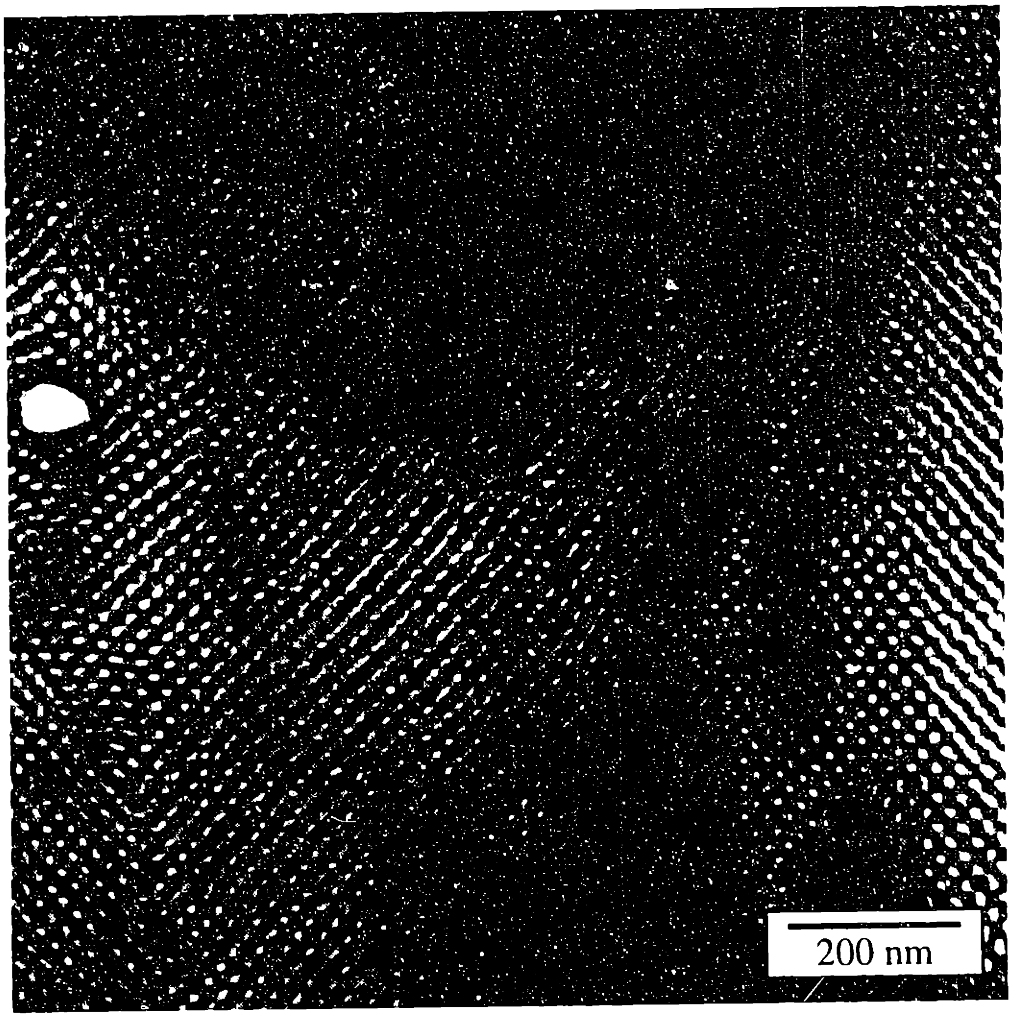

Figure 5-47: TEM image viewed down the original [0001] axis of a roll-cast SIS 15k-72k-15k sample stretched to 624%, irradiated and unloaded to 120% at parallel incidence (see Figure 5-26). The initially hexagonal lattice is distorted by the deformation field (vertical). Note the faulting of the lattice in the lower left and right sides respectively.

image show white dots indicative of projections down the cylinder axis. Other parts of the TEM image show layer lines with modulations in the white layers. These layer lines have two dominant orientations with respect to the SD. They impinge to form boundaries that are reminiscent of twin boundaries (see Figure 5-47, lower right). Since a twin boundary is characterized by a twinning plane and a twin axis (Cullity, 1978), the grain boundaries viewed at parallel incidence cannot be called twin boundaries in the strictest sense, as the lattice is not clear enough at the boundary to discern both a twinning plane and a twinning axis.

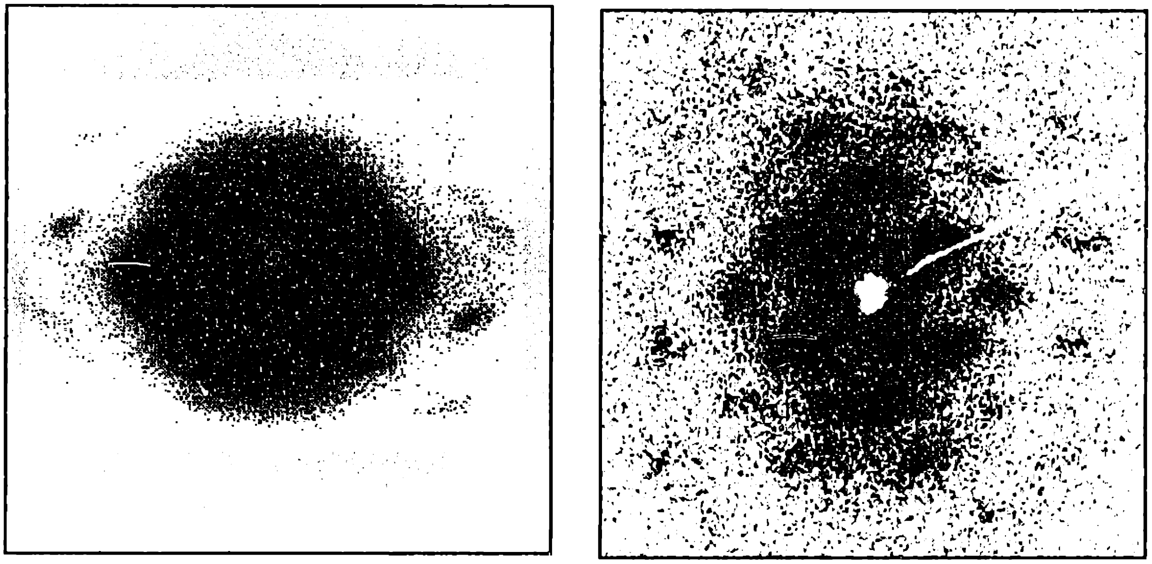

Figure 5-48: Left: SAXS pattern at parallel incidence (x-direction) of the sample stretched to 624%, irradiated and unloaded to 120%. The distorted hexagonal pattern is akin to the patterns in Figure 5-38 and Figure 5-39. Right: Optical transform of TEM negative used to make Figure 5-47.

A series of digital FFTs demonstrates the nature of the distorted hexagonal lattice more clearly (Figure 5-49). The digital transform of Figure 5-47, which is shown in Figure 5-49b, is almost identical to the optical transform in Figure 5-48. By thresholding the original FFT and passing the eight strongest peaks about the origin before performing the reverse FFT, the faults in the real space image (c) become more visible. In fact, keeping the four strongest peaks about the origin (f) is sufficient to reproduce the fault boundaries (see (e)), though the contrast is inverted in many of the cylinders (compare (e) with (c)). The spacing between the fault boundary on the left and the fault boundary on the right in Figure 5-49c is approximately 0.7 μm. However, microscopy results over larger areas indicate that the fault boundaries are spaced aperiodically. The average fault boundary spacing is on the order of 0.1 μm. Finally, the peaks found along the two principal directions can be selected via thresholding and subsequent windowing (i). This case specifically examines the spatial frequencies used in the SAXS data to follow the distortion of the lattice in the y-z plane (e.g., to determine the Poisson ratio). The peaks parallel and perpendicular to the stretching direction (in (i)) correspond to the periodicities of the rectangular lattice (h) in these two principal directions. Using the unloading curves of Figures 5-41 and 5-44 for the $\sqrt{3}$ and $\sqrt{1}$ peaks at spacings of 160Å and 140Å respectively, one can deduce a strain of approximately 90% for the TEM image of Figure 5-47.

Figure 5-49: on page 185: Series of digital FFT pairs taken from Figure 5-47. (b) is the FFT of the original image (a) and agrees with the OT in Figure 5-48. Filtering the strongest peaks via thresholding (d) and (f) makes the faulting of the distorted hexagonal lattice clearer (c) and (e). Faulting is apparent in the lower left and all along the right side of the images. Filtering the peaks parallel and perpendicular to the SD provides an indication of the lattice (h) which is measured via SAXS by the $\sqrt{3}$ and $\sqrt{1}$ peaks, respectively.

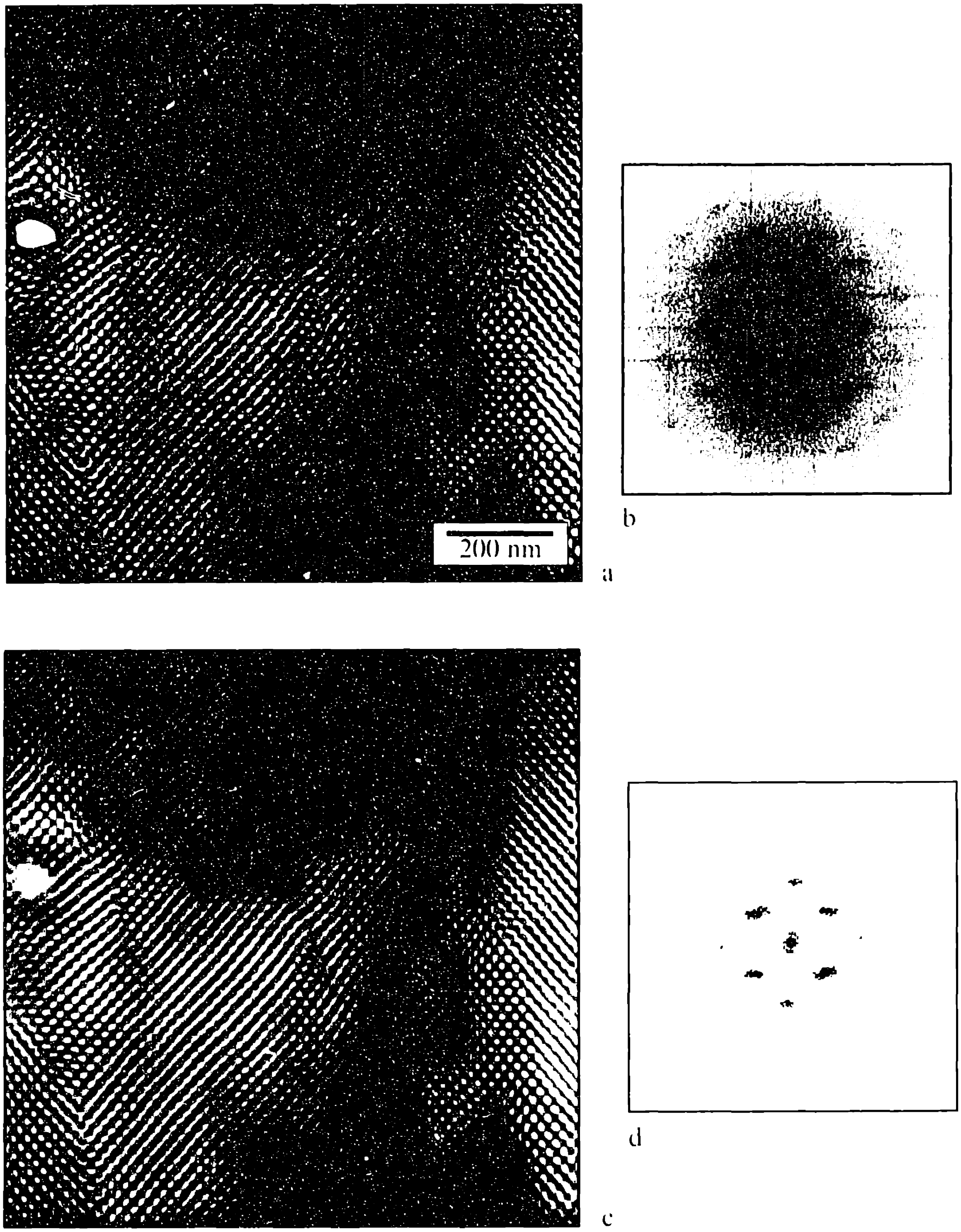

Figure 5-49 caption on page 184.

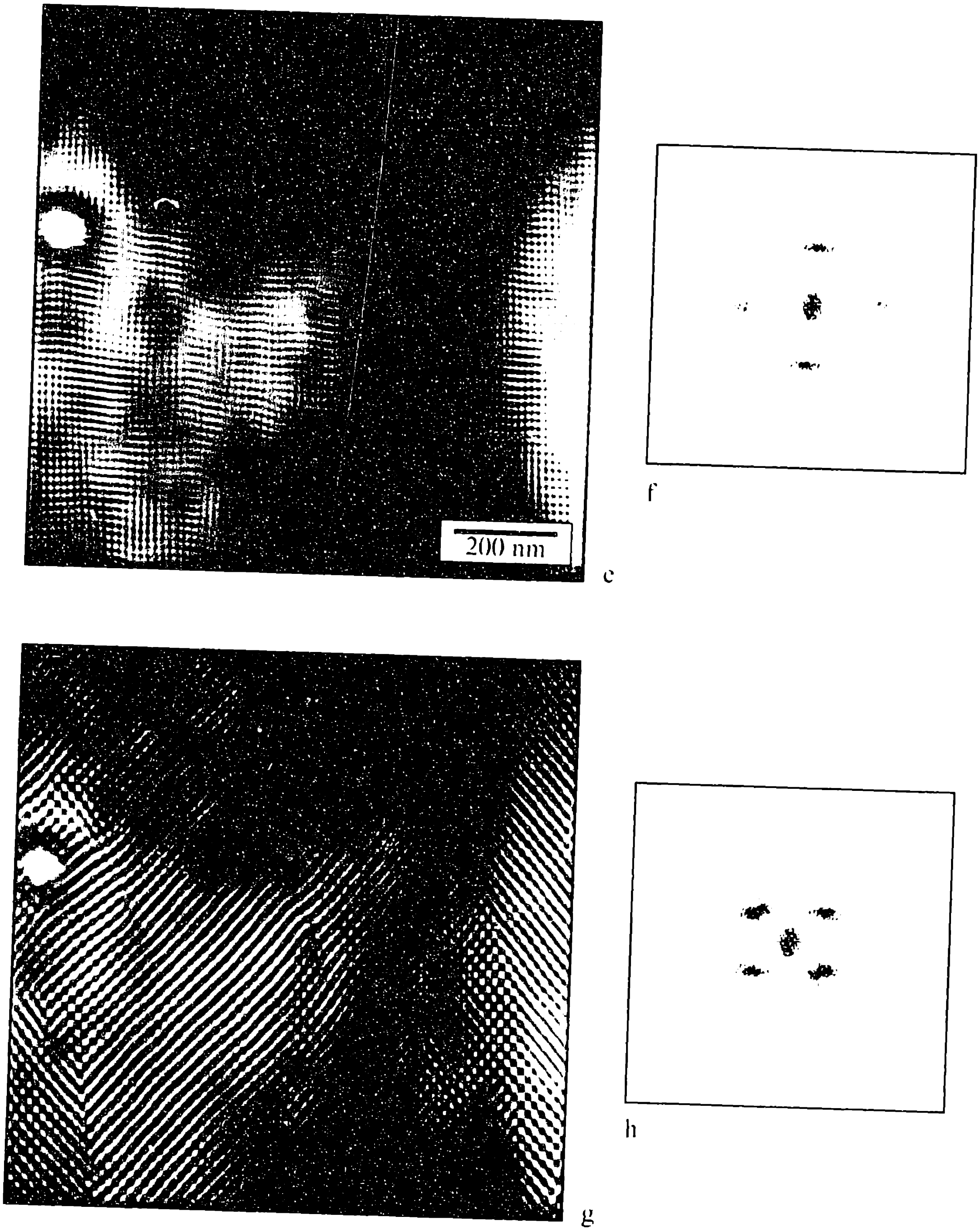

Figure 5-49 caption on page 184.

5.3.2.2 180% Deformation

Examination at parallel incidence of the sample with 180% permanent deformation shows the faulting even more markedly than in the sample with 120% permanent deformation (Figure 5-47). Figure 5-50 shows a parallel incidence micrograph clearly showing both "up" and "down" fault boundaries at a fairly acute angle. The distorted hexagonal lattice of Figure 5-47 is no longer distinguishable. The similarity of the 2-D SAXS pattern of the irradiated sample (Figure 5-51) is consistent with 2-D SAXS patterns

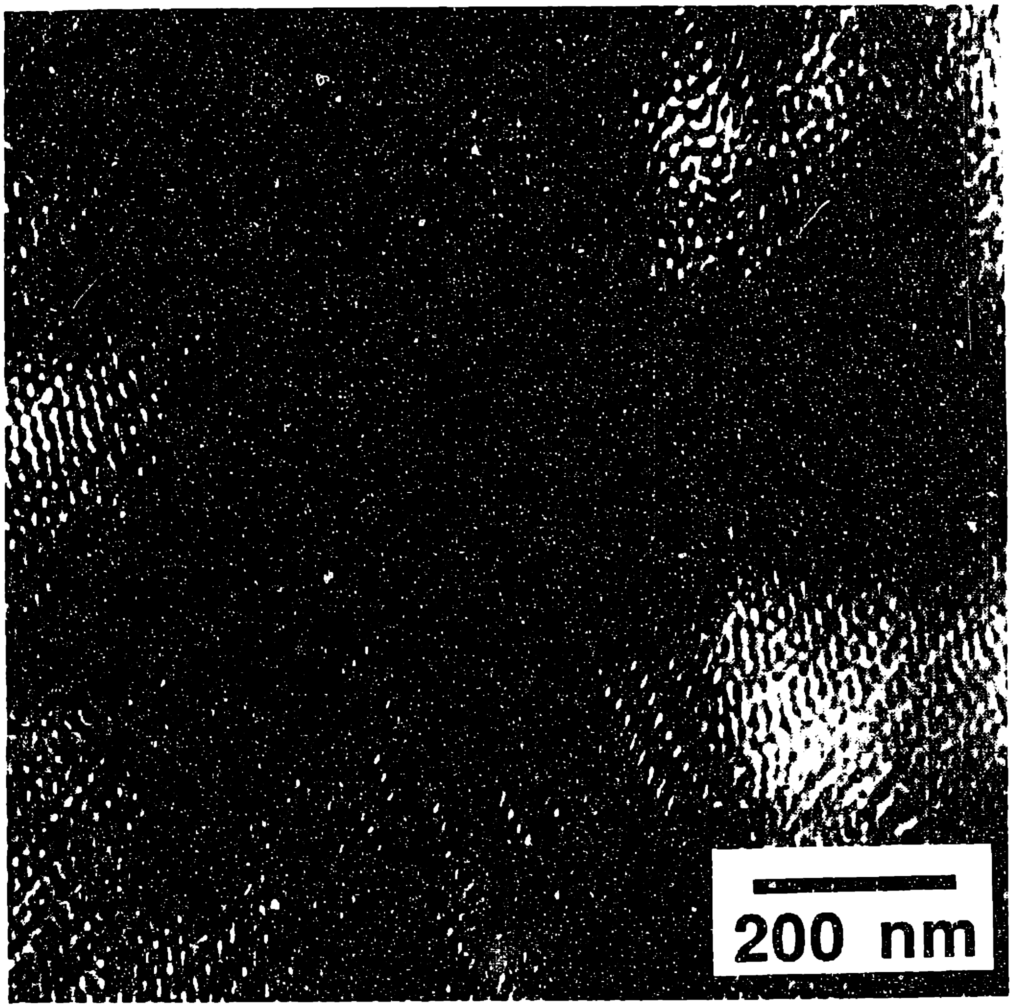

Figure 5-50: TEM image of a roll-cast SIS 15k-72k-15k sample stretched to 410%, irradiated and unloaded to 180% at parallel incidence. The distorted hexagonal lattice of Figure 5-47 has been reduced to a set of layer lines at two distinct orientations with respect to the deformation field (vertical). The layer lines have modulations in contrast and meet at boundaries which are aligned with the SD. Note the "up" and "down" orientation of faulting on the lower left and right sides, respectively.

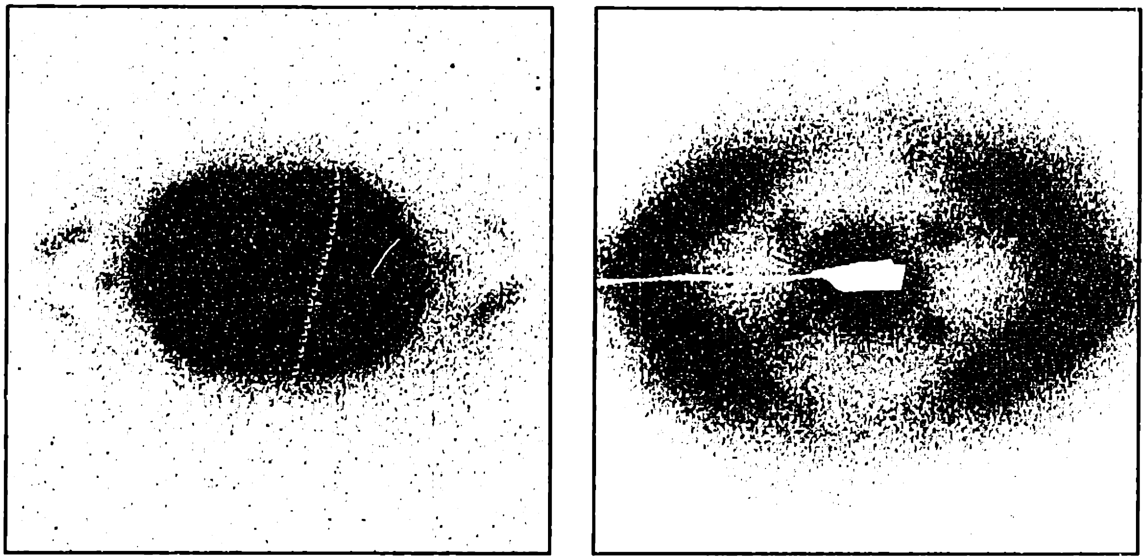

Figure 5-51: Left: SAXS pattern at parallel incidence (x-direction) of the sample stretched to 410%, irradiated and unloaded to 180%. The distorted hexagonal pattern is akin to the patterns between those in Figures 5-39 and 5-40. Right: Optical transform of TEM negative from Figure 5-50.

from the dynamic stretching experiment shown in Figure 5-39 (143% strain) and Figure 5-40 (374% strain). The OT in Figure 5-51 shows information on two length scales. At low values of q, there are four sharp spots which correspond to the spacing between the layers. These spots are equivalent to the strong four peaks in the SAXS pattern at left. At high values of q, the four streaks above and below the equator arise from the modulations within the layers. The streaking is due to the lack of perfect correlation of the modulations in the layers. To investigate the origin of the peaks at the different length scales, Fourier filtering was performed. Figure 5-52 shows a set of FFTs and their corresponding real space transforms. The image was taken from the tilt series (Figure 5-53 (g)). The digital transform shows the same basic pattern, with four strong inner spots and a pair of streaks at high q. The first image/FFT pair in Figure 5-52 represents equivalent views of the TEM micrograph in real (a) and reciprocal (b) space. Selecting the three peaks of the right "arm" of the X from the five inner peaks (d), results in a set of wavy layer lines tilted towards the right in the real space image (c). Figure 5-52 (e) was created by the inverse Fourier

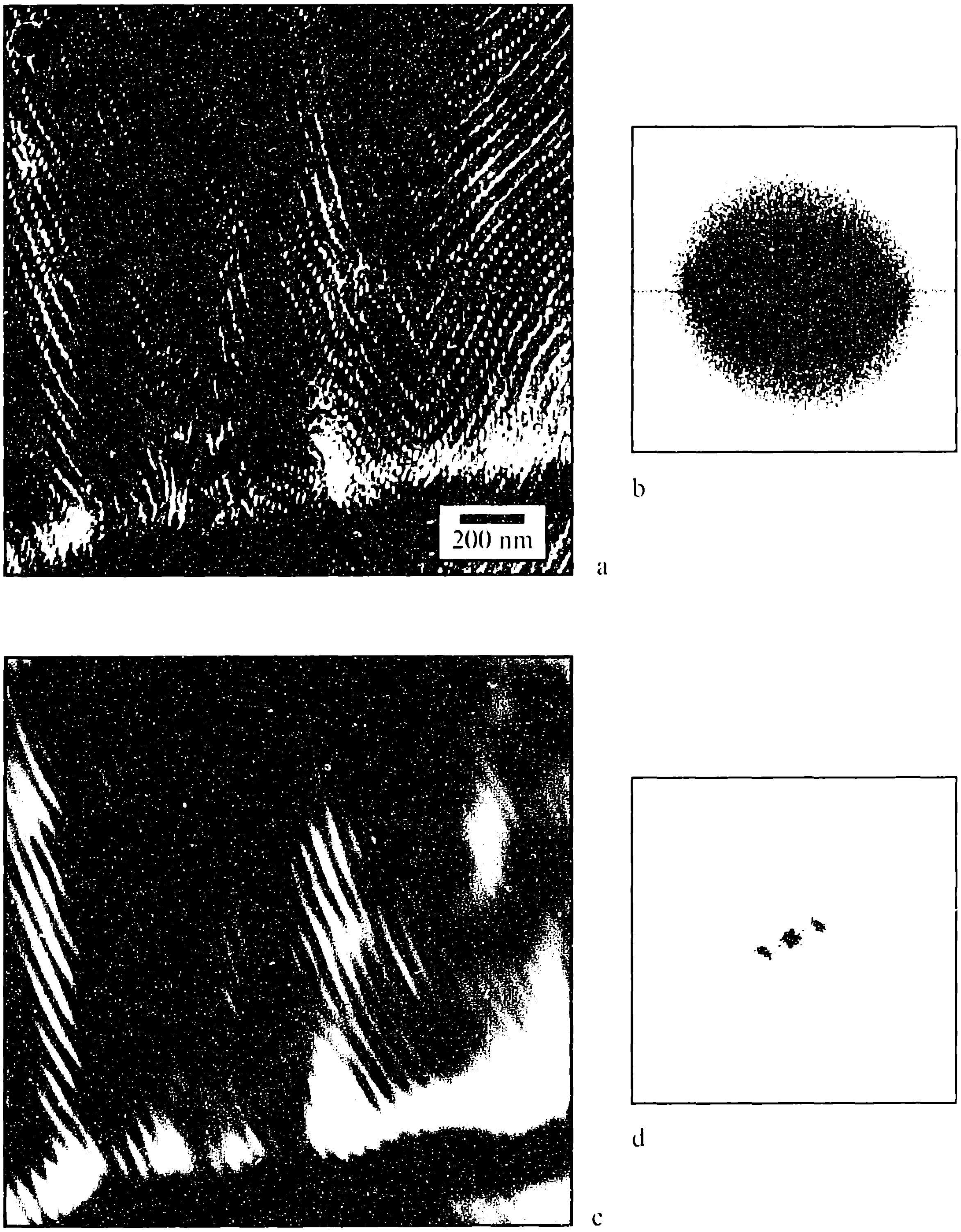

Figure 5-52 caption on page 195.

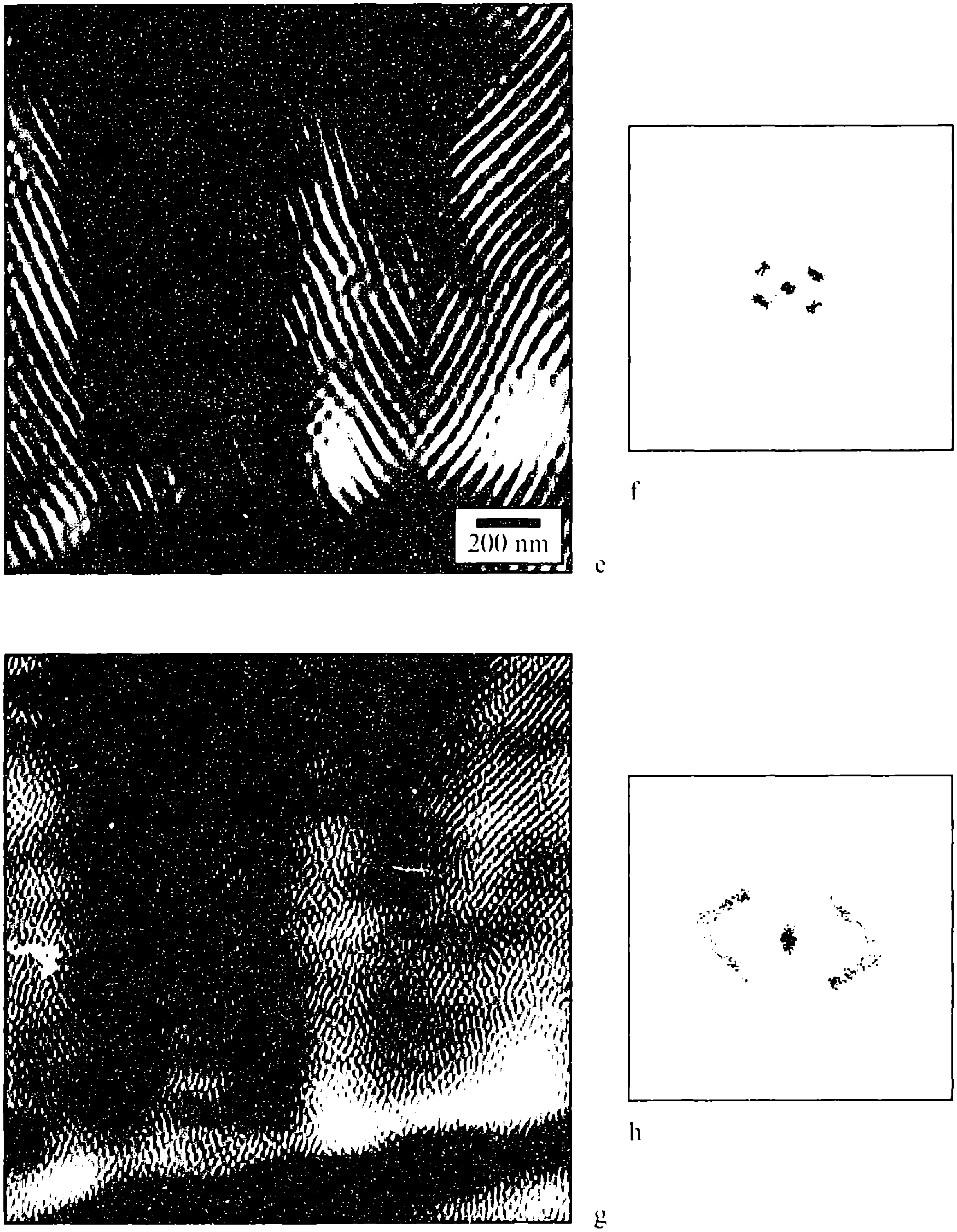

Figure 5-52 caption on page 195.

transform of (f) which selects the five sharp spots at low q. As can be seen in the real space image (d) these spots contain information about the layer spacings. Note that the boundaries between the two layer orientations can be discerned. The shape of the regions of layer lines between fault boundaries is long in the SD (z-direction) and thin normal to the SD (y-direction). The average correlation width between faults is approximately 0.2 µm. This small width causes a broadening of the corresponding peaks in the FFT (f) due to the shape transform effect mentioned earlier. Windowing the streaks at high q, (f) yields information about the modulations within the layers at smaller length scales not the layer lines nor the fault boundaries. Interpreting images based on Fourier filtering can be misleading as there are a variety of artifacts that can be introduced into the filtered image depending on the windowing conditions (Pradere et al., 1990). These images are only being used to distinguish the origin of the two sets of information contained in the OT of Figure 5-51.

Figure 5-52: on page 191: Series of digital FFT pairs taken from Figure 5-53 (g). (b) is the FFT of the original image (a). Passing the strongest pair of peaks in the right arm of the inner X (d) results in a fringe forming on the left side and slightly right of center in the image (c). Combining the strongest peaks in both arms of the inner X (f) results in both sets of fringes to make up a chevron pattern. Notice the cross-hatched regions at the boundaries between left and right fringes (e). This is an artifact of the filtering known as ghosting (Pradere and Thomas, 1990). Finally, the scattering at high q (h), arises from a finer scale modulation in contrast with the same orientation as the fringes observed at larger length scales (g). These modulations come from the cylinders within the layers seen in (a). Thus, the FFT (b) of the image (a) shows information on two length scales, the peaks at low q from the larger spacing between layers, and the scatter at high q from the inter-cylinder spacing within the layers.

In both Figure 5-48 and in Figure 5-51 the difference between the SAXS pattern and the OT is due primarily to a difference in sampling volume. As mentioned in Section 5.1.2.2, the OT comes from a sampling volume of approximately 1 μm^3, while the SAXS sampling volume is on the order of 1 mm^3. The essential elements of the lattice distortion at parallel incidence are common to both sets of reciprocal space data, however. In Figure 5-48 the six peaks making up the $\sqrt{1}$ peak family are present in both SAXS pattern and

OT, though in the former case there is much more streaking of the four non-equatorial peaks in the y-direction. In Figure 5-51 the four strong inner peaks in the OT correspond to the four most intense (and broadened) $\sqrt{1}$ peaks in the SAXS pattern. The diffuse scatter at high q observed clearly in the OT corresponds to the four faint peaks at the edges of the SAXS pattern. The $\sqrt{1}$ peaks along the equator are almost entirely suppressed by the zero of the form factor in the SAXS pattern and are altogether missing in the OT.

Tilting the TEM sample clarifies the origin of the contrast modulations within the layers. Figure 5-53 shows a tilt series of micrographs and their corresponding OTs. The layered structure with contrast modulations is observed at tilts of +10 and -10 degrees. The OTs are, however, asymmetric as one set of layer lines are obscured by overlapping cylinders. At a tilt angle of -30° the modulations have resolved themselves into white dots indicative of a projection down the cylinder axis. The OT has gained the other pair of the four inner spots as well as the outer streaks to become symmetric. It is clear from the tilt series that the cylinders are no longer oriented with their axes along the TEM section thickness direction, but have all been tilted by the deformation. The amount of tilt relative to the thickness of the section is such that a normal incidence TEM projection will result in an image made up of overlapping white (PS) and dark (stained rubber) regions. It is only because the spacing between cylinders in the stretching direction is so much larger than any other spacing that a layered structure is observed. The cylinders within the layer are spaced too closely to be distinguished at normal incidence and it is only by tilting the section with respect to the incident beam that the overlap is reduced to an extent that the individual cylinders can be resolved. The pattern of cylinders is chevron-like in nature, with cylinder-layers oriented at fixed angles with respect to the SD. The boundaries between layers are sharp, but since the cylinders are discrete in this plane, they are not significantly affected by the boundaries. The spacing between boundaries is even more variable than the chevron boundaries observed in perpendicular incidence.

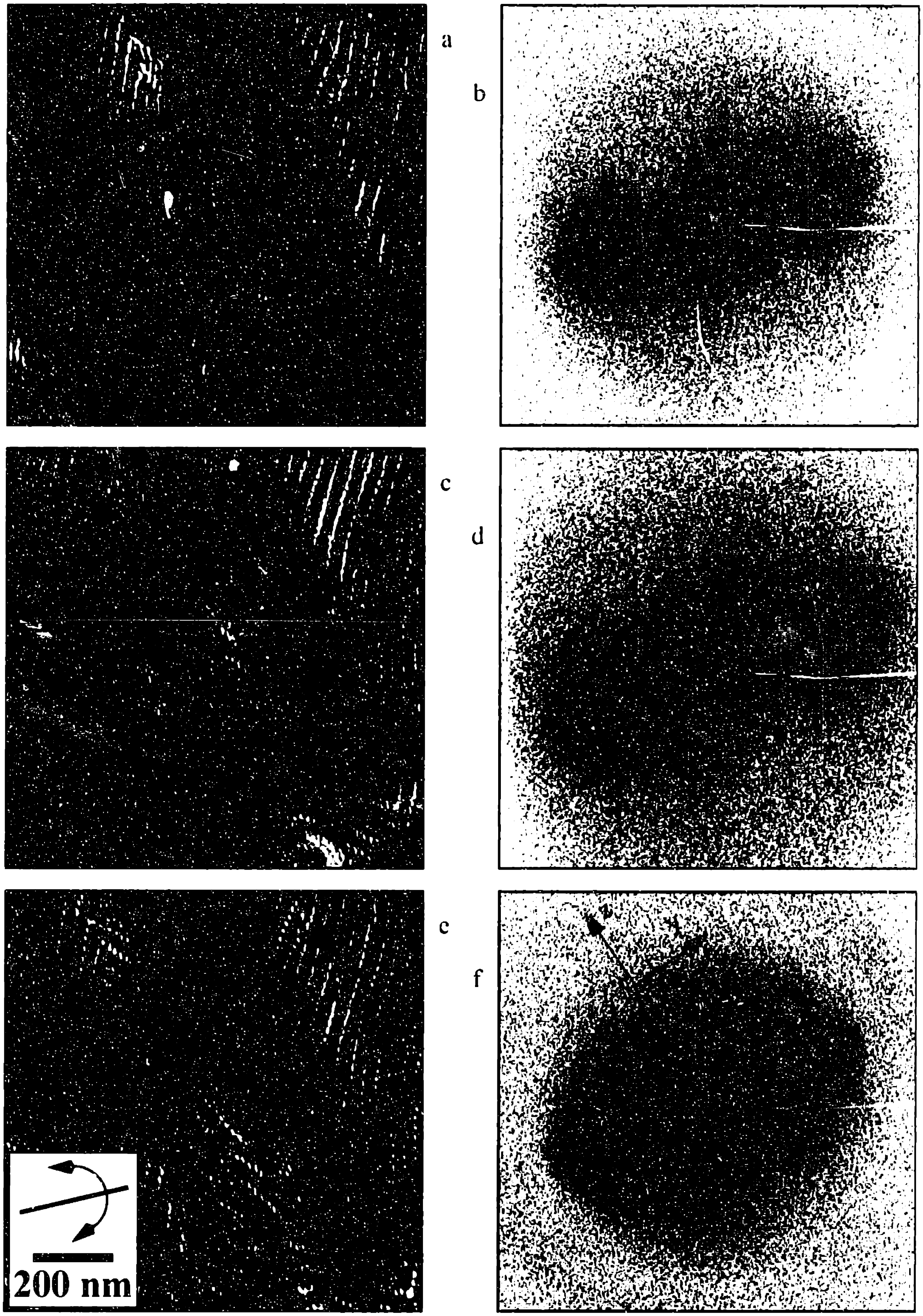

Figure 5-53 caption on page 201.

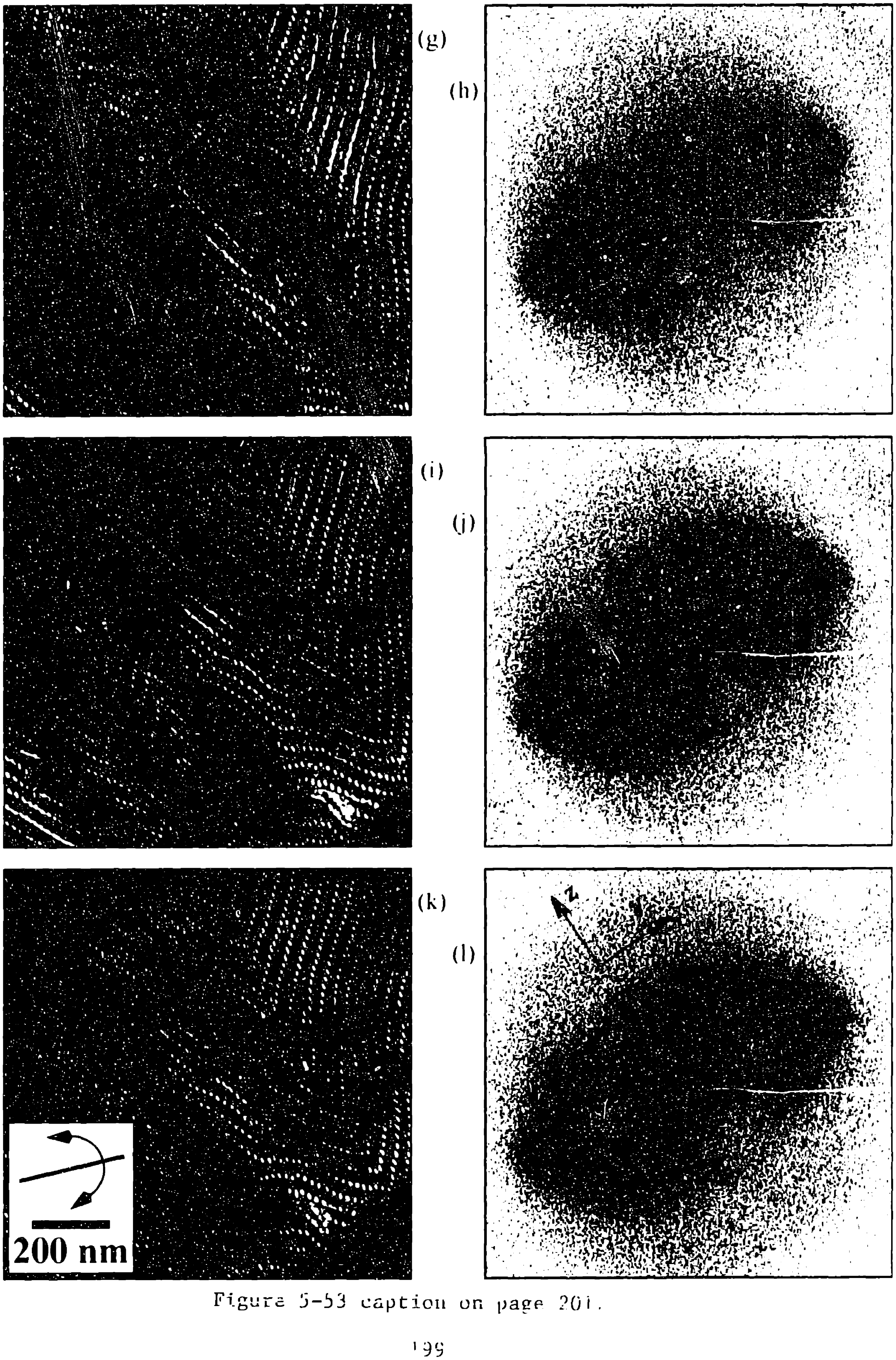

Figure 5-53 caption on page 201.

Figure 5-53: on page 197: TEM micrographs of a tilt series of a sample stretched in the perpendicular direction to 410%, irradiated, and unloaded to 180% and finally viewed along the cylinder axis (x-direction). Each real space image/optical transform pair is viewed at a different tilt angle about the tilt axis indicated: (a, b) at +10, (c, d) at -10, (e,f) at -20, and on page 199 (g, h) at -30, (i, j) at -40 and (k,l) at -45 degrees. Notice that as the tilt angle increases, the fine layers at small spacing in (a) are actually a result of overlapping cylinders in projection. The initial 1-D OT in (b) with a pair of peaks at low q and diffuse scatter at high q transforms via tilting to gain another pair of peaks and diffuse streaks. The peaks at low q contain the information about the large spacing between layers of cylinders (e.g. in (i)), while the streaks at high q reflects the smaller spacing between cylinders within the layers and the lack of long-range correlation between cylinders in adjacent layers in the y direction.

5.4 Stretching Direction Incidence

The irradiated samples enable information to be gained in all three orthogonal dimensions. Information about the SD cannot be gained in the dynamic experiments due to the restrictions imposed by the stretching apparatus. SAXS patterns of both the Raychem and the HVL samples indicate that the cylinders remain predominantly oriented in the x-z plane and do not rotate about the SD during the course of the deformation. Figure 5-54 shows SAXS data for the two irradiated samples. The pattern at left was taken at Princeton by Dr. D. A. Hajduk in Prof. S. M. Gruner's laboratory, while the pattern at right was taken at Brookhaven National Laboratory. In both cases the Bragg scattering is weak, mostly likely because the $(\bar{1}010)$ and $(10\bar{1}0)$ planes, which are the main contributors to the observed reflections, are near the zero of the form factor. The intense streaking emanating from the origin in the y-direction is due to void scatter. The irradiation of these samples causes voids which scatter light (observed in the whitening of the sample) and x-rays at low angles.

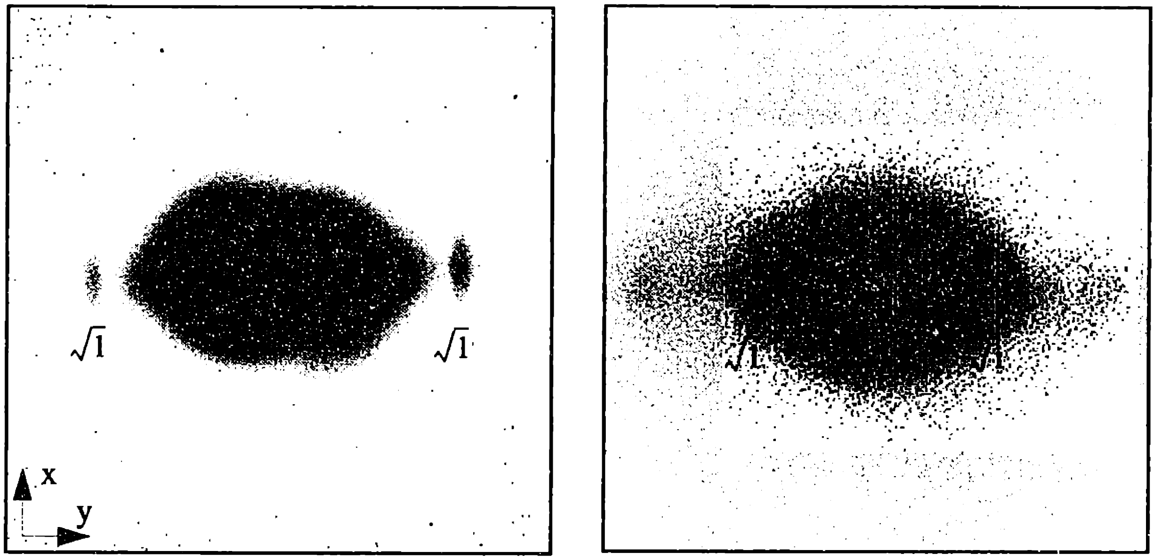

Figure 5-54: 2-D SAXS patterns with the x-ray beam incident along the SD (z-axis). Left: sample stretched to 620%, irradiated and unloaded to 120% strain. The pattern was taken at Princeton by Dr. D. A. Hajduk. Right: sample stretched to 410%, irradiated and unloaded to 180% strain. Note in both cases the absence of any significant rotation of the cylinders about the SD (z-axis). Note that the patterns are not printed at the same scale.

5.5 3-D Model of Deformed Structure at Large Deformations

The real and reciprocal space data at large deformations can be assembled into a 3-D model of the deformed structure. In perpendicular incidence (y-direction), the chevron structure is observed. Figure 5-55 shows a 2-D schematic of the chevron structure at approximately 180% deformation. The spacing of the tilt walls is aperiodic, but an average distance between walls (correlation length) is estimated to be approximately 5 μm.

The structure, when examined at parallel incidence (along the x-direction), is complicated by the discrete nature of the cylinders in the y-z plane. At large deformations the hexagonal lattice is not only distorted by the deformation, but also undergoes a localization phenomena whereby faults in the packing of the cylinders give rise to a second chevron-like texture. Figure 5-56 attempts to clarify this structure. The cylinders have arranged themselves into layers which appear reminiscent of twin boundaries often found in atomic crystals.

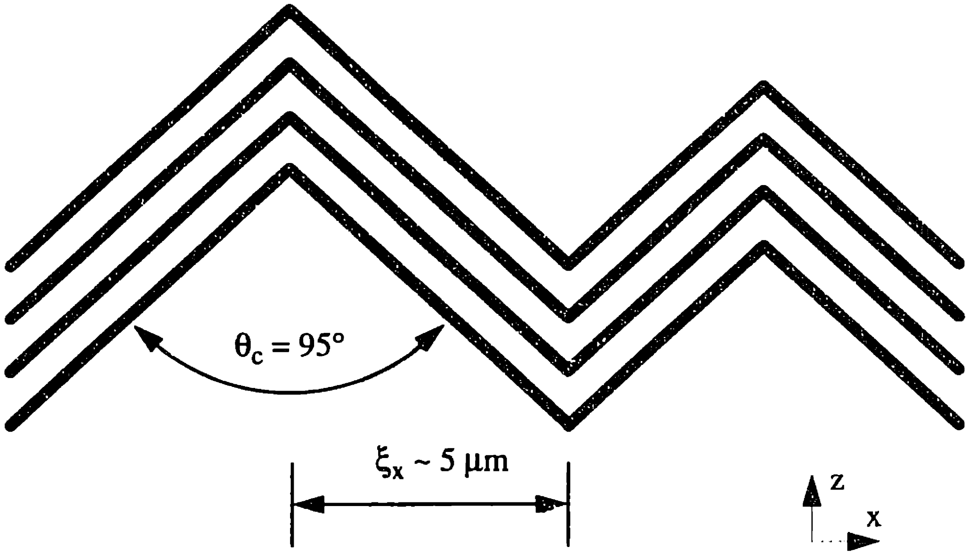

Figure 5-55: 2-D schematic of the chevron texture observed at perpendicular incidence for the irradiated sample at a strain of 180%. Though the tilt boundaries are spaced aperiodically, a correlation width (ξ_x) is estimated at approximately 5 μm.

Combining these two 2-D schematics with the fact that the cylinders do not rotate about the SD enables a 3-D schematic of a deformed "grain" to be drawn (Figure 5-57). All of the bent cylinders are "in phase" with one another so that the lateral packing (in the y-direction) is not constrained by the bending.

Due to the various sources of misalignment, the kinking of the cylinders is not expected to occur simultaneously and uniformly throughout the volume of the sample. Rather, areas of the greatest cylinder misalignment will serve as nucleation sites forming "grains" of bent cylinders which are initially uncorrelated from one another. Upon further deformation and transformation of undeformed material into kinked cylinders, the grains will begin to impinge. To minimize the elastic strain energy at these "impingement boundaries", the kinked cylinders must accommodate any misregistry in the phase difference of kinking and faulting.Figure 5-58 is one attempt to show how various kinked regions may meet upon impingement.

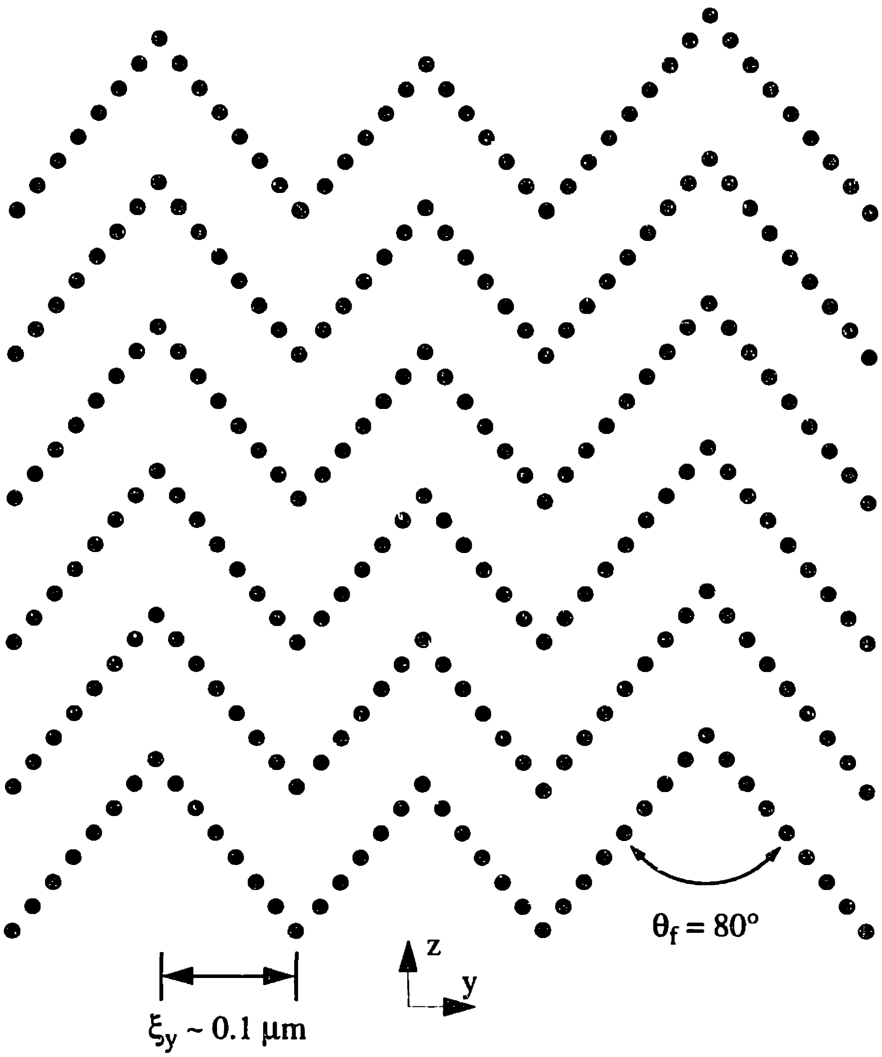

Figure 5-56: 2-D schematic of the faulting texture observed at parallel incidence for the irradiated sample at a strain of 180%. Though the fault boundaries are aperiodically spaced, a correlation width (ξ_y) is estimated at approximately 0.1 μm.

5.6 Mechanics of the Perpendicular Deformation

5.6.1 Low strain regime

In light of the available data, a mechanism is proposed to explain the deformation process during a perpendicular stretching experiment. As the sample begins to deform, the cylinders move apart along z in an affine manner. The SAXS data taken with the x-ray beam in both the perpendicular incidence (Figure 5-24) and the parallel incidence (Figure 5-42) show an increase in spacing between cylinders in the SD, which is nearly equal to the

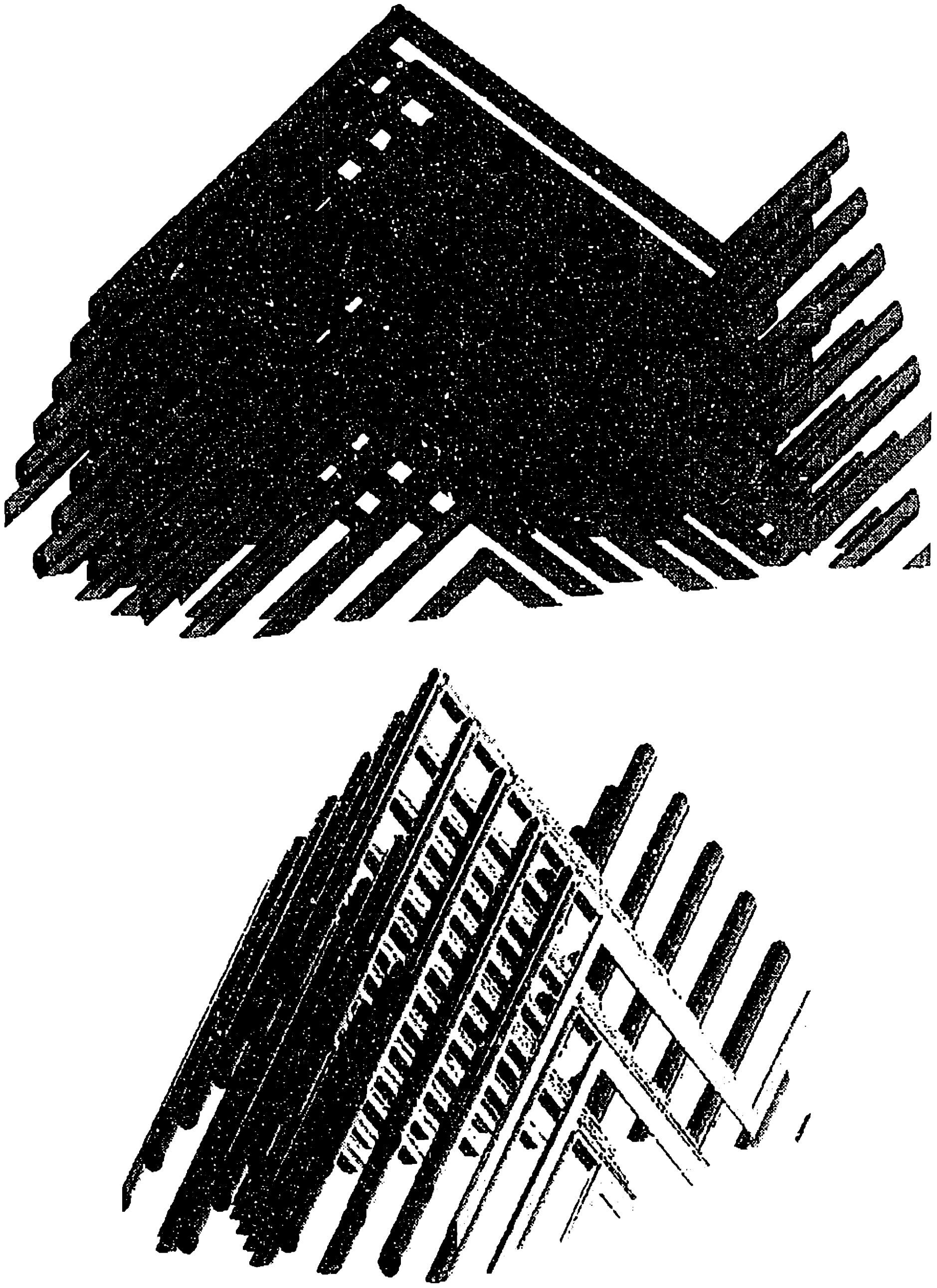

Figure 5-57: 3-D schematic model of the structure deformed to approximately 180%.
Top: perspective view emphasizing the bent cylinders.
Bottom: perspective view demonstrating a fault in the axial packing of the bent rods. Note that the fault angle in the bottom schematic is more acute than the chevron angle in the top schematic.

macroscopic applied strain. The rubber matrix, being intimately connected to the PS cylinder via covalent bonds, follows the movement of the cylinders. The cylinders therefore, act as markers for the deformation of the matrix. As the rubber expands in the

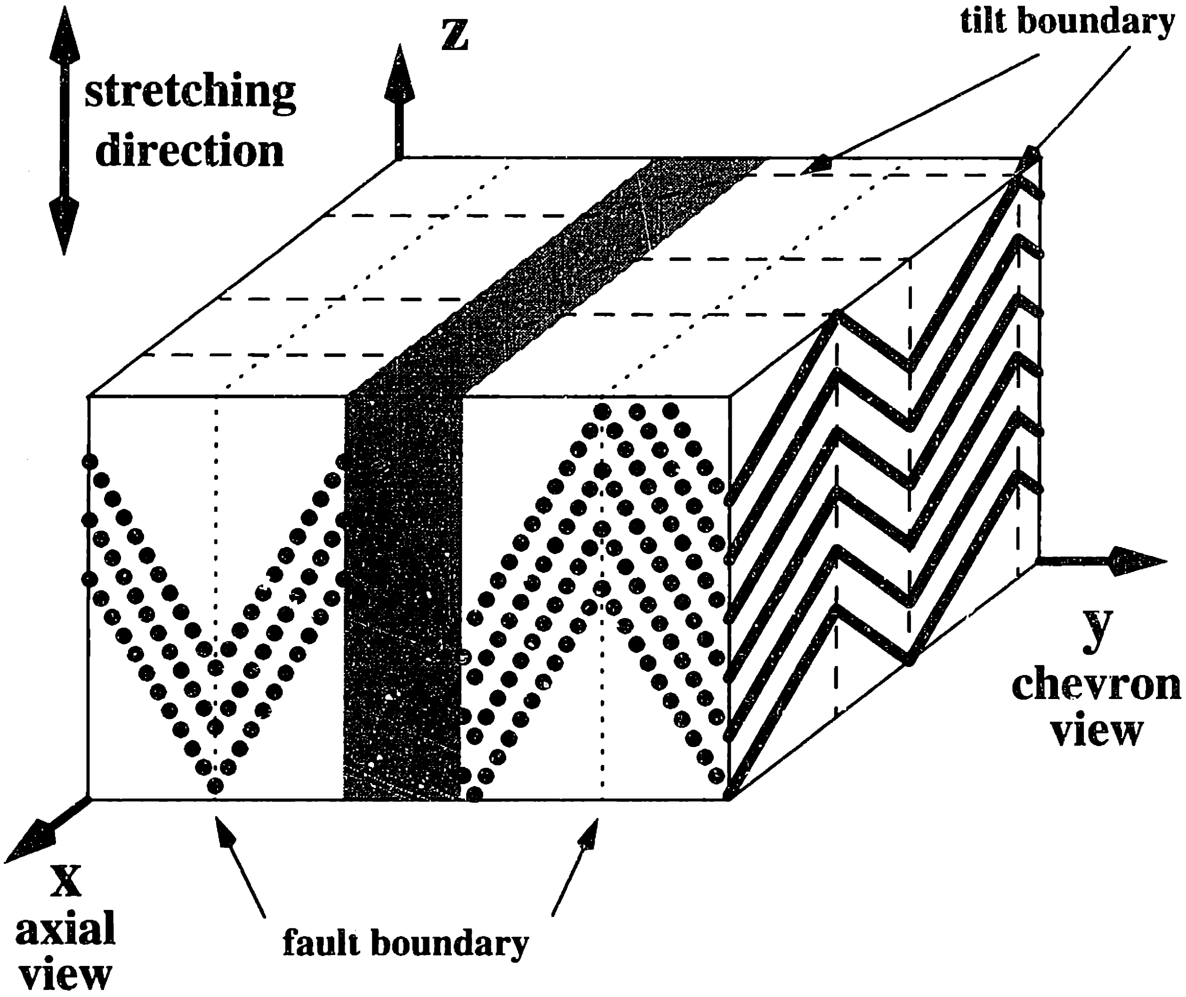

Figure 5-58: 3-D schematic model showing the relationship between two regions which have kinked independently of one another. The gray area represents the volume over which the tilt boundary shifts in the x-direction to "link-up" with the tilt boundary of the same direction. The lattice in the x-z plane readily accommodates these tilt boundary shifts by forming fault boundaries as needed.

SD, it contracts in the lateral direction in an attempt to preserve volume. This lateral contraction can be monitored by the movement of the Bragg peaks arising from the $(\bar{1}010)$ and $(10\bar{1}0)$ planes along the equator. Data from Figure 5-45 show that the lateral contraction in the y-z plane is larger than that expected for an ideal rubber. This surprising result can be understood if the anisotropy of the structure is kept in mind. While the matrix is being stretched in the SD, it attempts to contract in the plane normal to the SD in order to preserve volume. Since the cylinders are all oriented in the x-direction, the matrix is also constrained in the x-direction. The direction of least PS-resistance to contraction is therefore the y-direction, which then experiences a preferential contraction much greater than that of an unconstrained isotropic rubber.

For an ideal fiber-reinforced composite of perfectly oriented incompressible fibers (oriented along the x-direction) perfectly adhering to a rubbery matrix, one can anticipate that for every unit of perpendicular extension (along the z-direction), one unit of lateral contraction (along the y-direction) would result. The Poisson ratio in the y-z plane would be equal to 1, while the Poisson ratio in the x-z plane would equal 0. Hence, the rubbery matrix would continue to undergo a constant volume deformation. However, but due to the fibers aligned in the x-direction, the matrix deformation is constrained to the y-z plane. The Poisson ratio of approximately 0.9 as measured in Figure 5-45, (albeit with only four data points) agrees with a previous and more accurate measurement from the literature (see Figure 5-46).

Several possible reasons exist for why the experimentally measured Poisson ratio does not equal that of the ideal case. Perhaps the most significant of these is the misalignment of the cylinder axis with respect to the compression direction. If the cylinder normals are not perfectly aligned along the SD, the effectiveness of the cylinders in resisting the compressive force of the matrix is drastically reduced. Sample preparation and alignment may exacerbate this problem, e.g., the tensile specimen may be imperfectly mounted with respect to the SD. Furthermore, the average cylinder normal within the tensile specimen may not be aligned with the sample's long axis due to stamping misalignment. Indeed, a perfectly symmetric X-pattern during a perpendicular deformation experiment is rare (see Figure 5-19). The consequence of cylinder misalignment is that any change in the dimension of the sample in the x-direction reduces the need for the matrix to contract exclusively in the y-direction, thereby reducing the Poisson's ration in the y-z plane.

The constraint in deformation along the x-direction arises not only from the anisotropic morphology, but also potentially from the sample geometry itself. Roll-cast films used for SAXS deformation studies generally have a thickness of approximately 1-1.5 mm in the y-direction. At parallel incidence, the x-ray beam lies in the plane of the roll-cast film (along the x-direction). In these experiments, the tensile specimen has an approximately square cross-section. At perpendicular incidence, however, the x-ray beam is normal to the roll-cast film and the width of the sample is unlimited. Deformation experiments at various widths demonstrate that there is an influence of the cross-section aspect ratio on the load-bearing capacity of the sample (Figure 5-59). Here the width (w) of the sample is the dimension in the x-direction along the cylinder axis, while the thickness (t) is the dimension in the y-direction normal to the cylinder axis. This effect can be understood in terms of the limiting behavior of elastically deformable materials. A sample of infinite width and infinitesimal thickness would be in a state of plane strain under deformation as the width dimension could not change (Chou et al., 1967) (p. 69). As the cross-sectional aspect ratio approaches one, the deformation behavior is better characterized as uniaxial. Since the morphological constraint operates in the width direction, the plane strain condition is further accentuated.

5.6.2 Transition regime

As the axial stress on the PS cylinders increases, local regions of misalignment (defects) are no longer be able to support the compression. A moment between the applied compressive force and the component of cylinder misalignment develops and those moments along the y-axis are promoted at the expense of all others as their development relieves stress in the SD. The result is that the misaligned cylinders turn predominantly clockwise or counterclockwise in x-z plane due to the compression. Resisting the auto-catalytic increase in bending of the cylinders is the shear resistance of the rubber. As the cylinders turn, the rubber matrix between cylinders undergoes shear. This shear resistance

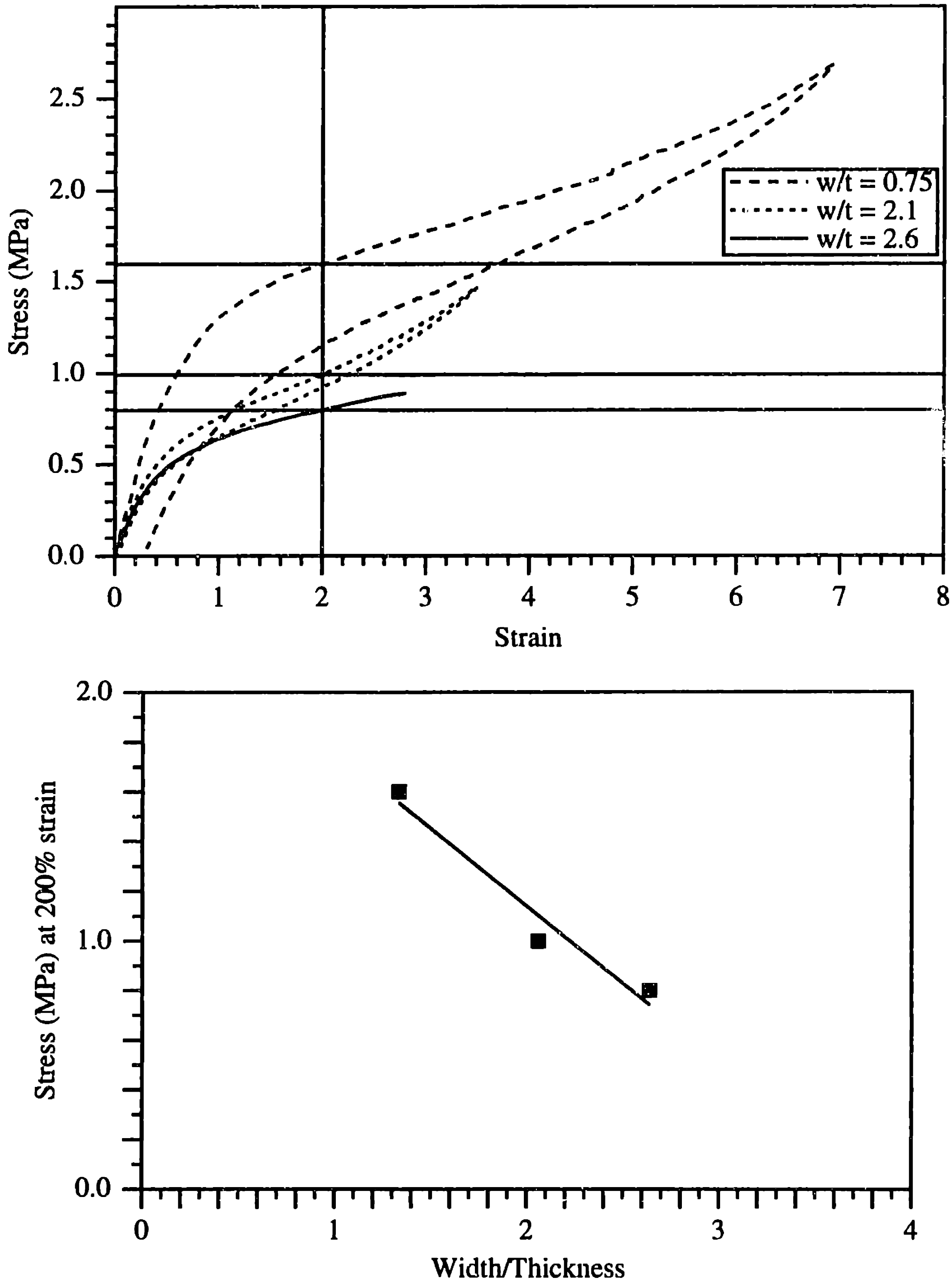

Figure 5-59: Top: Stress-strain plots of roll-cast SIS 15k-72k-15k samples at various cross-sectional aspect ratios. Bottom: Stress at 200% strain vs. cross-sectional aspect ratio (width/thickness). The solid line is a fit to the data: $y = -0.62x+2.4$ with $R^2 = 0.955$.

helps to prevent the misaligned cylinders from kinking immediately upon application of the compressive stress. Since the stress-strain curve does not exhibit a sharp yield point in shear, a specific shear strength for the rubber matrix does not exist. The shear resistance of the rubber matrix increases non-linearly.

Regions of varying degrees of misalignment are scattered throughout the volume of the sample. The kinking process therefore cannot occur simultaneously, but develops in a more continuous manner. Those regions of greater misalignment will nucleate kinks and these grow first, while well-aligned regions continue deforming yet remain unkinked.

In contrast, a perfectly aligned microdomain composite, upon reaching the critical stress, kinks catastrophically. From a continuum standpoint, the stress-strain curve of such an ideal sample would be that of the elastic-perfectly plastic type. The cylinders are stretched affinely until the critical strain at which the cylinders cooperatively kink. However, a continuum treatment ignores the impact of the chain stretching of the matrix rubber which gives the stress-strain curve its shape. Thus, the stress-strain curve at low strains is best modeled as a constrained rubber in plane strain (see Chapter 8). The stress-strain response of an ideal composite would be carry the constrained rubber to higher strains (and stresses) before kinking (Figure 5-60).

"A kink is a localized region of *axial* shear deformation where the deformed region is rotated with respect to the undeformed region." (Vezie, 1993) Kinking is a cooperative process occurring in highly anisotropic materials where easy planes of slip are parallel or nearly parallel to the direction of the applied compressive stress. Kinks can form via buckling or shear instabilities. Elastic buckling is defined for individual columns under axial compressive loads as the rapid increase of lateral deflection at a critical (buckling) stress (Argon et al., 1966). The critical stress is governing primarily by the *stiffness*

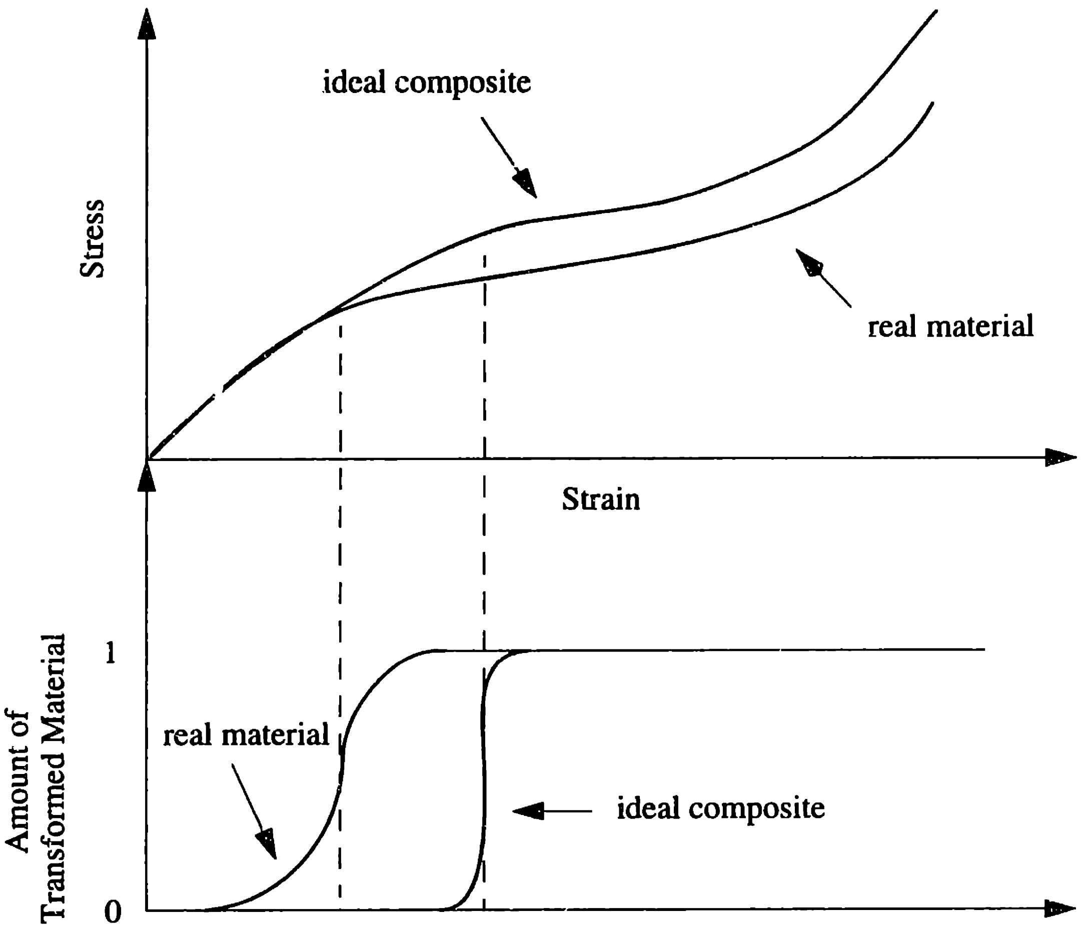

Figure 5-60: Top: Schematic stress-strain plot for a perfect composite vs. a real material in perpendicular deformation. Bottom: Schematic plot of the fraction of material that has undergone kinking. The ideal composite transforms catastrophically, while the transformation of the real material is more continuous.

(modulus) of the fiber. A shear instability, in contrast, is a localized slip from a resolved shear stress on the misoriented region and thus is determined by the shear *strength* of the material.

Kinking of the cylinders undergoing perpendicular deformation arises from a shear instability and not a buckling instability. The critical buckling stress cannot by reached for columns which contain defects or regions of misalignment, instead, it is the shear resistance of the matrix which determines the kinking stress and not the modulus of the PS. One way to help distinguish between kinking mechanisms would be to vary the shear resistance of the matrix and/or the modulus of the cylinders and look for a change in the critical strain for kinking. Both the number and distribution of defects are, however, expected to play a large role in this critical strain, which perhaps may mask the effect of varying the properties of the components.

The faulting observed at parallel incidence is a much less dramatic and absorbs almost no plastic strain energy. There is no qualitatively observable discontinuity in the SAXS patterns at parallel incidence during the deformation. As the hexagon lattice is compressed laterally, the cylinders move closer together (Figure 5-61). However, the reduction in spacing in the y-direction undergoes a transition at approximately 100% strain to a regime in which the spacing decreases only slightly with increasing deformation (see Figure 5-44). The faulting of the distorted lattice (cylinders undergoing shifting in the SD) to pack into a layered structure (Figure 5-56) is expected to be an even more diffuse and continuous process than kinking.

5.6.3 Large Strain Regime

After formation of the X-pattern at 130% strain (Figure 5-21) and splitting of the two $\sqrt{3}$ peaks, further motion of the $\sqrt{3}$ peaks occurs about the origin along the trace of a circle (Figure 5-22). This motion indicates a rotation of the scattering objects at constant q. TEM data (Figures 5-27 and 5-30) suggest, however, that the kinked cylinders turn towards the SD via a shearing process. The question of the mechanism of deformation beyond kinking, i.e., whether the cylinders move via pure rotation or shear, will be discussed in the next section.

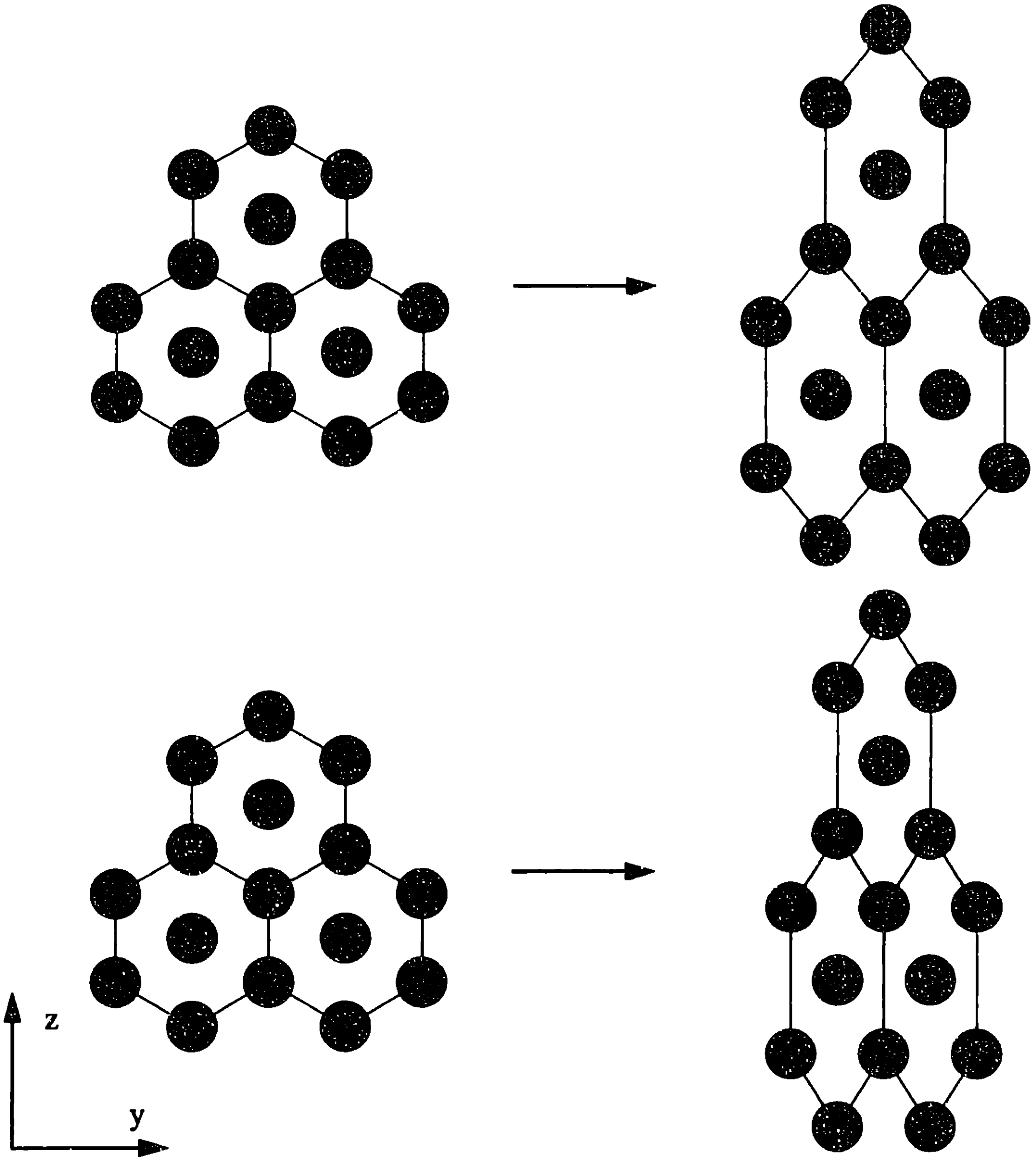

Figure 5-61: Schematic deformation of a 2-D hexagonal lattice to 50% strain (logarithm definition). Top: affine deformation with Poisson's ratio = 0.5. Bottom: non-affine deformation with Poisson's ratio = 1.

Figure 5-62 distinguishes the two cases in real and reciprocal space. Pure rotation requires that q_{rot} remains constant, while for pure shear, q_{shear} increases with θ. The model which accounts for both SAXS and TEM data combines a shearing mechanism with a concurrent increase in D-spacing of the $\sqrt{3}$ peak so that the $\sqrt{3}$ q-spacing remains fairly constant.

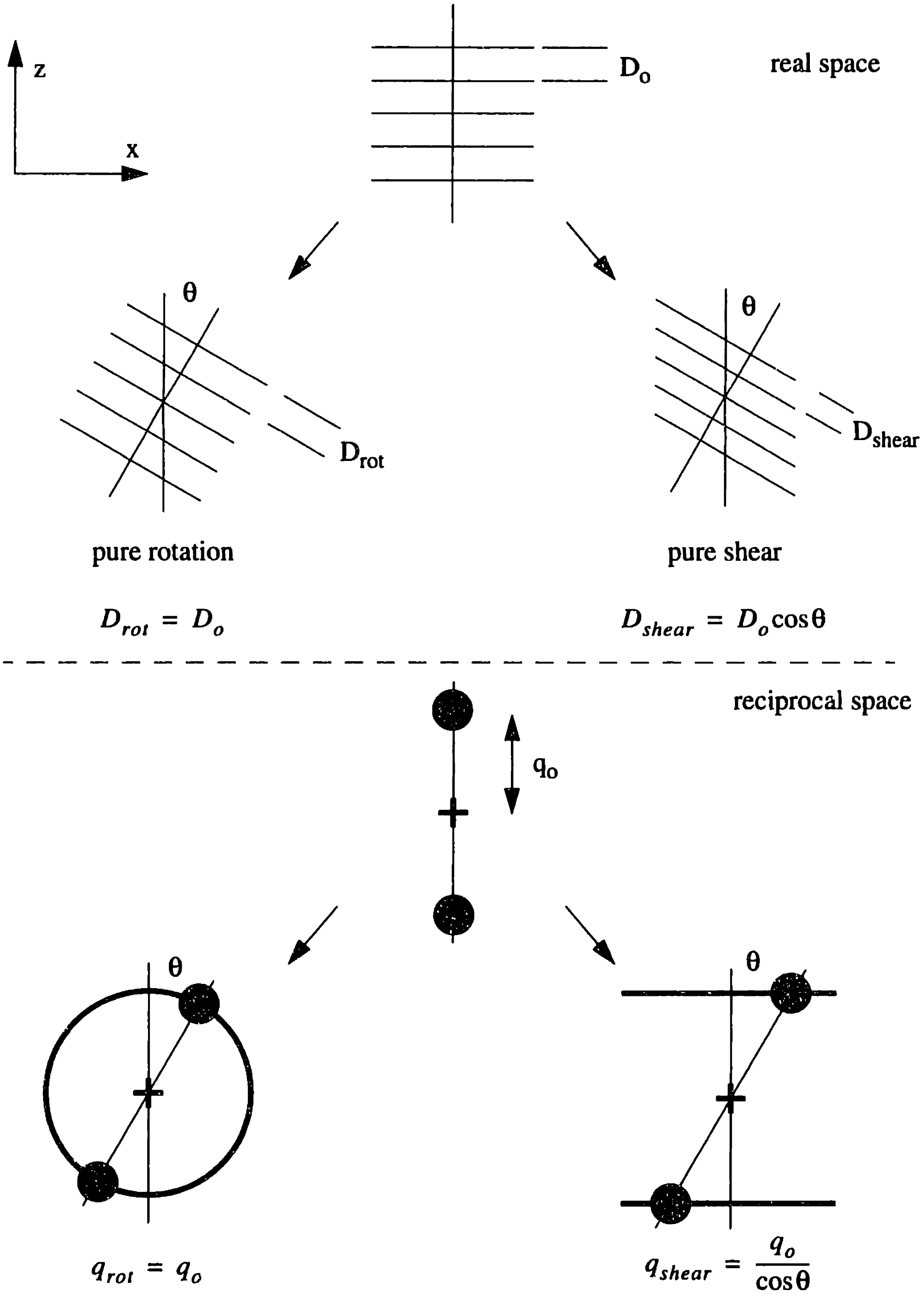

Figure 5-62: Schematic diagram distinguishing pure rotation (left) and pure shear (right) in real space (top) and reciprocal space (bottom) for a stack of rods of initial spacing D_0.

Figure 5-63 attempts to illustrate this shearing-plus-deformation model. $\boldsymbol{q}_{\sqrt{3}}$ can be broken into components parallel to ($q_{\parallel}$) and perpendicular to ($q_{\perp}$) the SD:

$$\boldsymbol{q}_{\sqrt{3}} = q_{\parallel}\hat{z} + q_{\perp}\hat{x}. \tag{5.2}$$

$|\boldsymbol{q}_{\sqrt{3}}|$ is measured at perpendicular incidence and remains fairly constant (Figure 5-22). $q_{\parallel}$ can also be measured because the $\sqrt{3}$ peak intersects the Ewald sphere on the y-z plane (Figure 5-63 top right). This streaking of the sqrt(3) peak to cut the y-z plane is primarily due to the shape transform effect (Section 5.2.2.1); the finite width of the subgrains and grains of tilted cylinders which broadens the reciprocal space peaks in the y-direction. $q_{\parallel}$ decreases with deformation such that $d_{\parallel} = 1/q_{\parallel}$ is linear (Figure 5-41). The linear increase in $d_{\parallel}$ with deformation beyond kinking indicates that shearing alone is not enough to explain the turning of the cylinders into the SD. Step 1 in Figure 5-63 is the shearing of the cylinders during turning, however step 2 is necessary to keep $|\boldsymbol{q}_{\sqrt{3}}|$ constant.

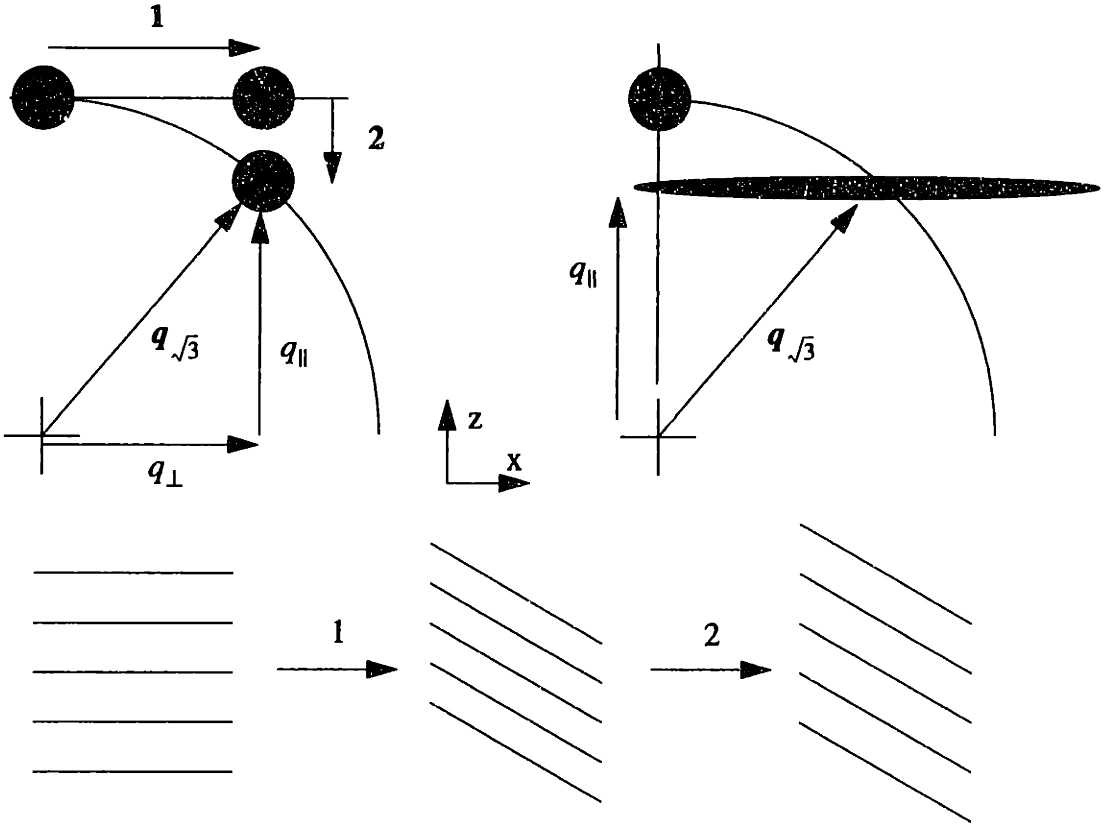

Figure 5-63: Schematic of the post-kink deformation process. The cylinders turn into the SD by undergoing shear (step 1) while simultaneously increasing in D-spacing (step 2). This shearing-plus-deformation model accounts for the motion of the $\sqrt{3}$ peak (along a circle) as well as the TEM data (chevron pattern). Both $q_{\parallel}$ and $|q_{\sqrt{3}}|$ can be measured as the $\sqrt{3}$ peak cuts the Ewald sphere on the y-z plane at x=0 (top right).

5.7 Bibliography

Argon, A. S., S. Backer, F. A. McClintock, G. S. Reichenbach, E. Orowan, M. C. Shaw and E. Rabinowicz (1966). Mechanical Behavior of Materials. Reading, Addison-Wesley.

Chou, P. C. and N. J. Pagano (1967). Elasticity: Tensor, Dyadic, and Engineering Approaches. Princeton, Van Nostrand.

Cullity, B. D. (1978). Elements of X-ray Diffraction. Reading, Addison-Wesley.

Hadziioannou, G., A. Mathis and A. Skoulios (1979). "'Monocristoux' de copolymeres trisequences styrene/isoprene/styrene presentant la structure cylindrique: II. Etude de la deformation par elongation." Colloid and Polymer Science **257**: 337-343.

Jones, R. M. (1975). Mechanics of Composite Materials. New York, McGraw-Hill.

Kim, K. Y. (1996). "Thermodynamics at finite deformation of an anisotropic elastic solid." Physical Review B **54**(9): 6245-6254.

Pradere, P. and E. L. Thomas (1990). "Image processing of partially periodic lattice images of polymers: The study of crystal defects." Ultramicroscopy **32**: 149-168.

Van Krevelen, D. W. (1990). Properties of Polymers: Their correlation with chemical structure; their numerical estimation and prediction from additive group contributions. Amsterdam, Elsevier Science Publishers.

Vezie, D. L. (1993). Ultrastructural studies of the mechanism governing compressive deformation in rigid-rod polymers. Ph. D. thesis, Massachusetts Institute of Technology.

Ward, I. M. (1975). Mechanical Properties of Solid Polymers. New York, John Wiley & Sons.

Chapter 6 Stress Relaxation

6.1 Introduction

The first deformation experiments of using SAXS as the morphology probe were carried out at Princeton University in the laboratory of Prof. S. M. Gruner with the assistance of Dr. D. A. Hajduk. The relatively low flux of the laboratory x-ray source prevented the acquisition of SAXS patterns at sufficient temporal resolution to capture the deformation process at constant strain-rate. Therefore, the first deformation experiments employed a staircase function for the strain-time history. The sample was stretched and then held while SAXS data was gathered for each successive strain increment. Upon reproducing the strain history on an Instron, it became apparent that the sample experienced significant stress decay during the hold portion of the experiment. The question naturally arose of whether the morphology was undergoing a similar relaxation during the course of the SAXS data acquisition. With the availability of high flux afforded by the synchrotron as well as the fast detection and automation capabilities of the X-12B beamline at Brookhaven, stress relaxation experiments were conducted in an attempt to answer this question.

There has been previous work both theoretical (Rubenstein et al., 1993; Turner, 1995) and experimental (Kan et al., 1980; Bard et al., 1987) on the relaxation behavior of ABA triblock copolymers. More work has been done on diblocks under various deformations (Witten et al., 1990; Wang, 1994), however, than for triblocks; only previous studies using triblock are considered here.

Rubenstein and Obukhov propose two types of disentanglement modes for triblock copolymer melts: the single chain mode whereby the endblock diffuses along the interface around fixed obstacles, and the collective mode which allows a single chain to disentangle with the rearrangement of the nearby chains. The penetration of the endblock through the midblock phase to eliminate the rare "permanent" loop entanglements is not considered likely in the strong segregation limit (SSL). Beyond the time scales for molecular relaxation, however, a defect-controlled regime is expected. The presence of defects in a deformed system raises the stress over that for a perfect sample. The stress relaxation mechanism at the longest time (lowest frequency) is one in which defects are expelled from the system via transport of chains to and from regions of deficiency in and excess of copolymer density per unit interface area respectively.

A second theoretical study suggests that the bridge-to-loop fraction could be determined by measurement of the bending modulus of a lamellar triblock copolymer melt (Turner, 1995). The bending modulus for a triblock copolymer composed entirely of bridging molecules is found be greater than that for a triblock copolymer of looping molecules. Therefore with a fixed deformation the stress can relax by a conversion of bridges to loops. This would presumably occur via penetration of an endblock through the midblock domain.

Stress relaxation data for several linear SBS triblock copolymers at small deformations is provided by (Bard and Chung, 1987). The aim of the study was to determine the equilibrium stress at a small strain to construct a stress-strain curve against which models could be compared. Three SBS samples of increasing molecular weight were prepared by casting from a solvent preferential to the rubber phase in order to isolate the PS domains. Three models based on rubber elasticity modified to account for the phase separated structure were compared. A model combining a contribution from the domains acting as chemical crosslinks as well as a contribution from trapped entanglements was found to reproduce the small-strain mechanical data best.

Perhaps the only study of the dynamic mechanical behavior of star block copolymers was carried out by Alward (Alward, 1985). The dynamic mechanical spectra (DMA) of a series of poly(styrene-isoprene) starblock copolymers with varying arm numbers at constant composition were determined. Though a DMA experiment does not measure the stress relaxation behavior directly, the rate of decay of the storage modulus as a function of increasing temperature corresponds to the decrease in modulus as a function of decreasing frequency and is indicative of the stress relaxation behavior of the system. As the arm number n increases for the SI $(7k\text{-}17k)_n$ series (Alward, 1985) (pp. 213-215), the slope of the plateau modulus decreases, implying that stress relaxation becomes slower as the number of arms increases. Note that SI $(7k\text{-}17k)_n$ series all have the cylinder morphology. The stress relaxation behavior of homopolymer stars has been studied (Kan et al., 1980; Richter et al., 1987; Richter et al., 1989; Richter et al., 1990) and it is well known that relaxation is significantly hindered by branching.

As indicated by both Rubenstein and Obukhov as well as Bard and Chung, the stress relaxation behavior for triblock copolymers is made up not only of molecular disentanglement processes of various kinds, but also of the influence of the shape, size and orientation of the domains within the rubber matrix. A recent rheological study (Ryu et al., submitted) of an oriented SIS cylinder morphology demonstrates a pronounced anisotropy of the dynamic shear modulus at a temperature above T_g(PS) perpendicular and parallel to the cylinder axis. The shear strain amplitude was kept well within the linear regime. The lower G' in the parallel direction was attributed to the ability of the PS endblock to diffuse along the interface in order to relieve the stress in the PI matrix. At $T<T_g$(PS) G' no longer exhibited anisotropy suggesting that this mode of disentanglement was no longer active.

To the author's knowledge, there have been no experiments which follow the domain morphology during a stress relaxation experiment at large tensile strain on triblock copolymer cylinders.

6.2 Results

6.2.1 Stress Relaxation Data

Deformation experiments in which a sample is deformed and held at fixed strain are called stress relaxation experiments. To investigate any potential morphological change during stress relaxation, successive SAXS patterns were taken as a function of relaxation time. Large holding strains were chosen in order to provide a large driving force for both chain and microdomain reorganization and rearrangement. Since the x-angle can be determined fairly accurately, samples were deformed with the SD normal to the cylinder axis (⊥ deformation).

In this chapter, two stress relaxation experiments on separate cylinder-forming thermoplastic elastomers are described. The first is a poly(styrene-butadiene-styrene) (SBS) linear triblock of block molecular weights 10-46-10 (x 10^3 gm/mol) and weight fraction 0.30 (vol. fraction: 0.27). The second has a star-like molecular architecture with 18 linear "arms" emanating from a common center. Each arm is a poly(styrene-isoprene) (SI) diblock of block molecular weights 11-34 (x 10^3 gm/mol) yielding a weight fraction of 0.24 (volume fraction: 0.21). The diblocks are arranged such that the star has a polyisoprene core with a polystyrene corona (see Figure 4-1). This material has been previously studied (Herman, 1986; Herman et al., 1987) and is known (via TEM) to form a cylinder morphology.

Figure 6-1 shows the stress-time history for the linear triblock and the star block copolymer after being stretched to 380% and 440% strain respectively. The relevant deformation parameters are reported in Table 6-1. The degree of morphological orientation

Table 6-1: Stress Relaxation Experiments

Sample	Gage (mm)	Width (mm)	Thickness (mm)	holding strain
SBS 10k-46k-10k	17.9	3.13	0.89	380%

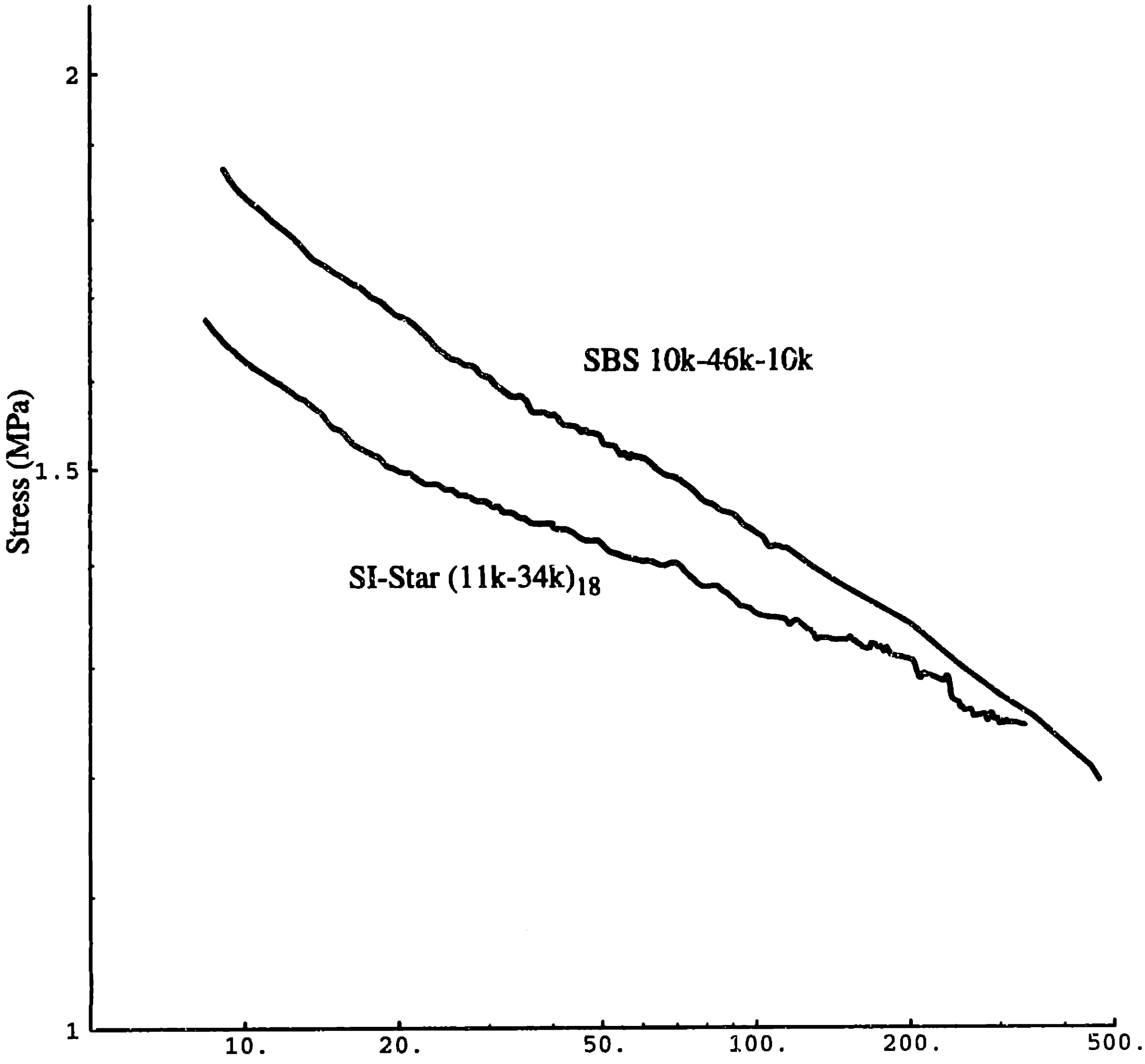

Figure 6-1: Stress relaxation of a linear triblock (SBS 10k-46k-10k) and a star block copolymer SI (11k-34k)$_{18}$ under a perpendicular deformation of 380% and 440% strain respectively. Note that despite being stretched to a smaller strain and a higher stress, the linear triblock relaxes faster than the star block copolymer. The time axis starts with the beginning of the deformation and is represented on a semi-log scale.

Table 6-1: Stress Relaxation Experiments

Sample	Gage (mm)	Width (mm)	Thickness (mm)	holding strain
SI Star (11k-34k)$_{18}$	15.2	3.11	0.76	440%

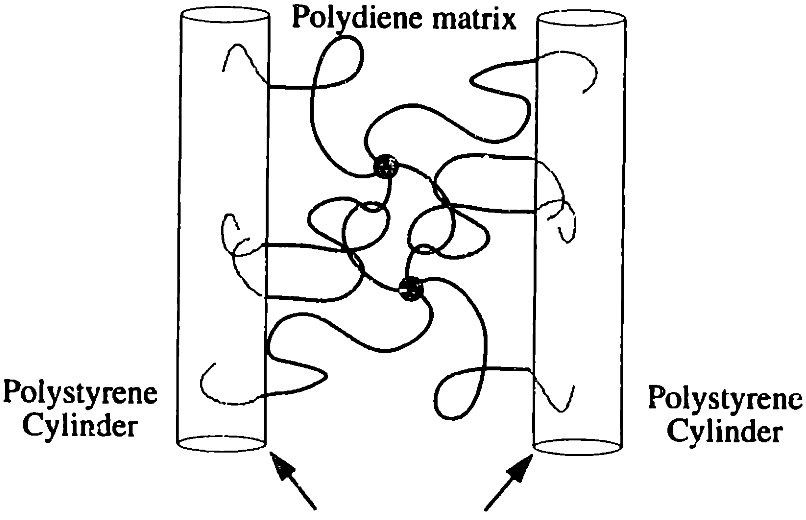

Figure 6-2: Two 4-armed stars with arms bridging the rubber matrix between two PS cylinders. The number of entanglements per unit volume increases rapidly as the arm number increases.

as measured by the azimuthal peak width (Figure 6-4) is comparable. Both samples have approximately the same cross-section (within 15%) and volume fraction (within 2%), but have rather different relaxation behavior. The linear triblock relaxes more rapidly than the star block copolymer. This is most likely due to the difference in molecular architecture which influences the entanglement density. Because of the larger number of arms, the star block copolymer sample contains many more entanglements within the rubbery domain than the linear triblock on a volume basis (see Figure 6-2). These entanglements inhibit molecular motion that would reduce chain stretching and thus the stress exerted by the sample at fixed strain (see section 6.3.2).

6.2.2 SAXS Data

6.2.2.1 Selected Patterns

Figure 6-3 shows the initial orientation of the samples via SAXS with x-rays at perpendicular incidence. Though both samples have a high degree of parallel orientation, the star shows a higher degree of overall orientation. The fact that the $\sqrt{1}$ peak is faint in

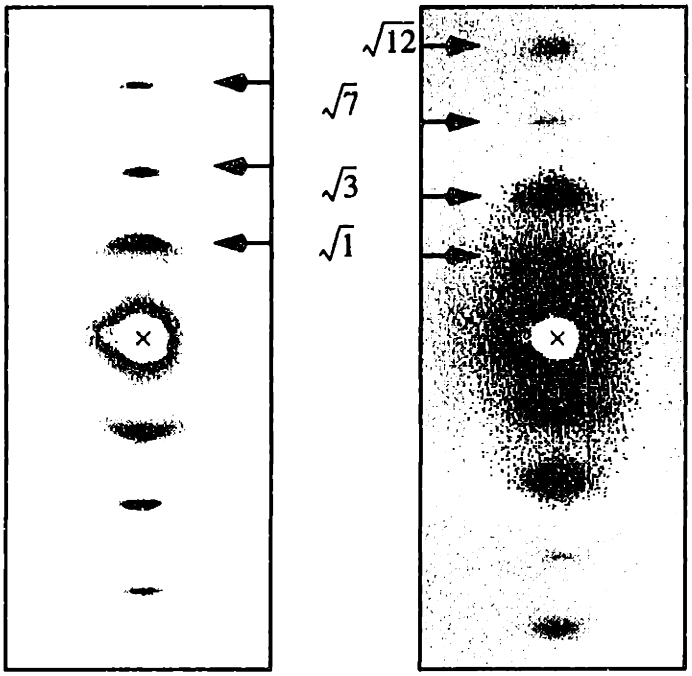

SBS 10k-46k-10k SI Star $(11k\text{-}34k)_{18}$

Figure 6-3: 2-D SAXS patterns of roll-cast SBS 10k-46k-10k linear triblock and SI $(11k\text{-}34k)_{18}$ star block copolymer viewed normal to the cylinder axis. Note that the degree of rotational misorientation of the star sample is less than that for the linear triblock. The azimuthal FWHMs of the $\sqrt{3}$ peaks are 5.5 and 4 degrees for the triblock and star respectively.

comparison to the $\sqrt{3}$ peak indicates that the hexagonal lattice has a smaller rotational distribution than for the linear triblock (see section in Chapter 5). 1-D peak profiles from radial integrations are shown in Figure 6-4. The peak positions are reported in Table 6-2.

Table 6-2: SBS and Starblock Peak Positions

Sample	peak #1 ($Å^{-1}$)	peak #2 ($Å^{-1}$)	peak #3 ($Å^{-1}$)	peak #4 ($Å^{-1}$)	Lattice Constant (Å)
SBS Linear Triblock	0.0247	0.0426	0.0647	-	294
Star Block Copolymer	0.0212	0.0371	0.0557	0.0740	342

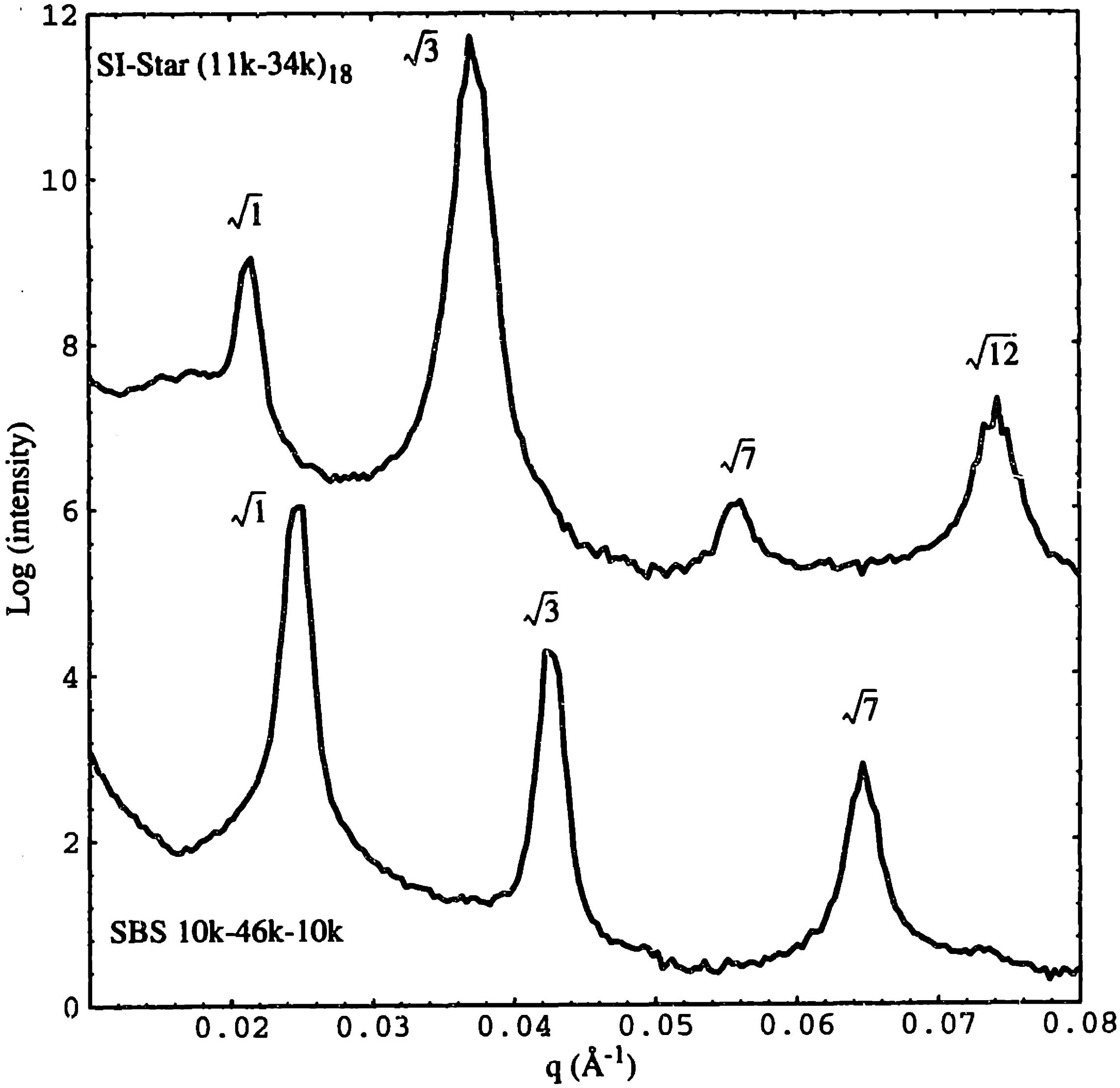

Figure 6-4: Left: Log intensity vs. q from radial integrations (over 20 degrees) of the patterns in Figure 6-3. The lattice constants are 294 Å and 342 Å for the linear triblock and star block copolymer respectively.

Stretching both samples to large deformation causes kinking which is manifested in the scattering pattern by the transformation of the 1-D profile of Figure 6-3 into an X. Figure 6-5 and Figure 6-6 shows the SAXS patterns at perpendicular incidence at the very start of and very end of the stress relaxation experiment for the linear triblock and the star block copolymer respectively. There is little qualitative change in the patterns despite an

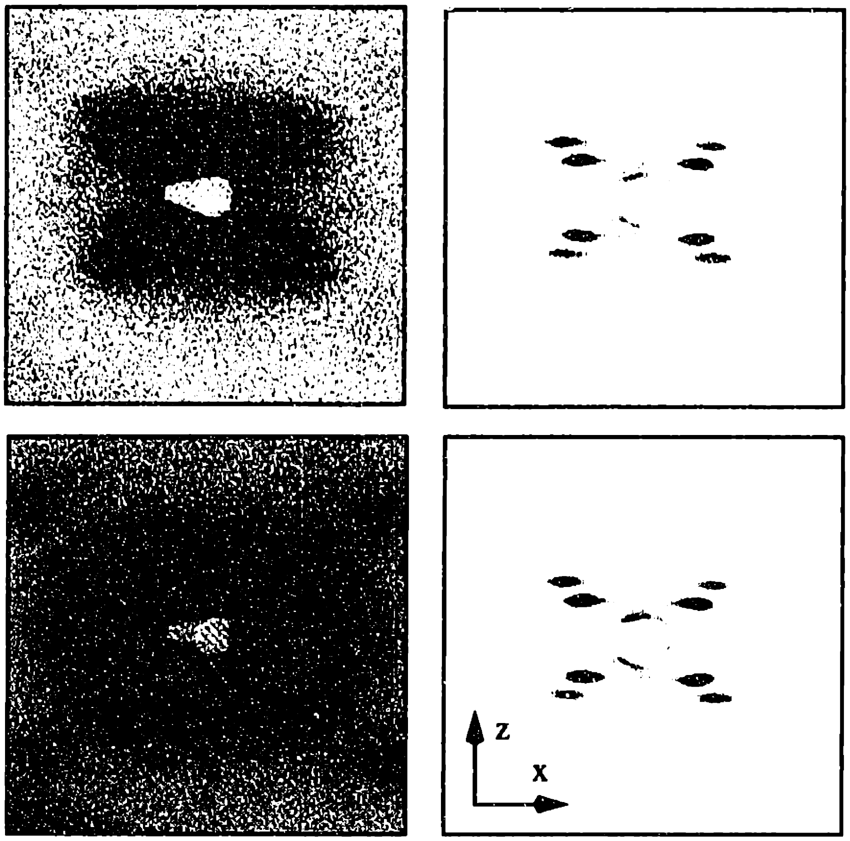

Figure 6-5: 2-D SAXS patterns after 20 seconds (top pair) and after 310 minutes (bottom pair) of stress relaxation for SBS 10k-46k-10k at perpendicular incidence. No qualitative change in the pattern as a consequence of stress relaxation is observable.

approximately 30% drop in stress after 5 hours. The lower left pattern in Figure 6-6 shows a loss in peak sharpness and intensity of the weaker peaks as well as a broadening of the strongest ($\sqrt{3}$) peak in the SD.

6.2.3 Peak Motion

The position of the $\sqrt{3}$ peak maximum as function time for both samples remains approximately constant. There is no experimentally significant change in either the X-angle or the d-spacing. Figure 6-7 shows both a linear and semi-log plot of the X-angle as a function of time for both samples. The X-angle shows no evidence of obeying a power law. The $\sqrt{3}$ d-spacing change is reported in Figure 6-8. Again, the $\sqrt{3}$ d-spacing remains constant (within experimental error) for the duration of the stress relaxation experiment.

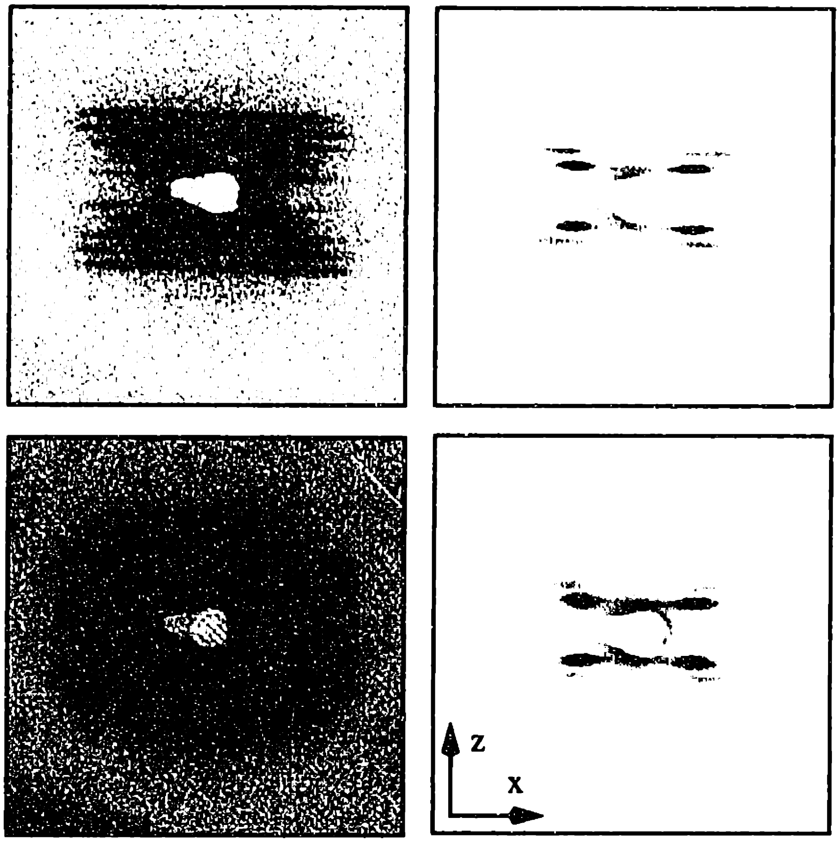

Figure 6-6: 2-D SAXS patterns after 10 seconds (top pair) and after 340 minutes (bottom pair) of stress relaxation for the SI (11k-34k)$_{18}$ star block copolymer at perpendicular incidence. There is a subtle loss of peak sharpness in the weak, high q peaks in the bottom left figure.

6.2.3.1 Sample Transmission

A plot of strain in the y-direction (transverse - thin) as measured by sample transmission vs. time for both the linear triblock and the star block copolymer is shown in Figure 6-9. In contrast to the lack of peak motion in the x-z plane, the samples undergo dramatic strain relaxation during the stress relaxation. As the samples are deformed to their holding strains, the thickness direction undergoes compressive strain. Approximately 85% of this compression in the thickness direction is recovered during the course of the stress relaxation experiment.

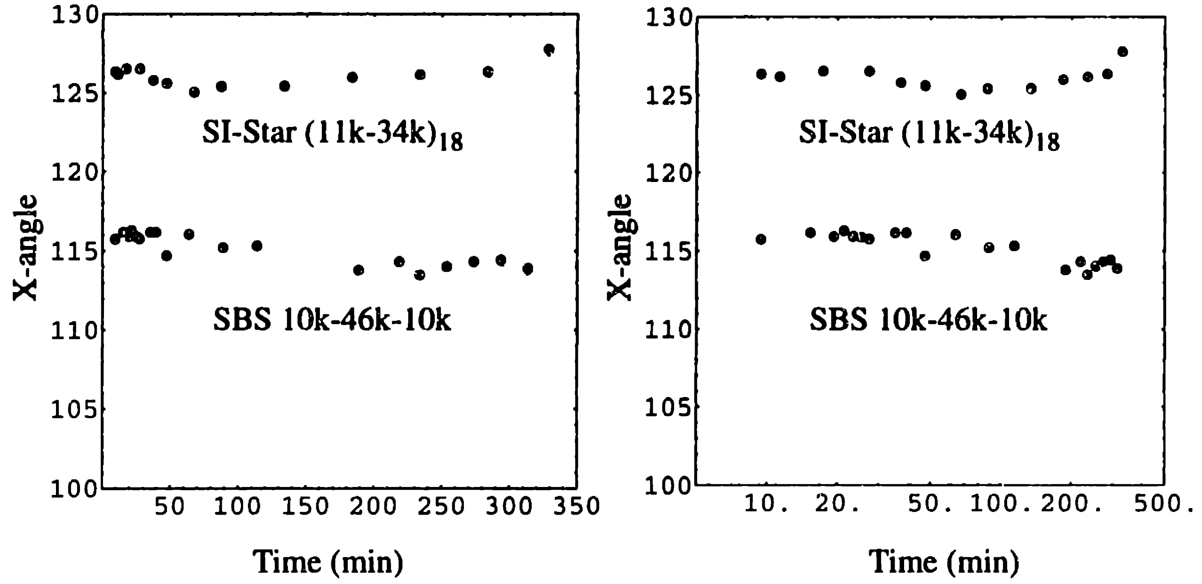

Figure 6-7: X-angle vs. time for the SBS 10k-46k-10k triblock copolymer and the SI (11k-34k)$_{18}$ star block copolymer in a perpendicular stress relaxation experiment. The angle between arms of the X (X-angle - see Figure 6-5 and Figure 6-6) remains constant over 1.5 orders in time. The scatter of a few degrees is within experimental error. Plotting the data either on a linear plot (left) or a semi-log plot (right) does not show a clear trend.

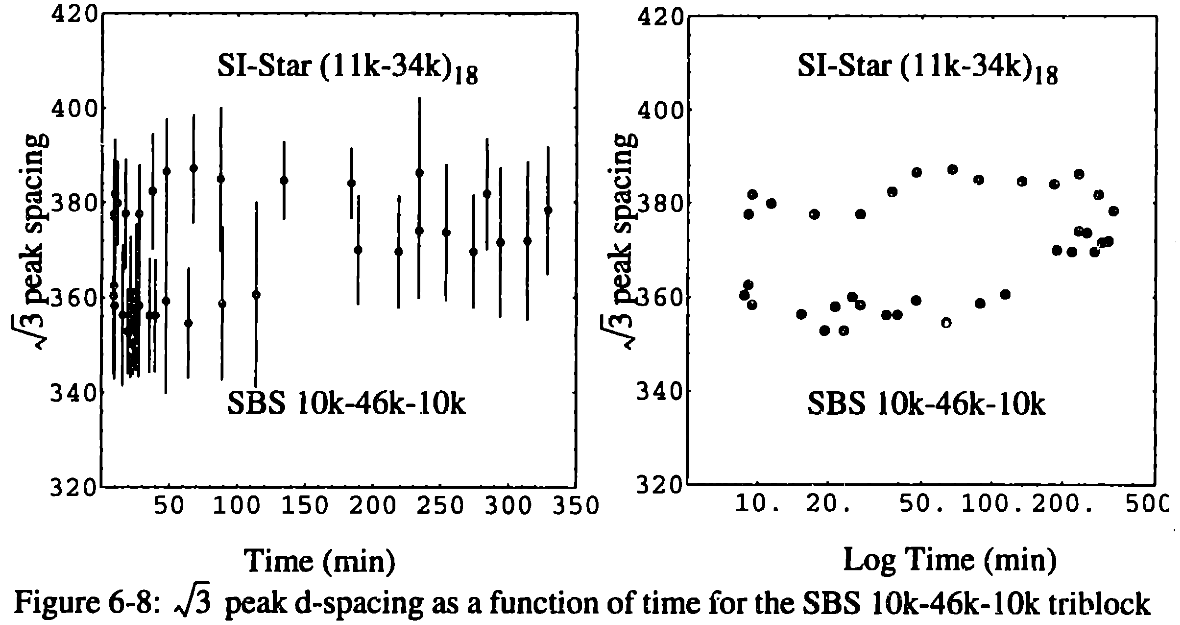

Figure 6-8: $\sqrt{3}$ peak d-spacing as a function of time for the SBS 10k-46k-10k triblock copolymer and the SI (11k-34k)$_{18}$ star block copolymer in a perpendicular stress relaxation experiment. The d-spacing remains constant over 1.5 orders in time. The error bars in the plot at left represent twice the standard deviation of the d-spacing of all four $\sqrt{3}$ peaks in each X-pattern. The error thus includes any asymmetry in the X due to sample misalignment. The $D_{\sqrt{3}}$ -spacing is approximately independent of time when observed in either a linear plot (left) or a semi-log plot (right).

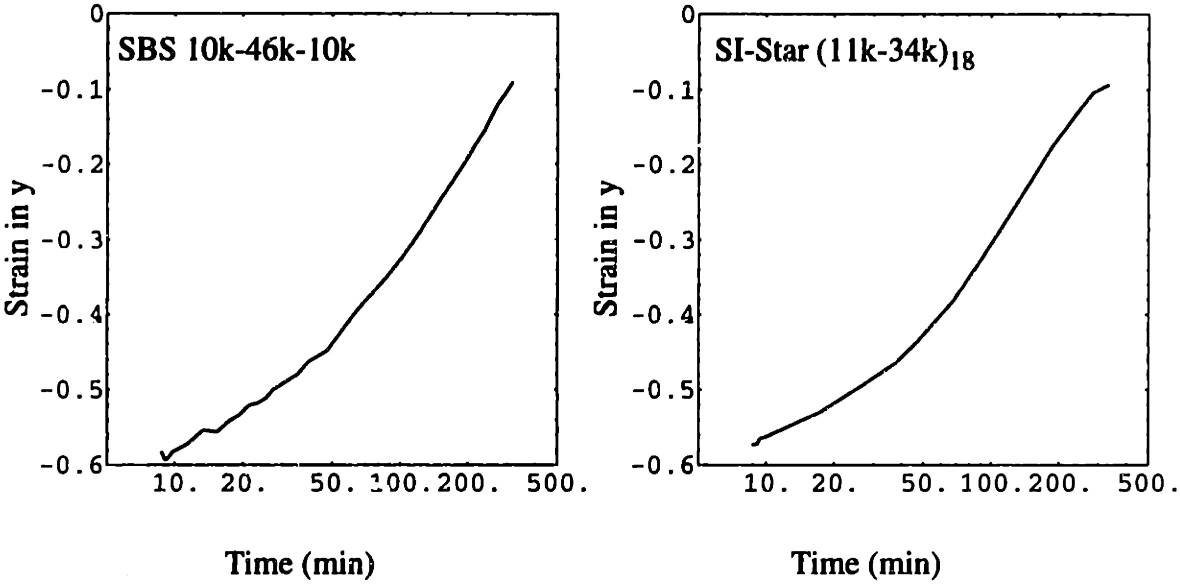

Figure 6-9: Plots of strain in the thickness (y) direction as a function log time for the perpendicular stress relaxation experiments of the SBS 10k-46k-10k linear triblock (left) and the SI $(11k\text{-}34k)_{18}$ star block copolymer (right). The strain is based on measurement of the sample transmission during the experiment. In both cases the samples relax back to nearly their initial thicknesses.

6.3 Discussion

6.3.1 Stress Relaxation Mechanism

The absence of significant change in the SAXS pattern despite a significant drop in stress is somewhat surprising. The stress-strain behavior of a TPE is thought to be quite closely coupled to morphology. The unambiguous data at hand indicates that the picture is somewhat more complicated.

Since the X-angle and the d-spacing remain constant, the orientation and position of the kinked cylinders remain fixed *in the x-z plane* during stress relaxation. The drop in stress must then be ascribed to a change in chain conformation at fixed domain orientation within this plane. Since SAXS acts as a morphological probe, information on chain conformation and motion is indirect and based on the available morphological (domain) data.

During the course of a perpendicular deformation process, the matrix material experiences a tensile deformation along the SD and upon kinking an additional shear along the cylinder axis (see section 5.6.3). A schematic of the resulting chain conformation is shown in Figure 6-10. In order to relieve bridging-chain-stretching, the junctions will move (diffuse) along the IMDS. This reduction in chain stretching in the SD lowers the overall stress and does not require a change in domain orientation or spacing in the x-z plane.

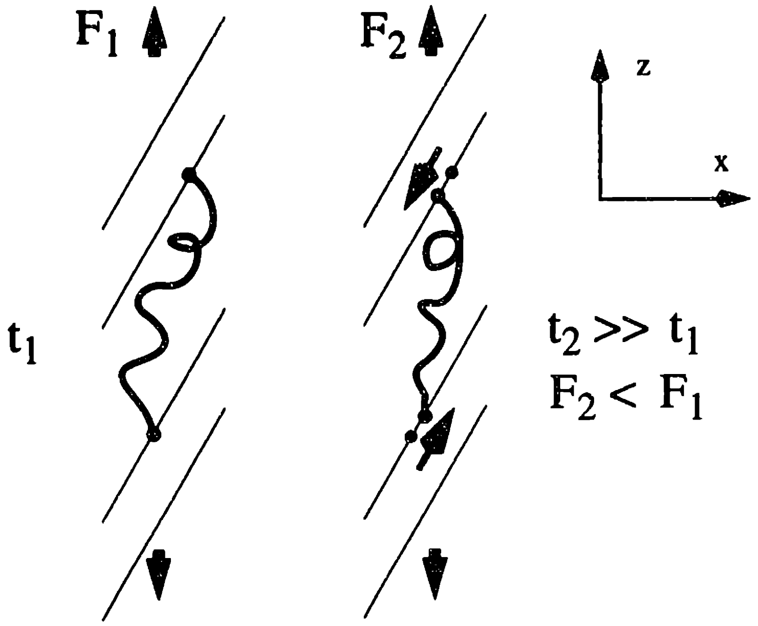

Figure 6-10: Schematic of stretched and sheared bridging chain in between a section of kinked cylinders (shaded). At fixed strain the junctions will migrate along the IMDS to relieve chain stretching.

In conjunction with a relaxation of the tensile strain of the bridging chain in the SD, there is a corresponding relaxation of the compressive strain in the y-direction. Again, motion of the bridging-chain junctions along the IMDS will occur to relieve chain compression. Since the dimension of the sample in the thickness direction is far less constrained than that in the x-direction, the thickness of the sample *increases* (as observed in Figure 6-9).

6.3.2 Effect of Chain Architecture

A linear triblock copolymer can be considered a two-armed star, which is the minimum number of arms necessary for a block copolymer to "span" or bridge two domains. Increasing the number of arms of a star block copolymer increases the likelihood that each molecule will act as a bridge. Assuming that each arm has an equal probability of being in the same or disparate domain, a simple calculation can be made which determines the bridging fraction vs. arm number. In the linear case the second arm may either be located in another domain (which results in a bridge) or in the same domain as the first arm (which results in a loop). Figure 6-11 illustrates the possibilities. The bridging fraction in this case is 1/2. Extending the argument to a star with 3 arms results in a bridging fraction of 3/4. Figure 6-12 shows how adding one arm increases the bridging fraction. The bridging fraction is not changed if the third arm is located in a third domain. That is, the rough estimate does not depend on the third dimension. The functional form for the bridging fraction (F) vs. the arm number (n) is:

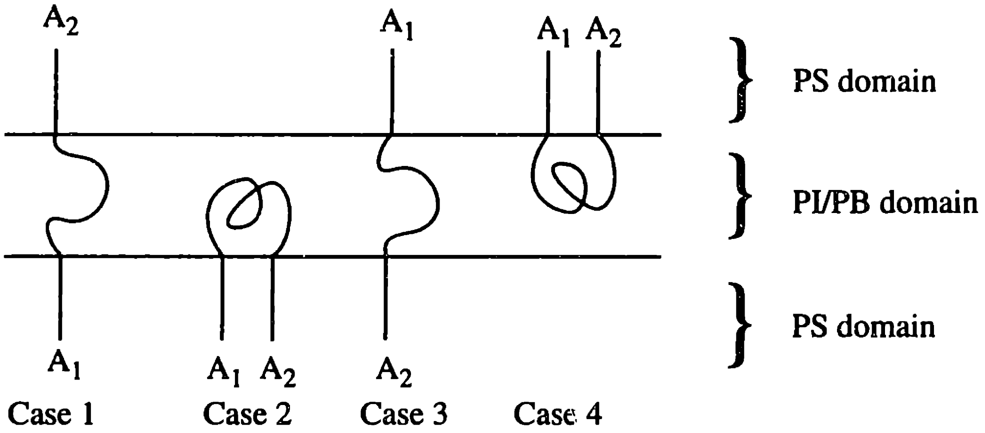

Figure 6-11: Schematic conformations of a linear triblock with arms A_1 and A_2 either located in opposite domains or in the same domain. When the PS arms are located in opposite domains, the rubber (polybutadiene or polyisoprene) block "bridges" the opposing domains. The bridging fraction for a "star" block copolymer with 2 arms is 2/4 = 1/2.

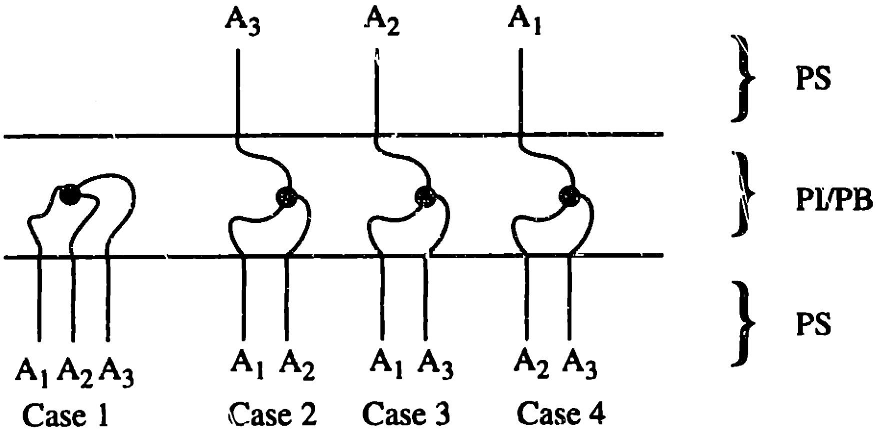

Figure 6-12: Schematic conformations of a 3-armed star block copolymers with arms A_1, A_2 and A_3 either located in opposite domains or in the same domain. Half of the total number of possibilities are shown as the top and bottom domains may be exchanged. As the number of arms in the star block copolymer increases, the number of bridging events increases while the number of looping events remains fixed. Here, the bridging fraction is 6/8 = 3/4 for a 3-armed star.

$$F(n) = \frac{\sum_{i=1}^{n-1} 2^{n-i}}{2^n}. \qquad (6.3)$$

As an example, a 2-armed star (n = 2) has a bridging fraction F(2) = 1/2. This function is plotted in Figure 6-13. Thus a star block copolymer with a sufficient large number of arms will be very effective in connecting domains together. The 18-armed star under discussion is a highly bridged molecule, with arms connecting several domains. This conformational state is to be contrasted with the linear triblock copolymer molecule which has at best a 50% chance to bridge two domains.

The relaxation behavior of an 18-armed vs. a 2-armed star block copolymer molecule is expected to be very different, especially in light of the possibility of the interpenetration of the bridging blocks. Assuming that the reduction of chain stretching is possible only via movement of chain junctions along the IMDS, a highly branched star block copolymer molecule will have much more difficulty relieving chain stretching. Many arms of the star will be located in various domains. Bridging blocks from other molecules will be catenated with the star further constraining molecular motion. The highly branched

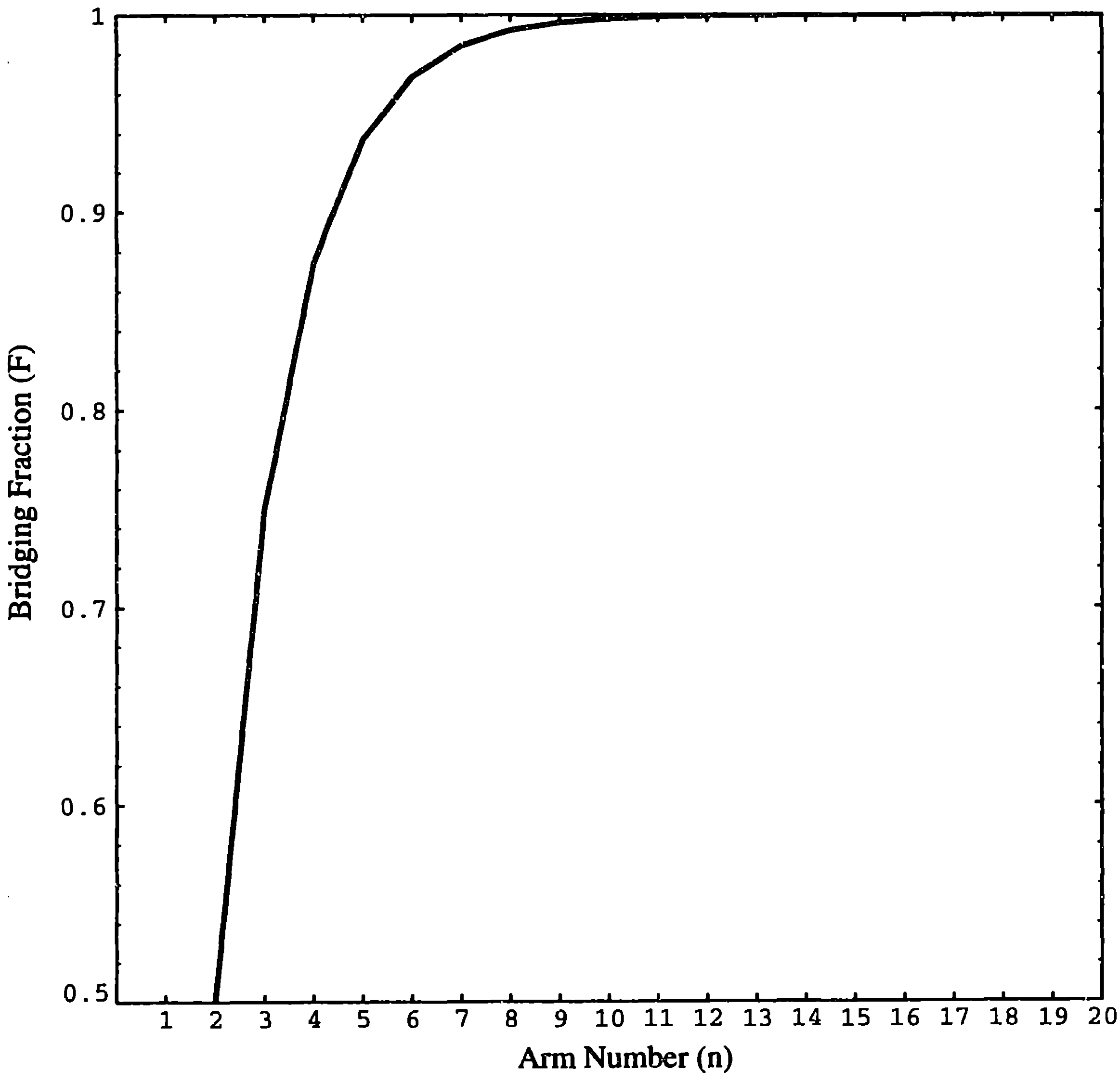

Figure 6-13: Plot of equation (6.3), the bridging fraction (F) vs. the arm number (n). Note that as the number of arms in the star block copolymer increases, the bridging fraction rapidly rises towards unity. Almost every 18-armed star block copolymer molecule is bridging at least two domains together.

star will find itself unable to relieve a significant amount of chain stretching without considerable molecular rearrangement. The bridging blocks will remain highly stretched for a far longer time than in the simple 2-armed case.

6.4 Bibliography

Alward, D. B. (1985). A morphological study of a series of multiarmed star block copolymers of polyisoprene and polystyrene. Ph. D. thesis, University of Massachusetts.

Bard, J. K. and C. I. Chung (1987). Chapter 12: Research on thermoplastic elastomers. Thermoplastic Elastomers: A Comprehensive Review. N. R. Legge, G. Holden and H. E. Schroeder. Munich, Hanser: 303-323.

Herman, D. S. (1986). A compositional study of the morphology of 18-armed poly(styrene-isoprene) star-block copolymers. Masters thesis, University of Massachusetts.

Herman, D. S., D. J. Kinning, E. L. Thomas and L. J. Fetters (1987). "A compositional study of the morphology of 18-armed poly(styrene-isoprene) star block copolymers." Macromolecules **20**: 2940-2942.

Kan, H.-C., J. D. Ferry and L. J. Fetters (1980). "Rubbers networks containing unattached macromolecules. 5. Stress relaxation is Styrene-butadiene-styrene block copolymer with unattached linear and star polybutadienes." Macromolecules **13**: 1571-1577.

Richter, D., B. Farago, L. J. Fetter, J. S. Huang and B. Ewen (1990). "On the relation between structure and dynamics of star polymers in dilute solution." Macro. **23**: 1845-1856.

Richter, D., B. Farago, J. S. Huang, F. L. J. and B. Ewen (1989). "A study of single arm relaxation in a PS star polymer by neutron spin echo spectroscopy." Macro. **22**: 468-472.

Richter, D., B. Stuehn, B. Ewen and D. Nerger (1987). "Collective relaxation of star polymers-A neutron spin-echo study." Physical Review Letters **58**(23): 2462-2465.

Rubenstein, M. and S. P. Obukhov (1993). "Power-law-like stress relaxation of block copolymers: disentanglement regime." Macro. **26**: 1740-1750.

Ryu, C. Y., M. S. Lee, D. A. Hajduk and T. P. Lodge (submitted). "Structure and rheological properties of matched asymmetric diblock and triblock copolymers." Journal of Polymer Science: Polymer Physics.

Turner, M. S. (1995). "The bending modulus of triblock copolymer lamellae: Stress relaxation via the bridge-to-loop process." Macromolecules **28**: 6878-6882.

Wang, Z.-G. (1994). "Response and instabilities of the lamellar phase of diblock copolymers under uniaxial stress." Journal of Chemical Physics **100**(3): 2298-2309.

Witten, T. A., L. Leibler and P. A. Pincus (1990). "Stress relaxation in the lamellar copolymer mesophase." Macro. **23**(3): 824-829.

Chapter 7 Parallel Deformation

7.1 Introduction

A large strain deformation study of an oriented cylinder morphology along the cylinder axis is complicated by yielding and necking. The localization of the deformation occurs at relatively small strains (< 10%) and in an ideally loaded sample occurs at a position randomly located along the gage length. A detailed study of the necking process and the resulting strain non-uniformity along the gage length was carried out by (Odell et al., 1977). The overall results presented in this chapter are in agreement with the previous study. However, new data and interpretation add further details to the deformation model. Additionally, points of contention based on SAXS results are pointed out in the discussion.

7.2 Constant Strain-Rate Deformation

7.2.1 Stress-Strain Behavior

Figure 7-1 shows a typical stress-strain curve for a roll-cast sample of SIS 15k-72k-15k in parallel deformation. The initial linear loading indicates a modulus of approximately 120 MPa. The curve shows a clear yield point of 3.6 MPa at 9% strain followed by a plateau of constant stress. A further increase in stress is observed at strains > 200%. A residual plastic deformation of approximately 25% remains after unloading from a deformation of 350%. In contrast to roll-cast SIS 15k-72k-15k in perpendicular deformation, a much larger hysteresis is exhibited in parallel deformation (compare Figure 7-1 with Figure 5-12).

7.2.2 Selected Patterns

The initial degree of order is seen in the top SAXS pattern of Figure 7-2. The partial diffraction ring just inside the first peak is of unknown origin. It disappears during loading, but reappears during unloading (see Figure 7-5). Apparently, the material giving rise to this diffraction does not deform in the same way as the rest of the sample. In subsequent discussions these arcs will be ignored. The azimuthal width of the $\sqrt{3}$ peak is 9.4 degrees. There is evidence of a second lattice slightly rotated from the first (see Figure 7-3), but the

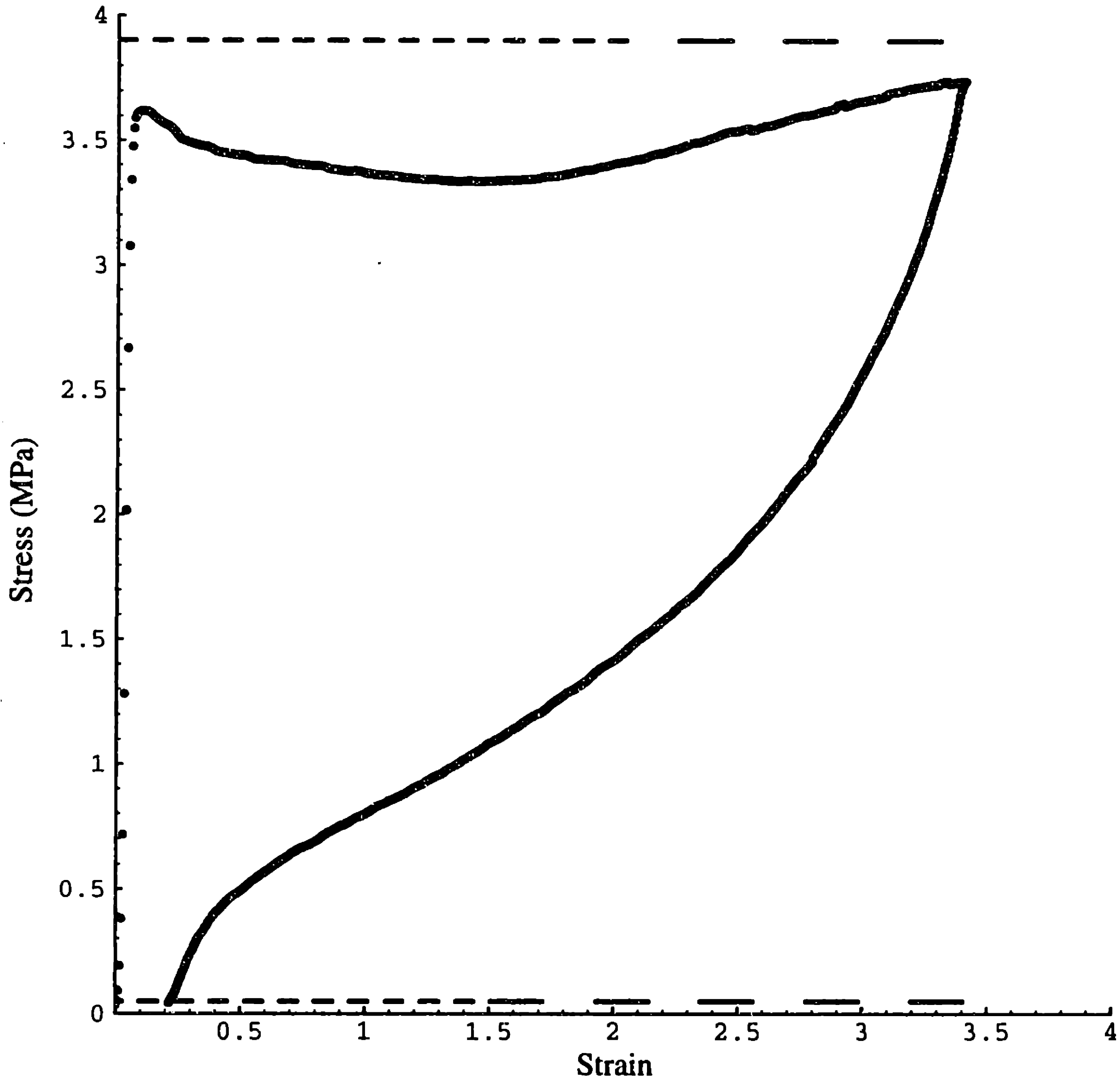

Figure 7-1: Stress-strain plot of SIS 15k-72k-15k in parallel deformation. Yield occurs at stress = 3.6 and strain = 9% while the modulus is approximately 120 MPa. The dashed lines at top and bottom indicate data acquisition periods for the loading and unloading cycles respectively.

fraction of the sample with the rotated lattice is small compared with the main population. Slight lattice rotations such as this one are not uncommon in roll-cast films that are especially thick. The $\sqrt{1}$, $\sqrt{3}$ and $\sqrt{7}$ reflections are clearly observed, but a faint $\sqrt{9}$ and $\sqrt{12}$ peak can also be seen in the data.

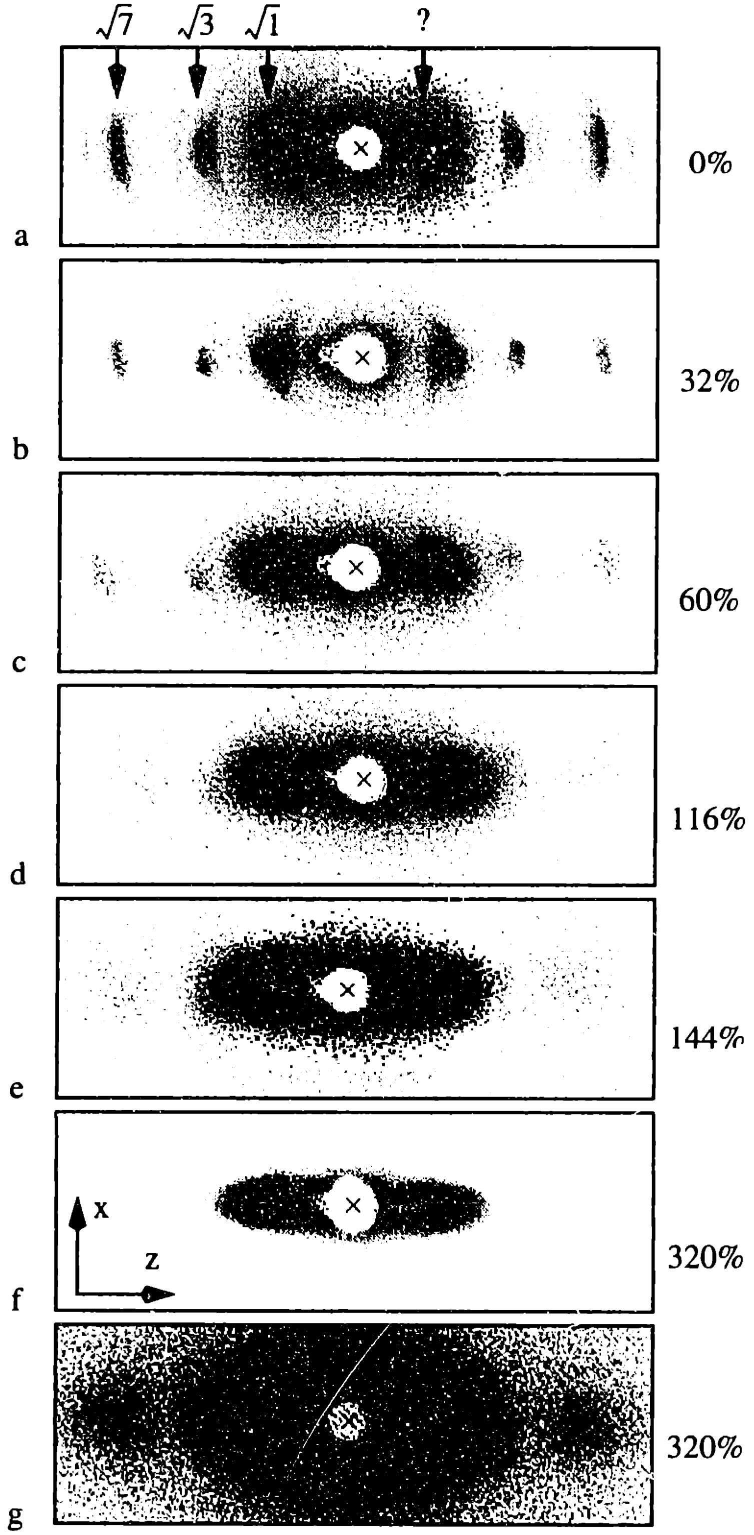

Figure 7-2: 2-D SAXS patterns during loading of SIS 15k-72k-15k in a parallel deformation perpendicular incidence experiment. The average strain during the acquisition is shown at right. The SD is vertical. (g) is (f) thresholded at a much lower value. Note the diffuse scatter at high values of q separated from the intense scatter near the origin by the zero of the form factor.

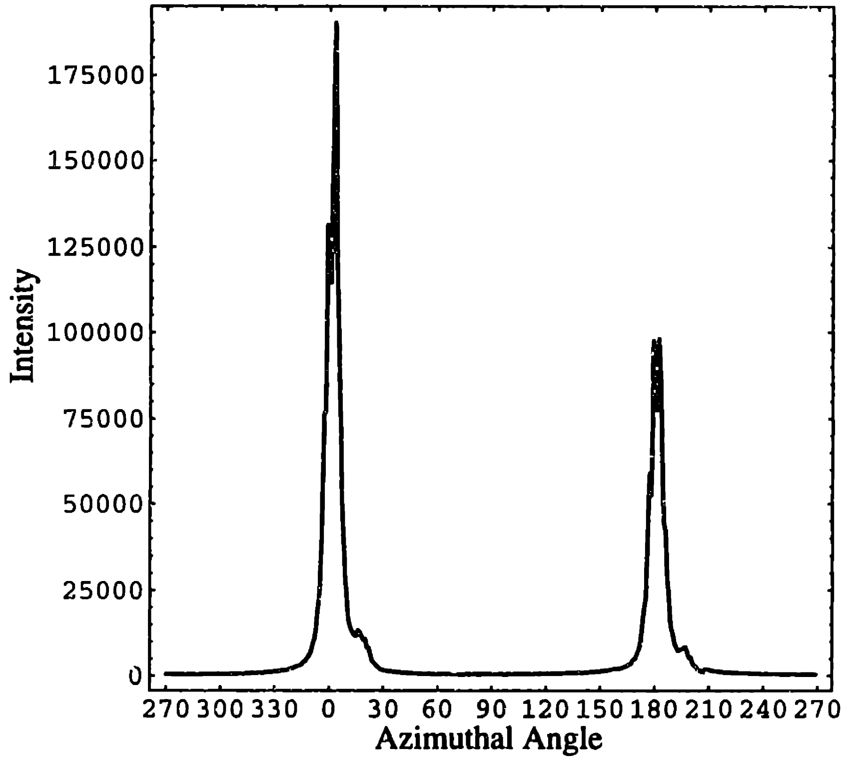

Figure 7-3: Azimuthal scan at constant radial width for the $\sqrt{1}$ peak of the top SAXS pattern in Figure 7-2. The small peak to the right of the main spike represents a fraction of cylinders slightly rotated with respect to the main population. The average FWHM for the two strong peaks is 8.5 degrees.

In this deformation experiment a neck is formed at approximately 9% strain near one of the grips. There is a slight azimuthal sharpening of the $\sqrt{1}$ peak within the first 30% strain as well as a loss of relative intensity for the peaks at higher q. Azimuthal integrations about the equator show that the peaks do not move towards the origin (see Figure 7-4). By 120% nominal strain the pattern shows evidence of a transformation. The $\sqrt{1}$ peaks have broadened in both the x and z directions. In addition, there is a growth of intensity connecting the $\sqrt{1}$ peak with the origin just above and below the equator. At the highest strain reached, the diffraction pattern is dominated by 2 pairs of streaks located just above and below the equator. The streaks terminate at high q_z in diffuse scatter. The $\sqrt{1}$ peak is no longer distinguishable.

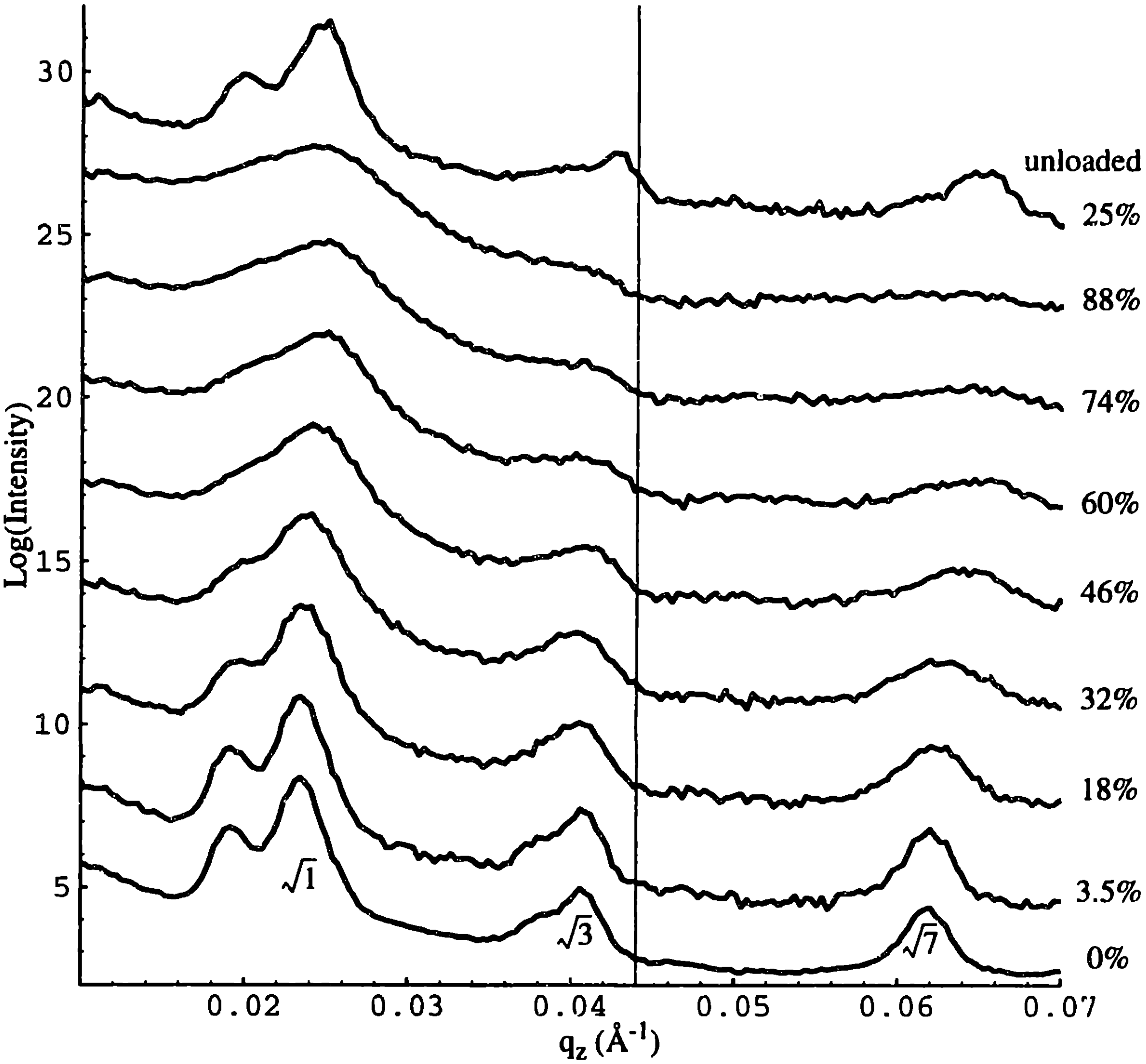

Figure 7-4: Plots of log intensity vs. q_z taken from azimuthal integrations +/- 25° about the z-axis as a function of deformation. Data from the first eight patterns during loading and the last pattern after unloading is shown (see Figure 7-1). The thin line at $q_z = 0.044$ Å^{-1} represents the position of the zero of the form factor. Note that the peaks broaden and shift slightly to higher q during the deformation.

Upon unloading, the separation between jets in the SD increases (compare patterns at 140% and 98% in Figure 7-5 vs. 320% in Figure 7-2), while the intensity of the jets decreases. The $\sqrt{1}$ peak appears abruptly at 98% as a sharp dot of intensity. Remarkably,

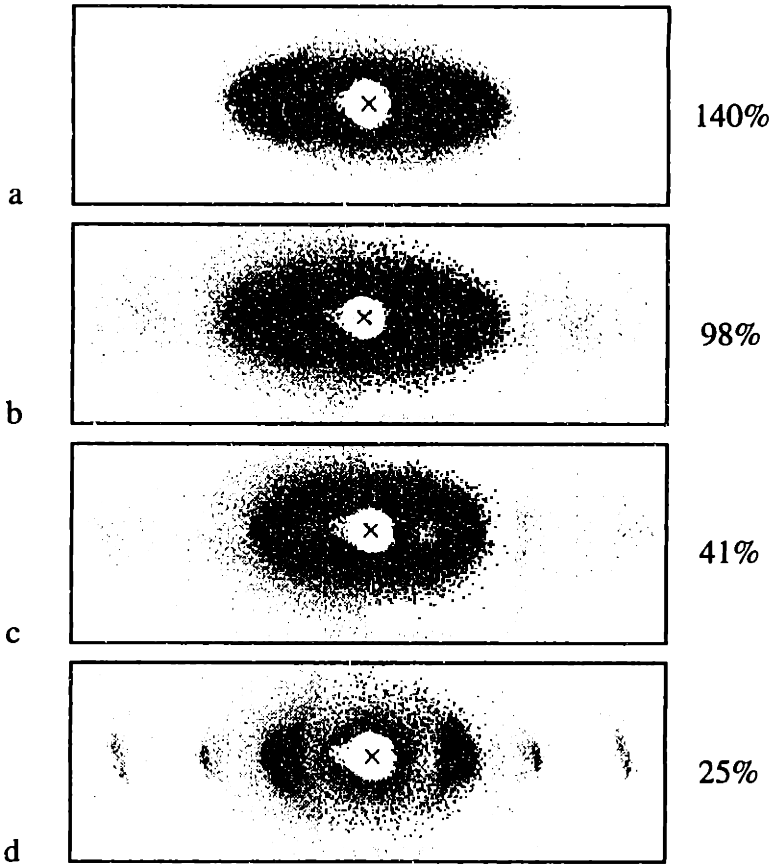

Figure 7-5: 2-D SAXS patterns during unloading of SIS 15k-72k-15k in a parallel deformation perpendicular incidence experiment. The source of the inclined arcs in these patterns is unclear.

the final unloaded pattern shows little evidence of the deformation, having regained the $\sqrt{3}$ and $\sqrt{7}$ peaks. The peak positions are slightly shifted to higher q as a result of the deformation (compare Figure 7-4 top with Figure 7-4 bottom).

7.2.3 Transverse Strain

Figure 7-6 shows the results of measuring sample transmission as a function of macroscopic deformation. The transmission data has been converted to strain in the thickness (y) direction assuming Beer's Law. There is only a 4% change in thickness up to a strain of 60%. Thereafter there is a sudden and continuous reduction of thickness until the SD is reversed. The thickness monotonically increases during unloading, but at a slower

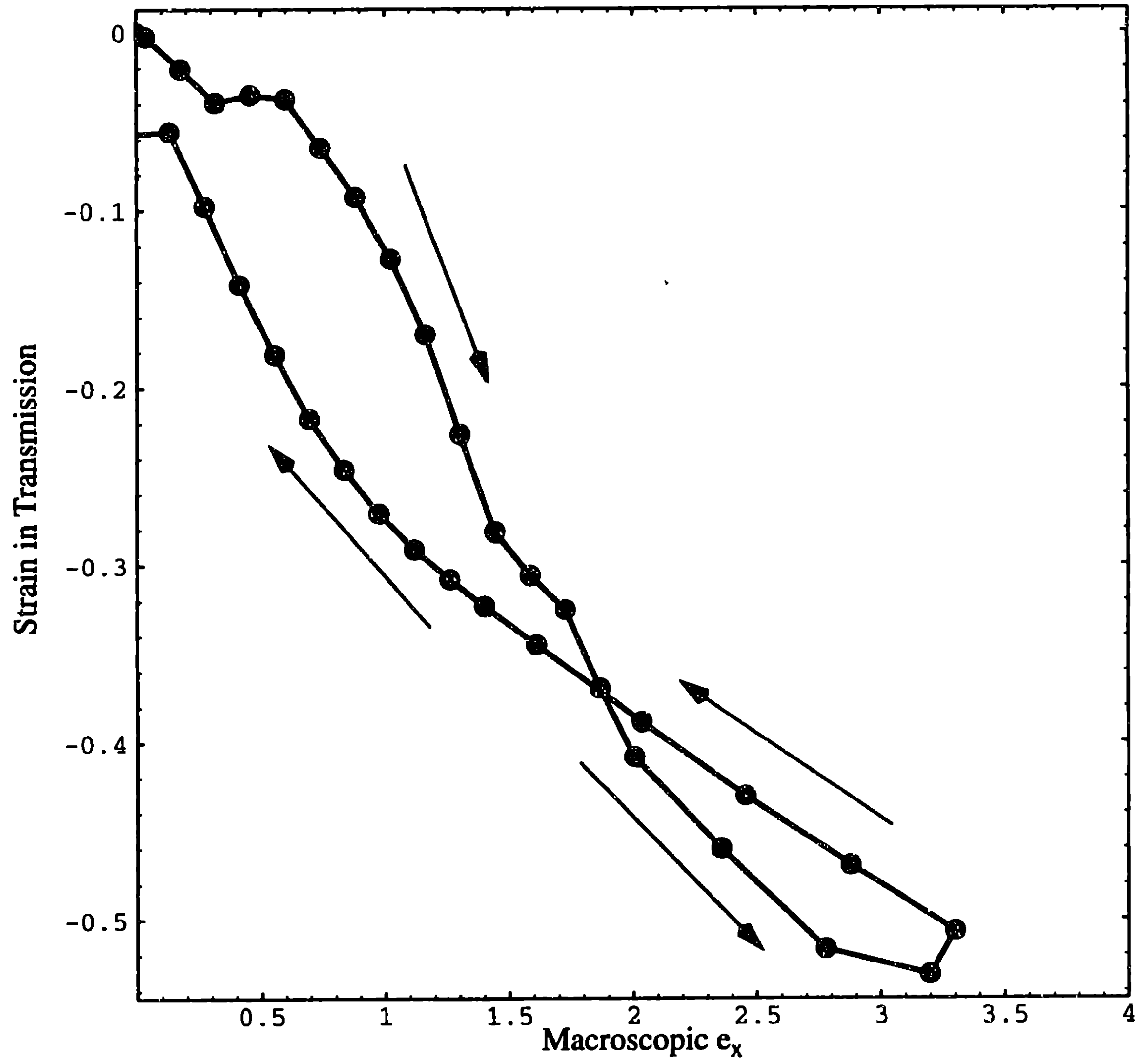

Figure 7-6: Plot of strain based on sample transmission vs. applied deformation. Arrows indicate the course of the deformation.

rate than during loading. A -6% strain remains upon completion of unloading. Note that macroscopic strain no longer represents the strain in the probed region once the neck forms. The local strain in the probed region is a discontinuous function of the macroscopic strain. After neck formation, the local strain remains fixed until the neck passes through the probed region. After the probed region has fully necked, the local strain again remains constant until the onset of drawing, where it increases steadily as a function of applied (macroscopic) strain.

7.3 Irradiated Samples

7.3.1 Raychem

An irradiation experiment similar to the one discussed in Chapter 5 was also conducted in parallel deformation. A roll-cast SIS 15k-72k-15k sample was stretched to 600%, irradiated with 34 Mrad of 800 keV electrons until break. The residual strain was 115%. The stress-time history is shown in Figure 7-7. The ratio of deformation captured to the holding strain (115/600 = 19%) in this instance is almost identical to that for the perpendicular deformation and irradiation experiment of Chapter 5 (see Figure 5-26). One might expect a larger amount of deformation to be captured for parallel deformation than

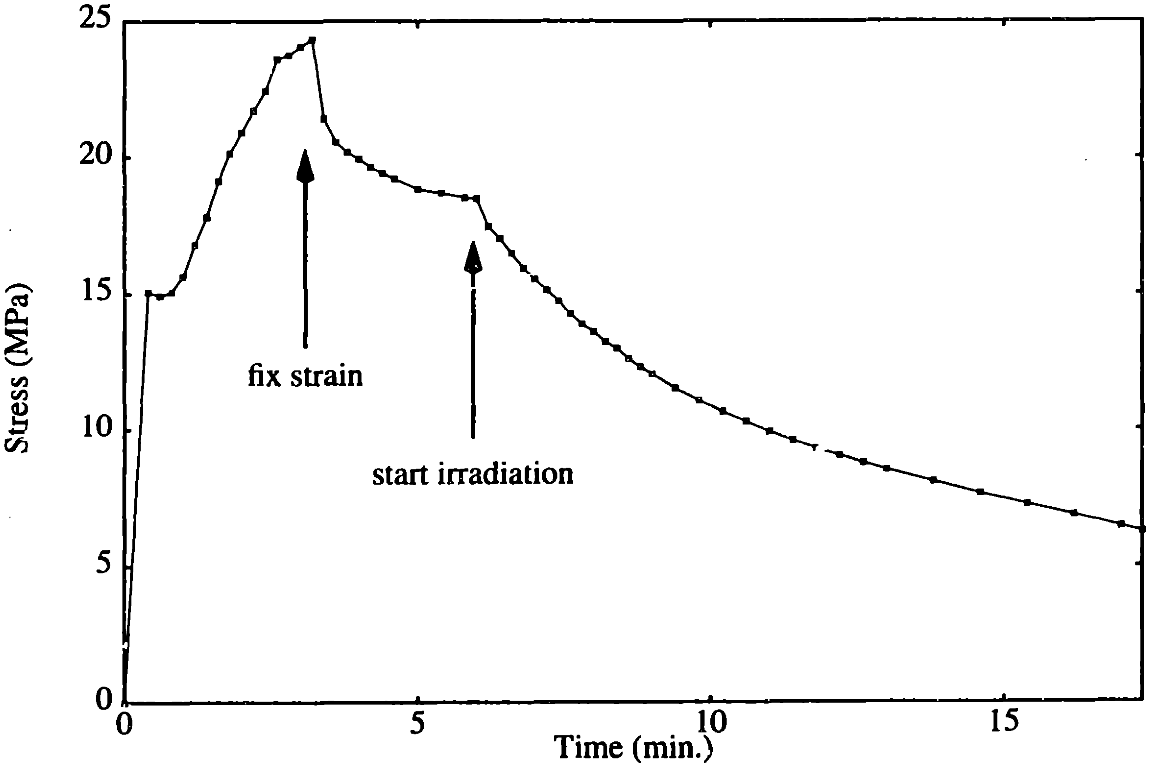

Figure 7-7: Stress-time history for the parallel stretch and irradiation experiment at Raychem. The sample was stretched to 600% strain and after approximately 4 minutes of stress relaxation, an 800 keV electron beam at a current of 1.2 mA was applied. Irradiation continued until break for a total dose of 340 kGy (34 MRad). The residual strain was measured to be approximately 115%.

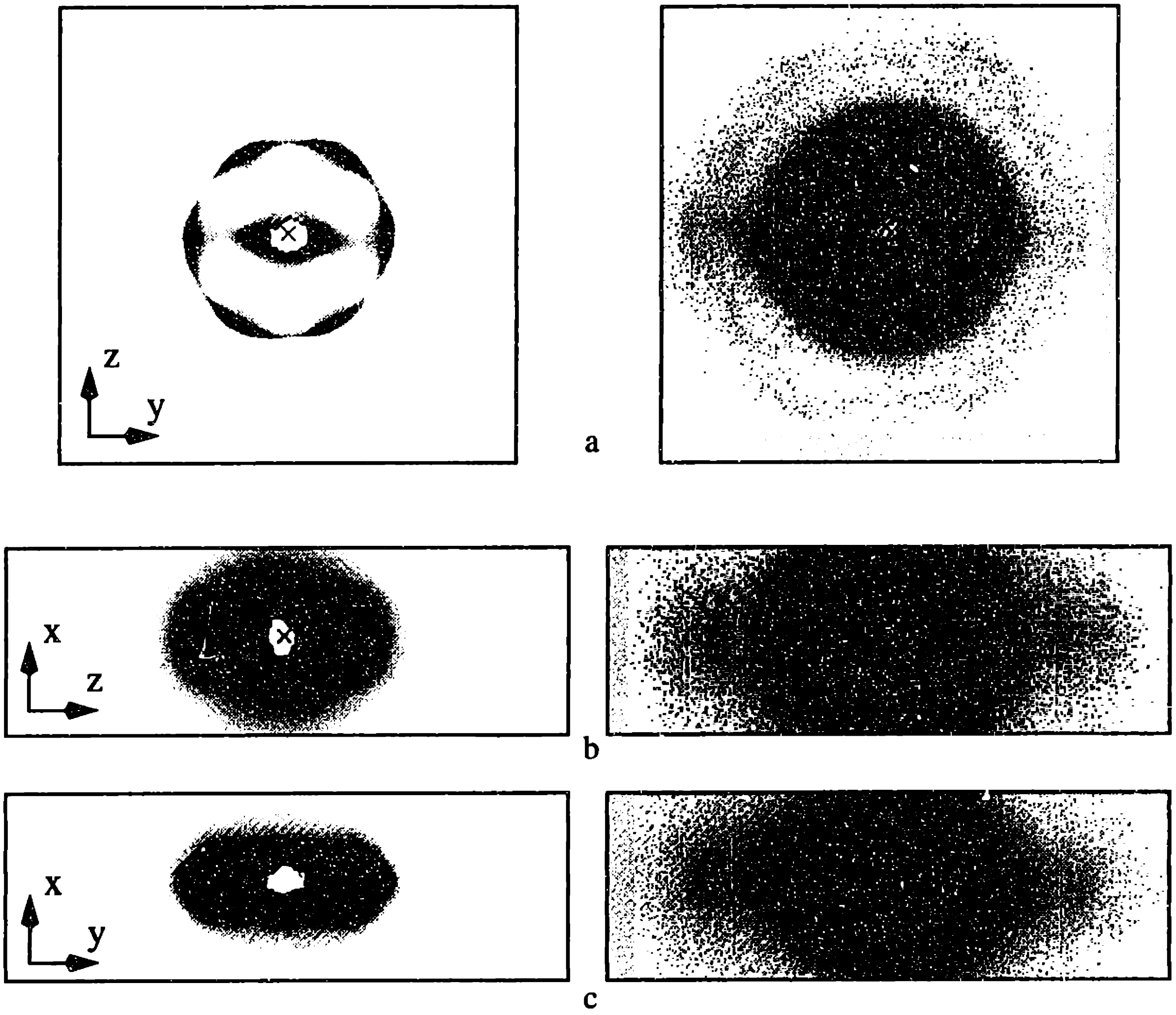

Figure 7-8: 2-D SAXS patterns along the three principle directions of a roll-cast SIS 15k-72k-15k deformed to 600% strain, irradiated and unloaded to 115% strain. The stress-time history is shown in Figure 7-7. The patterns on the left have been thresholded at a high level while the patterns on the right have been thresholded at a lower level.

for perpendicular deformation as the residual strain is greater for the former case. However, there is a greater degree of stress relaxation for parallel deformation and in this case the sample under parallel deformation broke sooner (after 11 minutes) than the one under perpendicular deformation (after 13 minutes).

2-D SAXS patterns taken of the irradiated sample along the 3 principle axes are presented in Figure 7-8. Most significantly, the pair of patterns (a) shows a view down the SD. The hexagonal symmetry of the patterns is quite apparent. From these patterns one concludes that the cylinders have not rotated away from the SD. (b) and (c) are reminiscent of the pattern in Figure 7-5 (c), which shows remnants of the lobe pattern as well as the strong $\sqrt{1}$ peaks on the equator. The two views orthogonal to the SD, (b) and (c), are different, however. In (b) the lobes above and below the equator are stronger relative to the $\sqrt{1}$ peaks on the equator than in (c). This difference in relative intensity can be explained by realizing that (b) is a section through (a) in the z-direction. The $\sqrt{1}$ peak intensity along the z-direction is at a minimum when compared with the $\sqrt{1}$ peak intensity along the y-direction. The lobe intensity is most likely the same at all azimuthal angles in the y-z plane and the difference in patterns (b) and (c) are due to a difference in $\sqrt{1}$ peak intensity and in thresholding.

7.4 Discussion

7.4.1 Previous Work

The yielding and necking deformation mechanism was elucidated by Odell and Keller using a combination of local strain measurements along the gage length, TEM on a yielded sample and birefringence. The mechanism of yielding in parallel deformation is discussed in terms of two composite theories: the shear lag theory and the random break theory.

The shear lag theory states that the axial stress on a cylinder builds as a function of distance from the cylinder end due to load transfer from the matrix. The result is that longer cylinders experience greater stresses. When the matrix stress in the cylinder (at its center) exceeds a critical stress (in this case, yield) the cylinder breaks. Thus for a given strain there is a critical length below which the cylinders will not break. The critical length can be calculated as a function of applied strain and shows an asymptotic increase as the critical length approaches 1000 Å.

The random break theory assumes a random distribution of breaks along the cylinder axis throughout the structure. The cylinder segments are assumed to have an equal length and to remain unstrained, but bear the load which is transferred to them from the elastically strained matrix. The applied strain is accommodated by the breaks between the cylinder segments and the matrix. Since the breaks are randomly distributed, the elastically strained matrix elements between cylinder carry various amounts of load depending on how near an adjacent break is to the center of the cylinder. Equilibrium for the central cylinder occurs when it has moved in response to the load from the 6 surrounding cylinder segments such that the average strain in the connecting matrix elements is minimized. A calculation can be made which relates the expected stress in the middle of a cylinder segment as a function of strain and segment length. Equating this stress with the breaking stress of a cylinder results in a relationship between applied strain and cylinder segment length very similar to that for the shear lag theory. Odell and Keller feel that the advantage of the random break theory is that the assumptions are more reasonable than for the shear lag theory. Though the functional form of the relationship between applied strain and segment length is different for the two theories, the qualitative result is the same: the applied strain must increase asymptotically for the cylinder segments to continue breaking. In this author's opinion, the shear lag concept provides an easier-to-grasp explanation for why the cylinders should break into smaller and smaller segments with increasing strain.

Perhaps one of the most significant results in the paper by Odell and Keller is the direct visualization of breaks between cylinder segments via TEM on a yielded sample. The sample was deformed and stored in the deformed state "until the stress had relaxed". In this way, a permanent set was introduced to the sample so that the breaks between cylinders remain and do not heal. A second potential complication, that of overlapping cylinders in the projected image of the microtomed section, was overcome by cutting sections thin enough to contain one or at most two cylinders. They used a combination of chemical hardening (via OsO4 staining) and thermal hardening (via cooling to liquid nitrogen temperatures*). The results show rods of average lengths from about 700Å to about 1100Å which are parallel to the SD. Although, Odell and Keller were not the first to directly visualize cylinder segments in a parallel deformation sample which had been yielded, the extra precautions in sample preparation enabled estimates of segment lengths to be made.

7.4.2 Progression of the Deformation

The contribution to the state of knowledge for the parallel deformation of the cylinder morphology in the present work lies in two areas. SAXS measurements on a sample under constant-strain-rate deformation probe the morphology at a single position along the gage length as a neck forms and propagates. Secondly, SAXS characterization of a sample which retains a significant amount of deformation provides direct evidence that the cylinders do not rotate away from the SD. This second conclusion contradicts the results obtained by Pakula and coworkers (Pakula et al., 1985), but is in agreement with the earlier studies of Pedemonte and coworkers (Pedemonte et al., 1976) as well as Keller and coworkers (Odell and Keller, 1977). The significance of these contributions will be made apparent through a discussion of the four regimes of a parallel deformation experiment.

As the sample is deformed, the yield point is quickly reached and a neck forms somewhere along the gage length. These two stages of the deformation, the initial linear (and reversible) regime and yielding/neck formation occur within 10% strain. Thereafter, the strain in the sample along the gage length is nonuniform. The structure of the sample can broadly be divided into a necked area and an unnecked area separated by a transition zone. The cylinders within the necked region have undergone a transformation which is readily seen in the SAXS patterns of Figure 7-2 taken at 60% and 116% strain. Deformation of the sample beyond yield occurs primarily through conversion of unnecked material and

---

*. Note that the exact microtoming conditions (sample temperature, knife temperature and speed, etc.) were not specified.

the corresponding movement of the transition zone along the gage length. This regime of neck propagation occurs at fairly constant load and represents a dynamic equilibrium between the unnecked material with the necked material at lower and higher stresses respectively. Increasing strain drives the reaction forward until conversion is complete. Neither the necked or the unnecked material undergoes significant change during neck propagation until full conversion. Measurement of the sample transmission (Figure 7-6) indicates that the thickness in the unnecked region changes only 4% until the region probed begins the transformation (at strains > 60%). This 4% thickness change may be accounted for by the slight initial sharpening of the sqrt(1) peaks indicating a "straightening" of the cylinders in the SD.

The transformation of the unnecked material occurs in a transition zone which represents a gradient in strain between the unnecked material with a strain of only a few % to the necked material with a strain of 80% (as measured by Odell and Keller)*. The width of the transition zone on the order of the length of the gage region (see Figure 9 in (Odell and Keller, 1977)). Such a situation could account for the thickness strain data beyond 60% deformation. As the transition zone enters the probe region, the thickness is expect to decrease dramatically. Once the probed region has been fully necked, the thickness should again stabilize. Indeed, a slight change in the slope of the thickness strain is observed at 144%. However, if the transition zone has reached the end of the gage length and consumed all unnecked material before fully converting the probed region, no such stabilization in thickness will be observed. Instead, the fourth and final regime of deformation, that of drawing, will begin.

---

*. Note that these values were measured on Kraton 102 which is an SBS having block molecular weights of approximately 11-61-11 and a composition of 25 wt% PS. In addition, Kraton 102 is known to contain a significant (20%) fraction of diblock. The triblock copolymer discussed in this chapter is an SIS 15k-72k-15k with no detectable diblock fraction.

After the entire gage length area has been transformed to fully necked material (of approximately 80% strain), subsequent increase in strain results in a stress increase uniformly along the gage length. The neck is drawn down with a continuous uniform decrease in thickness and width. The minimum in the stress-strain curve beyond yield (Figure 7-1) corresponds approximately with the inflection in the thickness strain curve (Figure 7-6).

7.4.3 Structure of Necked Material as a Function of Strain

The forgoing discussion of the general progression of a parallel deformation experiment has not included the structure of the necked material itself. The SAXS signature for the necked material is shown most clearly in Figure 7-2 at 320%. At this point the material has not only been necked, but also drawn. Four lobes of intensity extend out just above and below the equator from the origin. The pattern is consistent with strong fluctuations in electron density separated by large distances along the SD with poor correlation normal to the SD. There is a diffuse maximum as one travels along the equator at the $\sqrt{1}$ peak position. The four-lobe pattern can be interpreted in terms of PS cylinder segments separated by gaps of low electron density aligned with the SD. It is not immediately clear from the SAXS patterns whether the spacing of the lobes in the SD refers to the length of the cylinder segments or the break length. Consideration of the patterns during unloading suggests a conclusion. The lobe spacing *increases* during the course of unloading (compare patterns at 320%, 140% and 98%). This *increase* in q-spacing corresponds to a *decrease* in d-spacing of the scattering objects along the SD. Finally the lobes disappear entirely at the completion of unloading.

The lobe pattern must be due to scattering from the breaks between cylinders. The distance between PS cylinder segments along the SD are largest at the highest stresses and essentially fall to zero as the sample is unloaded. The strength of the intensity of the lobes is a result of the large electron density difference between the PS cylinder and the gaps between cylinders, which are likely only partially filled in with matrix rubber.

The cylinder break model for the necked material implies that there are three distinct levels of electron density; that of the PS cylinder segment, that of the rubber matrix and finally that due to whatever amount of material occupies the breaks between PS cylinder segments. The four lobe pattern is characteristic of void scattering, but from voids that have a fairly well-defined period (or height) along the SD. The width of the peak along the SD is due to either a distribution of break length or a lack of long-range break-periodicity along the SD. The two possibilities cannot be distinguished with the SAXS data at hand.

7.5 Bibliography

Odell, J. A. and A. Keller (1977). "Deformation behavior of an SBS copolymer." Polymer Engineering and Science **17**(1): 544-559.

Pakula, T., K. Saijo, H. Kawai and T. Hashimoto (1985). "Deformation behavior of SBS triblock copolymer with cylindrical morphology." Macromolecules **18**: 1294-1302.

Pedemonte, E., G. Dondero, F. de Candia and G. Romano (1976). "Correlation between physical-mechanical properties and morphological features of cruciform styrene-butadiene block copolymers." Polymer **17**: 72-76.

Chapter 8 Conclusions and Suggestions for Future Work

8.1 Conclusions

The primary goal was to investigate the morphology as a function of deformation in an oriented triblock copolymer system with the aim of providing a detailed deformation mechanism at the microdomain scale. Key to this effort was the preparation and characterization of a well-defined initial morphological state of orientation. Roll-Casting provides samples with the cylinder axis highly aligned in the flow direction with the closest packed $(10\bar{1}0)$ planes parallel to the film surface. Generally, the orientation distribution of a cylinder about its normal is smaller than the orientation distribution of grains of cylinders about the cylinder axis. In other words, the cylinders have a better axial than lateral correlation. Defects, which are observed in TEM (see section 5.1.2), evidence themselves in the azimuthal broadening of peaks in the 2-D SAXS patterns. Roll-cast samples with a cylindrical morphology can best be characterized as having near-parallel cylinders packed on a hexagonal net with a dominant rotational orientation such that the closest packed plane is parallel to the film surface.

The deformed microstructure depends on the orientation of the force to the cylinder axis. Samples display an initial low strain regime with little morphological change separated by a morphological transition from the high strain regime. These two structural regimes are reflected in the stress-strain diagram depending on the deformation direction.

8.1.1 Perpendicular Deformation

In deformation perpendicular to the cylinder axis, the rubber matrix acts as the primary load bearing agent up to strains of approximately 100%. The deformation is affine as indicated by a linear increase in the Bragg peak spacing. The shape of the stress-strain curve up to this point approximates that of a Gaussian network, which has the form (Treloar, 1944):

$$\sigma_{zz} = NkT\left((e_{zz}+1) - \frac{1}{(e_{zz}+1)^2}\right) \tag{8.1}$$

where N is the number of network chains per unit volume, σ_{zz} is the engineering stress and e_{zz} the engineering strain in the SD. Figure 8-1 illustrates the shape of equation (8.1). The

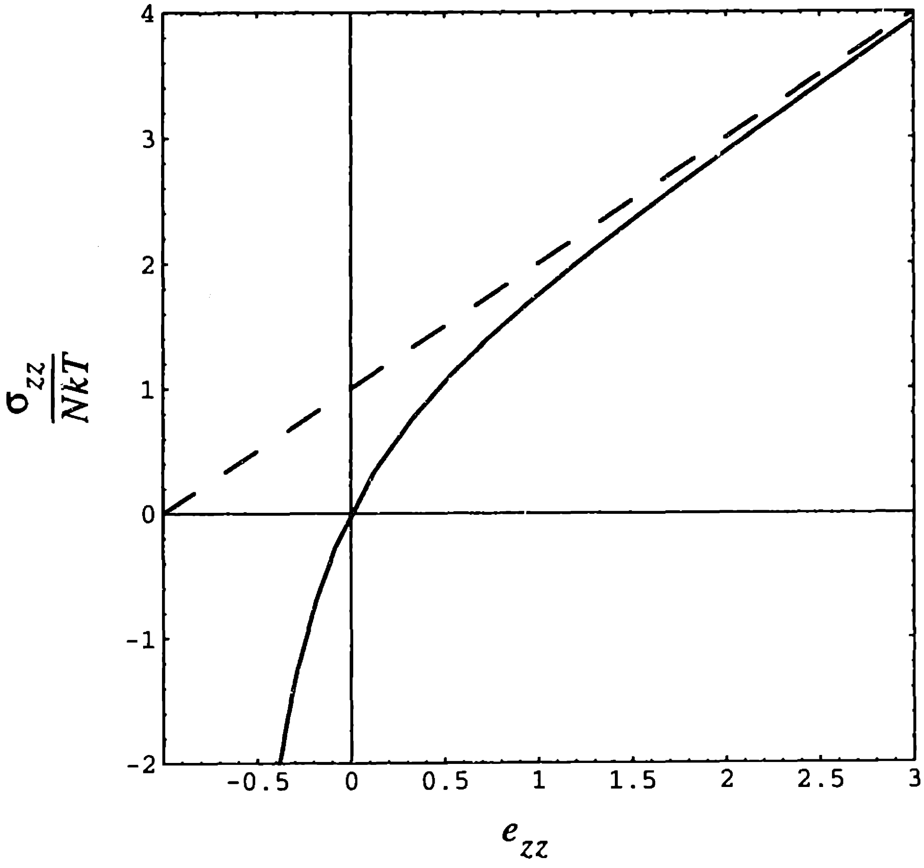

Figure 8-1: Plot of engineering stress vs. extension ratio (solid line) for a Gaussian network (equation (8.1)). The dashed line indicates how the deformation asymptotically approaches linear behavior at large strains.

analogy of a triblock TPE in a perpendicular deformation to a cross-linked rubber needs qualification on two counts, however. The cylinders acts as stiff reinforcements effectively constraining the rubber matrix in the x-direction. The measured Poisson's ratio in the y-z plane (υ_{yz}) of 0.9 indicates that the matrix is in a stress state approaching that of plane strain. Secondly, the matrix chains do not have an initial Gaussian conformation, but are stretched away from the intermaterial dividing surface (IMDS). The network of rubbery midblocks is characterized by weakly stretched chains with average trajectories away from the cylinder surface and endpoints anchored either in the same cylinder (looping conformations) or in an opposing cylinder (bridging conformations). Thus, equation (8.1) describing the elastic behavior of a Gaussian network would have to be modified to describe the elastic regime of an anisotropic network of chains in a state of plane strain.

The continuous broadening of the $\sqrt{3}$ peak at perpendicular incidence indicates that kinking occurs over a range of strains. There is no localization of the deformation with the stress-strain curve displaying a continuous decrease in slope before kinking is clearly detected via SAXS. The kinking transition represents a cross-over from a state of plane strain to a less constrained uniaxial state of stress and occurs simultaneously over the whole sample. The onset of the kinking transition limits further rapid increase of stress as strain increases. Once the plane strain condition is lifted, the stress increases at a rate slower than that shown in Figure 8-1 by equation (8.1).

The PS cylinders undergo kinking via a shear instability due to the increasing compressive stress along the cylinder axis. The compression is a consequence of the Poisson effect as the rubber matrix attempts to maintain its volume by contracting in a plane normal to the SD. The cylinders, however, resist the contraction of the matrix in the axial (x) direction. This resistance sets up a negative pressure along the cylinder axis which grows as the rubber is strained further. Regions of local cylinder misalignment serve as kink nucleation sites to relieve this pressure. The constraint on the rubber matrix in the x-direction is released as the cylinders turn towards the SD. The strain at which the kinking transition begins depends on the greatest cylinder misorientation. Although the kinking instability would theoretically be expected to occur at a critical strain, the misorientation about the cylinder normals in experimental samples causes kinking to occur over a range of strains with the majority of the transformation coinciding with the formation of the X pattern in the perpendicular incidence experiment. The growth of the kinked regions is expected to occur quickly in the SD. The kinked site introduces a force component normal to the cylinder axis. Adjacent unkinked cylinders in compression are biased to kink cooperatively in the same sense as the kink nucleus. The growth of kinking along the cylinder axis occurs more slowly in response to non-axial components of force from adjacent kinked regions. The compressive stress on the remaining unkinked cylinders is replaced by a torque transmitted by the kinking cylinders. At a certain distance from the adjacent kink, the torque becomes large enough to initiate a second kink of opposite sense. The scenario repeats itself as the deformation continues.

Once the sample is fully kinked, further deformation causes the cylinders to undergo shearing and dilation as they turn towards the SD. The upturn of the stress-strain curve at the highest strains is a result of the chain extension. Indeed a WAXS study of (Sakamoto et al., 1993) shows that the chains become highly oriented in the SD at large deformations.

8.1.2 Parallel Deformation

When the deformation direction is parallel to the cylinder axis, the PS cylinders bear the load and the stress increases in a linear manner until a sharp yield point is encountered. This linear response is characteristic of glassy PS in tension. It is the onset of the morphological instability, the formation of a neck, that is clearly indicated on the stress-strain curve as the yield point. In contrast to the perpendicular deformation case, the morphological transformation of the unnecked material during neck propagation occurs over a wide range of strain. The instability is localized to one or perhaps two areas along the gage length and does not occur simultaneously throughout the sample. Further deformation beyond neck propagation is a homogenous drawing of the sample during which the gaps between cylinders increase in both size and number. Upon unloading, the break spacing decreases, essentially disappearing as the cylinder segments rejoin.

The similarities between the morphological evolution with deformation in the parallel and perpendicular directions are superficial. A small strain elastic regime separated by a morphological transition from a large strain regime is characteristic of a highly anisotropic material undergoing a large strain deformation. Both the pathway of the deformation and the morphological endstate at high strain are different. Homogeneous and cooperative kinking in perpendicular deformation stands in contrast to a localized necking and neck propagation following by drawing in parallel deformation. The anisotropy of kinked and faulted cylinders does not progress to a pseudo-uniaxial array of cylinder segments aligned in the SD. There is no "universal" large strain morphological endstate. The asymptotic increase of the stress at high strain is due in large part to the approach of the rubber blocks to full extension, primarily in shear.

8.1.3 Stress Relaxation

The conclusion that the stress relaxation from a large perpendicular deformation occurs via a midblock conformational relaxation at constant morphological orientation rests on two observations:

- SAXS patterns at perpendicular incidence show no observable change during a 30% drop in stress
- a decrease in sample x-ray transmission interpreted as an increase in sample thickness during relaxation

These observations lead to a model where the junctions move (diffuse) along the IMDS in order to reduce chain stretching in the rubber. The conformational rearrangement includes the relaxation of chain compression in the y-direction causing the sample thickness to increase. Any bulk dilatation in the rubber is removed by this process. The stress relaxation is driven by the tendency for the rubber midblocks to return to a less stretched conformation.

8.2 Future Work

Discussion of future work will be broken into two areas, deformation mechanics and exploration of the effect of varying molecular structure on the mechanical behavior.

8.2.1 Deformation Mechanics

8.2.1.1 Small Strain Perpendicular Deformation

Micromechanical modeling of the kinking transition is an area ripe for further investigation. Though the small-strain mechanical properties of the oriented cylinder morphology have been successfully determined in terms of the elastic compliance tensor (Arridge et al., 1972), the stress-strain response has not been satisfactorily explained or modeled. The concept that the composite in perpendicular deformation responds as a constrained elastomer can be extended to attempt a quantitative fit to the stress-strain curve up to the kinking transition. The constitutive relation would (at zeroth order) contain rubber elasticity with a plane strain constraint. Details, such as the hexagonal packing and volume fraction of the cylinders as well as the anisotropy of the rubber chain conformations would be added to refine the model. A plane-strain rubber-elasticity model is expected to successfully reproduce the shape of the experimental stress-strain curve. The rubber chains essentially act as entropy springs between the glassy cylinders and are prevented from motion in the cylinder direction.

8.2.1.2 Large Strain Perpendicular Deformation

Once the cylinders have undergone kinking, a second model could be constructed to fit the stress-strain curve at high deformations. There are a number of hardening mechanisms to incorporate in such a model: the plastic working hardening due to bending of the PS hinges, shear elasticity both along the bent cylinder and in the plane normal to the cylinder axis, and finally a possible bulk elasticity contribution if the rubber experiences bulk dilation. The SBS and SIS triblock copolymers studied here do not, however, undergo strain-induced crystallization (Sakamoto et al., 1995) as they do not have a high enough 1,4 cis content (Hashimoto et al., 1985).

8.2.1.3 Large Strain Parallel Deformation

Measurements of the axial periodicity of the void lattice as a function of deformation suggest a reevaluation of models put forth by Odell and Keller (Odell et al., 1977). A treatment based on modern short fiber reinforced composites (Abrate, 1985) may be able to fit a stress-strain curve once the material begins drawing. First, however, the strain at the onset of drawing must be determined. A careful study of neck formation and propagation, perhaps on pre-notched samples (samples which have a reduction in cross-section to encourage controlled neck formation), following the procedure of (Odell and

Keller, 1977), would provide answers to questions such as: what is the width of the strain gradient during neck propagation?, Does the necked region remain at constant strain during neck propagation? Does drawing occur uniformly along the gage length?

8.2.1.4 Measurement of Chain Conformation

Several techniques are available which can probe the molecular orientation of the rubbery midblock.

Small-angle neutron scattering (SANS) on a triblock copolymer system with a deuterated midblock can determine the single chain scattering function (P(q)) once the scattering from the microdomain structure (S(q)) is removed via contrast matching. Measurements of chain conformation parallel to (Hadziioannou et al., 1982; Hasegawa et al., 1985; Hasegawa et al., 1987) and perpendicular to (Hasegawa et al., 1985; Hasegawa et al., 1987) the lamellar IMDS of styrene-diene diblock systems have been made. A similar attempt has been made on the spherical morphology (Richards et al., 1995), this time examining the midblock conformation of a triblock as a function of deformation. No attempt has been made to study the rubber midblock chain conformation in the matrix microdomain space of a cylinder morphology, let alone as a function of deformation.

Infrared dichroism can be used to probe the degree of orientation in rubber chains (Zhao, 1992; Sakamoto et al., 1993). Recent developments in infrared microscopy suggests experiments to examine the feasibility of observing variations in molecular orientation as a function of deformation.

As a final molecular probe, WAXS has been used to observe the degree of molecular alignment in an isotropic linear SBS triblock copolymer (Sakamoto et al., 1993). Dynamic WAXS could complement dynamic SAXS measurements to provide both morphological and molecular data simultaneously.

8.2.1.5 Stress Relaxation

To test the model put forth in section 8.1.3, a perpendicular stress relaxation experiment with the incident beam parallel to the cylinder axis would provide direct evidence for the change in thickness of the sample in the y direction. Movement of the $(10\bar{1}0)$ peak towards the origin would indicate an increase in the lattice spacing along the y direction. If this peak indeed stays fixed during the relaxation, the sample cannot be changing lateral dimension and the cause for the change in sample transmission would lie elsewhere. One possible alternative could account for a change in sample transmission without a concomitant change in thickness. If the electron density of the two phases changes during the course of the relaxation, the absorbed intensity could change. This explanation would require an increase in the electron density of both the rubber phase and the styrene phase to cause a decrease in the sample transmission during stress relaxation. A decrease of electron density of either phase is not expected during loading in a perpendicular deformation, however.

8.2.2 Influence of Structure

The molecular and morphological structure can be varied to extend the structure-property relationships for thermoplastic elastomers. The following are suggestions for structural modifications (molecular and morphological) which are expected to have a measurable impact on mechanical properties:

8.2.2.1 Variation in Degree of Orientation

As the quality of orientation decreases, the kinking transition is expected at smaller strains in a perpendicular stretch. As cylinder misorientation increases, yielding and necking may no longer be observed in a parallel deformation experiment. As the cylinder structure approaches an isotropic state, grain boundary compatibility and grain size (and size distribution) are expected to contribute to a response made up of some combination of a perpendicular deformation and a parallel deformation. Samples with a controlled grain boundary structure can be manufactured via the solvent welding of two oriented films at a well-defined orientation with respect to one another.

8.2.2.2 Molecular Weight Influence

Triblock copolymers of low enough molecular weight lose some of their mechanical properties due to their proximity to the ODT (Morton, 1983).The strengthening mechanism at high strains for triblocks of increasing molecular weight is less understood (Chen et al., 1977; Hashimoto et al., 1979). The mobility of the PS chains (and hence the rate of stress relaxation) is significantly slowed for large molecular weight triblocks at high strain. A homologous series of systematically increasing molecular weight (at constant composition) would provide further clues to this molecular weight effect.

Perhaps the greatest impact on the mechanical properties of TPEs is their molecular make-up. The following discussion is divided up in terms of copolymers that can be synthesized by a living polymerization and those synthesized by other means.

8.2.2.3 Molecular Influence - Living Polymerizations

Table 8-2: Triblock Copolymers that can Function as TPEs.

copolymer type	reference
poly(α-methylstyrene-isoprene-α-methylstyrene)	(Fetters et al., 1969) (Tung et al., 1986)
poly(α-methylstyrene-dimethylsiloxane-α-methylstyrene)	(Morton et al., 1975)
poly(α-methylstyrene-isobutylene-α-methylstyrene)	(Li et al., 1995) (Fodor et al., 1995)
poly(styrene-isobutylene-styrene)	(Koshimura et al., 1992) (Fodor et al., 1996)
poly(p-methyl-b-butadiene-p-methylstyrene)	(Tung and Lo, 1986) (Quirk et al., 1986)
poly(p-methylstyrene-isobutylene-p-methylstyrene)	(Fodor and Faust, 1996)
poly(methylmethacrylate-isobutylene-methylmethacrylate)	(Kennedy et al., 1991)
poly(ethylene-ethylenepropylene-ethylene)	(Kofinas et al., 1995)
poly(ethylene-ethylene-co-1-butene-ethylene)	(Morton, 1983)
poly(styrene-butadiene-4-vinylpyridine)	(Arai et al., 1980)
poly(styrene-ethylene-co-1-butene-methylmethacrylate)	(Auschra et al., 1993)
poly(styrene-butadiene-methylmethacrylate)	(Krappe et al., 1995)
poly(styrene-co-p-tert-butylstyrene-b-butadiene-b-styrene-co-p-tert-butylstyrene)	(Chen et al., 1987)

Table 8-2 provides a collection of references and gives a flavor for the chemical variety of TPEs that can be synthesized via living polymerizations. Anionic polymerization results in the most precise molecular control, but there are other living polymerization mechanisms which enable a wider variety of monomers to be polymerized in a controlled manner (Quirk et al., 1991). New monomers and post-polymerization processes are variables which can add another dimension to the structure and hence the mechanical response to deformation. These structural features include: endblock crystallization, variation in the T_g difference between mid- and endblocks and finally novel morphologies as a consequence of asymmetric endblocks (ABC triblocks).

8.2.2.4 Molecular Influence - Step Polymerizations*

There have been numerous developments in the synthesis of TPE's to optimize properties for particular applications (Walker, 1979; Holden, 1987; Bhowmick et al., 1988; Fodor and Faust, 1996; Tonelli et al., 1996). Detailed studies on the interplay between molecular characteristics and morphological features in determining the macroscopic mechanical properties have been carried out, but for many reasons, (most having to do with the degree of synthetic control; step vs. anionic polymerization) morphological control of segmented multiblock copolymer systems is much more difficult than that of styrene/diene block copolymers. Consequently, the level of structure-property understanding is much greater in the latter case. Utilizing the rational approach of molecular and morphological control followed by the judicious application of structural probes during well-defined deformation experiments, a much greater quantitative understanding of structure-property relationships for segmented multiblock copolymers is possible.

---

*· This section has previously appeared in (Honeker et al., 1996).

In segmented (multiblock) copolymers, such as polyurethanes and polyether-esters, one of the units of the soft segment is usually an oligomer of 1,000 - 4,000 molecular weight. This oligomer is linked into a multiblock chain of alternating hard and soft sequences, each chain containing from 10 to 100 blocks (see Figure 8-2:). These materials are typically made by a rapid bulk step growth polymerization, which leads to a significant distribution in the compositions and molecular weights of copolymer molecules, rather than by precisely-controlled anionic polymerization. As an example, consider polyurethane elastomers. There are two main synthesis procedures. The first is the prepolymer method in which a prepolymerized soft segment (either a polyether or polyester) is reacted with a prepolymerized polyurethane. The second is the one shot method in which the soft segment (macrodiol) is mixed with a chain extender (diol) and a diisocyanate (Meckel et al., 1987; Odian, 1991; Petrovic et al., 1991). The first method gives a narrower distribution of hard segment lengths, because the prepolymer has a Flory-distribution in molecular weight (Flory, 1953). In the one-shot method, simultaneous reaction of the three species leads to a competition between the chain extender and soft segment for the diisocyanate. Even in the case where the soft segment is anionically polymerized (e.g. a polybutadiene soft segment), the hard segment is always polydisperse (Petrovic and Ferguson, 1991).

In both polymerization methods, the final molecular (and thus morphological) make-up of a segmented thermoplastic elastomer is extremely sensitive to the reaction conditions and processing. As the molecular weight increases, the hard segments and soft segments become incompatible, thereby phase separating, and the linking reactions occur at the phase boundary which can upset the local stoichiometry. This may be problematic, for if the polymers are to achieve a high molecular weight, precise stoichiometry must be maintained. Temperature and molecular weight can influence the relative reactivity of the various components, which would broaden the molecular weight. Finally, both the glass transition and crystallization can hinder or stop the polymerization reaction if T_g and/or T_c reach the polymerization temperature. Solution polymerization can alleviate some of these difficulties, but the potential for polymer-solvent interactions is introduced, which would present a further set of polymerization variables and problems. Recently, however, an effort has been made to synthesize model polyurethanes with well-defined segment length distributions thus enabling a control of the morphology not unlike that found in anionically-synthesized block copolymers (Eisenbach et al., 1992; Eisenbach et al., 1995).

In addition to the sequence length distributions in both the hard and soft blocks and the overall fairly broad (M_w/M_n of at least 2) molecular weight distribution there are other molecular features which make segmented multiblock copolymers more complex than triblock copolymers. As suggested by Figure 8-2, the nanometer scale microdomain geometry for random multiblock copolymers will involve a variety of domain sizes and shapes, as well as multiple loop and bridge conformations for the soft segments. Moreover, for many multiblock copolymers, the hard segment selected is crystalline, so that in addition to microphase separation, crystallization of the hard segment also serves to drive the self assembly process. The soft segment can crystallize and/or hydrogen-bond with the hard segment, introducing yet another influence on the final morphology. Overall, primarily due to the lack of synthetic control, the complexity of the physical structure of segmented multiblock copolymers leads to less precise correlations for structure-property

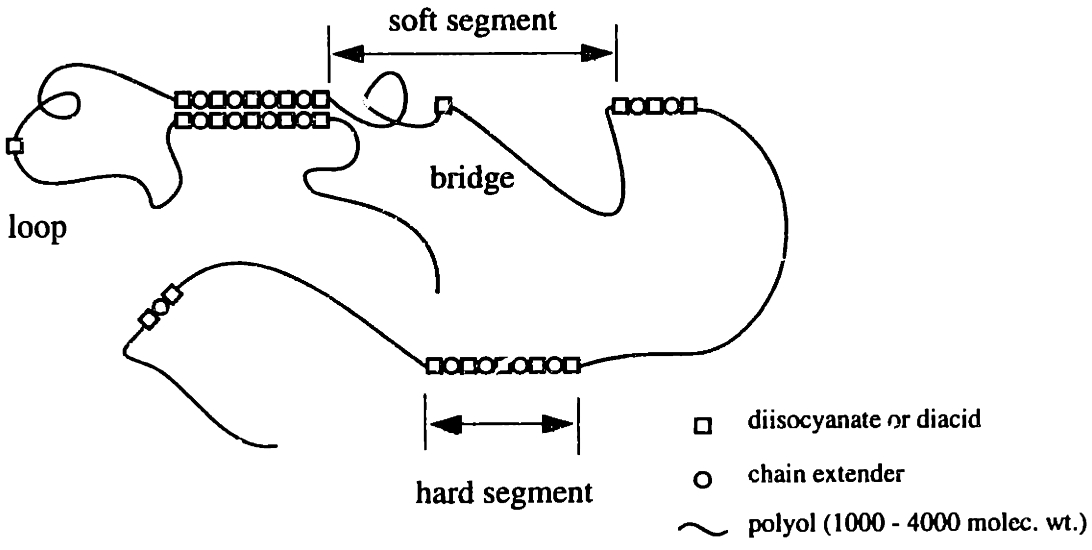

Figure 8-2: Schematic diagram of the chain architecture of a typical random multiblock copolymer molecule. The case shown is for a polyurethane/elastomer comprised of a hard segment based on diisocyanate or for a polyether ester comprised of a hard segment based on a diacid.

relationships than in the styrene-diene ABA TPEs. Many structural models used to describe the mechanical properties of segmented multiblocks are based on elasticity models of filled and unfilled rubbers (Petrovic and Ferguson, 1991) in contrast to anionically-synthesized block copolymers where small strain composite theory describes the mechanical response for several of the established morphologies quite well.

8.3 Bibliography

Abrate, S. (1985). "The mechanics of short-fiber-reinforced composites: A review." Rubber Chemistry and Technology **59**: 384-404.

Arai, K., T. Kotaka, Y. Kitano and K. Yoshimura (1980). "Poly(styrene-b-butadiene-b-4-vinylpyridine) three-block polymers. Synthesis, characterization, morphology, and mechanical properties." Macromolecules **13**: 1670-1678.

Arridge, R. G. C. and M. J. Folkes (1972). "The mechanical properties of a 'single crystal' of SBS copolymer - a novel composite material." Journal of Physics Part D: Applied Physics **5**: 344-358.

Auschra, C. and R. Stadler (1993). "New ordered morphologies in ABC triblock copolymers." Macromolecules **26**: 2171-2174.

Bhowmick, A. K. and H. L. Stephens, Eds. (1988). Handbook of Elastomers: New Developments & Technology. New York, Marcel Dekker.

Chen, J. C. and L. J. Fetters (1987). "Structure-property relationships for thermoplastic block terpolymers containing poly(styrene-p-tert-butylstyrene) copolymer end segments." Polymer Engineering and Science **27**(17): 1300-1309.

Chen, Y.-D. M. and R. E. Cohen (1977). "The influence of molecular weight on the large deformation behavior of SBS triblock copolymer elastomers." Journal of Applied Polymer Science **21**: 629-643.

Eisenbach, C. D., T. Heinemann, A. Ribbe and E. Stadler (1992). "Chain architecture and molecular self-organization of polyurethanes: Perspectives for thermoplastic elastomers." Die Angewandte Makromolekulare Chemie **202/203**: 221-241.

Eisenbach, C. D. and E. Stadler (1995). "Synthesis and properties of segmented poly(ether-urethanes) with specially designed and symmetrically chain-folding poly(n-alkylurethane) hard segments." Macromolecular Chemistry and Physics **196**(6): 1981-1997.

Fetters, L. J. and M. Morton (1969). "Synthesis and properties of block polymers. 1. Poly-a-methlstyrene-polyisoprene-poly-a-methylstyrene." Macromolecules **2**(5): 453-458.

Flory, P. J. (1953). Principles of Polymer Chemistry. Ithaca, Cornell University Press.

Fodor, Z. and R. Faust (1995). "Polyisobutylene-based thermoplastic elastomers. II. Synthesis and characterization of poly(p-methylstyrene-block-isobutylene-block-p-methylstyrene) triblock copolymers." Journal of Macromolecular Science: Pure and Applied Chemistry **A32**(3): 575-591.

Fodor, Z. and R. Faust (1996). "Polyisobutylene-based thermoplastic elastomers. IV. Synthesis of poly(styrene-block-isobutylene-block-styrene) triblock copolymers using n-butyl chloride as solvent." Journal of Macromolecular Science Pure and Applied Chemistry **A33**(3): 305-324.

Hadziioannou, G., C. Picot, A. Skoulios, M.-L. Ionescu, A. Mathis, R. Duplessix, Y. Gallot and J.-P. Lingelser (1982). "Low-angle neutron scattering study of the lateral extension of chains in lamellar styrene/isoprene block copolymers." Macromolecules **15**: 263-267.

Hasegawa, H., T. Hashimoto, H. Kawai, T. P. Lodge, E. J. Amis, C. J. Glinka and C. C. Han (1985). "SANS and SAXS studies on molecular conformation of a block polymer in microdomain space." Macromolecules **18**: 67-78.

Hasegawa, H., H. Tanaka, T. Hashimoto and C. C. Han (1987). "SANS and SAXS studies on molecular conformation of a block polymer in microdomain space. 2. contrast matching technique." Macromolecules **20**: 2120-2127.

Hashimoto, T., M. Fujimura, K. Saijo, H. Kawai, J. Diamant and M. Shen (1979). Strain-induced plastic-to-rubber transition of a SBS block copolymer and its blend with PS. Multiphase Polymers. S. L. Cooper and G. M. Estes, ACS Advances in Chemistry Series: 257-275.

Hashimoto, T., K. Saijo, M. Kosc, H. Kawai, A. Wasiak and A. Ziabicki (1985). "Oriented crystallization of cross-linked polybutadiene rubber. 2. Small-angle and wide-angle x-ray scattering." Macromolecules **18**: 472-482.

Holden, G. (1987). Chapter 13: Applications of thermoplastic elastomers. Thermoplastic Elastomers. N. R. Legge, G. Holden and H. E. Schroeder. Munich, Hanser: 481-506.

Honeker, C. C. and E. L. Thomas (1996). "Impact of morphological orientation in determining mechanical properties in block copolymers systems." Chemistry of Materials **8**(8): 1702-1714.

Kennedy, J. P., J. L. Price and K. Koshimura (1991). "Novel thermoplastic elastomer triblocks of a soft polyisobutylene midblock connected to two hard PMMA stereocomplex outer blocks." Macromolecules **24**: 6567-6571.

Kofinas, P. and R. E. Cohen (1995). "Melt processing of semicrystalline E/EP/E triblock copolymers near the order-disorder transition." Macromolecules **28**: 336-343.

Koshimura, K. and H. Sato (1992). "Application study of styrene-isobutylene-styrene block copolymer as a new thermoplastic elastomer." Polymer Bulletin **29**: 705-711.

Krappe, U., R. Stadler and I. Voigt-Martin (1995). "Chiral assembly in amorphous ABC triblock copolymers. Formation of a helical morphology in PS-PB-PMMA block copolymers." Macromolecules **28**: 4558-4561.

Li, D. and R. Faust (1995). "Polyisobutylene-based thermoplastic elastomers. III. Synthesis, characterization, and properties of Poly(α-methylstyrene-b-isobutylene-b-α-methylstyrene) triblock copolymers." Macromolecules **28**: 4893-4898.

Meckel, W., W. Goyert and W. Wieder (1987). Thermoplastic polyurethane elastomers. Thermoplastic Elastomers: A Comprehensive Review. N. R. Legge, G. Holden and H. E. Schroeder. Munich, Hanser: 13-46.

Morton, M. (1983). "Structure-property relations in amorphous and crystallizable ABA triblock copolymers." Rubber Chemistry and Technology **56**: 1096-1110.

Morton, M., Y. Kesten and L. J. Fetters (1975). Thermoplastic elastomers based on polysiloxanes. Polymerization and Polycondensation Processes. N. A. Platzer. New York, John Wiley and Sons. **26:** 113-121.

Odell, J. A. and A. Keller (1977). "Deformation behavior of an SBS copolymer." Polymer Engineering and Science **17**(1): 544-559.

Odian, G. (1991). Principles of Polymerization. New York, John Wiley & Sons.

Petrovic, Z. S. and J. Ferguson (1991). "Polyurethane elastomers." Progress in Polymer Science **16**: 695-836.

Quirk, R. P. and J. Kim (1991). "Recent advances in thermoplastic elastomer synthesis." Rubber Chemistry and Technology **64**(3): 450-468.

Quirk, R. P., M. T. Sarkis and D. J. Meier (1986). Phase-selective curing of poly(p-methylstyrene-b-butadiene-b-p-methylstyrene). Advances in Elastomers and Rubber Elasticity. J. Lal and J. E. Mark. New York, Plenum Press: 143-155.

Richards, R. W. and G. Welsh (1995). "Deformation of matrix macromolecules in a uniaxially extended styrene-isoprene-styrene linear triblock copolymer." European Polymer Journal **31**(12): 1197-1206.

Sakamoto, J., S. Sakurai, K. Doi and S. Nomura (1993). "Molecular orientation of SBS triblock copolymer with cylindrical microdomains of polystyrene." Polymer **34**(23): 4837-4840.

Sakamoto, N. and T. Hashimoto (1995). "Order-disorder transition of low molecular weight polystyrene-block-polyisoprene. 1. SAXS analysis of two characteristic temperatures." Macromolecules **28**: 6825-6834.

Tonelli, C., T. Trombetta, M. Scicchitano, G. Simeone and G. Ajroldi (1996). "New fluorinated thermoplastic elastomers." Journal of Applied Polymer Science **59**: 311-327.

Treloar, L. R. G. (1944). "Stress-strain data for vulcanized rubber under various types of deformation." Transactions of the Faraday Society **440**: 59-70.

Tung, L. H. and G. Y. Lo (1986). Diene triblock polymers with styrene-alpha-methylstyrene copolymer end blocks. Advances in Elastomers and Rubber Elasticity. J. Lal and J. E. Mark. New York, Plenum Press: 129-142.

Walker, B., Ed. (1979). Handbook of Thermoplastic Elastomers. New York, Van Nostrand Reinhold.

Zhao, Y. (1992). "Structural changes upon annealing in a deformed SBS triblock copolymer as revealed by infrared dichroism." Macromolecules **25**: 4705-4711.

Appendix A Diffraction Theory

A.1 Introduction

This appendix provides an introduction to diffraction from crystalline systems. Although block copolymers are completely amorphous materials on an atomic scale, they are nevertheless ordered on a length scale of 10-100 nm. The microstructure can be thought of as "crystalline" with the caveat that the "atoms" of the "crystal" are amorphous domains of the minority component in a matrix of the majority component. Hence, a diffraction treatment in terms of a lattice is more appropriate than a scattering treatment in terms of correlation functions. Diffraction from a perfect crystal is described by a convolution of the unit cell with a lattice, while the unit cell can be described by placing the appropriate atoms at their respective positions within the cell. A brief introduction to convolutions and how they relate to Fourier transforms is included. Both the "atoms" and "lattice" of a block copolymer structure contain imperfections that are reflected in the diffraction pattern. A short discussion of three types of crystal imperfections and their respective impact on the diffraction pattern follows the description of diffraction from a perfect lattice.

A.2 Scattering from an Atom

The deflection of an incident wavefront due to its interference with correlated scattering centers is known as diffraction. These scattering points can be of any scale ranging from the nuclei of atoms diffracting in a neutron beam to the pilings of a pier diffracting ocean waves. Here we will be concerned with the diffraction (scattering) of x-rays by the electrons in the atoms of the sample under investigation.

X-rays impinging on a sample may be absorbed or scattered. The scattered photons are either coherent, if no energy is lost in the collision, or incoherent, if energy is lost. This distinction is based on the fact that photons that have lost an unknown amount of energy during interaction with the electrons in the sample are reradiated at a wavelength other (larger) than the initial incident wavelength. The resulting photons of a distributed wavelength cannot interfere (destructively or constructively) with the coherent photons and hence only contribute to a diffuse background.

Only coherent scattering is of interest in a diffraction experiment as it is the relative phases of parts of the beams with respect to one another that contain information on the relative positions of the scattering centers and hence the structure of the sample. It will become apparent that the diffracted wave function (amplitude and phase) contains all the information necessary to reconstruct the electron density distribution of the sample.

In Figure A-1, a single electron fixed in space (at O) will scatter an initially unpolarized incident x-ray beam to yield an amplitude component both parallel and perpendicular to the plane AOP. The incident plane wave accelerates the electron in the direction of the electric field. Under classical scattering conditions, the electron oscillates with the same frequency as the incident wave and reradiates x-rays in directions that are normal to the acceleration direction. Perpendicular and parallel components of the scattered electric field in the plane AOP are given by equations (A.1) and (A.2) respectively.

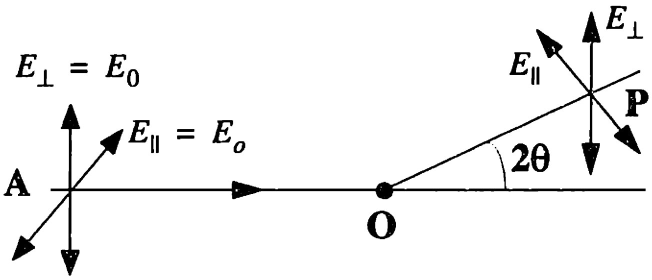

Figure A-1: Unpolarized x-ray beam impinges on electron at O.

$$E_\perp = \frac{e^2}{mc^2}\frac{E_o}{r} \tag{A.1}$$

$$E_\parallel = \frac{E_o}{r}\frac{e^2}{mc^2}\cos 2\theta \tag{A.2}$$

The resulting radiation has the same frequency and hence wavelength (or energy) as the oscillating electron.

As the intensity is related to the amplitude as $I = \frac{c}{8\pi}EE^*$, where E^* is the complex conjugate of E, the Thompson formula yields the intensity measured in the plane AOP:

$$I_e = I_o \frac{e^2}{mc^2} \frac{1 + (\cos(2\theta))^2}{2R^2} \qquad \text{with } I_o = \frac{c}{8\pi}|E_o|^2 \qquad (A.3)$$

The factor e^2/mc^2 is known as the Thompson scattering factor where e is the charge of an electron, m its mass and c the speed of light. I_e, the intensity (in energy/unit solid angle/sec) of scattering radiation from an electron is often used to normalize experimental data that have been measured in absolute units.

Diffraction only occurs in the presence of more than one scatterer (in this case an electron). Therefore it is necessary to consider the amplitude (A) of the radiation scattered from a group of electrons, say, those of an atom.

$$A = f|E| \text{ where } f \le Q \text{ (total number of electrons in the atom)} \qquad (A.4)$$

f describes the number of electrons which contribute to the scattered amplitude and is known as the atomic structure factor.

The corresponding intensity can be written in terms of the intensity scattered by one electron:

$$I = |f|^2 I_e. \qquad (A.5)$$

The structure of such a sample is then represented as $|f|^2$, sometimes called the absolute intensity.

The scattered amplitude from two electrons (e_1 and e_2) separated by a distance r can be constructed following the treatment of (Porod, 1982) and is outlined below (Figure A-2). Let e_1 be the origin at the coordinate system and $\mathbf{S_0}$ and $\mathbf{S_1}$ be unit vectors in the incident and scattered wave directions, respectively. At a distant point in the direction of $\mathbf{S_1}$, rays from e_1 and e_2 become parallel; i.e. at a distance » $|\boldsymbol{r}|$. The phase difference between the

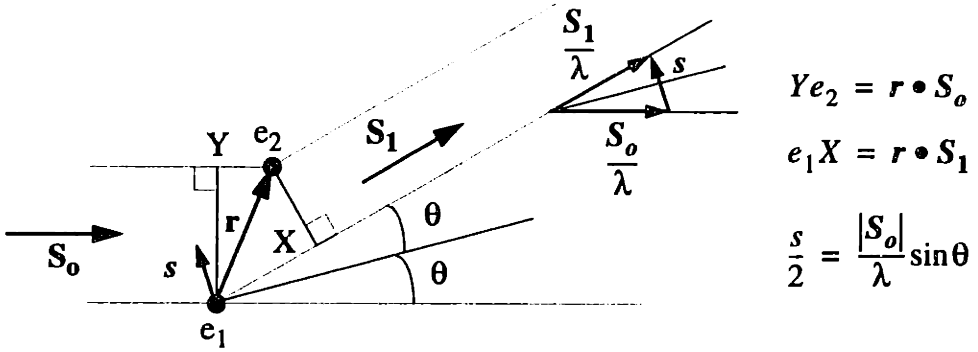

Figure A-2: Geometry of the scattering of two electrons.

scattered rays in terms of the path difference is:

$$\frac{\Delta\phi}{2\pi} = \frac{e_1X - Ye_2}{\lambda} = \frac{\boldsymbol{r} \bullet (\boldsymbol{S_1} - \boldsymbol{S_o})}{\lambda} = \boldsymbol{r} \bullet \boldsymbol{s} \tag{A.6}$$

where s is defined as the scattering vector (see Figure A-2). The scattering vector has magnitude:

$$s = |\boldsymbol{s}| = \frac{2\sin\theta}{\lambda} \tag{A.7}$$

and gives the direction of momentum transfer in the elastic collision between photon and electron. The amplitude (A_2) of the diffracted wave will result from the interference of the scattered wave components of e_1 and e_2. In the Fraunhofer limit, the scattering factor can be written in complex form (see Section A.6):

$$f_2 = \frac{A_2}{A_e} = \frac{A_e e^0 + A_e e^{2\pi i \boldsymbol{r} \bullet \boldsymbol{s}}}{A_e} \tag{A.8}$$

Generalizing to many electrons which are distributed in a structure that can be divided into volume elements dV, small in comparison to 1/s, yields a continuous form for f(s):

$$f(s) = \int_{V_r} \rho(r) e^{2\pi i \boldsymbol{r} \bullet \boldsymbol{s}} dV_r \tag{A.9}$$

where $\rho(\boldsymbol{r})$ is the electron density in dV_r located at **r**. To simplify notation one can replace 2πs with **q** and write:

$$f(\boldsymbol{q}) = \int \rho(\boldsymbol{r}) e^{i\boldsymbol{q} \bullet \boldsymbol{r}} d^3\boldsymbol{r} \tag{A.10}$$

where f(**q**) is commonly called the atomic form factor.

With the amplitude of scattering from an atom defined, the theoretical development of x-ray diffraction can be divided into two separate treatments: scattering from regularly spaced atoms (crystalline materials) and scattering from randomly spaced atoms (amorphous materials). The next section provides a flow diagram of the theoretical approaches characterizing the scattering from samples at the extremes of order. As we are interested in structure on a supermolecular scale (domains), small-angle scattering will be considered. A cursory examination of the diffraction patterns in Chapters 5-7 do not necessarily allow an obvious classification of the structure into the above subdivisions. On the one hand, the patterns show a degree of order that cannot be described by any random or nearly random arrangement of scattering objects. Yet these patterns do not reflect a periodicity typically found in small molecule crystalline materials. The framework needed to describe this type of scattering generally falls in between the traditional descriptions of scattering from crystalline and amorphous materials. Concepts from both treatments are necessary to understand more fully the attempts that have been made to analyze these unique patterns.

A.3 X-ray Diffraction - The Big Picture

The intensity of x-ray scattering can be built up by taking the square of the modulus of the structure factor (F(**q**)) of the electron density (ρ(**r**)) of the sample which is equivalent to the double sum of the electron density over the position vectors $\mathbf{r}_l$ and $\mathbf{r}_{l'}$. This equation holds for all samples regardless of structure, but this intensity can be reduced to a simpler form depending on the extent of order in the system.

If it is known that the sample has random distribution of scattering centers (a structure that can be characterized as amorphous on some length scale), then the intensity is broken up into a component characterizing interparticle interferences (S(**q**)) and a

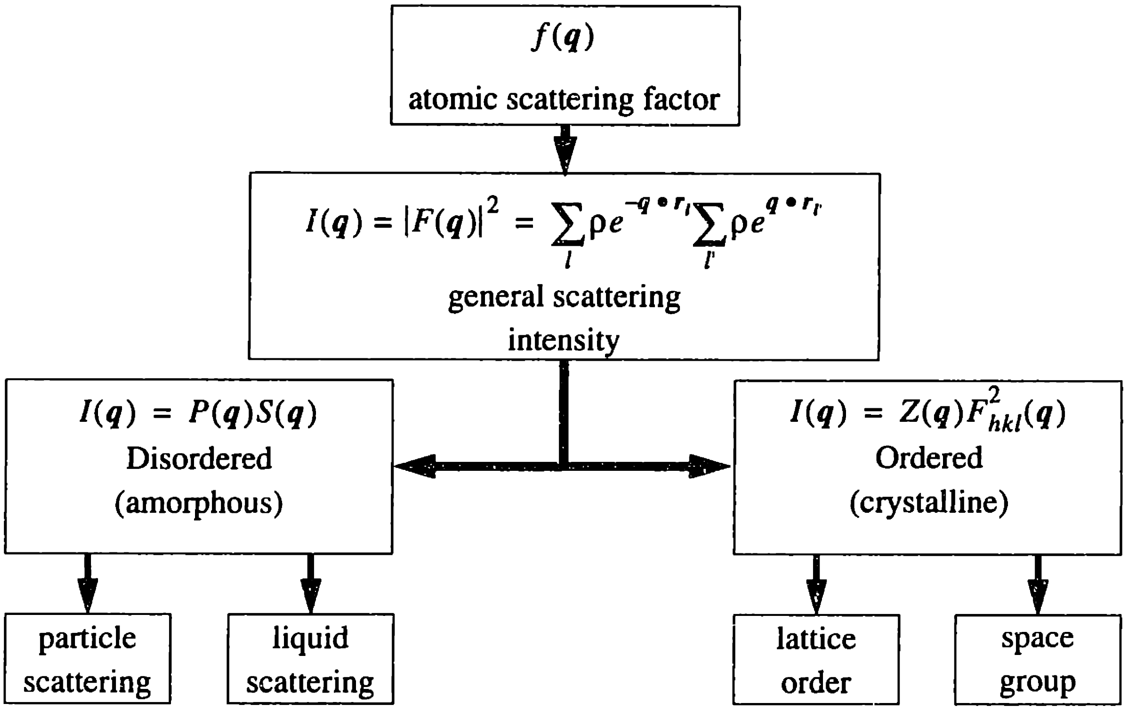

component describing intraparticle interference (P($\mathbf{q}$)). If the scattering centers are embedded in a matrix of uniform electron density and the distances between centers are uncorrelated, then S($\mathbf{q}$) approaches 1 and scattering from the individual particles (particle scattering) dominate the intensity in the limit of dilution. If the scattering centers behave as point scatterers, then scattering from the system will reveal information about the distance distribution (through S($\mathbf{q}$)) in the form of a pair-correlation function.

If the system is known to be highly ordered and the scattering centers have a crystalline regularity, then the intensity is represented by the structure factor $F_{hkl}(\mathbf{q})$ (modulus squared), describing the shape of the scattering centers and their distribution within the unit cell. In a general structure (i.e., one without a center of symmetry) the structure factor is a complex number. This factor is, however, modulated by the various imperfections of the lattice that are captured by the lattice factor Z($\mathbf{q}$). Z($\mathbf{q}$) can be thought to sample $F_{hkl}(\mathbf{q})$ at particular windows of q-space. Diffraction of ordered samples can be seen not only to give precise spacial information concerning the basic building blocks of the crystal, but also information on the quality of the lattice order. The quality of order in the present block copolymer system justifies the diffraction approach which is outlined in the following sections.

A.4 Fourier Transforms and Convolutions

Equation (A.10) is an example of a Fourier integral and several properties of Fourier analysis are exploited in diffraction theory. Just as the structure factor of an atom can be found by the Fourier transform of the electron density in equation (A.10), so, too, can the electron density be determined by the *inverse* transform of $f(\boldsymbol{q})$

$$\rho(\boldsymbol{r}) = \frac{1}{(2\pi)^3}\int f(\boldsymbol{q})e^{i\boldsymbol{q}\bullet\boldsymbol{r}}\mathrm{d}^3\boldsymbol{q} \tag{A.11}$$

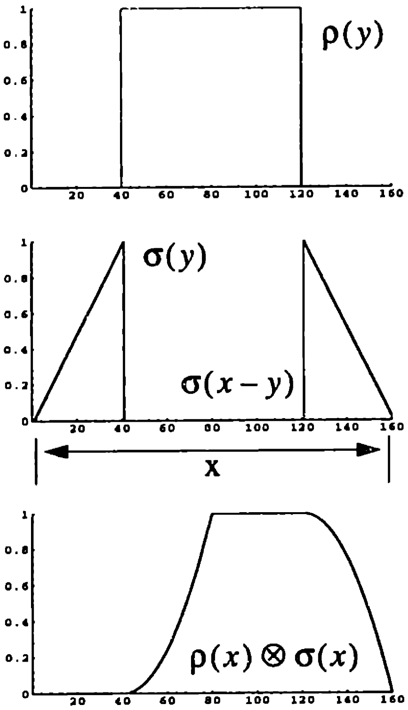

Figure A-3: The convolution operation on two functions $\rho(x)$ and $\sigma(x)$. See (A.12).

The complementary relationship between $f(\boldsymbol{q})$ and $\rho(\boldsymbol{r})$ is often expressed by calling the functions a *Fourier pair.* One function contains the same information as the other, only in a different form. One represents the structure in r-space while the other in q-space. Both equations (A.10) and (A.11) are equivalent statements of the Fourier Theorem.

In conjunction with the Fourier Theorem, another powerful tool in the understanding of the diffraction of complex objects is that of convolution. The convolution of two functions ρ(x) and σ(x) is represented by a convolution product:

$$\rho(x)\otimes\sigma(x) = \int_0^{\infty}\rho(y)\sigma(x-y)dy \tag{A.12}$$

An illustration of the mathematical operation is given in Figure A-3. In general, the convolution of two functions will be broader than the broadest of the two, but will have some similarity with the broader of the two.

The convolution operation is not to be confused with the correlation operation:

$$\sigma(x) \otimes \rho(\bar{x}) = \int_{0}^{\infty} \sigma(y)\rho(y+x)dy \tag{A.13}$$

A particular case of correlation is the correlation of a function with its inverse; i.e. the correlation of $\rho(\boldsymbol{r})$ with $\rho(\bar{\boldsymbol{r}})$. The correlation of $\rho(\boldsymbol{r})$ with itself is denoted the auto-correlation of $\rho(\boldsymbol{r})$ and is generally indicated as the Q-function

$$Q(\boldsymbol{r}) = \rho(\boldsymbol{r}) \otimes \rho(\bar{\boldsymbol{r}}) = \int_{V_{r'}} \rho(\boldsymbol{r}')\rho(\boldsymbol{r}'+\boldsymbol{r})dV_{r'} \tag{A.14}$$

Auto-correlation of $\rho(\boldsymbol{r})$ is to be distinguished from self-convolution:

$$P(\boldsymbol{r}) = \rho(\boldsymbol{r}) \otimes \rho(\boldsymbol{r}) = \int_{V_{r}} \rho(\boldsymbol{r}')\rho(\boldsymbol{r}-\boldsymbol{r}')dV_{r'} \tag{A.15}$$

If the two functions operated on are the same, then the prefix auto- or self- is used in front of the operator. Q(**r**) always contains a center of symmetry regardless of ρ(**r**), while P(**r**) is not generally centro-symmetric. If ρ(**r**) is centrosymmetric ($\rho(\boldsymbol{r}) = \rho(\bar{\boldsymbol{r}})$), then $Q(\boldsymbol{r}) = P(\boldsymbol{r})$. If ρ(**r**) describes a periodic lattice, then Q(**r**) is known as the Patterson function.

An important link between the convolution operation and the Fourier transform is known as the Convolution Theorem. The theorem states that if $A(\boldsymbol{q})$ and $S(\boldsymbol{q})$ are the Fourier transforms of $\rho(\boldsymbol{r})$ and $\sigma(\boldsymbol{r})$ respectively, then the Fourier transform of the product of $\rho(\boldsymbol{r})$ and $\sigma(\boldsymbol{r})$ is the convolution of the Fourier transforms of $\rho(\boldsymbol{r})$ and $\sigma(\boldsymbol{r})$ respectively:

$$\int \rho(\boldsymbol{r})\sigma(\boldsymbol{r})e^{-i\boldsymbol{q}\bullet\boldsymbol{r}}\mathrm{d}^{3}\boldsymbol{r} = \int A(\boldsymbol{q}_1)S(\boldsymbol{q}-\boldsymbol{q}_1)\mathrm{d}^{3}\boldsymbol{q}_1 = A(\boldsymbol{q}) \otimes S(\boldsymbol{q}) \tag{A.16}$$

In other words, the Fourier transform of the product of two functions is equal to the convolution product of the Fourier transform of the respective functions separately. The inverse convolution theorem is written:

$$\frac{1}{(2\pi)^3}\int A(\boldsymbol{q})S(\boldsymbol{q})e^{-i\boldsymbol{q}\bullet\boldsymbol{r}}\mathrm{d}^{3}\boldsymbol{q} = \rho(\boldsymbol{r}) \otimes \sigma(\boldsymbol{r}) \tag{A.17}$$

The most important application of the convolution theorem in diffraction is in the Fourier transform of the intensity (from (A.5) and (A.10)):

$$i(\boldsymbol{q}) = f(\boldsymbol{q})f^{*}(\boldsymbol{q}) = \int \rho(\boldsymbol{r}_1)e^{i\boldsymbol{q}\bullet\boldsymbol{r}_1}\mathrm{d}^3\boldsymbol{r}_1 \int \rho(\boldsymbol{r}_2)e^{-i\boldsymbol{q}\bullet\boldsymbol{r}_2}\mathrm{d}^3\boldsymbol{r}_2 \qquad \text{(A.18)}$$

where f* is the complex conjugate of f. Combining terms yields:

$$i(\boldsymbol{q}) = \iint \rho(\boldsymbol{r}_1)\rho(\boldsymbol{r}_2)e^{i\boldsymbol{q}\bullet(\boldsymbol{r}_1-\boldsymbol{r}_2)}\mathrm{d}^3\boldsymbol{r}_1\mathrm{d}^3\boldsymbol{r}_2 \qquad \text{(A.19)}$$

With the substitution of $\boldsymbol{r} = \boldsymbol{r}_1 - \boldsymbol{r}_2$ (A.19) can be written as:

$$i(\boldsymbol{q}) = \iint \rho(\boldsymbol{r}+\boldsymbol{r}_2)\rho(\boldsymbol{r}_2)e^{i\boldsymbol{q}\bullet\boldsymbol{r}}\mathrm{d}^3\boldsymbol{r}\mathrm{d}^3\boldsymbol{r}_2 \qquad \text{(A.20)}$$

Applying the Convolution Theorem (equations (A.17) and (A.14)):

$$FT^{-1}\left\{\frac{1}{(2\pi)^3}i(\boldsymbol{q})\right\} = Q(\boldsymbol{r}) = \rho(\boldsymbol{r}) \otimes \rho(\bar{\boldsymbol{r}}) \qquad \text{(A.21)}$$

Thus, given the auto-correlation of the electron densities of the sample, the intensity can be determined by the Fourier transformation of (A.21) or:

$$i(\boldsymbol{q}) = FT\{Q(\boldsymbol{r})\} \qquad \text{(A.22)}$$

A.5 Scattering from Crystals

A.5.1 Ideal Crystals

A.5.1.1 Reciprocal Lattice

In describing the diffraction from a crystal, one must first define the crystal in a more mathematical sense. A crystal is a repetition of a unit (an individual or group of atoms) in three dimensions. The smallest volume, that, upon repetition, builds up the crystal, is called the unit cell and is often used to represent the crystal. The repetition is described by the vectors $\mathbf{a}_1$, $\mathbf{a}_2$, $\mathbf{a}_3$, which are called the lattice vectors. The positions of all atoms within the crystal are written in terms of $\mathbf{a}_1$, $\mathbf{a}_2$ and $\mathbf{a}_3$, but the origin can be chosen arbitrarily. Figure A-4 details the definition of $\boldsymbol{R}_m^n$ which determines the location of any atom within the crystal from an arbitrary origin.

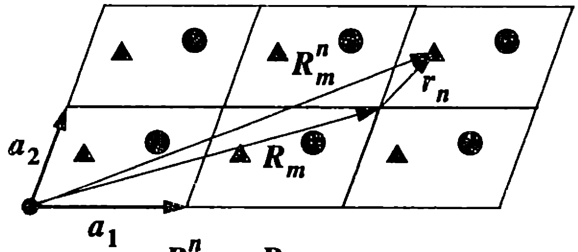

$$R_m^n = R_m + r_n$$

Figure A-4: Two dimensional representation of the periodic property of the a crystal.

$\mathbf{R_m}$ is a vector from the crystal origin to the unit cell origin and is written in terms of the number of unit cells which need to be traversed in the directions of the crystal axes.

$$R_m = m_1 a_1 + m_2 a_2 + m_3 a_3 \tag{A.23}$$

$\mathbf{r_n}$ describes the position of the nth scatterer within the unit cell. In the conceptual framework of Bragg's law, scattering is visualized to consist of specular reflection of the x-rays off the lattice planes. The planes are most conveniently described by a vector (H_{hkl}) normal to them with magnitude proportional to the inverse of the spacing between them. It can be shown (Warren, 1969) that this vector can be written in terms of the Miller indices (*hkl)*. These indices represent a set of parallel planes, one of which passes through the origin and with next nearest plane intercepts the crystallographic axes at a_1/h, a_2/k, and a_3/l. H_{hkl} can also be introduced in terms of the reciprocal vectors q_1, q_2, q_3:

$$H_{hkl} = hq_1 + kq_2 + lq_3 \tag{A.24}$$

The reciprocal vectors q_1, q_2, q_3 are defined to be perpendicular to the plane containing the crystal axes having opposing indices:

$$q_1 = \frac{2\pi a_2 \times a_3}{a_1 \bullet a_2 \times a_3} \qquad q_2 = \frac{2\pi a_3 \times a_1}{a_1 \bullet a_2 \times a_3} \qquad q_3 = \frac{2\pi a_1 \times a_2}{a_1 \bullet a_2 \times a_3} \tag{A.25}$$

One important relation between the vectors a_1, a_2, a_3 and q_1, q_2, q_3 is:

$$a_i \bullet q_j = \begin{cases} 2\pi & i = j \\ 0 & i \neq j \end{cases} \tag{A.26}$$

The factor in the denominator ($\boldsymbol{a}_1 \bullet \boldsymbol{a}_2 \times \boldsymbol{a}_3$) represents the volume of the cell and works as a normalizing factor so that the vector $\boldsymbol{H}_{hkl}$ has a magnitude proportional to the inverse of the spacing between planes.

$$d_{hkl} = \frac{2\pi}{|\boldsymbol{H}_{hkl}|} \tag{A.27}$$

The reciprocal vectors $\boldsymbol{q}_1, \boldsymbol{q}_2, \boldsymbol{q}_3$ describe a lattice in reciprocal space which is useful in studying diffraction problems.

A.5.1.2 Development of the Structure Factor for an Ideal Crystal

Starting with the scattered amplitude from one atom (m, n) in the crystal observed at a distance:

$$E = A_o f_n e^{i\boldsymbol{q} \bullet \boldsymbol{R}_n^m} \tag{A.28}$$

Here, A_0 contains the prefactor associated with Thompson scattering. The exponent contains the phase factor which takes into account the location of the origin. The scattered amplitude from the unit cell (at $\mathbf{R}_m$) can be written:

$$F_{R_m}(\boldsymbol{q}) = \sum_n A_o f_n e^{i\boldsymbol{q} \bullet \boldsymbol{R}_n^m} = e^{i\boldsymbol{q} \bullet \boldsymbol{R}_m} \sum_n A_o f_n e^{i\boldsymbol{q} \bullet \boldsymbol{r}_n} = e^{i\boldsymbol{q} \bullet \boldsymbol{R}_m} F_u(\boldsymbol{q}) \tag{A.29}$$

$F_u(\boldsymbol{q})$ can be thought of as the Fourier transform of the electron density distribution of the unit cell:

$$F_u(\boldsymbol{q}) = \int_{V_{cell}} \rho_{cell} e^{i\boldsymbol{q} \bullet \boldsymbol{r}} \tag{A.30}$$

The electron density distribution of a crystal can be constructed by placing the electron density of the unit cell at each lattice point. Mathematically, the crystal is rigorously described by the convolution of the unit cell with a lattice of delta functions specifying the location of each unit cell position:

$$\rho_{crystal}(\boldsymbol{r}) = \rho_{cell} \otimes \sum_{m_1 m_2 m_3} \delta^3(\boldsymbol{r} - \boldsymbol{R}_m) \tag{A.31}$$

The scattered amplitude of the crystal is then the Fourier transform of the convolution product in (A.31),

$$F_{crystal}(\boldsymbol{q}) = \int \rho_{crystal}(\boldsymbol{r}) e^{i\boldsymbol{q} \bullet \boldsymbol{r}} \qquad (A.32)$$

which, with the use of the inverse of the Convolution Theorem (A.17), can be written:

$$F_{crystal}(\boldsymbol{q}) = F_{cell}(\boldsymbol{q}) \sum_{hkl} \delta^3(\boldsymbol{q} - \boldsymbol{H}_{hkl}) \qquad (A.33)$$

The Fourier transform of a series of delta functions in real space results in a series of delta functions in reciprocal space. Just as a unit cell is found whenever $\mathbf{r} = \mathbf{R}_m$ in (A.31), so will an infinite amplitude be found when $\mathbf{q} = \mathbf{H}_{hkl}$. The Fourier transform requires the relationship between $\mathbf{R}_m$ and $\mathbf{H}_{hkl}$ to be:

$$\boldsymbol{R}_m \bullet \boldsymbol{H}_{hkl} = 2\pi N \qquad (A.34)$$

where N is any integer. This is a restatement of Bragg's law and it is seen that the scattering amplitude from a crystal is made up of the sampling of the structure factor of the unit cell at the positions of the reciprocal lattice vectors.

A.5.2 Non-ideal Crystals

As perfect crystals are very rare, account must be made of the influence of the various kinds of imperfections on the scattering from real crystals. These imperfections include the boundaries of the crystal, thermal fluctuations of the atoms about their lattice sites (type I distortions), lattice distortions of type II (paracrystalline distortion) as well as other less important crystal imperfections.

A.5.2.1 Finite Crystal Size

The effect of finite crystal size is most easily recognized by multiplying a 'window' function with the electron density distribution function of the perfect crystal $\rho_{crystal}$ of equation (A.31). The window function can be defined as:

$$W(x) = \begin{cases} 1 \text{ for } \frac{-1}{2} \le x \le \frac{1}{2} \\ 0 \text{ otherwise} \end{cases} \qquad (A.35)$$

A crystal of size N_1, N_2, N_3 can be described by:

$$\rho_{finite}(x, y, z) = \rho_{crystal}(x, y, z)\, W\left(\frac{x}{N_1}\right) W\left(\frac{y}{N_2}\right) W\left(\frac{z}{N_3}\right) \tag{A.36}$$

Now, applying the Fourier transform in conjunction with the convolution theorem, the amplitude of scattering from a crystal with finite size can be written:

$$F_{finite}(\mathbf{q}) = F_{crystal}(\mathbf{q}) \otimes \left(\operatorname{sinc}\left(\frac{q_1 N_1}{2}\right)\operatorname{sinc}\left(\frac{q_2 N_2}{2}\right)\operatorname{sinc}\left(\frac{q_3 N_3}{2}\right)\right) \tag{A.37}$$

where sinc(x) is defined as:

$$\operatorname{sinc}(x) = \frac{\sin(x)}{x} \tag{A.38}$$

Sinc(x) has the form shown in Figure A-5. The intensity scattered from a crystal will be proportional to the square of the modulus of the structure factor (Warren, 1969).

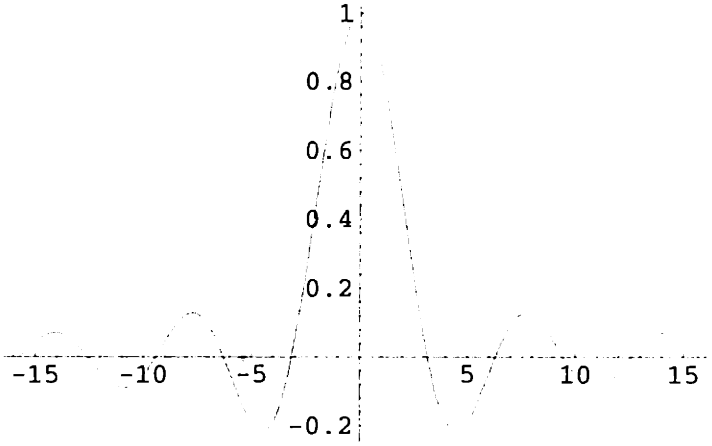

Figure A-5: A plot of equation (A.38), the sinc(x) function from -5π to +5π. The full-width-at-half-max (FWHM) is 0.379.

$$I \sim \left|F_{cell}\right|^2 \left(\left(\frac{\sin\left(\frac{N_1}{2} q_1 \bullet a_1\right)}{\sin\left(\frac{q_1 \bullet a_1}{2}\right)}\right)^2 \left(\frac{\sin\left(\frac{N_2}{2} q_2 \bullet a_2\right)}{\sin\left(\frac{q_2 \bullet a_2}{2}\right)}\right)^2 \left(\frac{\sin\left(\frac{N_3}{2} q_3 \bullet a_3\right)}{\sin\left(\frac{q_3 \bullet a_3}{2}\right)}\right)^2 \right) \tag{A.39}$$

The term within the brackets results from the summation of Equation (A.29) over all unit cells within a crystal of size N_1, N_2, N_3. The resulting sum of exponentials can be expanded into a geometrical progression and rewritten into a single term.

Taking the square of the modulus of this term and simplifying yields functions of the form:

$$\left(\frac{\sin(Nx)}{\sin(x)}\right)^2 \tag{A.40}$$

This function is plotted in Figure A-6 for N = 20. As N increases, the function approximates

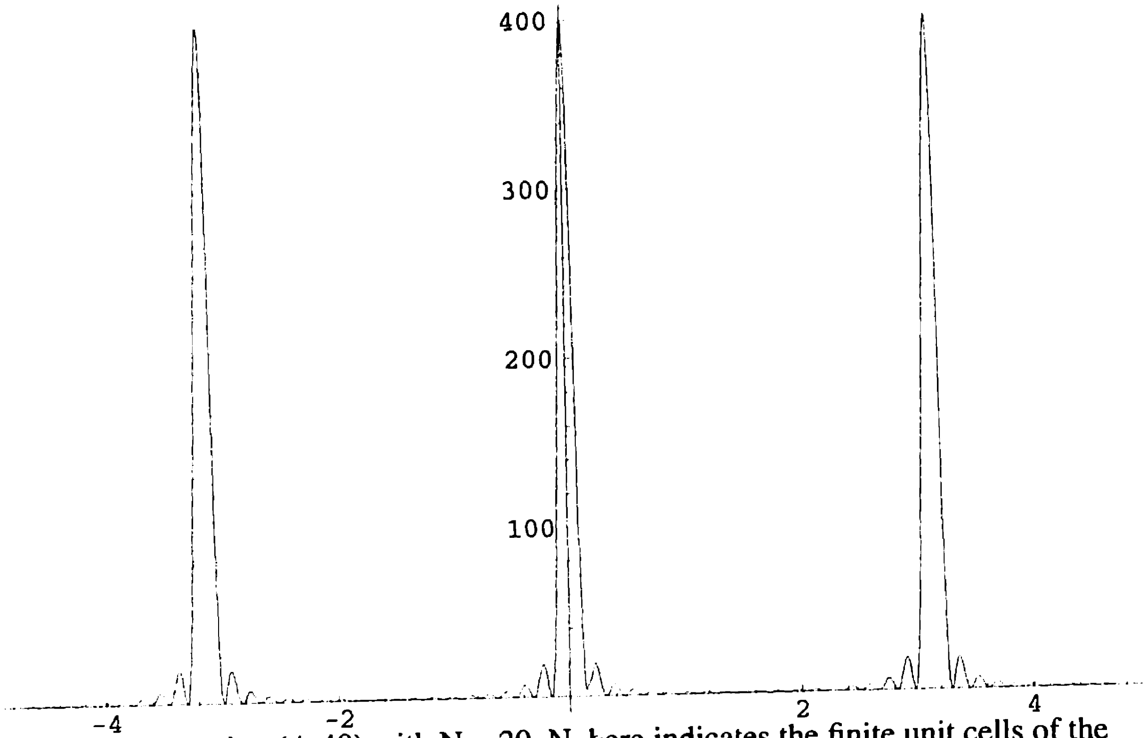

Figure A-6: Equation (A.40) with N = 20. N, here indicates the finite unit cells of the crystal. As N becomes large, only the peaks at integral multiples of π remain and the function approximates an infinite series of equally-spaced delta-functions.

a series of one-dimensional delta-functions.

It is important to note that as the crystal becomes smaller (decreasing N), *every* observed diffraction peak becomes broader by the same relative amount.

A.5.2.2 Thermal Fluctuations

The effect of thermal vibrations on scattered radiation is such to introduce a further broadening factor. In any diffraction experiment, a time average of the atomic positions is taken. Because of the vibrations of the atoms, the x-rays effectively diffract off atoms with smeared-out positions which are only weakly dependent on the neighboring atoms. The strategy is to introduce a fluctuation distance δ into Equation (A.32) and to take an average over all δ. If the fluctuations are independent of **r** (spherically symmetric thermal vibrations - an approximation at best), then it can be shown that the peaks are smeared in a Gaussian manner (Warren, 1969).

$$\langle e^{q \bullet \delta} \rangle \approx e^{\frac{-(q \bullet \delta)^2}{2}} \tag{A.41}$$

This type of exponential thermal fluctuation correction is known as the Debye-Waller factor. Due to the strong q dependence, the amplitudes of the high angle peaks are diminished quickly. Note that the peak shape remains unchanged by the multiplication of this temperature factor. The factor only decreases as q increases, diminishing the higher order diffraction. Distortions of the structure in which the scatterer has a positional Gaussian distribution, independent of its neighbors, are known as type I distortions.

A.5.2.3 Paracrystalline Distortions

Lattices with distortions of the second kind (type II distortions) are characterized by short range order but lack long range order. The model introduced by Hosemann and coworkers (Hosemann et al., 1962) to describe the effects of these distortions is known as the paracrystalline model. In principle, the paracrystalline model can account for the scattering of all structures with order ranging from that of a perfect crystal to that of the amorphous state. As long as any local lattice can be discerned, distortions are introduced in the form of an independent distance distribution function describing the probability of locating the next neighbor, which serve to destroy the long range periodicity. The overall effect is to damp out (reduce peak height and increase the peak width) the higher order delta functions encountered in the lattice factor (Z(q)) of a perfect lattice. The principles of the ideal 3-dimensional paracrystal are based on a 1-dimensional paracrystalline lattice as shown in Figure A-7.

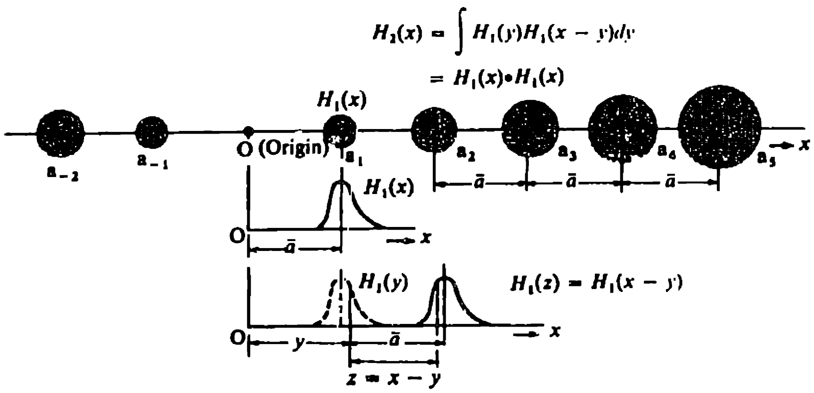

Figure A-7: One-dimensional paracrystalline lattice. Dark regions surrounding the lattice points indicate probabilities of finding atoms. (Taken from (Kakudo et al., 1972) p. 126).

Let $H_1(y)$ be the probability of finding a_1 at a distance y from the origin. The probability of finding a_2 located a distance z from a_1 (at the end of y) will be $H_1(y)H_1(z)$. The total probability of finding a_2 at a distance x (x = y + z) from the origin (i. e., $H_2(x)$), is not merely the product above. The result can be understood by noting that there exists a large number of (y, z) pairs which sum to give x = y + z for a fixed x. For each pair there is a certain probability $H_1(y)H_1(z)$ of finding a_2. The total $H_2(x)$ is simply the sum of these probabilities over y for fixed x (z = x-y):

$$H_2(x) = \int_{-\infty}^{\infty} H_1(y)H_1(x-y)dy \tag{A.42}$$

which is recognized as an auto-convolution product:

$$H_2(x) = H_1(x) \otimes H_1(x) \tag{A.43}$$

The probability of finding the n-th lattice point at a distance x from the origin is written:

$$H_n(x) = \underbrace{H_1 \otimes H_1 \otimes \ldots H_1}_{\text{n-1 fold}} \tag{A.44}$$

The properties of H(x) are such that:

1) $\int_{-\infty}^{\infty} H_1(x)dx = 1$

2) $$H_{-1}(x) = H_1(-x) \quad \text{(centrosymmetric)}$$

3) $$\int_{-\infty}^{\infty} xH_1(x)dx = \bar{a}$$

The one-dimensional (1-D) paracrystal is extended into three-dimensions (3-D) by building up 1-D lattices each with their own probability distribution function. Three lattice vectors $\mathbf{a}_1$, $\mathbf{a}_2$, and $\mathbf{a}_3$ describe the average spacing between lattice points in three orthogonal directions. The 3-D paracrystalline lattice is then defined by the vectors and the corresponding nearest neighbor probabilities H_{100}, H_{010}, and H_{001} which might result in a structure shown in Figure A-8.

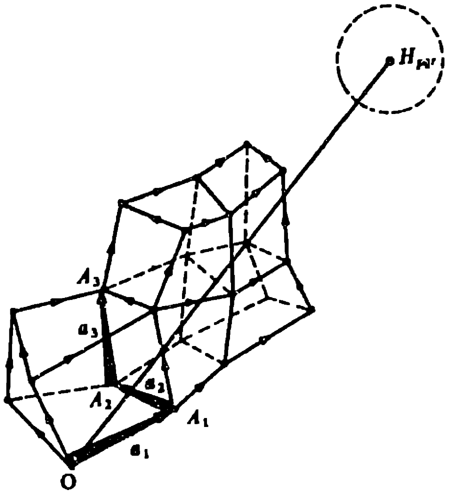

Figure A-8: Three-dimensional paracrystalline lattice. $\mathbf{a}_1$, $\mathbf{a}_2$, and $\mathbf{a}_3$ indicate average lattice vectors to lattice point A_1, A_2, and A_3. H_{pqr} represents the probability of finding an atom pth along $\mathbf{a}_1$, qth along $\mathbf{a}_2$ and rth along $\mathbf{a}_3$. (Taken from (Kakudo and Kasai, 1972) p. 127).

The probability that any given atom is located at a distance $\mathbf{x}$ from the origin can be determined in an analogous manner to the 1-D case. Let $H_{pqr}(\mathbf{x})$ be the probability that $\mathbf{x}$ will locate a point (atom) p-th in $\mathbf{a}_1$, q-th in $\mathbf{a}_2$ and r-th in $\mathbf{a}_3$.

$$\begin{aligned} H_{pqr}(x) = H_{000} &\otimes H_{100} \otimes H_{100} \otimes \ldots (H_{100} && \text{<- (p-1) fold} \\ &\otimes H_{010} \otimes H_{010} \otimes \ldots (H_{010} && \text{<- (q-1) fold} \\ &\otimes H_{001} \otimes H_{001} \otimes \ldots H_{001})) && \text{<- (r-1) fold} \end{aligned} \tag{I.9}$$

where H_{000} is a point-function (3-D delta-function) located at the origin.

In order to determine the total probability of finding an atom at **x** one must sum up the probabilities H_{pqr} over all paths through the lattice:

$$\text{total probability} = \sum_{p=-\infty}^{\infty}\sum_{q=-\infty}^{\infty}\sum_{r=-\infty}^{\infty} H_{pqr} \tag{A.45}$$

$$= \sum_{p=-\infty}^{\infty} H_{p00} \otimes \sum_{q=-\infty}^{\infty} H_{0q0} \otimes \sum_{r=-\infty}^{\infty} H_{00r} = z(\boldsymbol{x})$$

The function z(x), as derived for this case of an ideal 3-D paracrystalline lattice is to be contrasted to the 3-D series of delta functions describing an ideal lattice (see (A.31)) which guarantees finding a lattice point at a certain distance from the origin. In order to determine the lattice factor (Z(q)) in reciprocal space, it is necessary to Fourier transform z(x). The steps necessary become quite involved. Details can be found in (Hosemann and Bagchi, 1962) (pp. 306-310). Here, only the significant steps are outlined.

Let H_{100}, H_{010}, and H_{001} be H_k with k = 1, 2, 3 and $F_k(q) = FT(H_k(x))$. From the Convolution Theorem and the fact that $H_k(x)$ is real:

$$\begin{aligned} \text{F.T.}(H_{p00}) &= F_{100}^{p} && \text{for } p > 0 \\ &= 1 && \text{for } p = 0 \\ &= F_{100}^{*|p|} && \text{for } p < 0 \end{aligned} \tag{A.46}$$

and so on. The Fourier transform of each sum in (A.45) can be written:

$$K_k(q) = \sum_{p=1}^{\infty} (F_k^p + F_k^{*p}) - 1 \tag{A.47}$$

Here the index p is used in place of the indices p, q, and r in (A.45). The lattice factor is therefore:

$$Z(\boldsymbol{q}) = \prod_{k=1}^{3} K_k = K_1 K_2 K_3 \tag{A.48}$$

The sum (A.47) can be written in terms of a limit with M playing the role of the number of unit cells in the paracrystal:

$$K_k(q) = \lim_{M \to \infty} 2Re\left(\frac{1 - F_k^{M+1}}{1 - F_k}\right) - 1 \tag{A.49}$$

which can be rewritten:

$$K_k(q) = \lim_{M \to \infty} Re\left(\frac{2 - 2F_k^{M+1} - 1 + F_k}{1 - F_k}\right) . \tag{A.50}$$

Breaking up the term into two parts:

$$\begin{aligned} K_k(q) &= Re\left(\frac{1 + F_k}{1 - F_k}\right) + \lim_{M \to \infty} Re\left(\frac{-2F_k^{M+1}}{1 - F_k}\right) \\ &= Re\left(\frac{1 + F_k}{1 - F_k}\right) + K(0) \end{aligned} \tag{A.51}$$

where

$$K(0) = -2 \lim_{M \to \infty} \frac{Re(1 - F_k^*)F_k^{M+1}}{\left|1 - F_k\right|^2} \tag{A.52}$$

The complex F_k can be represented by modulus and phase:

$$\begin{aligned} F_k(q) &= \left|F_k\right| e^{-i\bar{a} \bullet q} \\ F_k^* &= \left|F_k\right| e^{i\bar{a} \bullet q} \\ \text{where } \bar{a} &= \int_{-\infty}^{\infty} x H_k(x) dV_x \end{aligned} \tag{A.53}$$

Substituting (A.53) into (A.52) we get:

$$K(0) = \lim_{M \to \infty} \left|F_k\right|^M \frac{\sin\left(M + \frac{1}{2}\right)(\bar{a} \bullet q)}{\sin\frac{(\bar{a} \bullet q)}{2}} . \tag{A.54}$$

Since $\left|F_k\right| \to 1$ only near $q = 0$ and $M \to \infty$, K(0) represents a sharp peak at the origin. Subtracting K(0) from $K_k(q)$ leaves the information about the higher order diffraction. Rewriting the first term in (A.51):

$$Re\left(\frac{1 + F_k}{1 - F_k}\right) = \frac{1 - \left|F_k\right|^2}{1 + \left|F_k\right|^2 - 2Re(F_k)} \tag{A.55}$$

Finally,

$$K_k(q) - K(0) = \frac{1 - |F_k|^2}{1 + |F_k|^2 - 2|F_k|\cos \boldsymbol{q} \bullet \bar{a}} \tag{A.56}$$

with

$$|F_k| \sim e^{-\frac{1}{2}\boldsymbol{q} \bullet \boldsymbol{T} \bullet \boldsymbol{q}} \tag{A.57}$$

where T is a symmetric fluctuation tensor such that

$$\boldsymbol{q} \bullet \boldsymbol{T} \bullet \boldsymbol{q} = 4\pi^2 \sum_k^3 \sum_i^3 T_{ik} q_i q_k$$

$$\text{with } T_{ik} = \begin{bmatrix} \Delta^2 x_{11} & \Delta^2 x_{12} & \Delta^2 x_{13} \\ \Delta^2 x_{21} & \Delta^2 x_{22} & \Delta^2 x_{23} \\ \Delta^2 x_{31} & \Delta^2 x_{32} & \Delta^2 x_{33} \end{bmatrix} \tag{A.58}$$

where $\Delta^2 x_{ij}$ is the square of the standard deviation of the fluctuation of an atom located in the *i* direction, but fluctuating in the *j* direction.

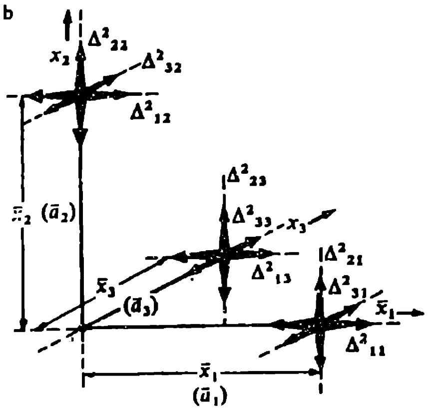

Figure A-10: Paracrystalline fluctuations in terms of the three lattice vectors $\mathbf{a}_1$, $\mathbf{a}_2$, and $\mathbf{a}_3$. (Taken from (Kakudo and Kasai, 1972) p. 132).

A.5.3 SAXS of Polymers

Up until now, we have considered diffraction of x-rays from the electron clouds surrounding the atoms. The recognition that the relationship between the structure and the amplitude of the scattering is naturally described by Fourier transforms, leads to the conceptual understanding that reciprocal (Fourier) space, as described by **s,** can equivalently contain the structure as described by **r** in real space. Mathematically, this relationship is observed in the product $\boldsymbol{q} \bullet \boldsymbol{r}$ found in all calculations of the phase of scattered x-rays relative to the incident beam. Magnitudes of **q** are reciprocal to magnitudes of **r**. Indeed, Bragg's law, which describes the scattering from atoms arranged on a space lattice is simply a restatement of this relationship:

$$1 = \frac{d_{hkl} 2 \sin\theta}{\lambda} = d_{hkl}|s| = d_{hkl}\frac{|q|}{2\pi} \qquad \text{(A.59)}$$

As d and λ are on the same order of size, diffraction in these crystals occurs over a relatively wide range of angles, hence in performing crystallography one generally conducts wide-angle x-ray scattering (WAXS).

As the real space dimensions become large, **q** (or rather θ at fixed λ) necessarily becomes small. The dimensions of interest in small-angle scattering (SAXS) are much larger than the Å scale typically ranging from 100's to 1000's of Å. At this length scale it is not actually the interference between the electron clouds of neighboring atoms which needs to be considered, but rather the fluctuations in electron density on this larger length scale which is important. As a consequence, perfect crystals and homogeneous materials in general do not scatter x-rays at low angles. SAXS from polymers is predominantly due to two kinds of inhomogeneity of the length scale discussed here: a) alternations between crystalline and amorphous regions, or more generally regions of different phases, and b) microvoids. It is mainly for this reason that the theories developed to treat small-angle scattering have focused on the diffuse scatter from large scale correlations of regions with varying electron density. Sharp Bragg reflections, in contrast, are not observed very often, as there are few materials with periodicities of 100's of Å.

The intensity of SAXS is proportional to the electron density difference squared. Therefore, it is clear that phases with only a small difference in electron density (which generally scales with bulk density) will only scatter weakly.

A.6 Complex Representation Of The Wave Amplitude Of X-rays Scattered From An Atom.

If ν is the frequency of the wave, the wave amplitude at any given time (t) and position (x) can be written as

$$E(x,t) = E_o \cos\left(2\pi \upsilon t - \frac{2\pi x}{\lambda}\right) . \tag{A.60}$$

Considering the classical scattering of x-rays by electrons in an atom, the total amplitude at a distant observation point can be derived as follows: Consider an incident beam, in a direction represented by an unit vector $\mathbf{S_0}$, of x-rays polarized perpendicular to the page incident on a group of electrons centered at O (see Figure A-11). The position of each electron is represented by $\mathbf{r_n}$ and the direction of observation by **S**.

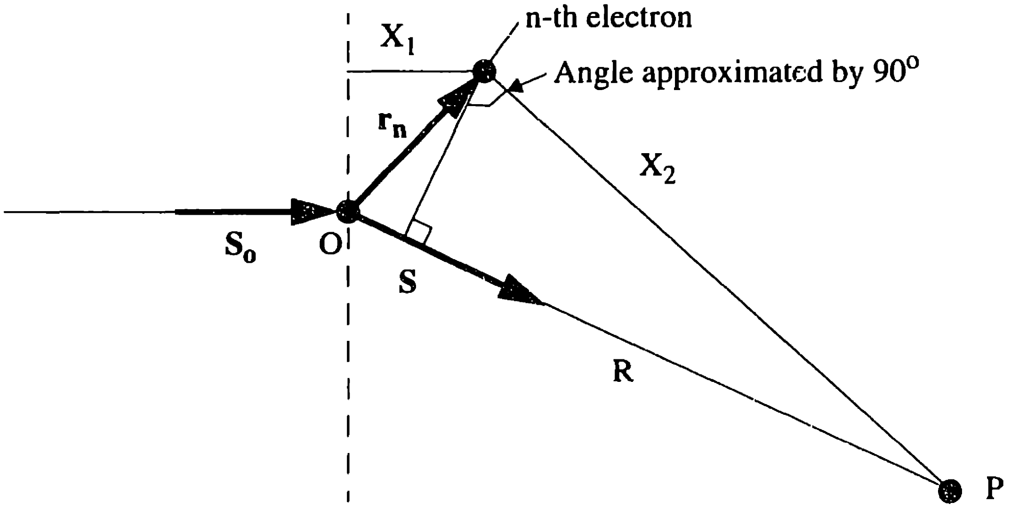

Figure A-11: Scattering observed from distance point P from a pair of electrons located at O and at $\mathbf{r_n}$ illuminated by a monochromatic plane wavefront.

The instantaneous electric field amplitude acting on electron n is:

$$E_1^n = E_o \cos\left(2\pi \upsilon t - \frac{2\pi X_1}{\lambda}\right) \tag{A.61}$$

while the magnitude and phase of the scattered beam as observed at distant point P must include the total pathlength with respect to the wavefront at O:

$$E_1^n = E_\perp \cos\left(2\pi\upsilon t - \frac{2\pi(X_1 + X_2)}{\lambda}\right) . \tag{A.62}$$

$E_\perp$ represents the amplitudes of the x-rays which are polarized perpendicular to the page and takes the form given in (A.1) (see main text). Applying the approximation that the distance $X_2 \gg |\boldsymbol{r}_n|$ (known as the plane wave approximation) $X_2 \rightarrow R$ in the denominator as well as $X_1 \rightarrow \boldsymbol{r}_n \bullet \boldsymbol{S}_o$ and $X_2 \rightarrow R - (\boldsymbol{r}_n \bullet \boldsymbol{S})$ in the argument of the cosine. Rearranging yields:

$$E_1^n = \frac{E_o e^2}{mc^2 R}\cos\left(2\pi\upsilon t - \frac{2\pi}{\lambda}(R - (\boldsymbol{S} - \boldsymbol{S}_o) \bullet \boldsymbol{r}_n)\right) . \tag{A.63}$$

Introducing the Euler relationship $e^{-ix} = \cos x - i\sin x$ with $i = \sqrt{-1}$, Equation A.1 can be written in complex notation as:

$$E = E_o e^{i\left(2\pi\upsilon t - \frac{2\pi x}{\lambda}\right)} . \tag{A.64}$$

Applying this notation to equation (A.60) yields:

$$E_1^n = \frac{E_o e^2}{mc^2 R} e^{2\pi i\left(\upsilon t - \frac{R}{\lambda}\right)} e^{\frac{2\pi i}{\lambda}(\boldsymbol{S} - \boldsymbol{S}_o) \bullet \boldsymbol{r}_n} \tag{A.65}$$

The total amplitude at P due to scattering by all the electrons in the group surrounding O yields:

$$E_{group} = \frac{E_o e^2}{mc^2 R} e^{2\pi i\left(\upsilon t - \frac{R}{\lambda}\right)} \sum_n e^{\frac{2\pi i}{\lambda}(\boldsymbol{S} - \boldsymbol{S}_o) \bullet \boldsymbol{r}_n} \tag{A.66}$$

This classical derivation assumes that all scattering is unmodified (i.e., elastic). This, however, is not the case. Quantum mechanical calculations demonstrate that the total scattered intensity due to elastic and inelastic collisions sum to give the intensity predicted by classical theory. A proper treatment of the elastic component necessitates the concept of a delocalized electron charge density (ρ) surrounding the atom. The scattered amplitude is multiplied by the element ρdV and summed to give the proper wave mechanical treatment of the electric field. The discrete summation of the scattering due to the electrons in an atom reduces to an integration of the contribution of the scattering from each element of the electron cloud surrounding the nucleus. The scattered amplitude from an atom is therefore:

$$E_{Atom} = \frac{E_o e^2}{mc^2 R} e^{2\pi i\left(\nu t - \frac{R}{\lambda}\right)} \int e^{\frac{2\pi i}{\lambda}(S - S_o) \bullet r_n} \rho dV_r \tag{A.67}$$

f, the scattering factor per electron is defined as the integral and represents the unmodified (elastic) scattering per electron expressed in electron units. The intensity of scattering from an atom is typically represented as:

$$i = \frac{I_{atom}}{I_o} = |f|^2 \tag{A.68}$$

and f is often written in terms of q:

$$f(q) = \int e^{iq \bullet r} \rho(r) dV_r \tag{A.69}$$

with

$$q = \frac{2\pi}{\lambda}(S - S_o) \, . \tag{A.70}$$

A.7 Bibliography

Hosemann, R. and S. N. Bagchi (1962). Direct Analysis of Diffraction by Matter. Amsterdam, North Holland.

Kakudo, M. and N. Kasai (1972). X-ray Diffraction by Polymers. Amsterdam, Elsevier.

Porod, G. (1982). General Theory. Small Angle X-ray Scattering. O. Glatter and O. Kratky. London, Academic Press: 17-51.

Warren, B. E. (1969). X-ray Diffraction. New York, Dover.